Solution-Processed Metal Oxide Gate Dielectrics and Their Implementations in Zinc Oxide Based Thin Film Transistors

Umar Muhammed Dikko

Msc Electronics and Electrical Engineering

A thesis submitted in partial fulfilments for the degree of Doctor of Philosophy

Engineering Department, Lancaster University, UK

February 2023

Abstract

Thin-film transistors (TFTs) based on oxide semiconductors are a promising technology for a host of large-volume electronic applications. Whilst progress on solution-processed oxide semiconductors has been rapidly advancing, research efforts towards the development of new dielectrics has been relatively slow, with most of the reported work performed using conventional dielectrics based in SiO_2. As a result, the majority of oxide transistors reported to date operate at relatively high voltages and hence consume significantly more power. In order to circumvent this bottleneck, recent work has been focussing on the development of low-voltage oxide transistors, including the use of high-k dielectrics, and several candidates have already been investigated and were mostly deposited by costly vacuum-based techniques.

This thesis investigates the properties of high-k metal oxides dielectrics as well as their implementation in TFTs, deposited by spray pyrolysis, a simple and versatile technique that combines high yield and large area compatibility.

In particular, the structural, optical, surface and electronic properties of tantalum aluminate ($TaAlO_x$), hafnium titanate ($HfTiO_4$) and zirconium silicate ($ZrSiO_4$) were studied as along with their performance as gate dielectric for TFTs implementing ZnO semiconducting channels. In all cases, stoichiometric $TaAlO_x$, $HfTiO_4$ and $ZrSiO_4$ films deposited at < 550 °C were found to be amorphous with surface roughness of < 1 nm. The optical bandgap varies between 4.9 eV and 8.8 eV, 5.8 eV and 3.8 eV, and 5.8 eV and 8 eV for $TaAlO_x$, $HfTiO_4$ and $ZrSiO_4$ films respectively. Their dielectric constant values vary between 24 and 7, 14 and 60, and 23 and 4.2 while their leakage current density at 1 MV/cm were between 10^{-6} A/cm^2 and 10^{-10} A/cm^2, 10^{-7} A/cm^2 and 10 A/cm^2, and 10^{-5} A/cm^2 and 10^{-4} A/cm^2 respectively. Particularly, the stoichiometric $TaAlO_x$, $HfTiO_4$ and $ZrSiO_4$ films exhibited the bandgap of 5.4 eV, 4.4 eV, 6.1 eV, dielectric constant of 13, 30, 12 and leakage current density at 1 MV/cm of 10^{-8} A/cm^2, 0.3 A/cm^2, 10^{-7} A/cm^2 respectively.

The performance of ZnO – based TFTs employing stochiometric $TaAlO_x$, $HfTiO_4$ and $ZrSiO_4$ gate dielectric showed promising characteristics such as low voltage operation of 4 V, high electron mobility of 16 cm^2/Vs, 7 cm^2/Vs, 57 cm^2/Vs, high current modulation ratio of 10^5, 10^7, 10^6, low subthreshold swing of 0.56 V/dec, 0.17 V/dec, 0.28 V/dec, interface trap density of 7.7 x 10^{12} cm^{-2}, 2.1 x 10^{12} cm^{-2}, 10^{13} cm^{-2} and threshold voltage of 3.2 V, 0.6 V, 0.1 V respectively.

In addition, the effect of post-deposition annealing (at 800 °C for 30 mins in air) on $HfTiO_4$ films were investigated. Stochiometric $HfTiO_4$ films were crystalline of an orthorhombic structure, surface roughness of 1.95 nm, optical bandgap of 4.36 eV, dielectric constant of 38 and leakage current density of 5 mA/cm^2 at 1 MV/cm.

These remarkable findings significantly demonstrated the achievement of a high-performance high-k metal oxide gate dielectrics as alternatives to the conventional SiO_2 for future integration into wide areas of electronic application.

Declaration

I hereby declare that this thesis is my own and has not been submitted in substantially the same form for the award of a higher degree elsewhere.

Umar Muhammed Dikko

Date: ………16th February, 2023…………

Signature…………………………………..……….

Acknowledgments

All praise and glory be to Allah, the All Mighty, for granting me the opportunity to witness the beginning and the ending of my research. My profound gratitude goes to my beloved mum, Hajiya Fatima Zauro and my dad Engr. M. U. Zauro who have been helpful, financially and whose constant love, support and guidance have been a source of courage and strength all through. I owe much to my brothers; Abdulmalik, Shehu, Abubakar and Bello and sisters; Aisha, Ramatu and Maryam for their unquantifiable support throughout the duration of my research program.

I wish to express my deep gratitude to my supervisor Dr. George Adamopoulos, for his concise and friendly advice, encouragement, understanding and patience in reading my thesis and making necessary corrections. Sir, I am immensely grateful for your endless effort and contributions towards my success. Furthermore, I would like to extend my gratitude to Prof Anthony Krier and Dr. Peter Carrington for their valuable feedbacks during my research. I would also like to extend my gratitude to my colleagues; Giorgos Antoniou, Ahmad Mohamed and Dimitris Afouxenidis for their support and contributions. Thank you very much I owe you a lot.

To that point, I should further express my gratitude to my friends for inspiring me and for all the good times we had together; Saud Aloltaibi, Farid Bello, Sadadi Ojoatre, Chiemela Victor Amaechi, Mohamed Milad and others that I did not mention.

Finally, I should give a special shout-out to the Mudans' (Mummy, Naima, Munira, Munir, Maryam, Hauwa & Aisha) for their well wishes and prayers, specifically Naima Mudan. Thank you very much for all the sacrifices you have to endure in making sure that I am up to the task that was put before me. Thank you very much for always preparing me for my presentations, indeed you have supported me emotionally from the beginning of my research until the end. Thank you very much for the encouragement, motivation and for always being there for me during my trying times. I pray Allah SWT bless you abundantly, Ameen.

Dedicated to my father

Late Engr. Mohammed Umar Zauro

Table of Contents

Abstract 2

Declaration 3

Acknowledgments 4

List of Figures 10

List of Tables 15

Thesis Outline 16

1 Introduction 17

1.1 Metal Oxides Based Thin Film Transistors 18

1.2 Thin-film Deposition techniques 19

1.2.1 Vacuum-based Deposition 20

1.2.1.1 Metal Organic Chemical Vapour Deposition (MOCVD) 20

1.2.1.2 Sputtering 20

1.2.1.3 Molecular Beam Epitaxy (MBE) 21

1.2.1.4 Thermal Evaporation 22

1.2.1.5 Pulsed Laser Deposition (PLD) 23

1.2.1.6 Atomic Layer Deposition (ALD) 23

1.2.2 Solution-based Deposition 24

1.2.2.1 Spin coating 24

1.2.2.2 Dip coating 25

1.2.2.3 Spray pyrolysis 25

1.3 References 28

2 Theory and Operational Characteristics 36

2.1 Introduction 37

2.2 Metal-Insulator-Metal (MIM) Devices 37

2.2.1 Impedance Spectroscopy 38

2.2.2 Leakage Current Conduction Mechanisms 39

2.2.2.1 Schottky Emission (SE) Conduction mechanism 40

2.2.2.2 Fowler Nordheim (FN) Tunneling Conduction mechanism 41

2.2.2.3 Poole-Frenkel (PF) Conduction mechanism 43

2.3 Metal Oxide Semiconductor (MOS) Operation 44

2.3.1 Accumulation 45

2.3.2 Depletion ... 46

2.3.3 Inversion regime ... 47

2.4 Metal Oxide Semiconductor Field Effect Transistor (MOSFTET) ... 47

2.4.1 Mobility (μ) ... 50

2.4.2 Current modulation ratio ... 50

2.4.3 Threshold/Turn on Voltage ... 51

2.4.4 Subthreshold swing (SS) ... 52

2.5 References ... 53

3 Experimental: Deposition and Characterization ... 55

3.1 Introduction ... 56

3.2 Experiment ... 56

3.2.1 Spray Pyrolysis ... 56

3.2.2 TGA)/ (DSC) ... 60

3.2.3 Thermal Evaporation ... 61

3.3 Characterization ... 62

3.3.1 Single Wavelength Ellipsometry ... 62

3.3.2 X-ray Diffraction (XRD) ... 63

3.3.3 Atomic Force Microscopy (AFM) ... 66

3.3.4 Ultraviolet Visible (UV-Vis) spectroscopy ... 67

3.3.5 Impedance spectroscopy ... 70

3.3.6 Fourier Transform Infrared Spectroscopy (FTIR) ... 71

3.3.7 I – V measurement ... 72

3.4 References ... 73

4 Tantalum Aluminate $Ta_{1-x}Al_xO_y$ Thin Films ... 77

4.1 Introduction ... 78

4.2 Precursors ... 89

4.2.1 Thermal Properties of Precursors ... 89

4.3 Thin Film Deposition & Characterisation ... 91

4.4 UV-Vis Spectroscopy ... 92

4.5 Structural/Surface Properties ... 96

4.5.1 Grazing Incidence X-Ray Diffraction (GIXRD) ... 96

4.5.2 Atomic Force Microscopy ... 97

4.6 Electrical Properties 99
4.6.1 Impedance Spectroscopy 99
4.6.2 I – V characterization 102
4.6.3 Field Effect Measurement 107
4.7 Conclusion 113
4.8 References 114
5 Hafnium Titanate $Hf_{1-x}Ti_xO_y$ Thin Films 123
5.1 Introduction 124
5.2 Precursors 130
5.2.1 Thermal Properties of Precursors 130
5.3 Thin Film Deposition & Characterization 132
5.4 UV-Vis Spectroscopy 132
5.5 Fourier Transform Infrared Spectroscopy (FTIR) 136
5.6 Structural and Surface Properties 137
5.6.1 Grazing Incidence X-Ray Diffraction (GIXRD) 137
5.6.2 Atomic Force Microscopy (AFM) 138
5.7 Electrical Properties 139
5.7.1 Impedance Spectroscopy 140
5.7.2 I – V Characterization 143
5.7.3 Field Effect Measurement 145
5.8 Conclusion 148
5.9 Effects of Post-deposition Annealing of $Hf_{1-x}Ti_xO_y$ Films 150
5.10 UV-Vis Spectroscopy 150
5.11 Structural and Surface Properties 152
5.11.1 GIXRD 152
5.11.2 AFM 154
5.12 Electrical Properties 154
5.12.1 Impedance spectroscopy 154
5.12.2 I – V measurements 157
5.13 Conclusion 160
5.14 References 162

6 Zirconium Silicate $Zr_{1-x}Si_xO_y$ Thin Films 169
6.1 Introduction 170
6.2 Precursors 174
6.3 Thermal Properties of Precursor 175
6.4 Thin Film Deposition & Characterization 176
6.5 UV-Vis Spectroscopy 177
6.6 Fourier Transform Infrared Spectroscopy (FTIR) 181
6.7 Structural and Surface Properties 181
6.7.1 Grazing Incidence X-Ray Diffraction (GIXRD) 182
6.7.2 Atomic Force Microscopy (AFM) 183
6.8 Electrical Properties 184
6.8.1 Impedance Spectroscopy 184
6.8.2 I – V Characterization 188
6.8.3 Field Effect Measurement 191
6.9 Conclusion 197
6.10 References 198
7 Summary, Conclusions and Further Work 204
7.1 Summary 205
7.2 Conclusion 208
7.3 Further Work 209
7.4 References 211

List of Figures

FIGURE 1- 1. A SCHEMATIC OF MOCVD SYSTEM [28]. 20
FIGURE 1- 2. A SCHEMATIC OF A TYPICAL SPUTTERING SYSTEM [29]. 21
FIGURE 1- 3. A SCHEMATIC OF A TYPICAL MBE SYSTEM [32]. 22
FIGURE 1- 4. A SCHEMATIC OF A THERMAL EVAPORATION SYSTEM [32]. 22
FIGURE 1- 5. A SCHEMATIC OF A PLD SETUP [35]. 23
FIGURE 1- 6. A SCHEMATIC OF AN ALD CYCLE [36]. 24
FIGURE 1- 7. AN ILLUSTRATION DESCRIBING THE STAGES OF A SPIN COATING PROCESS [38]. 25
FIGURE 1- 8. AN ILLUSTRATION OF A TYPICAL DIP COATING PROCESS [39]. 25

FIGURE 2- 1. METAL-INSULATOR-METAL (MIM) STRUCTURE. 37
FIGURE 2- 2. EQUIVALENT CIRCUIT OF A MIM CAPACITOR [7]. 38
FIGURE 2- 3. CLASSIFICATIONS OF CONDUCTION MECHANISMS [1]. 40
FIGURE 2- 4. ENERGY BAND DIAGRAM OF SCHOTTKY EMISSION (SE) IN METAL-INSULATOR-METAL (MIM) STRUCTURES. 40
FIGURE 2- 5. ENERGY BAND DIAGRAM OF FOWLER NORDHIEM (FN) IN METAL-INSULATOR-METAL (MIM) STRUCTURES. 41
FIGURE 2- 6. ENERGY BAND DIAGRAM OF DIRECT TUNNELING (DT) IN METAL-INSULATOR-METAL (MIM) STRUCTURES. 42
FIGURE 2- 7. ENERGY BAND DIAGRAM OF POOLE FRENKEL (PF) EMISSION IN METAL-INSULATOR-METAL (MIM) STRUCTURES. 43
FIGURE 2- 8. A SCHEMATIC OF A METAL OXIDE SEMICONDUCTOR FIELD EFFECT TRANSISTOR (MOSFET). 44
FIGURE 2- 9. ENERGY BAND DIAGRAM OF AN IDEAL MOS CAPACITOR EMPLOYING N-TYPE SEMICONDUCTOR AT EQUILIBRIUM (V_{APP}=0). (1) Qϕ_M: ϕ_M IS THE METAL WORK FUNCTION, (2) Qχ_I: χ_I IS THE ELECTRON AFFINITY OF THE INSULATOR, (3) Qχ: χ IS THE ELECTRON AFFINITY OF THE SEMICONDUCTOR, (4) E_G/2: E_G IS THE BAND GAP OF THE SEMICONDUCTOR, (5) Qϕ_N: ϕ_N IS THE FERMI POTENTIAL WITH RESPECT TO THE CONDUCTION BAND EDGE, (6) QΨ_{BN}: Ψ_{BN} IS THE FERMI POTENTIAL WITH RESPECT TO THE MID-GAP EDGE. 45
FIGURE 2- 10. SCHEMATIC OF AN ENERGY-BAND DIAGRAM OF A MOS CAPACITOR OPERATING IN AN ACCUMULATION REGIME. 46
FIGURE 2- 11. SCHEMATIC OF AN ENERGY-BAND DIAGRAM OF A MOS CAPACITOR OPERATING IN A DEPLETION REGIME 46
FIGURE 2- 12. SCHEMATIC OF AN ENERGY-BAND DIAGRAM OF A MOS CAPACITOR OPERATING IN AN INVERSION REGIME. 47
FIGURE 2- 13. TRANSFER CHARACTERISTICS (A) ENHANCEMENT MODE AND (B) DEPLETION MODE MOSFETS FOR AN N-TYPE SEMICONDUCTOR. 48
FIGURE 2- 14. SCHEMATICS SHOWING SOME OF THE MOST CONVENTIONAL TFT STRUCTURES, ACCORDING TO THE POSITION OF THE GATE ELECTRODE AND TO THE DISTRIBUTION OF THE ELECTRODES RELATIVELY TO THE SEMICONDUCTOR [22]. 49
FIGURE 2- 15. TYPICAL A) OUTPUT AND B) TRANSFER CHARACTERISTICS OF A N-TYPE OXIDE TFT [22]. 51

FIGURE 3- 1. A TYPICAL WATER BOILING GRAPH CURVE AT 1 ATMOSPHERE [8]. 58
FIGURE 3- 2. SPRAY PYROLYSIS TECHNIQUE FOR THIN-FILM DEPOSITION [9]. 59
FIGURE 3- 3. AN IMAGE SHOWING VARIETY OF SUBSTRATES DURING SPRAY COATING PROCESS ON A PREHEATED SURFACE. 59
FIGURE 3- 4. SCHEMATIC OF A TYPICAL TGA/DSC CURVE OF ALUMINIUM ACETYLACETONATE POWDER. 61
FIGURE 3- 5. A SCHEMATIC OF A TYPICAL ELECTRON BEAM SOURCE THERMAL EVAPORATION SYSTEM [28]. 62

Figure 3- 6. Single wavelength ellipsometer setup [29]. 63
Figure 3- 7. Schematic of X-ray Diffraction from a periodic atomic structure. 64
Figure 3- 8. Schematic of X-ray Diffractometer measurement [34]. 65
Figure 3- 9. Schematic of X-ray Diffractometer measurement [34]. 65
Figure 3- 10. Illustration of GIXRD at (a) high incident angle and, (b) at low incident angle [35]. 66
Figure 3- 11. A schematic of AFM setup [36]. 67
Figure 3- 12. The extrapolation of a linear curve of a Tauc plot to determine the direct E_G of ZnO thin films. 68
Figure 3- 13. The E_U plot of ZnO thin films. 69
Figure 3- 14. Optical path of a UV-Vis spectrometer [41]. 70
Figure 3- 15. An example of geometric capacitance as a function of frequency of Ta_2O_5 films. 71
Figure 3- 16. Schematic of interferometer used in FTIR [43]. 72

Figure 4- 1. Unit cell of β-Ta_2O_5 (space group Pccm). Ta: purple and O: dark grey. The unit cell boundaries are displayed as dashed lines [27]. 79
Figure 4- 2. Crystal structure of δ-Ta_2O_5. Light balls correspond to Ta atoms while dark circles correspond to O atoms [35]. 79
Figure 4- 3. Band gap and dielectric constant of selected metal oxides [52]. 82
Figure 4- 4. Calculated band offsets of selected dielectrics. The values are normalised to the VBM of ZnO. The dotted line indicates the minimum of 1 eV for CBO [23]. 83
Figure 4- 5. The crystalline structure of α-Al_2O_3. Blue balls: Al atoms, Red balls: O atoms [58]. 84
Figure 4- 6. Thermogravimetric analysis (black line) and differential scanning calorimetry (blue line) of 4 mg $TaCl_5$ powder. 90
Figure 4- 7. Thermogravimetric analysis (black line) and differential scanning calorimetry (blue line) of 9 mg $Al(acac)_3$ powder. 91
Figure 4- 8. A schematic of a metal-insulator-metal (MIM) stack of glass/ITO/ $Ta_{1-x}Al_xO_y$/Al gate dielectric. 92
Figure 4- 9. Transmittance %T spectra of $Ta_{1-x}Al_xO_y$ films for different [Al] to [Ta] ratios. 92
Figure 4- 10. Tauc plots of as-deposited $Ta_{1-x}Al_xO_y$ films with different [Al] to [Ta] ratios. 93
Figure 4- 11. Optical bandgap of $Ta_{1-x}Al_xO_y$ films as a function of the [Al]/ [Al+Ta] atomic ratio. The solid line is a guide to the eye. 94
Figure 4- 12. Absorption coefficient spectra of $Ta_{1-x}Al_xO_y$ films with different [Al] to [Ta] ratios. 95
Figure 4- 13. Urbach tail energy, E_U of $Ta_{1-x}Al_xO_y$ films as function of the [Al]/ [Al + Ta] atomic ratio. The solid line is a guide to the eye. 95
Figure 4- 14. GIXRD patterns of selected $Ta_{1-x}Al_xO_y$ films deposited by spray pyrolysis on silicon substrates. 96
Figure 4- 15. AFM friction and topography images of $Ta_{1-x}Al_xO_y$ films on silicon substrates. 98
Figure 4- 16. Static dielectric constant dispersions of $Ta_{1-x}Al_xO_y$ films in the frequency range of 1kHz-4 MHz. 99
Figure 4- 17. Static dielectric constant of $Ta_{1-x}Al_xO_y$ films as a function of [Al]/ [Al + Ta] atomic ratio calculated at 1 kHz. The solid line is guide to the eye. 100
Figure 4- 18 Nyquist plots and equivalent circuit (inset) of (a) TaO_x (b) $Ta_{70}Al_{30}O_x$ (c) $Ta_{60}Al_{40}O_x$ (d) $Ta_{50}Al_{50}O_x$ (e) $Ta_{40}Al_{60}O_x$ and (e) AlO_x devices. 101
Figure 4- 19. Leakage current density (J) of $Ta_{1-x}Al_xO_y$ MIMs with different [Al] to [Ta] ratios. 102

Figure 4- 20. Leakage current density (J) of $Ta_{1-x}Al_xO_y$ films at 1 and 2 MV/cm as a function of [Al]/ [Al + Ta] atomic ratio. 102
Figure 4- 21. Leakage current density (J) versus optical bandgap of $Ta_{1-x}Al_xO_y$ films with different [Al] to [Ta] ratios. 103
Figure 4- 22. Schottky emission plots of (a) TaO_x (b) $Ta_{70}Al_{30}O_x$ (c) $Ta_{60}Al_{40}O_x$ (d) $Ta_{50}Al_{50}O_x$ (e) $Ta_{40}Al_{60}O_x$ and (e) AlO_x films. 104
Figure 4- 23. Fowler-Nordheim plots of (a) TaO_x (b) $Ta_{70}Al_{30}O_x$ (c) $Ta_{60}Al_{40}O_x$ (d) $Ta_{50}Al_{50}O_x$ (e) $Ta_{40}Al_{60}O_x$ and (e) AlO_x films. 105
Figure 4- 24. Poole-Frenkel plots of (a) TaO_x (b) $Ta_{70}Al_{30}O_x$ (c) $Ta_{60}Al_{40}O_x$ (d) $Ta_{50}Al_{50}O_x$ (e) $Ta_{40}Al_{60}O_x$ and (e) AlO_x films. 105
Figure 4- 25. (a) effective mass of the electron and (b) barrier height of $Ta_{1-x}Al_xO_y$ films as a function of [Al]/ [Al + Ta] atomic ratio. 107
Figure 4- 26. A schematic of deposited BG – TC ZnO-based TFT architecture employing $Ta_{1-x}Al_xO_y$ gate dielectric. 108
Figure 4- 27. (a) Transfer and (b) output characteristics of ZnO – based TFTs employing TaO_x gate dielectric. 108
Figure 4- 28. (a) Transfer and (b) output characteristics of ZnO – based TFTs employing $Ta_{70}Al_{30}O_y$ gate dielectric. 109
Figure 4- 29. (a) Transfer and (b) output characteristics of ZnO – based TFTs employing $Ta_{60}Al_{40}O_x$ gate dielectric. 109
Figure 4- 30. (a) Transfer and (b) output characteristics of ZnO – based TFTs employing $Ta_{50}Al_{50}O_x$ gate dielectric. 110
Figure 4- 31. (a) Transfer and (b) output characteristics of ZnO – based TFTs employing $Ta_{40}Al_{60}O_x$ gate dielectric. 110
Figure 4- 32. (a) Transfer and (b) output characteristics of ZnO – based TFTs employing as-deposited AlO_x gate dielectric. 111
Figure 4- 33. (a) Electron mobility (left axis) and current modulation ratio (right axis), (b) Threshold voltage (V_{TH}), (c) Subthreshold swing (SS) and (d) Interface trap density of ZnO – based TFTs employing $Ta_{1-x}Al_xO_y$ gate dielectric. 112

Figure 5- 1. The unit cells of three phases of HfO_2, showing the small atomic displacements, and presentation of the coordination environments during the transformation between the phases. The dark yellow circles represents Hf atoms while the red ones represents O atoms [5]. 124
Figure 5- 2. The unit cells of three polymorphs of TiO_2. (a) anatase, (b) rutile, and (c) brookite. The green spheres represent Ti atoms and the small red spheres represents O atoms [45]. 127
Figure 5- 3. TGA (black line) DSC (blue line) of 19 mg hafnium chloride powder. 131
Figure 5- 4. TGA (black line) and DSC (blue line) of 84 mg titanium chloride liquid. 131
Figure 5- 5. A schematic of a metal-insulator-metal (MIM) stack of glass/ITO/ $Hf_{1-x}Ti_xO_y$/Al gate dielectric. 132
Figure 5- 6. Transmittance %T spectra of as-deposited $Hf_{1-x}Ti_xO_y$ films for different [Ti] to [Hf] ratios. 133
Figure 5- 7. Tauc plots of as-deposited $Hf_{1-x}Ti_xO_y$ films with different [Ti] to [Hf] ratios. 133
Figure 5- 8. Optical bandgap of as-deposited $Hf_{1-x}Ti_xO_y$ films as a function of the [Ti]/ [Ti + Hf] atomic ratio. The solid line is a guide to the eye. 134
Figure 5- 9. Absorption coefficient spectra of as-deposited $Hf_{1-x}Ti_xO_y$ films with different [Ti] to [Hf] ratios. 135

Figure 5- 10. Urbarch tail energy (E_U) of as-deposited $Hf_{1-x}Ti_xO_y$ films as a function of the [Ti]/ [Ti + Hf] atomic ratio. The solid line is a guide to the eye. 135
Figure 5- 11. Absorbance spectra of as-deposited $Hf_{1-x}Ti_xO_y$ *films with different [Ti] to [Hf] ratios.* 136
Figure 5- 12. GIXRD patterns of as-deposited $Hf_{1-x}Ti_xO_y$ films deposited by spray pyrolysis on silicon substrates. 137
Figure 5- 13. AFM topography images (RMS roughness inset) of as-deposited $Hf_{1-x}Ti_xO_y$ *with different [Ti] to [Hf] ratios.* 139
Figure 5- 14. Static dielectric constant dispersions of as-deposited $Hf_{1-x}Ti_xO_y$ films in the frequency range between 1 kHz and 50 MHz. 140
Figure 5- 15. Static dielectric constant of as-deposited $Hf_{1-x}Ti_xO_y$ films as a function of [Ti]/ [Ti + Hf] atomic ratio calculated at 1 kHz. The solid line is a guide to the eye. 141
Figure 5- 16. Nyquist plots and equivalent circuit (inset) of as-deposited (a) HfO_x (b) $Hf_{75}Ti_{25}O_x$ (c) $Hf_{50}Ti_{50}O_x$ (d) $Hf_{25}Ti_{75}O_x$ and (e) TiO_x capacitors. 142
Figure 5- 17. Leakage current density (J) of as-deposited $Hf_{1-x}Ti_xO_y$ films at 1 MV/cm as a function of [Ti]/ [Ti + Hf] atomic ratio. The solid line is a guide to the eye. 143
Figure 5- 18. Schottky emission plots of (a) HfO_x (b) $Hf_{75}Ti_{25}O_x$ (c) $Hf_{50}Ti_{50}O_x$ (d) $Hf_{25}Ti_{75}O_x$ and (e) TiO_x films. 144
Figure 5- 19. Fowler-Nordheim plots of (a) HfO_x (b) $Hf_{75}Ti_{25}O_x$ (c) $Hf_{50}Ti_{50}O_x$ (d) $Hf_{25}Ti_{75}O_x$ and (e) TiO_x films. 144
Figure 5- 20. Poole-Frenkel plots of (a) HfO_x (b) $Hf_{75}Ti_{25}O_x$ (c) $Hf_{50}Ti_{50}O_x$ (d) $Hf_{25}Ti_{75}O_x$ and (e) TiO_x films. 145
Figure 5- 21. BG – TC ZnO-based TFT architecture employing $Hf_{1-x}Ti_xO_y$ gate dielectric. 146
Figure 5- 22. (a) Transfer and (b) output characteristics of ZnO – based TFTs employing as-deposited HfO_x gate dielectric. 146
Figure 5- 23. (a) Transfer and (b) output characteristics of ZnO – based TFTs employing as-deposited stoichiometric $Hf_{1-x}Ti_xO_y$ gate dielectric. 147
Figure 5- 24. Band diagrams of ZnO, HfO_2, $Hf_{50}Ti_{50}O_x$ and TiO_2 and estimated conduction and valence band offsets on ZnO. 148
Figure 5- 25. Tauc plots of $Hf_{1-x}Ti_xO_y$ films with different [Ti] to [Hf] ratios after annealing at 800 °C for 30 mins in air. 150
Figure 5- 26. Optical bandgap of $Hf_{1-x}Ti_xO_y$ films as a function of the [Ti]/ [Ti +Hf] atomic ratio after annealing at 800 °C for 30 mins in air. 151
Figure 5- 27. Urbarch tail energy (E_U) of $Hf_{1-x}Ti_xO_y$ films as a function of the [Ti]/ [Ti + Hf] atomic ratio after annealing at 800 °C for 30 mins in air. 152
Figure 5- 28. GIXRD patterns of annealed $Hf_{1-x}Ti_xO_y$ films with different [Ti] to [Hf] ratios. 153
Figure 5- 29. AFM topography images (RMS roughness inset) of $Hf_{1-x}Ti_xO_y$ films with different [Ti] to [Hf] ratios after annealing at 800 °C for 30 mins in air. 154
Figure 5- 30. Static dielectric constant dispersions of $Hf_{1-x}Ti_xO_y$ films in the frequency range of 1 kHz – 50 MHz after annealing at 800 °C for 30 mins in air. 155
Figure 5- 31. Static dielectric constant of $Hf_{1-x}Ti_xO_y$ films as a function of [Ti]/ [Ti + Hf] atomic ratio after annealing at 800 °C for 30 mins in air. 155
Figure 5- 32. Nyquist plots and equivalent circuit (inset) of annealed (a) $Hf_{75}Ti_{25}O_x$ (b) $Hf_{50}Ti_{50}O_x$ and (c) $Hf_{25}Ti_{75}O_x$ films. 156
Figure 5- 33. Leakage current density (J) of $Hf_{1-x}Ti_xO_y$ films at 1 MV/cm as a function of [Ti]/ [Ti + Hf] atomic ratio after annealing at 800 °C for 30 mins in air. 157

Figure 5- 34. Leakage current density versus voltage of stochiometric $Hf_{1-x}Ti_xO_y$ films after annealing at 800 °C for 30 mins in air 158
Figure 5- 35. Schottky plots of annealed (a) $Hf_{75}Ti_{25}O_x$ (b) $Hf_{50}Ti_{50}O_x$ and (c) $Hf_{25}Ti_{75}O_x$ films. . 159
Figure 5- 36. Fowler-Nordheim plots of annealed (a) $Hf_{75}Ti_{25}O_x$ (b) $Hf_{50}Ti_{50}O_x$ and (c) $Hf_{25}Ti_{75}O_x$ films. 159
Figure 5- 37. Poole-Frenkel plots of annealed (a) $Hf_{75}Ti_{25}O_x$ (b) $Hf_{50}Ti_{50}O_x$ and (c) $Hf_{25}Ti_{75}O_x$ films. 160

Figure 6- 1. The three polymorphs of ZrO_2: (a) cubic, (b) tetragonal and (c) monoclinic [20]. .. 171
Figure 6- 2. TGA (black line) and DSC (blue line) of 6 mg zirconium acetylacetonate powder. .. 175
Figure 6- 3. TGA (black line) and DSC (blue line) of 10 mg silicon chloride solution. 176
Figure 6- 4. A schematic of a metal-insulator-metal (MIM) stack of glass/ITO/ $Zr_{1-x}Si_xO_y$/Al gate dielectric. 177
Figure 6- 5. Transmittance T% of spray coated $Zr_{1-x}Si_xO_y$ films with different [Si^{4+}] to [Zr^{4+}] ratio deposited by spray pyrolysis on fused silica substrates. 177
Figure 6- 6. Tauc plots of spray coated $Zr_{1-x}Si_xO_y$ films with different [Si] to [Zr] ratios. 178
Figure 6- 7. Optical bandgap of $Zr_{1-x}Si_xO_y$ films as a function of the [Si]/ [Si + Zr] atomic ratio. The solid line is a guide to the eye. 179
Figure 6- 8. Urbach plots of $Zr_{1-x}Si_xO_y$ films with different [Si] to [Zr] ratios. 180
Figure 6- 9. Urbach tail energy (E_U) of $Zr_{1-x}Si_xO_y$ films as a function of [Si]/ [Si + Zr] atomic ratio. The solid line is a guide to the eye. 180
Figure 6- 10. FTIR spectra of as-deposited $Zr_{1-x}Si_xO_y$ films with different [Si^{4+}] to [Zr^{4+}] ratio. 181
Figure 6- 11. GIXRD patterns of $Zr_{1-x}Si_xO_y$ films deposited by spray pyrolysis on silicon substrates. 182
Figure 6- 12. AFM topography images (RMS roughness inset) of $Zr_{1-x}Si_xO_y$ films with different [Si] to [Zr] ratios on silicon substrates. 183
Figure 6- 13. RMS values of $Zr_{1-x}Si_xO_y$ films as a function of [Si]/ [Si + Zr] atomic ratio. 184
Figure 6- 14. Static dielectric constant dispersions of $Zr_{1-x}Si_xO_y$ films in the frequency range of 1 kHz – 50 MHz. 185
Figure 6- 15. Static dielectric constant of $Zr_{1-x}Si_xO_y$ films (at 30 kHz) as a function of [Si]/ [Si + Zr] atomic ratio. The solid line is a guide to the eye. 186
Figure 6- 16. Nyquist plots and equivalent circuit (inset) of (a) ZrO_x (b) $Zr_{75}Si_{25}O_x$ (c) $Zr_{50}Si_{50}O_x$ (d) $Zr_{25}Si_{75}O_x$ and (e) SiO_x films. 187
Figure 6- 17. Static dielectric constant versus optical bandgap of $Zr_{1-x}Si_xO_y$ films. The solid line is a guide to the eye. 188
Figure 6- 18. J @ 1 MV/cm of $Zr_{1-x}Si_xO_y$ films recorded at 1 MV/ as a function of [Si]/ [Si + Zr] atomic ratio. The solid line is guide to the eye. 189
Figure 6- 19. Schottky emission plots of (a) ZrO_x (b) $Zr_{75}Si_{25}O_x$ (c) $Zr_{50}Si_{50}O_x$ (d) $Zr_{25}Si_{75}O_x$ and (e) SiO_x films. 190
Figure 6- 20. Fowler-Nordheim plots of (a) ZrO_x (b) $Zr_{75}Si_{25}O_x$ (c) $Zr_{50}Si_{50}O_x$ (d) $Zr_{25}Si_{75}O_x$ and (e) SiO_x films. 190
Figure 6- 21. Poole-Frenkel plots of (a) ZrO_x (b) $Zr_{75}Si_{25}O_x$ (c) $Zr_{50}Si_{50}O_x$ (d) $Zr_{25}Si_{75}O_x$ and (e) SiO_x films. 191
Figure 6- 22. BG – TC ZnO-based TFT architecture employing $Zr_{1-x}Si_xO_y$ gate dielectric. 192
Figure 6- 23. (a) Transfer and (b) output characteristics of ZnO – based TFTs employing ZrO_x gate dielectric. 193

Figure 6- 24. (a) Transfer and (b) output characteristics of ZnO – based TFTs employing $Zr_{75}Si_{25}O_x$ gate dielectric 193
Figure 6- 25. (a) Transfer and (b) output characteristics of ZnO – based TFTs employing $Zr_{50}Si_{50}O_x$ gate dielectric. 194
Figure 6- 26. (a) Transfer and (b) output characteristics of ZnO – based TFTs $Zr_{25}Si_{75}O_x$ gate dielectric. 194
Figure 6- 27. (a) Transfer and (b) output characteristics of ZnO – based TFTs SiO_x gate dielectric. 195
Figure 6- 28. (a) Electron mobility (b) Current modulation ratio, (c) Threshold voltage, (d) Subthreshold swing (SS) and (e) Interface trap density of ZnO – based TFTs employing spray coated stoichiometric $Zr_{1-x}Si_xO_y$ gate dielectric. 196

List of Tables

Table 3- 1. Selected previous works carried out by spray pyrolysis technique (Al_2O_3: aluminium (III) oxide, Al $(NO_3).9H_2O$: aluminium nitrate nonahydrate, Al $(C_5H_7O_2)_3$: aluminium acetylacetonate, $AlCl_3$: aluminium (III) chloride, 2-ME: 2-methoxyethanol, MeOH: methanol, DMF: dimethylformamide, DIW: deionized water, EtOH: ethanol, Acac: acetylacetone, HfO_2: hafnium oxide, $HfCl_4$: hafnium (IV) chloride, ZrO_2: zirconium oxide, Zr $(C_5H_7O_2)_4$: zirconium acetylacetonate, ZnO: zinc oxide, Zn (OAc). $2H_2O$: zinc acetate dilhydrate, In_2O_3: indium oxide, In $(NO_3)_3$. H_2O: indium (III) nitrate hydrate, In $(C_2H_3O_2)_3$: indium (III) acetate, SnO_2: tin oxide, Sn $(CH_3CO_2)_2$: tin (II) acetate, La_2O_3: lanthanum oxide, La $(NO_3)_3.6H_2O$: lanthanum (III) nitrate hexahydrate). 60

Table 4- 1. Selected previous work on Ta_2O_5 gate dielectric and TFT characteristics (T_{dep}: deposition temperature, k: dielectric constant, J_{leak}: leakage current density, μ : electron mobility, SS: subthreshold swing, $I_{on/off}$: current modulation ratio, V_{th}: threshold voltage). 80
Table 4- 2. Selected previous work on solution processed Al_2O_3 gate dielectric and their TFT characteristics. 85
Table 4- 3. Selected previous work on solution processed metal aluminate gate dielectric and their TFT characteristics (LAO: lanthanum aluminate, HAO: hafnium aluminate, TAO: titanium aluminate, NAO: niobium aluminate, ZAO: zirconium aluminate, Ta-AO: tantalum aluminate). 88

Table 5- 1. Selected previous work on solution processed HfO_2 gate dielectric and their TFT characteristics. (T_{dep}: deposition temperature, k: dielectric constant, J_{leak}: leakage current density, μ : electron mobility, SS: subthreshold swing, $I_{on/off}$: current modulation ratio, V_{th}: threshold voltage). 126
Table 5- 2. Selected previous works on properties of HTO gate dielectric. 129

Table 6- 1. Selected previous work on solution processed ZrO_2 gate dielectric and their TFT characteristics (T_{dep}: deposition temperature, k: dielectric constant, J_{leak}: leakage current density, μ : electron mobility, SS: subthreshold swing, $I_{on/off}$: current modulation ratio, V_{th}: threshold voltage). 172
Table 6- 2. Review on selected reports on ZSO gate dielectrics. 174

Thesis Outline

The key outlines of the thesis are divided into two main parts. The first part comprises of four chapters, and it presents an overview on the theoretical aspect of the metal oxide dielectrics and its implementation as gate dielectrics for TFT applications. The second part comprises of the remaining chapters and was focussed on its experimental aspect including the summary, conclusion and recommendation for future study.

In chapter one, an introduction to the MOS-based TFTs as upgrades to other compound semiconductors was discussed. Additionally, the importance of high-k dielectrics and TCOs as gate electrodes for high performance TFT stack was also discussed. Also, several deposition techniques including the vacuum-based and solution-based techniques used for deposition of metal oxides thin films were also discussed.

In chapter two, the theory and operational characteristics of dielectrics and MOSFETs were discussed. For the dielectrics, the impedance characteristics and the leakage current conduction mechanisms of MIM-based devices were highlighted whereas for the MOSFETs, their mode of operations such as enhancement and depletion, their current and mobility equations both at linear and saturation regime were also highlighted.

In chapter three, the experiment and characterization techniques used for metal oxides deposition were discussed.

In chapter four, five and six, the investigations of tantalum aluminate, hafnium titanate and zirconium silicate thin films as well as their implementations in ZnO – based TFTs were studied.

Finally, in chapter seven, the summary and conclusion of the experimental chapters (i.e., 4, 5 & 6) were briefly summarized and the recommendations for future study were suggested.

1 Introduction

1.1 Metal Oxides Based Thin Film Transistors

The discovery of metal oxide semiconductors (MOS) in modern electronics today have shown tremendous attributes compared to other semiconductors such as hydrogenated amorphous silicon (a-Si:H), polycrystalline silicon (poly-si) and other III – V semiconductors. MOS have demonstrated excellent properties including excellent carrier mobility even in amorphous state, mechanical stress tolerance, compatibility with organic dielectric materials and high optical transparency [1]. MOS exhibits high optical transparency (above 80 %) in the visible spectrum region (400 – 700 nm) and wide bandgaps (E_g > 3 eV). Some of the most commonly used MOS are zinc oxide (ZnO), indium (III) oxide (In_2O_3) and tin oxide (SnO_2), copper oxide (CuO_2) and gallium oxide (Ga_2O_3).

Besides MOS, there are other metal oxide such as transparent conductive oxides (TCOs) and metal oxides dielectrics (MOD). The TCOs emerge as a vital component for the development of large number of modern devices such as flat panel displays (FPDs), touch screens, portable electronics flexible electronics and solar cells [1]. They are of high transparency (above 80 %) in visible spectrum region (400 – 700 nm) and high electrical conductivity (1 – 10^4 S/cm) [2]. In TFTs stack, TCOs are usually used as gate and source/drain (S/D) electrodes. An example of a typical TCO material used in TFTs is indium tin oxide (ITO). ITO is one of the most commercially used TCOs in display industries due to its excellent transparency and conductivity. It contains 10 % SnO_2 and 90 % In_2O_3. It has been deposited by several techniques including vacuum-based and solution-based techniques and its film's structure are polycrystalline in nature. There are other TCOs materials such as aluminium doped zinc oxide (AZO), antimony doped tin oxide (ATO) and fluorine doped tin oxide (FTO) [3].

The MOD on the other hand, are mainly the potential high-k dielectrics. Such high-k dielectrics includes the transition [4] and rare earth [5] metal oxides and are highly considered as potential candidates to replace the conventional silicon dioxide (SiO_2) gate dielectric. Oxides such as aluminium oxide (Al_2O_3), tantalum pentoxide (Ta_2O_5), yttrium (III) oxide (Y_2O_3), lanthanum (III) oxide (La_2O_3), zirconium oxide (ZrO_2), hafnium oxide (HfO_2) have already been reported as potential MOD [6]–[10].

MOS-based TFTs offers unique properties compared to other semiconductors (a-Si:H, poly-si and III – V semiconductors) due to its enhanced carrier mobility, high optical transparency, high switching speeds and low power consumption [11]. Additionally, they provide excellent chemical stability and robustness [12]. Such excellent characteristics make it suitable for production of high-performance technologies such as FPDs.

MOS-based TFTs have been manufactured by a diverse range of techniques for thin-film deposition such as the vacuum-based and solution-based techniques. The vacuum-based techniques include, sputtering [13]–[15], metal-organic-chemical vapor deposition (MOCVD) [16]. The solution-based techniques include, dip coating [17], spin coating [18]–[20] and spray pyrolysis [5][7]–[9][21]. Among the various MOS-based TFTs, ZnO – based TFT is considered as one of the most widely investigated TFTs particularly in solution processed methods.

Adamopoulos et al. [22], reported a transparent ZnO – based TFTs employing Y_2O_3 and Al_2O_3 MOD deposited by spray pyrolysis on glass substrates. ITO was used as the TCO gate electrode while Al metal was used as the S/D electrodes resulting to the stacks glass/ITO/Y_2O_3/ZnO/Al and glass/ITO/Al_2O_3/ZnO/Al. Initially, Al S/D electrodes were thermally deposited through shadow mask on glass/ITO/TMOD/ZnO stacks. Their analyses showed excellent characteristics such as low voltage operation (4 V), high current modulation ratio (10^5) and high carrier mobility of 7 cm^2/Vs and 34 cm^2/Vs for Al_2O_3 and Y_2O_3 gate dielectrics respectively.

Esro et al. [23], reported a transparent ZnO – based TFTs employing Nd_2O_3 TMOD deposited by spray pyrolysis on glass substrates. ITO was used as the TCO gate electrode while Al metal was used for the S/D electrodes resulting to the stack glass/ITO/Nd_2O_3/ZnO/Al. Initially, Al S/D electrodes were thermally deposited through shadow mask on glass/ITO/Nd_2O_3/ZnO stack. Their analyses showed excellent characteristics such as low voltage operation (4 V), high current modulation ratio (10^7) and high carrier mobility of 65 cm^2/Vs.

There are other reported solution processed transparent ZnO – based TFTs employing different MOD with ITO and Al metals serving as TCO gate electrode and S/D electrodes respectively [14][16][18][21]–[24]. Such reports tremendously showed high performance characteristics in terms of high carrier mobility, low operation voltage, low subthreshold swing and high current modulation ratio (up to 10^6).

This research is aimed at providing alternatives to the conventional Si-based transistors, by fabricating a MOS-based TFTs employing a high-k metal oxide gate dielectric, using a solution processable method that offers the advantage of cost efficiency, simplicity and large area compatibility compared to the oxides deposited by costly vacuum-based techniques. The findings of this research are to improve on the performance of the transistor in terms of electron mobility, high voltage operation and power consumption compared to the ones reported in literatures deposited by vacuum-based techniques. Such attributes can be improved by using a high-k metal oxide gate dielectric that exhibit a higher dielectric constant than the conventional SiO_2. The condition of choosing such high-k gate dielectric is that it must operate as an insulator by exhibiting a low leakage current density, higher dielectric constant than SiO_2 to prevent effect of current tunneling and wide bandgap of at least 5 eV. In addition to the wide bandgap, the conduction and valence band offsets must be at least 1 eV to prevent current injection into the oxide bands of the dielectric. Such characteristics of the high-k gate dielectric could tremendously enhance the performance of the TFTs in terms of low voltage operation, high carrier mobility, low off-current, high on-current, low power consumption, low subthreshold swing and interface trap density.

1.2 Thin-film Deposition techniques

There are several deposition techniques that have been used in fabrication of thin films. These techniques have been categorized in two groups namely, the vacuum-based and solution-based deposition techniques.

The vacuum-based deposition techniques are the ones that requires the use of vacuum chamber. These include the chemical vapour deposition (CVD) and physical vapour deposition (PVD). The CVD occur in a reactive chamber where volatile gaseous precursors react to produce dense thin films onto the heated substrate. A typical CVD technique is the metal-organic-chemical vapour deposition (MOCVD) and atomic layer deposition (ALD). The PVD technique on the other hand, involves the vaporisation of a material by a way of resisting heating to produce dense thin films onto the substrate. The PVD technique includes the thermal evaporation, sputtering and molecular beam epitaxy (MBE).

The solution-based deposition techniques involve the use of solutions for deposition of thin films. The solutions are prepared by dissolving precursors in the desired solvents to obtain homogenous solution used for the deposition. The most commonly used solution-based techniques are, spin coating, dip coating and spray pyrolysis [1].

1.2.1 Vacuum-based Deposition

1.2.1.1 Metal Organic Chemical Vapour Deposition (MOCVD)

The MOCVD is a CVD technique mainly employed for the growth of a single crystal III – V semiconductor layers on another semiconductor such as silicon wafer. In this technique, the precursor molecules are transported into the reaction chamber with the aid of a non-reactive carrier gas such as argon or nitrogen. The transported precursor undergoes gas-phase reaction and absorbed at the surface of the substrate and at same time diffuses to preferential sites leading to thin film growth. Finally, the gaseous reaction product and non-reacted molecules are desorbed and escape out of the reaction chamber. Figure 1-1 show a schematic of a typical MOCVD system.

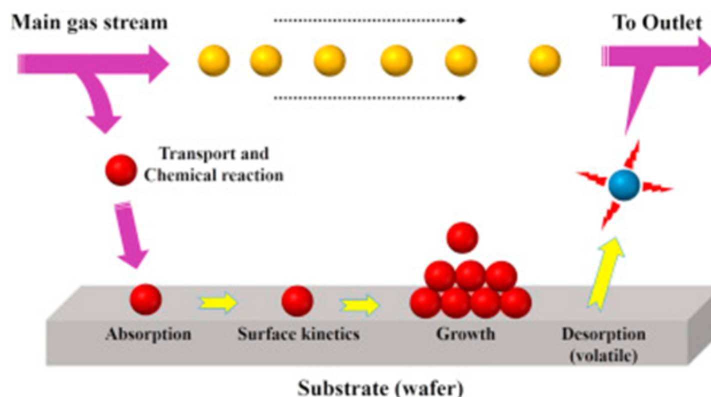

Figure 1- 1. A schematic of MOCVD system [28].

1.2.1.2 Sputtering

The sputtering deposition technique is PVD technique that involves the process of depositing a target material also referred to as source onto a substrate. In this technique, a voltage is applied between the target and the substrate. The target is attached to the cathode while the substrate is attached to the anode. A plasma is generated in the vacuum by the ionization of a sputtering gas usually an inert gas such as argon. These ions bombard the

target material and sputters off the material to be deposited. The most commonly used sputtering deposition for thin-film transistor is the magnetron sputtering (others include DC (diode), RF (radio frequency) and reactive sputtering) in which a magnet is placed behind the target to enhance bombardment by ionized gases to increase the growth rate and film uniformity [1]. Figure 1-2 show a schematic of a typical sputtering system.

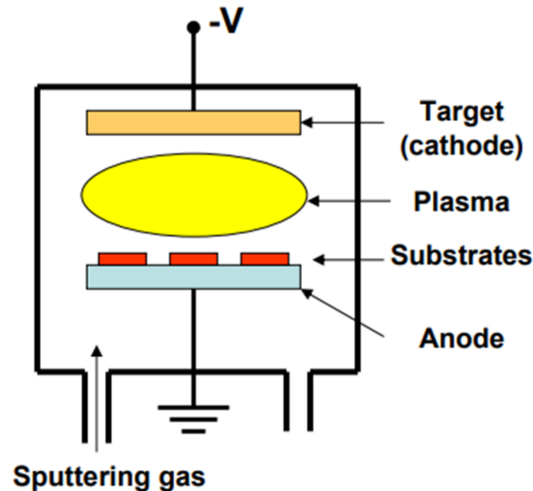

Figure 1- 2. A schematic of a typical sputtering system [29].

1.2.1.3 Molecular Beam Epitaxy (MBE)

This technique requires an ultra-high vacuum (10^{-11} torr) to grow single-crystal epitaxial films with precise control of thickness, composition and morphology. Films are grown on single-crystal substrates through the evaporation of the elements or molecular constituents of the films with a separate Knudsen effusion source cells onto the substrate [30]. Sufficient heating (high temperature) must be applied on the substrate in other to achieve growth [31]. Figure 1-3 show a schematic of a typical MBE system.

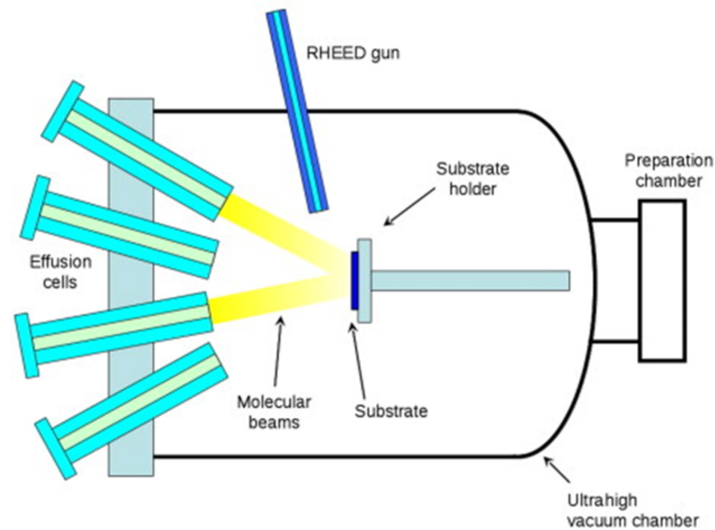

Figure 1- 3. A schematic of a typical MBE system [32].

1.2.1.4 Thermal Evaporation

Thermal evaporation is among the oldest thin film deposition techniques specifically employed for deposition of metal and metal alloys. The process mainly consists of evaporation from the source and condensation at the substrate's surface in a chamber (10^{-6} mbar). The process requires a generated vapour of a sublime source material under vacuum. This vapour is further transported onto the substrate where it condenses to produce solid films [30]. This technique can use two types of sources i.e. resistive and electron beam source [33]. Figure 1-4 show an illustration of a typical thermal evaporation system.

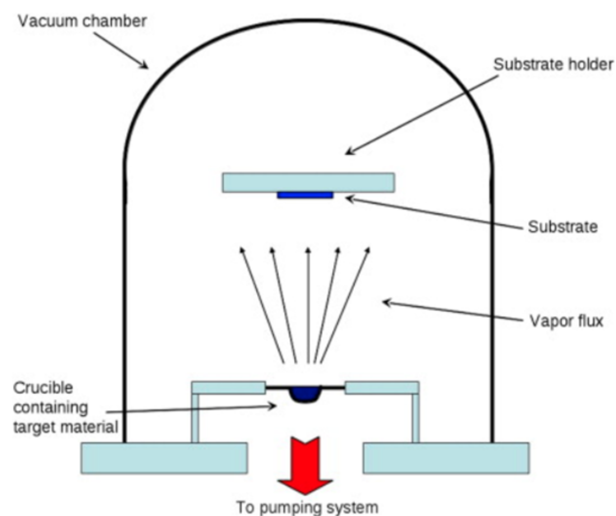

Figure 1- 4. A Schematic of a thermal evaporation system [32].

1.2.1.5 Pulsed Laser Deposition (PLD)

The pulsed laser deposition (PLD) technique involves three basic steps [34]: ablation of target material, formation of a highly energetic plume and the growth of the film on the substrate. Figure 1-5 show a schematic of a PLD system.

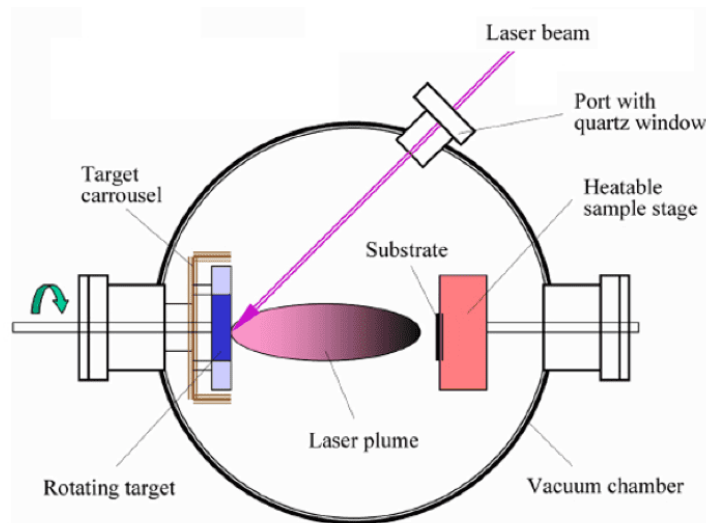

Figure 1- 5. A schematic of a PLD setup [35].

The laser beam is usually inclined at 45º to strike the target material. As a result, there is a formation of a highly energetic plume that vaporises and deposited as a thin film on the substrate facing the target.

1.2.1.6 Atomic Layer Deposition (ALD)

The atomic layer deposition (ALD) technique is another technique known for its self-limiting control of thin films grown on the substrates. Its deposition process requires the use of alternating precursors that react with the substrate in the chamber. The first precursor is introduced into the reaction chamber where it reacts with substrate in a self-limiting manner leading to the formation of a monolayer on the substrate surface. A non-reactive carrier inert gas such as nitrogen is sequentially purged into the reaction chamber to eliminate the unreacted precursor and the reaction by-products. Similarly, the second precursor is introduced into the reaction chamber to produce a second monolayer on the substrate surface and again purged by the non-reactive carrier gas to eliminate unwanted reaction by-products. The final film thickness depends on the number of the ALD cycles. Figure 1-6 show an illustration of an ALD cycle.

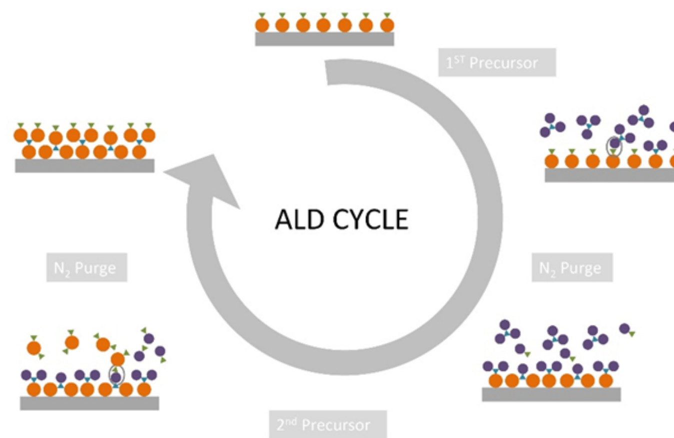

Figure 1- 6. A schematic of an ALD cycle [36].

1.2.2 Solution-based Deposition

1.2.2.1 Spin coating

Spin coating is one of the commonly used solution-based techniques for thin film deposition. It offers the advantage uniform thin film deposition at a very fast rate with thickness ranging from a few nanometres to few microns [37]. Figure 1-7 describes the stages involve in the spin coating process. The spin coating process begins with deposition of the fluid on the substrate while it is spinning either at low speed or stationary, followed by the rotation or spinning of the substrate at a very high speed (usually > 600 rpm), to enable the coating fluid to be uniformly distributed across the substrate by the centrifugal force. The fluid further flung off as the solvent evaporates leaving behind coated thin film. The coated films further undergo post thermal treatment at suitable temperatures (depending on the material composition) to ensure formation of quality films. it is important to mention that the quality of the film thickness depends on the spinning speed, solution and solvent viscosity, volatility and concentration. The major disadvantage of spin coating process is the loss of large amount of fluid due to its spreading beyond the target caused by the centrifugal force. As a result, this technique is not suitable for large-scale manufacturing.

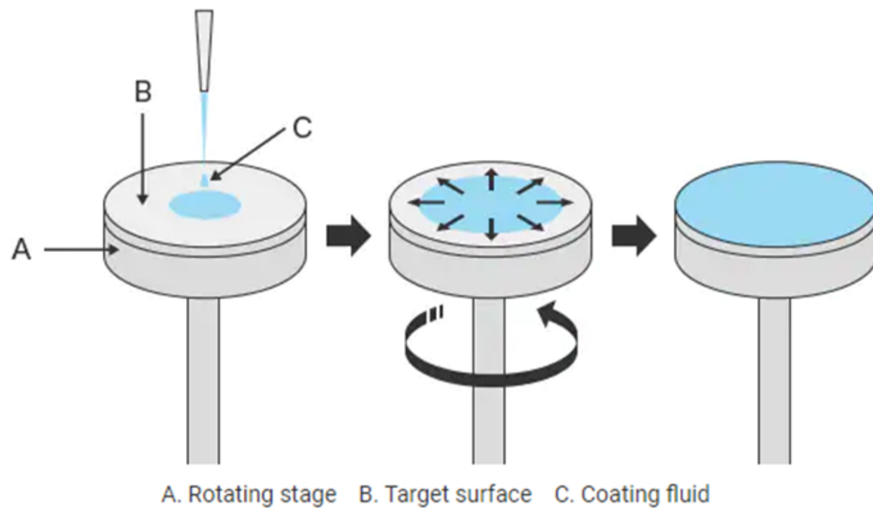

Figure 1- 7. An illustration describing the stages of a spin coating process [38].

1.2.2.2 Dip coating

Dip coating is another solution processed based technique for thin film deposition. It begins with immersion of substrates into the precursor solution, followed by the removal of the substrate at a constant speed into the atmosphere, thereby resulting to the formation of a homogenous liquid film at the surface of the substrate. The substrate is further dried at room temperature to eliminate volatile solvents and undergo chemical reactions that produces thin films. Similar to spin coating, post thermal treatment is required after evaporation to ensure formation of quality films. Figure 1-8 shows an illustration of a typical dip coating process.

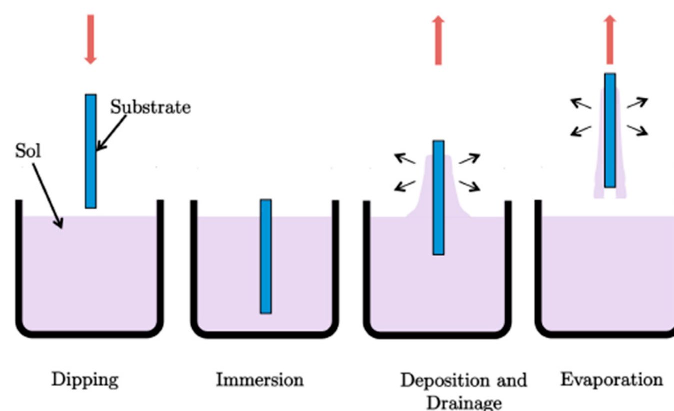

Figure 1- 8. An illustration of a typical dip coating process [39].

1.2.2.3 Spray pyrolysis

Spray pyrolysis involves the process of atomizing a solution and heating the droplets to produce solid particles. The process begins with preparation of precursor's solution of the

desired material that is spray-coated on a pre-heated substrate by a spray gun using a non-reactive carrier gas such as nitrogen gas.

An explicit review of this technique will later be discussed in chapter three of this thesis because it is the method employed for the deposition of metal oxide films.

Table 1-1 present some examples of metal oxide films deposited by several deposition techniques including the vacuum and solution-based techniques.

Table 1-1. (Ta_2O_5: Tantalum (V) oxide, Nd_2O_3: Neodymium (III) oxide, ZrO_2: Zirconium oxide, Sc_2O_3: Scandium (III) oxide, Y_2O_3: Yttrium (III) oxide, Er_2O_3: Erbium (III) oxide, Al_2O_3: Aluminium (III) oxide, MgO: Magnesium oxide, $LaAlO_3$: Lanthanum aluminate, SnO_2: Tin oxide, IGZO: Indium-Gallium-Zinc oxide, HfO_2: Hafnium oxide, HAO: Hafnium aluminate, TiO_2: Titanium oxide, WO_3: Tungsten (III) oxide, In_2O_3: Indium (III) oxide, ZnO: Zinc oxide).

Deposition Techniques	Metal oxides	Ref
Vacuum-based Deposition		
MOCVD	Ta_2O_5	[40]
	Nd_2O_3	[41], [42]
	ZrO_2	[43]
	Sc_2O_3	[44]
	Y_2O_3	[45][44]
	Er_2O_3	[44]
Sputtering	Al_2O_3	[46]
	Nd_2O_3	[36][37]
	ZrO_2	[38][39]
	$LaAlO_3$	[51]
	Y_2O_3	[52]
MBE	MgO	[53]
	Nd_2O_3	[54]
	$LaAlO_3$	[55]
	Y_2O_3	[56]
Thermal evaporation	MgO	[57]
	Nd_2O_3	[51][52]
	SnO_2	[60]
PLD	Al_2O_3	[61]
	Nd_2O_3	[62]
	$LaAlO_3$	[63]
	IGZO	[64]
ALD	HfO_2	[41]
	Nd_2O_3	[65]
	Al_2O_3	[66]
	$LaAlO_3$	[67]
	Y_2O_3	[68]
Solution-based Deposition		
Spin coating	HfO_2	[69]–[73]
	Ta_2O_5	[74]–[76]
	Al_2O_3	[77]–[80]
	HAO	[81]

	ZrO_2	[80][81]
Dip coating	TiO_2	[84]
	WO_3	[85]
	Al_2O_3	[86]
	In_2O_3	[87]
	ZrO_2	[88]
	ZnO	[89]

1.3 References

[1] X. Yu, T. J. Marks, and A. Facchetti, "Metal oxides for optoelectronic applications," *Nat. Mater.*, vol. 15, no. 4, pp. 383–396, 2016.

[2] H. Hosono and K. Ueda, "Transparent Conducting Oxides," in *Springer Handbook of Electronic and Photonic Materials*, 2nd ed., S. Kasap and P. Capper, Ed. Springer International Publishing, 2017, p. 1.

[3] K. L. Chopra, S. Major, and D. K. Pandya, "Transparent conductors-A status review," *Thin Solid Films*, vol. 102, no. 1, pp. 1–46, 1983.

[4] R. Engel-Herbert, Y. Hwang, J. Cagnon, and S. Stemmer, "Metal-oxide-semiconductor capacitors with ZrO_2 dielectrics grown on $In_{0.53}Ga_{0.47}As$ by chemical beam deposition," *Appl. Phys. Lett.*, vol. 95, no. 6, pp. 62903–62908, 2009.

[5] S. Stemmer, J. P. Maria, and A. I. Kingon, "Structure and stability of La_2O_3/SiO_2 layers on Si(001)," *Appl. Phys. Lett.*, vol. 79, no. 1, pp. 102–104, 2001.

[6] G. Adamopoulos, S. Thomas, D. D. C. Bradley, M. A. McLachlan, and T. D. Anthopoulos, "Low-voltage ZnO thin-film transistors based on Y_2O_3 and Al_2O_3 high- k dielectrics deposited by spray pyrolysis in air," *Appl. Phys. Lett.*, vol. 98, no. 12, pp. 1–4, 2011.

[7] F. H. Alshammari, P. K. Nayak, Z. Wang, and H. N. Alshareef, "Enhanced ZnO thin-film transistor performance using bilayer gate dielectrics," *ACS Appl. Mater. Interfaces*, vol. 8, no. 35, pp. 22751–22755, 2016.

[8] M. Esro, R. Mazzocco, G. Vourlias, O. Kolosov, A. Krier, W. I. Milne, and G. Adamopoulos, "Solution processed lanthanum aluminate gate dielectrics for use in metal oxide-based thin film transistors," *Appl. Phys. Lett.*, vol. 106, no. 20, 2015.

[9] G. Adamopoulos, S. Thomas, P. H. Wöbkenberg, D. D. C. Bradley, M. A. Mclachlan, and T. D. Anthopoulos, "High-Mobility Low-Voltage ZnO and Li-Doped ZnO Transistors Based on ZrO_2 High- k Dielectric Grown by Spray Pyrolysis in Ambient Air," pp. 1894–1898, 2011.

[10] M. Esro, G. Vourlias, C. Somerton, W. I. Milne, and G. Adamopoulos, "High-mobility ZnO thin film transistors based on solution-processed hafnium oxide gate dielectrics," *Adv. Funct. Mater.*, vol. 25, no. 1, pp. 134–141, 2015.

[11] J. F. Wager, "Transparent Electronics," *Appl. Phys.*, vol. 300, no. 5623, pp. 1245–1247, 2003.

[12] Ü. Özgür, Y. I. Alivov, C. Liu, A. Teke, M. A. Reshchikov, S. Dogan, V. Avrutin, S. -J. Cho, anf H. Morkoc, "A comprehensive review of ZnO materials and devices," *J. Appl. Phys.*, vol. 98, no. 4, pp. 1–103, 2005.

[13] P. F. Carcia, R. S. McLean, M. H. Reilly, and G. Nunes, “Transparent ZnO thin-film transistor fabricated by rf magnetron sputtering,” *Appl. Phys. Lett.*, vol. 82, no. 7, pp. 1117–1119, 2003.

[14] E. Fortunato, A. Pimentel, L. Pereira, A. Goncalves, G. Lavareda, H. Aguas, I. Ferreira, C. N. Carvalho, and R. Martins, “High field-effect mobility zinc oxide thin film transistors produced at room temperature,” *J. Non. Cryst. Solids*, vol. 338–340, pp. 806–809, 2004.

[15] H. Q. Chiang, J. F. Wager, R. L. Hoffman, J. Jeong, and D. A. Keszler, “High mobility transparent thin-film transistors with amorphous zinc tin oxide channel layer,” *Appl. Phys. Lett.*, vol. 86, no. 1, pp. 2003–2006, 2005.

[16] J. Jo, O. Seo, H. Choi, and B. Lee, “Enhancement-mode ZnO thin-film transistor grown by metalorganic chemical vapor deposition,” *Appl. Phys. Express*, vol. 1, no. 4, pp. 0412021–0412023, 2008.

[17] Y. Ohya, T. Niwa, T. Ban, and Y. Takahashi, “Thin film transistor of ZnO fabricated by chemical solution deposition,” *Appl. Phys.*, vol. 40, no. 1, pp. 297–298, 2001.

[18] B. J. Norris, J. Anderson, J. F. Wager, and D. A. Keszler, “Spin-coated zinc oxide transparent transistors,” *J. Phys. D. Appl. Phys.*, vol. 36, no. 20, pp. 148–151, 2003.

[19] B. Sun, R. L. Peterson, H. Sirringhaus, and K. Mori, “Low-temperature sintering of in-plane self-assembled ZnO nanorods for solution-processed high-performance thin film transistors,” *J. Phys. Chem. C*, vol. 111, no. 51, pp. 18831–18835, 2007.

[20] B. S. Ong, C. Li, Y. Wu, and R. Loutfy, “Stable, solution-processed, high-mobility ZnO thin-film transistors,” *J. Am. Chem. Soc.*, vol. 129, no. 10, pp. 2750–2751, 2007.

[21] D. Afouxenidis, R. Mazzocco, G. Vourlias, P. J. Livesley, A. Krier, W. I. Milne, O. Kolosov, and G. Adamopoulos, “ZnO-based thin film transistors employing aluminum titanate gate dielectrics deposited by spray pyrolysis at ambient air,” *ACS Appl. Mater. Interfaces*, vol. 7, no. 13, pp. 7334–7341, 2015.

[22] G. Adamopoulos, S. Thomas, D. D. C. Bradley, M. A. McLachlan, and T. D. Anthopoulos, “Low-voltage ZnO thin-film transistors based on Y_2O_3 and Al_2O_3 high- k dielectrics deposited by spray pyrolysis in air,” *Appl. Phys. Lett.*, vol. 98, no. 12, pp. 1–4, 2011.

[23] M. Esro, O. Kolosov, V. Stolojan, P. J. Jones, W. I. Milne, and G. Adamopoulos, “Solution-Processed Neodymium Oxide/ZnO Thin-Film Transistors with Electron Mobility in Excess of 65 cm V^{-1} s^{-1},” *Adv. Electron. Mater.*, vol. 3, no. 4, pp. 1–8, 2017.

[24] D. Afouxenidis, “ZnO-based Thin Tilm Transistor employing Niobium Aluminate Gate Dielectrics Deposited by Spray Pyrolysis at Ambient air,” Lancaster University, 2018.

[25] M. Esro, O. Kolosov, P. J. Jones, W. I. Milne, and G. Adamopoulos, “Structural and electrical characterization of SiO_2 gate dielectrics deposited from solutions at moderate

temperatures in air," *ACS Appl. Mater. Interfaces*, vol. 9, no. 1, pp. 529–536, 2017.

[26] G. Adamopoulos, A. Bashir, S. Thomas, W. P. Gillin, S. Georgakopoulos, M. Shkunov, M. A. Baklar, N. Stingelin, R. C. Maher, L. F. Cohen, D. D. C. Bradley, and T. D. Anthopoulos, "Spray-deposited Li-doped ZnO transistors with electron mobility exceeding 50 cm^2/Vs," *Adv. Mater.*, vol. 22, no. 42, pp. 4764–4769, 2010.

[27] G. Adamopoulos, A. Bashir, P. H. Wöbkenberg, D. D. C. Bradley, and T. D. Anthopoulos, "Electronic properties of ZnO field-effect transistors fabricated by spray pyrolysis in ambient air," *Appl. Phys. Lett.*, vol. 95, no. 13, pp. 2007–2010, 2009.

[28] W. Choi, N. Choudhary, G. H. Han, J. Park, D. Akinwande, and Y. H. Lee, "Recent development of two-dimensional transition metal dichalcogenides and their applications," *Mater. Today*, vol. 20, no. 3, pp. 116–130, 2017.

[29] "Sputtering Vacuum Evaporation." [Online]. Available: http://users.wfu.edu/ucerkb/Nan242/L07-Sputtering_a.pdf. [Accessed: 11-May-2020].

[30] W. Kern and K. Schuergraf, "Deposition technologies and applications: introduction and overview," in *Handbook of Thin-Film Deposition Processes and Techniques*, 2nd ed., K. Seshan, Ed. New York: Noyes Publications, 2002, pp. 11–43.

[31] F. Rinaldi, "Basics of Molecular Beam Epitaxy," *Annual Report 2002*. Ulm, pp. 1–8, 2002.

[32] R. J. Martin-Palma and A. Lakhtakia, "Vapor-Deposition Techniques," in *Engineered Biomimicry*, Kindle., Pennsylvania: Elsevier Inc., 2013, pp. 383–398.

[33] D. A. Jameel, "Thin Film Deposition Processes," *Int. J. Mod. Phys. Appl.*, vol. 1, no. 4, pp. 193–199, 2015.

[34] S. Anil, J. Venkatesan, M. S. Shim, E. P. Chalisserry, and S.-K. Kim, "Bone response to calcium phosphate coatings for dental implants," in *Bone Response to Dental Implant Materials*, 1st ed., A. Piattelli, Ed. Elsevier Ltd-Woodhead Publishing, 2017, pp. 65–88.

[35] M. Bellardita, A. D. Paola, S. Yurdakal, and L. Palmisano, "Preparation of Catalysts and Photocatalysts Used for Similar Processes," in *Heterogeneous Photocatalysis*, G. Marci and L. Palmisano, Ed. Palermo: Elsevier B.V, 2019, pp. 25–56.

[36] "Atomic Layer Deposition," *ctecnano coating technologies*. [Online]. Available: https://ctechnano.com/coating-technologies/what-is-atomic-layer-deposition-ald/. [Accessed: 12-May-2020].

[37] A. Mishra, N. Bhatt, and A. K. Bajpai, "Nanostructured superhydrophobic coatings for solar panel applications," in *Nanomaterials-Based Coatings: Fundamentals and Aplications*, P. N. Tri, S. Rtimi, and C. M. O. Plamondon, Ed. Elsevier Inc., 2019, pp. 397–424.

[38] Keyence, “Spin Coating,” in *Coating and Dispensing Technology*, KEYENCE, 2019, p. 18.

[39] M. Aymerich, A. I. Gómez-Varela, E. Álvarez, and M. T. Flores-Arias, “Study of different sol-gel coatings to enhance the lifetime of PDMS devices: Evaluation of their biocompatibility,” *Materials (Basel).*, vol. 9, no. 9, 2016.

[40] N. O. and H. F. H. Chiba, K. Tada, T. Furukawa, T. Yamamoto, T. Yotsuya, “Low temperature MOCVD of Ta_2O_5 dielectric thin films from $Ta[NC(CH_3)_3][OC(CH_3)_3]_3$ and O_2,” *J. Ceram. Soc. Japan*, vol. 124, no. 5, pp. 510–514, 2016.

[41] A. C. Jones, H. C. Aspinall, P. R. Chalker, R. J. Potter, K. Kukli, A. Rahtu, M. Ritala, and M. Leskela, “Some recent developments in the MOCVD and ALD of high-k dielectric oxides,” *Mater. Chem.*, vol. 14, pp. 3101–3112, 2004.

[42] G. Bonnet, M. Lachkar, J. C. Colson, and J. P. Larpin, “Characterization of thin solid films of rare earth oxides formed by the metallo-organic chemical vapour deposition technique, for high temperature corrosion applications,” *Thin Solid Films*, vol. 261, no. 1–2, pp. 31–36, 1995.

[43] A. C. J. and P. R. Chalker, “Some recent developments in the chemical vapour deposition of electroceramic oxides,” *Phys. D Appl. Phys.*, vol. 36, no. 6, pp. R80–R95, 2003.

[44] A. P. Milanov, K. Xu, S. Cwik, H. Parala, T. de los Arcos, H. W. Becker, D. Rogalla, R. Cross, S. Paul, and A. Devi, “Sc_2O_3, Er_2O_3, and Y_2O_3 thin films by MOCVD from volatile guanidinate class of rare-earth precursors,” *Dalt. Trans.*, vol. 41, pp. 13936–13947, 2012.

[45] W. J. Varhue, M. Massimo, J. M. Carrulli, V. Baranauskas, E. Adams, and E. Broitman, “Deposition of Y_2O_3 by plasma enhanced organometallic chemical vapour deposition using an electron cyclotron resonance source,” *Vac. Sci. Technol. A*, vol. 11, no. 4, p. 1870, 1993.

[46] S. Sellner, A. Gerlach, S. Kowarik, F. Schreiber, H. Dosch, S. Meyer, J. Pflaum, and G. Ulbricht, “Comparative study of the growth of sputtered aluminum oxide films on organic and inorganic substrates,” *Thin Solid Films*, vol. 516, no. 18, pp. 6377–6381, 2008.

[47] T-M. Pan, J-D. Lee, W-H. Shu, and T-T. Chen, “Structural and electrical properties of neodymium oxide high-k gate dielectrics,” *Appl. Phys. Lett.*, vol. 89, no. 23, p. 232908, 2006.

[48] M. Imura, T. Tanaka, M. Homma, and M. Okada, “Nonlinear Current-Voltage Characteristics of Double-Layered ZnO/R_xO_y (R=La, Ce, Pr, Nd) Sputtered Films,” *Mater. Trans. JIM*, vol. 35, no. 10, pp. 730–734, 1994.

[49] A. Hojabri, "Structural and optical characterization of ZrO_2 thin films grown on silicon and quartz substrates," *J. Theor. Appl. Phys.*, vol. 10, no. 3, pp. 219–224, 2016.

[50] K. Yildiz, U. Akgil, B. Coskun, and Y. Atici, "Rf-sputtering deposition of nano-crystalline zirconia thin films with high transparency," *Mater. Lett.*, vol. 94, pp. 161–164, 2013.

[51] E. Sader, H. Schmidt, K. Hradil, and W. Wersing, "RF-magnetron sputtered lanthanum aluminate buffer layers on silicon," *Supercond. Sci. Technol.*, vol. 4, no. 8, p. 371, 1991.

[52] J. J. Araiza, M. Cardenas, C. Falcony, V. M. Mendez-Garcia, M. Lopez, and G. Contreras-Puente, "Structural, optical and electrical characteristics of yttrium oxide films deposited by laser ablation," *Vac. Sci. Technol. A*, vol. 16, no. 6, p. 3305, 1998.

[53] W. Y. Chen, J. S. Chen, and J. S. Jeng, "Suppression of Oxygen Vacancy and Enhancement in Bias Stress Stability of High-Mobility ZnO Thin-Film Transistors with N_2O Plasma Treated MgO Gate Dielectrics," *ECS Solid State Lett.*, vol. 2, no. 6, p. P287, 2013.

[54] A. Fissel, Z. Elassar, O. Kirfel, E. Bugiel, M. Czernohorsky, and H. J. Osten, "Interface formation during molecular beam epitaxial growth of neodymium oxide on silicon," *Appl. Phys.*, vol. 99, no. 7, p. 074105, 2006.

[55] S. Gaillard, Y. Rozier, C. Merckling, F. Ducroquet, M. Gendry, and G. Hollinger, "$LaAlO_3$ films prepared by MBE on $LaAlO_3$(001) and Si(001) substrates," *Microelectron. Eng.*, vol. 80, pp. 146–149, 2005.

[56] J. C. Vyas, G. P. Kothiyal, K. P. Muthe, D. P. Gandhi, A. K. Debnath, S. C. Sabharwal, and M. K. Gupta, "Growth of yttria and dysprosium thin films by molecular beam epitaxy and their characterization," *Cryst. Growth*, vol. 130, no. 1–2, pp. 59–66, 1993.

[57] W. Y. Chen, J. S. Jeng, and J. S. Chen, "Improvement of Mobility in ZnO Thin Film Transistor with an Oxygen Enrinched MgO Gate Dielectric," *ECS Solid State Lett.*, vol. 1, no. 5, p. N17, 2012.

[58] T. Busani, R. Devine, and P. Gonon, "Structural Effects in the Dielectric Constant of Rare-Earth Oxides: Nd_2O_3," *ECS Trans.*, vol. 1, no. 5, p. 331, 2006.

[59] M. D. Kannan, S. K. Narayandass, C. Balasubramania, and D. Mangalaraj, "Structure and Electrical Properties of Thermally Evaporated Nd2O3 Thin Films," *Phys. Status Solidi Appl. Mater. Sci.*, vol. 128, p. 427, 1991.

[60] H. A. K. and H. Koelmans, "A tin oxide field-effect transistor," *Solid. State. Electron.*, vol. 7, no. 9, pp. 701–702, 1964.

[61] P. Katiyar, C. Jin, and R. J. Narayan, "Electrical properties of amorphous aluminum oxide thin films," *Acta Mater.*, vol. 53, no. 9, pp. 2617–2622, 2005.

[62] V. D. Kushkov, A. M. Zaslavskii, A. V. Zverlin, and A. V. Melnikov, “Rare-earth oxide polymorphism in films,” *Mater. Sci. Lett.*, vol. 10, pp. 1111–1112, 1991.

[63] C. M. Carlson, J. C. Price, P. A. Parilla, D. S. Ginley, D. Niles, R. D. Blaugher, A. Goyal, M. Paranthaman, D. M. Kroeger, and D. K. Christen, “Laser-ablated epitaxial $LaAlO_3$ buffer layers on biaxially textured Ni substrates for superconducting tapes,” *Phys. C Supercond.*, vol. 304, no. 1–2, pp. 82–88, 1998.

[64] K. Nomura, H. Ohta, A. Takagi, T. Kamiya, M. Hirano, and H. Hosono, “Room-temperature fabrication of transparent flexible thin-film transistors using amorphous oxide semiconductors,” *Nature*, vol. 432, no. November, pp. 488–492, 2004.

[65] H. O. and T. Katsumata, “Interfacial reactions between thin rare-earth-metal oxide films and Si substrates,” *Appl. Phys. Lett.*, vol. 78, p. 1832, 2001.

[66] J. B. Kim, D. R. Kwon, K. Chakrabarti, and C. Lee, “Improvement in Al_2O_3 dielectric behaviour by using ozone as an oxidant for the atomic layer deposition technique,” *Appl. Phys.*, vol. 92, no. 11, p. 6739, 2002.

[67] L. Niinisto, M. Nieminen, J. Paivasaari, J. Niinisto, M. Putkonen, and M. Nieminen, “Advanced electroni and optoelectronic materials by Atomic Layer Deposition: An overview with special emphasis on recent progress in processing of high-k dielectrics and other oxide materials,” *Phys. Status Solidi*, vol. 201, no. 7, pp. 1443–1452, 2004.

[68] J. Niinisto, M. Putkonen, and L. Niinistro, “Processing of Y_2O_3 Thin Films by Atomic Layer Deposition from Cyclopentadienyl-Type Compounds and Water as Precursors,” *Chem. Mater.*, vol. 16, no. 15, pp. 2953–2958, 2004.

[69] J. Chung, Y. J. Tak, W. G. Kim, J. W. Park, T. S. Kim, J. H. Lim, and H. J Kim, “Low-temperature fabrication of solution-processed hafnium oxide gate insulator films using a thermally purified solution process,” *J. Mater. Chem. C*, vol. 6, no. 18, pp. 4928–4935, 2018.

[70] J. Weng, W. Chen, W. Xia, J. Zhang, Y. Jiang, and G. Zhu, “Low-temperature solution-based fabrication of high-k HfO_2 dielectric thin films via combustion process,” *J. Sol-Gel Sci. Technol.*, vol. 81, no. 3, pp. 662–668, 2017.

[71] J. D. Oh, J. W. Kim, D. K. Kim, and J. H. Choi and J. H. Choi, “Low-voltage organic transistors and inverters using HfO_x dielectrics,” *Org. Electron.*, vol. 30, pp. 131–135, 2016.

[72] C. Avis, Y. G. Kim, and J. Jang, “Solution processed hafnium oxide as a gate insulator for low-voltage oxide thin-film transistors,” *J. Mater. Chem.*, vol. 22, no. 34, pp. 17415–17420, 2012.

[73] Y. N. Gao, Y. L. Xu, J. G. Lu, J. H. Zhang, and X. F. Li, “Solution processable amorphous hafnium silicate dielectrics and their application in oxide thin film transistors,” *J. Mater.*

Chem. C, vol. 3, no. 43, pp. 11497–11504, 2015.

[74] J. Heo, S. Y. Park, J. W. Kim, S. Song, Y. J. Yoon, J. Jeong, H. Jang, K. T. Lee, J. H. Seo, B. Walker, and J. Y. Kim, "Implementation of Low-Power Electronic Devices Using Solution-Processed Tantalum Pentoxide Dielectric," *Adv. Funct. Mater.*, vol. 28, no. 28, pp. 1–8, 2018.

[75] R. C. Frunza, B. Kmet, M. Jankovec, M. Topic, and B. Malic, "Ta_2O_5-based high-K dielectric thin films from solution processed at low temperatures," *Mater. Res. Bull.*, vol. 50, pp. 323–328, 2014.

[76] S. Y. Park, J. Heo, Y. J. Yoon, J. W. Kim, H. Jang, B. Walker, and J. Y. Kim, "Synergistic combination of amorphous indium oxide with tantalum pentoxide for efficient electron transport in low-power electronics," *J. Mater. Chem. C*, vol. 7, no. 15, pp. 4559–4566, 2019.

[77] X. Zhang, B. Wang, W. Huang, Y. Chen, G. Wang, L. Zeng, W. Zhu, M. J. Bedzyk, W. Zhang, J. E. Medvedeva, A. Facchetti, and T. J Marks, "Synergistic Boron Doping of Semiconductor and Dielectric Layers for High-Performance Metal Oxide Transistors: Interplay of Experiment and Theory," *J. Am. Chem. Soc.*, vol. 140, no. 39, pp. 12501–12510, 2018.

[78] A. Lui', G. Liu', H. Zhu, B. Shin, E. Fortunato, R. Martins, and F. Shan', "Low-power organic field-effect transistors and complementary inverter based on low-temperature processed Al_2O_3 dielectric," *Org. Electron.*, vol. 34, pp. 118–123, 2016.

[79] F. Shan, A. Liu, H. Zhu, W. Kong, J. Liu, B. Shin, E. Fortunato, R. Martins, and G. Liu, "High-mobility p-type NiO_x thin-film transistors processed at low temperatures with Al_2O_3 high-k dielectric," *J. Mater. Chem. C*, vol. 4, no. 40, pp. 9438–9444, 2016.

[80] A. Liu, G. Liu, H. Zhu, B. Shin, E. Fortunato, R. Martins, and F. Shan, "Eco-friendly, solution-processed In-W-O thin films and their applications in low-voltage, high-performance transistors," *J. Mater. Chem. C*, vol. 4, no. 20, pp. 4478–4484, 2016.

[81] X. Li, L. Zhu, Y. Gao, and J. Zhang, "Solution-Processed Low-Operating-Voltage Thin-Film Transistors With Bottom-Gate," *IEEE Trans. Electron Devices*, vol. 62, no. 3, pp. 875–881, 2015.

[82] S. W. Kim, M. C. Nguyen, A. H. T. Nguyen, S. J. Choi, H. M. Ji, J. G. Cheon, K. M. Yu, J. H. Kim, S. Y. Cho, and R. Choi, "Solution-Processed Rb-Doped Indium Zinc Oxide Thin-Film Transistors," vol. 39, no. 9, pp. 2018–2021, 2018.

[83] R. N. Bukke, C. Avis, M. N. Naik, and J. Jang, "Remarkable Increase in Field Effect Mobility of Amorphous IZTO Thin-Film Transistors with Purified ZrO_x Gate Insulator," *IEEE Electron Device Lett.*, vol. 39, no. 3, pp. 371–374, 2018.

[84] S. M. Kumbhar, S. S. Shevate, A. R. Patil, S. K. Shaikh, and K. Y. Rajpure, "Dip coated TiO_2

based metal-semiconductor-metal ultraviolet photodetector for UV A monitoring," *Superlattices Microstruct.*, vol. 141, p. 106490, 2020.

[85] V. C. Ferrari, I. S. Dupim, V. Sousa, and F. L. Souza, "Photoactive multilayer WO_3 electrode synthesized via dip-coating," *Ceram. Int.*, vol. 44, no. 18, pp. 22983–22990, 2018.

[86] H. Ennaceri, D. Barrit, A. Khaldoun, A. Benyoussef, and A. Ennaoui, "Deposition of transparent Aluminum Oxide (Al_2O_3) films on silvered CSP mirrors," in *Proceedings of 2014 International Renewable and Sustainable Energy Conference, IRSEC 2014*, 2014, pp. 114–119.

[87] G. Ramanathan and K. R. Murali, "Dip Coated Indium Oxide Films and Their Optical Constants," *Trans. Electr. Electron. Mater.*, vol. 21, pp. 513–518, 2020.

[88] P. J. Jodlowski, D. K. Chlebda, R. J. Jedrzejczyk, A. Dziedzicka, L. Kuterasinski, and M. Sitarz, "Characterisation of well-adhered ZrO_2 layers produced on structured reactors using the sonochemical sol–gel method," *Appl. Surf. Sci.*, vol. 427, pp. 563–574, 2018.

[89] S. Kim, G. Nam, H. Yoon, H. Park, H. Choi, J. S. Kim, J. S. Kim, D. Y. Kim, S-O. Kim, and J-Y. Leem, "Structural, optical, and electrical properties of ZnO thin films deposited by sol-gel dip-coating process at low temperature," *Electron. Mater. Lett.*, vol. 10, no. 4, pp. 869–878, 2014.

2 Theory and Operational Characteristics

2.1 Introduction

Dielectric materials are insulators due to their ultra-low electrical conductivity and wide energy gap (E_g > 3 eV) [1]. They consist of negatively charged particles that are strongly bounded to nearby positively charged particles which limit their movement [2]. A dielectric material can be in a form of solid, liquid or gas. A typical example of a solid dielectric is SiO_2, while water is that of a liquid dielectric and air for the gas. When an external electric field is applied to the dielectric, the electric charges become polarized and reoriented towards the dielectric polarization. A good dielectric material must exhibit high dielectric strength.

Dielectrics are used as capacitors in complementary metal oxide semiconductor (CMOS) technologies and in memory applications. The performance of a dielectric can be investigated by its metal-insulator-metal (MIM) structure. In fact, most of the electronic devices used today are based on MIM structures. A good MIM device should be of high capacitance and low leakage current for its implementation in CMOS technologies. The capacitance of a MIM device is directly related to the dielectric constant of the insulator and inversely proportional its thickness. This means that the capacitance is strongly affected by the physical thickness (t) of the insulator. With continuous scaling of CMOS devices, there is a limitation to the physical thickness of the conventionally used SiO_2 $(t < 2\ nm)$. This results to an excessive large leakage current tunneling through the insulator, resulting to high power consumption of CMOS device [3]–[6]. Such issues could be solved by replacing SiO_2 with insulators with higher dielectric constant.

In this chapter, an overview of MIM, MOS and MOSFET device architectures and operation is discussed.

2.2 Metal-Insulator-Metal (MIM) Devices

The properties of the dielectric thin films are investigated by a simple metal-insulator-metal (MIM) device. A typical MIM structure (also known as parallel plate capacitor) consists of two metal contact, sandwiching an insulator between them as shown in Figure 2-1.

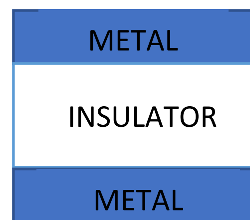

Figure 2- 1. Metal-Insulator-Metal (MIM) structure.

The capacitance of a dielectric material can be derived from two parallel conductive (metal) plates sandwiching a thin film of dielectric material (insulator) and is given as:

$$C = \frac{k\varepsilon_o \,.\, A}{t} \tag{2.1}$$

Where, (ε_o) is the permittivity of free space (8.85 x 10^{-12} F/m), (k) is the permittivity of the dielectric material (dielectric constant), (A) is the area of the capacitor and (t) is the film thickness. Figure 2-2 show a schematic of a typical equivalent circuit used to analyse MIM characteristics and its frequency response.

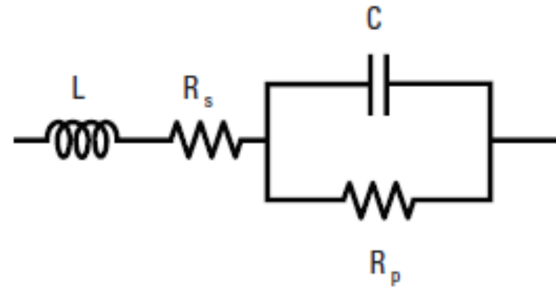

Figure 2- 2. Equivalent circuit of a MIM capacitor [7].

In Figure 2-2, the quantities L, R_s, R_p and C_p are the inductance, series resistance, parallel resistance and parallel capacitance of the MIM capacitor.

2.2.1 Impedance Spectroscopy

The dielectric properties of a MIM capacitor are investigated by its impedance characteristics. Impedance (Z) is sum of resistance and the reactance in an alternating current (AC) circuit and can mathematically be expressed as:

$$Z = R + jX \tag{2.2}$$

Where, (R) and (X) are real resistance and imaginary reactance of an electrical circuit respectively. The unit of Z is Ohms. From equation (2.2), the magnitude the impedance (Z) as well as the phase angle (θ) could be determined.

$$|Z| = \sqrt{R^2 + X^2} \; and \; \theta = \tan^{-1}\left(\frac{X}{R}\right) \tag{2.3}$$

The phase angle (θ) describes the nature of the system. For example, if $(\theta) = 0$, the system is a pure resistor, if $(\theta) = -90$, the system is a pure capacitor, and if $(\theta) = +90$, it is a pure inductor.

As for the imaginary reactance, the system could be capacitive or inductive. The capacitive and inductive impedance could further be expressed as:

$$X_C = \frac{-1}{\omega C} \; and \; X_L = \omega L \tag{2.4}$$

Where, $(\omega = 2\pi f)$ is the angular frequency and (f) is the frequency. For an AC circuit consisting of a series resistor, capacitor and inductor, the total impedance (Z) could be expressed as:

$$Z = R + jX \xleftrightarrow{X = X_L - X_C} Z = R + j(X_L - X_C) \Leftrightarrow Z = R + j\left(\omega L - \frac{1}{\omega C}\right) \quad (2.5)$$

The admittance (Y) is the reciprocal of the impedance (Z).

$$Y = \frac{1}{Z} = \frac{1}{R + jX} = \frac{R}{R^2 + X^2} - j\frac{X}{R^2 + X^2} = G + jB \quad (2.6)$$

Where, (G) and (B) are the conductance and susceptance of the dielectric.

An important parameter of an ideal capacitor is the quality factor (Q), defined as the ratio of the capacitive reactance (X_C) to the series resistance (R).

$$Q = \frac{X_C}{R} \quad (2.7)$$

The dissipation factor (D) also known as loss tangent $(\tan\delta)$ is the reciprocal of (Q).

$$D = \frac{1}{Q} = \frac{R}{X_C} \quad (2.8)$$

2.2.2 Leakage Current Conduction Mechanisms

The term "leakage current" refers to an unwanted flow of current within a dielectric material that increases power consumption as well as deteriorating the performance of the device. The leakage current in dielectrics may strongly depend on the thickness of the dielectric, material composition or trap density of the films [8]. Such factors can be explained by the current conduction mechanisms that governs the current transport in dielectric thin films. These current conduction mechanisms are classified into two groups namely: the electrode-limited and the bulk-limited conduction mechanisms [1][8][9].

The electrode-limited conduction mechanism depends on the structure of the electrode-dielectric interface. In these mechanisms, parameters such as the barrier height at the electrode-dielectric interface and effective mass of the oxide could be extracted. The bulk-limited conduction mechanism on the other hand, depends on the electronic structure of the bulk material itself. In these mechanisms, parameters such as trap density, trap levels, trap spacing, dielectric relaxation time and carrier drift mobility could be extracted [1][10].

The electrode-limited conduction mechanism is the Schottky emission (SE), Fowler Nordheim (FN), Direct tunneling (DT) and Thermionic field emission conduction mechanisms while the bulk-limited conduction mechanism is the Poole-Frenkel (PF), Hopping conduction, Ohmic conduction, Space-charge-limited conduction, Ionic conduction and Grain boundary-limited conduction mechanism. Amongst the various conduction mechanisms, the so-called SE, FN, PF (for thin film) and DT (for ultra-thin film, < 3 nm) conduction mechanisms have been considered as dominant conduction mechanisms for good insulators [12][13].

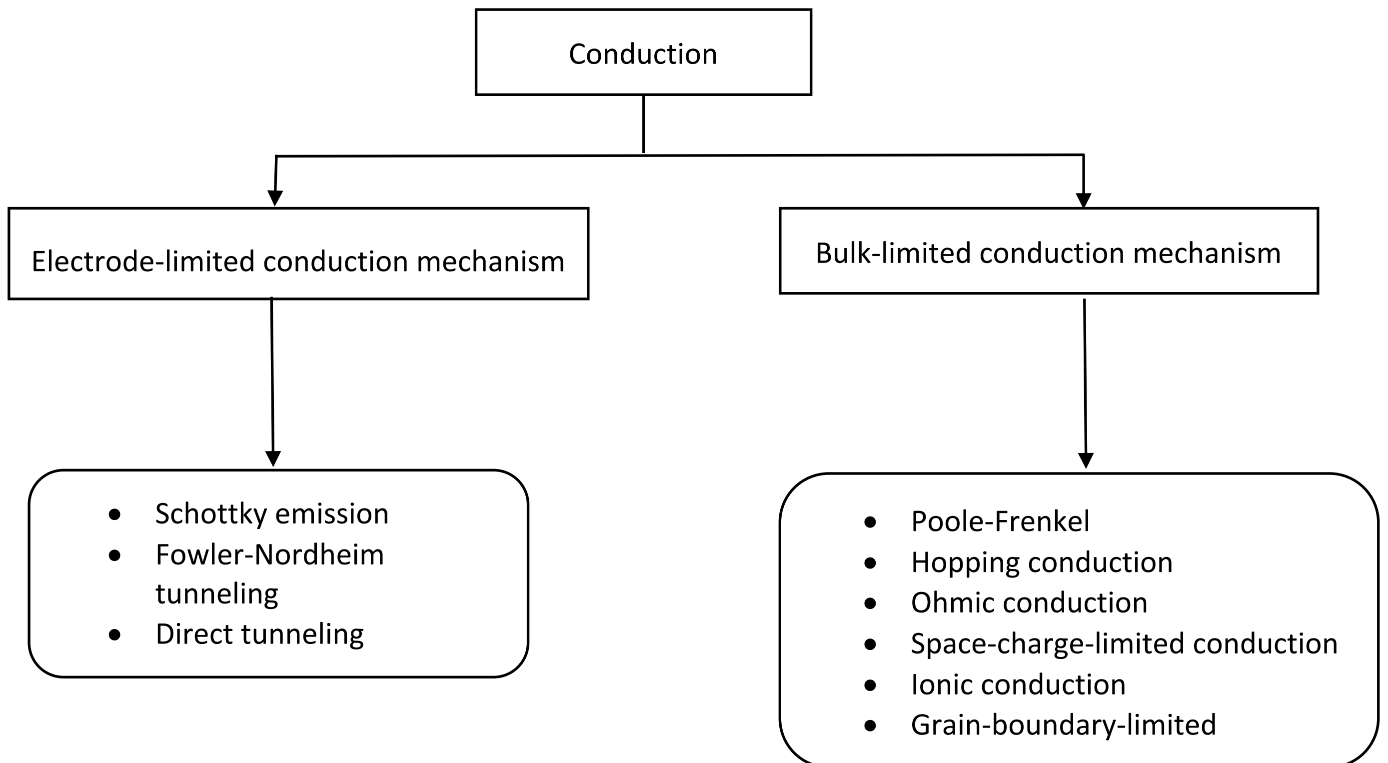

Figure 2- 3. Classifications of conduction mechanisms [1].

2.2.2.1 Schottky Emission (SE) Conduction mechanism

The Schottky emission (SE) conduction mechanism occurs due to thermal activation of the electrons. The electrons in the metal have sufficient energy to overcome the energy barrier at the metal-dielectric interface and diffuse to the dielectric as illustrated in Figure 2-4. Such type of conduction mechanism mostly occurs in oxides at relatively high temperatures [1][10]–[15].

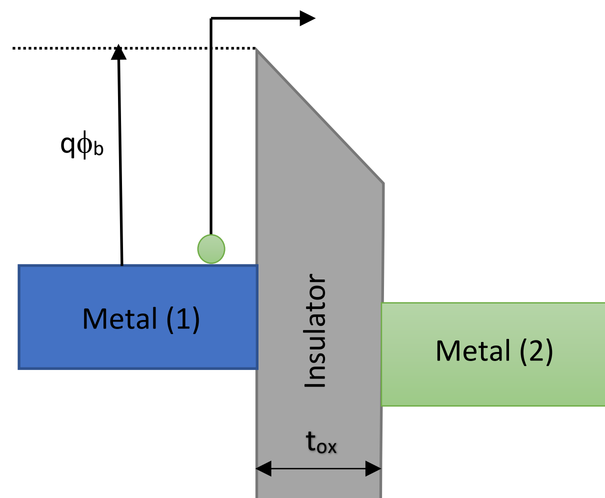

Figure 2- 4. Energy band diagram of Schottky emission (SE) in metal-insulator-metal (MIM) structures.

The expression of the Schottky emission is given by [10][15]:

$$J_{SE} = A^{*}T^{2}\, exp\left[\frac{-q\left(\phi_b - \sqrt{qE/4\pi\varepsilon_r\varepsilon_o}\right)}{K_B T}\right] \tag{2.9}$$

Where,

$$A^{*} = \frac{4\pi q k^{2} m^{*}}{h^{3}} = \frac{120 m^{*}}{m_o} \tag{2.10}$$

(J_{SE}) is the Schottky emission current density, (A^{*}) is the effective Richardson constant, (m_o) and (m^{*}) are the free electron and effective mass respectively, (T) is the temperature, (q) is the electronic charge, (ϕ_b) is the Schottky barrier height, (E) is the electric field across the dielectric, (K_B) is the Boltzmann's constant, (h) is the Planck's constant and finally, both (ε_o) and (ε_r) are the permittivity in vacuum and the dielectric constant of the material respectively.

2.2.2.2 Fowler Nordheim (FN) Tunneling Conduction mechanism

The Fowler Nordheim (FN) tunneling occurs when an electron penetrates through the triangular potential barrier into the conduction band of the dielectric due to an applied electric field. The FN tunneling effect is similar to that of direct tunneling (DT). The only difference is that the FN tunneling effect occur at oxide with thicker films while the DT effect occur at thin oxides (< 3 nm). The FN tunneling conduction mechanism is dominant when the current-voltage characteristics is measured at very low temperatures. Figure 2-5 and Figure 2-6 show the energy band diagram of FN and DT conduction mechanism in metal-insulator-metal (MIM) structures respectively.

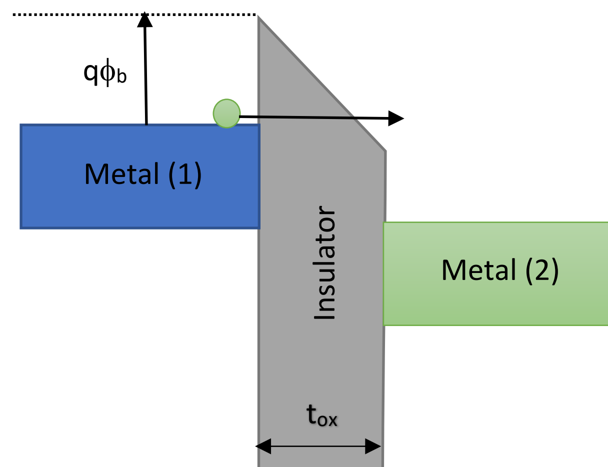

Figure 2- 5. Energy band diagram of Fowler Nordhiem (FN) in metal-insulator-metal (MIM) structures.

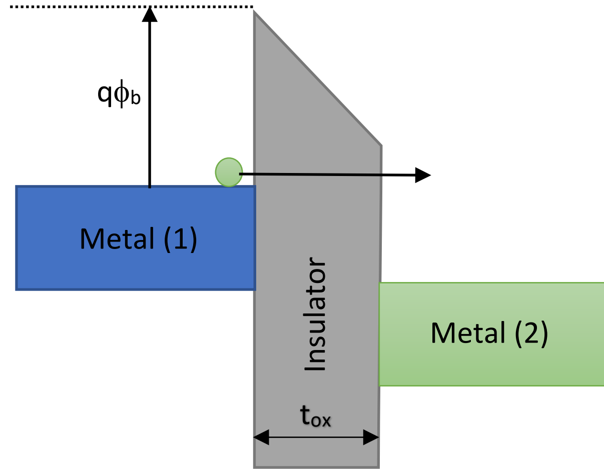

Figure 2- 6. Energy band diagram of Direct tunneling (DT) in metal-insulator-metal (MIM) structures.

The current equation of Fowler Nordheim (FN) is given as [1]:

$$J_{FN} = \frac{q^3E^2}{8\pi hq\phi_b} exp\left[\frac{-8\pi(2qm_T^*)^{1/2}}{3hE}\phi_b^{3/2}\right] \tag{2.11}$$

Where (m_T^*) is the tunneling effective mass in the dielectric while other notations have been previously defined.

Whereas, the current equation of Direct tunneling (DT) is given as [13][16]:

$$J_{DT} \approx exp\left\{\frac{8\pi\sqrt{2q}}{3h}(m^*\phi_b)^{1/2} . k . t_{ox,eq}\right\} \tag{2.12}$$

Where (k) is the relative dielectric constant of the oxide and ($t_{ox,eq}$) is the equivalent oxide thickness (EOT). According to Yeo et al.[16], the direct tunneling current (J_{DT}) strongly depend on the dielectric constant (k), barrier height (ϕ_b) and tunneling effective mass (m_T^*).

N.B the parameters (m^*) and (ϕ_b), could further be determined from the intercept of the SE plot ($\ln(J/T^2)$ versus $\sqrt{E}$) and the slope of FN plot ($\ln(J/E^2)$ versus $1/E$) assuming ($m_{ox}^* = m_T^*$) [14].

The intercept from SE plot is given by:

$$Intercept = \ln\left(120\frac{m_{ox}^*}{m_o}\right) - \frac{q\phi_b}{K_BT} \tag{3.17}$$

While the slope of the FN plot can be expressed as:

$$slope = -6.83 \times 10^{7}\sqrt{\frac{m_T^*}{m_o}\phi_b^3} \qquad (3.18)$$

2.2.2.3 Poole-Frenkel (PF) Conduction mechanism

The Poole Frenkel (PF) conduction occurs when electrons are trapped and excited into conduction band of the dielectric. This type of conduction mechanism is similar to that of Schottky emission because it involves thermal excitation of trapped electrons. The trapped electrons can be released from their trapping centres by an electric field. This electric field reduces the Coulomb potential energy of the electrons and increases the probability of the electrons to be thermally excited out of the trapping centres and jump into the conduction band of the dielectric. Figure 2-7 illustrate the energy band diagram of the PF conduction mechanism.

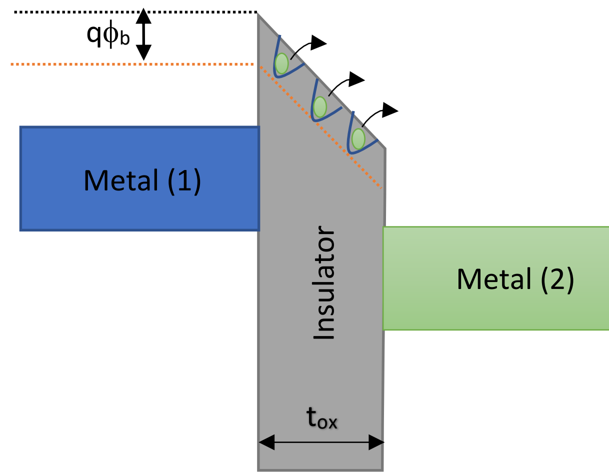

Figure 2- 7. Energy band diagram of Poole Frenkel (PF) emission in metal-insulator-metal (MIM) structures.

The current equation of Poole Frenkel (PF) emission is given as [13][17]:

$$J_{PF} = q\mu N_c E \,.\, exp\left[\frac{-q\left(\phi_T - \sqrt{qE/\pi\varepsilon_i\varepsilon_o}\right)}{K_B T}\right] \qquad (2.13)$$

Where (μ) is the electronic drift mobility, (N_c) is the density of states in the conduction band, (ϕ_T) is the trap energy level.

It is important to note that the current transport in dielectrics strongly depends on the composition of the dielectric material, thickness of the dielectric, traps and trap levels in the dielectric and the materials used as electrodes as well as their work functions. Based on that, it has been shown that the current transport in dielectrics is governed by one or two conduction mechanisms [1][8][9][12]. The Schottky emission (SE) and Poole-Frenkel (PF) conduction mechanisms are dominant at high temperature and low electric field while the Fowler Nordhiem (FN) conduction mechanism is dominant at low temperature and high electric field.

2.3 Metal Oxide Semiconductor (MOS) Operation

Metal oxide semiconductor (MOS) capacitor is a three-component structure that consist of metal gate, dielectric and a semiconductor. A MOS capacitor is considered as one of the main components of the modern CMOS technologies. The performance of a Metal oxide semiconductor field effect transistor (MOSFET) strongly relies on the performance of the MOS capacitor as it is the core component of the MOSFET. A MOSFET is a typical MOS capacitor with two metal-semiconductor junctions at two ends as illustrated in Figure 2-8.

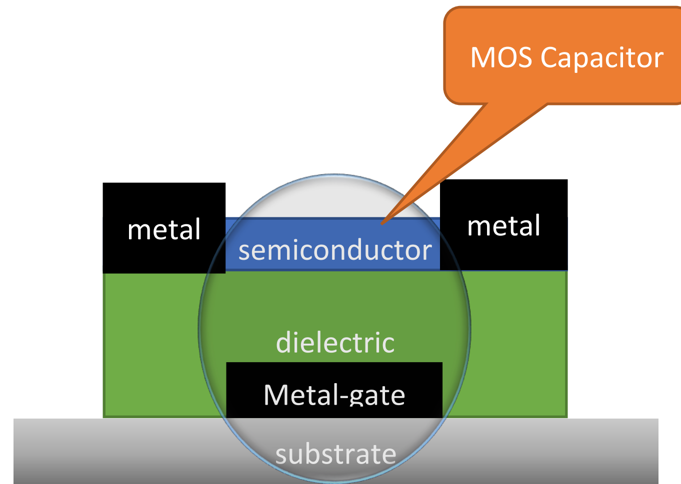

Figure 2- 8. A schematic of a metal oxide semiconductor field effect transistor (MOSFET).

The principles of operation of a MOS capacitor can be studied by using the energy-band diagrams. A MOS capacitor is said to be ideal if the following conditions are satisfied [17]:

a) When there is an equilibrium between the metal work function ϕ_m and the semiconductor work function ϕ_s (i.e., $\phi_m = \phi_s$). In this case, the energy levels must be flat in the absence of the applied voltage.

b) Furthermore, there should exist no charge in the oxide and at oxide-semiconductor interface.

Figure 2-9 show an illustration of an energy-band diagram of an unbiased ideal MOS capacitor.

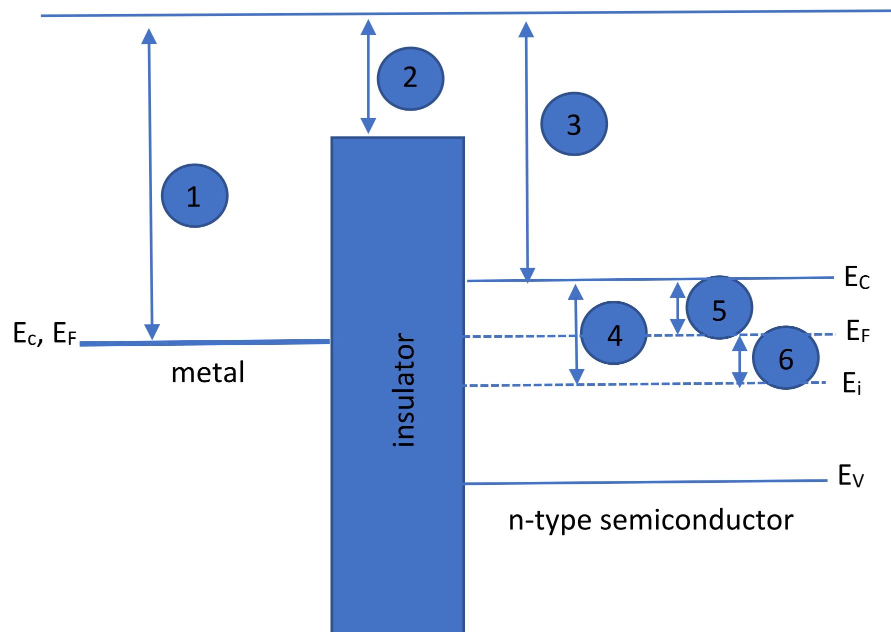

Figure 2- 9. Energy band diagram of an ideal MOS capacitor employing n-type semiconductor at equilibrium (V_{app}=0). (1) $q\phi_m$: ϕ_m is the metal work function, (2) $q\chi_i$: χ_i is the electron affinity of the insulator, (3) $q\chi$: χ is the electron affinity of the semiconductor, (4) $E_g/2$: E_g is the band gap of the semiconductor, (5) $q\phi_n$: ϕ_n is the Fermi potential with respect to the conduction band edge, (6) $q\psi_{Bn}$: ψ_{Bn} is the Fermi potential with respect to the mid-gap edge.

As seen in Figure 2-9, all the energy levels are flat due to absence of applied voltage (V_{app} = 0). When a positive or negative voltage is applied to the MOS capacitor, one of the three types of operation occur at the semiconductor-insulator interface. Such type of operations are known as accumulation, depletion and Inversion [17][18].

2.3.1 Accumulation

Considering an n-type semiconductor, when a positive voltage (V_g > 0) is applied to the gate of the MOS capacitor, a downward bending of the conduction band edge (E_c) occurs near the semiconductor-insulator interface. As the bending edges towards to the fermi energy level (E_f), electrons (majority carriers) are trapped and accumulated at the semiconductor-insulator interface as shown in Figure 2-10. Such type of operation is called an accumulation.

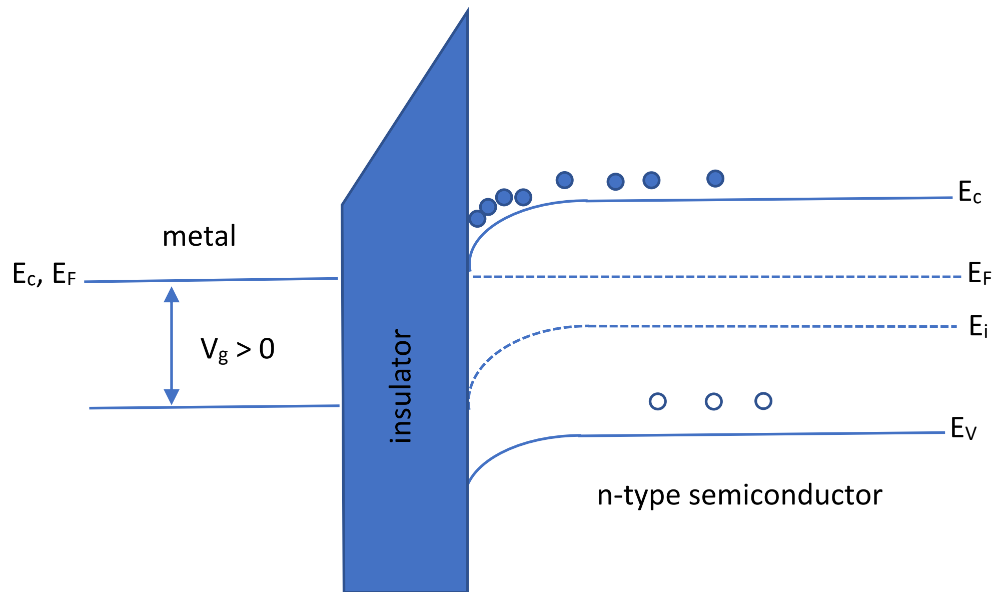

Figure 2- 10. Schematic of an energy-band diagram of a MOS capacitor operating in an accumulation regime.

2.3.2 Depletion

When a small negative voltage ($V_g < 0$) is applied to the gate of a MOS capacitor, an upward band bending at the semiconductor-insulator interface occur causing the majority carrier to deplete. Such type of operation is called the depletion regime as illustrated in Figure 2-11.

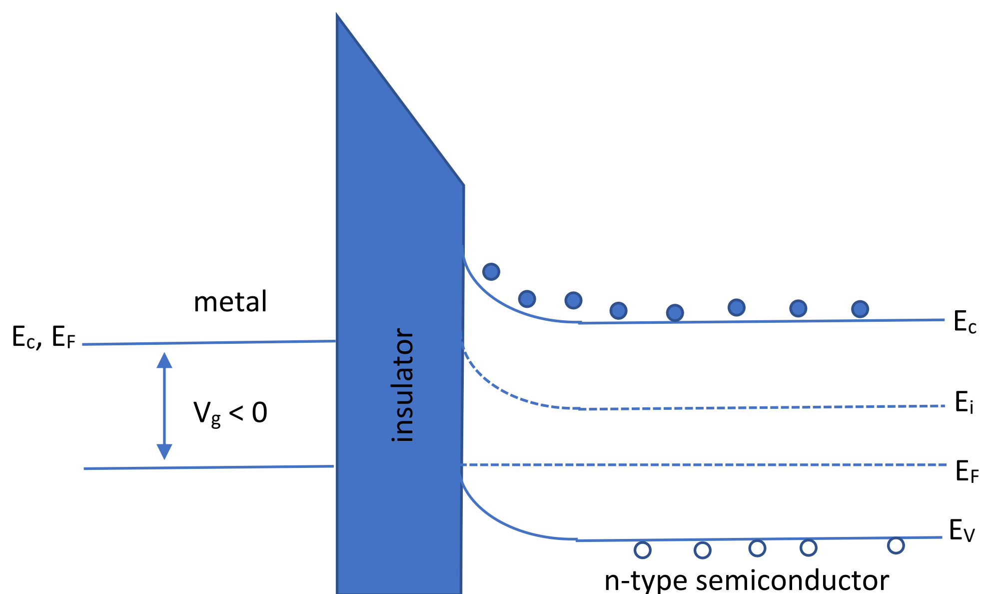

Figure 2- 11. Schematic of an energy-band diagram of a MOS capacitor operating in a depletion regime.

2.3.3 Inversion regime

When a large negative voltage is applied (V_g << 0) to the gate of a MOS capacitor, the upward band bending increases more causing the intrinsic energy E_i to traverse the E_f which further inverts the semiconductor from n-type to p-type. In this case, the holes (minority carriers) density at the semiconductor-insulator interface is larger than the electrons (majority carriers) leading to an inversion as shown in Figure 2-12. Such type of operation is called an inversion [19].

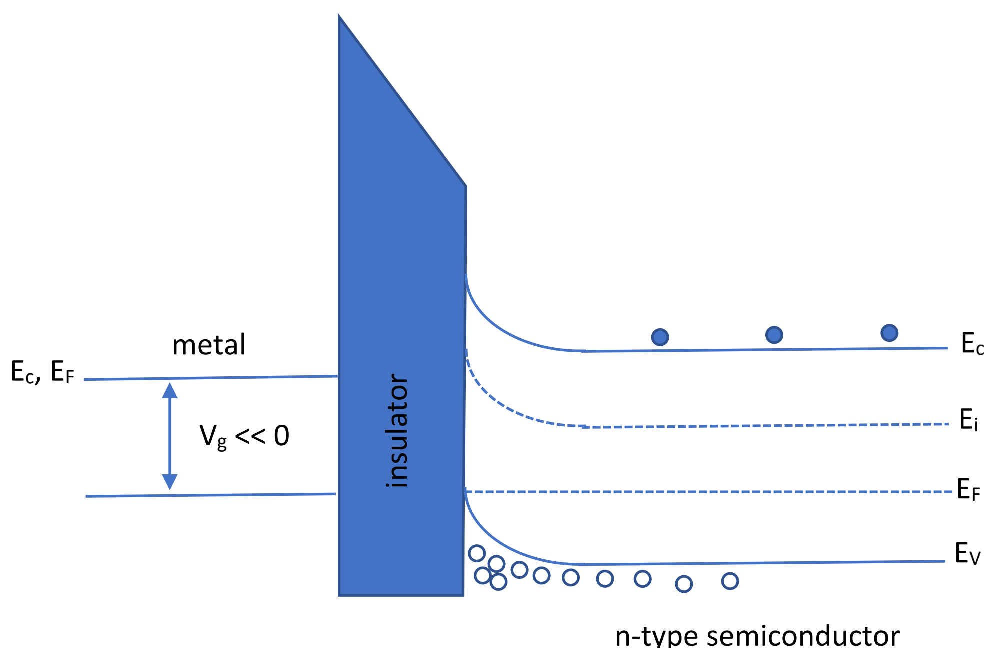

Figure 2- 12. Schematic of an energy-band diagram of a MOS capacitor operating in an inversion regime.

2.4 Metal Oxide Semiconductor Field Effect Transistor (MOSFTET)

A MOSFET is a type of MOS capacitor with two metal-semiconductor junctions at two ends as previously shown in Figure 2-9. These junctions are the "source" and "drain" electrodes, typically made of metals such as aluminium (Al), gold (Au), silver (Ag), copper (Cu), etc. The gate electrode is located between the source and drain electrodes, separated from the channel by a thin layer of oxide film (insulator).

MOSFETs can be categorized according to the type of its channel carriers and according to the state of the transistor with zero gate bias. For the channel carriers, the MOSFETs can be an n-channel or p-channel MOSFETs. In the n-channel MOSFETs, the electrons are the majority carriers and are excited by a more positive gate voltage, while in the p-channel, the holes are the majority carriers and are excited with more negative gate. For the state of the transistor with zero gate bias, the MOSFETs operates in two modes: enhancement or depletion mode.

The enhancement mode MOSFETs are the “normally off” by default and requires biasing at the gate terminal for the transistor to turn on. In other words, when there is a sufficient applied gate voltage, current conduction takes place between the source and drain terminal which causes the transistor to switch on. The voltage at which the transistor switches on is called the threshold voltage (V_T) or turn-on voltage (V_{on}). When V_G (also known as the gate-source voltage, V_{GS}) is greater than the V_T, the corresponding drain current increases and thus the transistor switches on. However, when V_{GS} is less than V_T, the current in the channel does not completely reduce to zero as there is a finite conduction that takes place in the channel. This finite conduction is referred to as subthreshold conduction and it occurs at the transistor’s weak inversion or depletion region also called the subthreshold region [20]. An important parameter of the subthreshold region is the subthreshold swing, defined as the amount of V_{GS} needed to increase the drain-source current (I_{DS}) level by an order of magnitude. The subthreshold swing can be obtained from the inverse slope of the I_{DS}-V_{GS} transfer characteristics curve [21].

$$SS = \frac{\partial V_{Gs}}{\partial(log_{10} I_{DS})} \tag{2.14}$$

The depletion mode on the other hand, are “normally on” devices that requires biasing at the gate terminal to turn off the transistor. In this case, the current conduction between the source and drain terminal is at its maximum level without biasing the V_{GS}. By biasing the V_{GS}, the transistor switches off and hence, no current conduction between the source and drain terminal. In other words, biasing the V_{GS} will deplete the carrier charges and the transistor switches off. Figure 2-13 show a typical transfer characteristic curve of a transistor operating in enhancement and depletion mode.

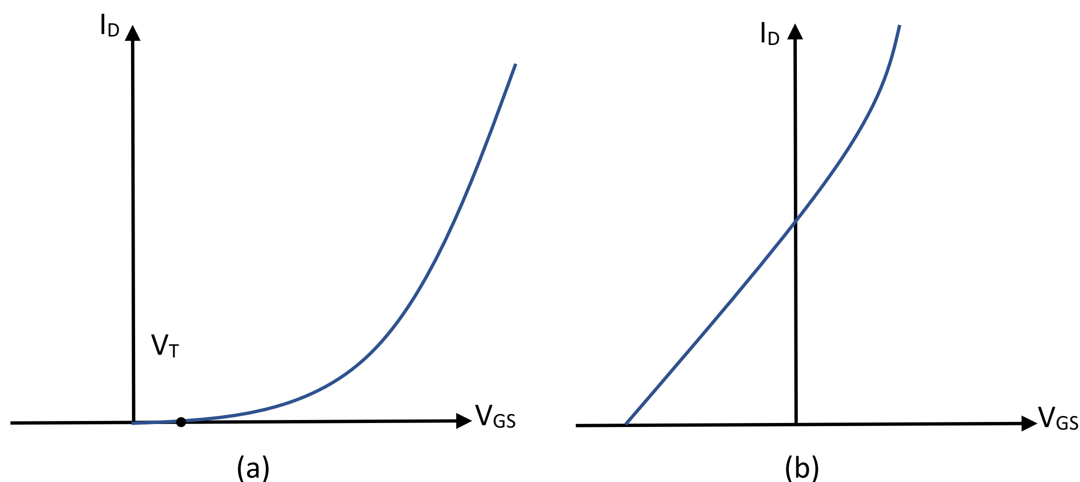

Figure 2- 13. Transfer characteristics (a) enhancement mode and (b) depletion mode MOSFETs for an n-type semiconductor.

Thin film transistors (TFTs) are typically MOSFETs, and consist of a dielectric layer, semiconductor layer, source and drain electrodes, and gate electrodes. The dielectric is sandwiched between the gate electrode and the semiconductor. The source and drain electrodes are typically made of metals (Al, Au, Ag, Ni etc.) and are deposited directly on the

semiconductor or at the opposite side of the semiconductor depending on the type of TFTs structure. The most used TFTs structures are shown in Figure 2-14. The operational concepts of these TFTs are based on the FET principles and the performance of these TFTs are governed by two important geometric parameters namely transistor's channel length (L) and width (W). The channel length of TFT is distance between the source and drain electrode while the channel width is the distance over which the source and drain electrodes run parallel to each other.

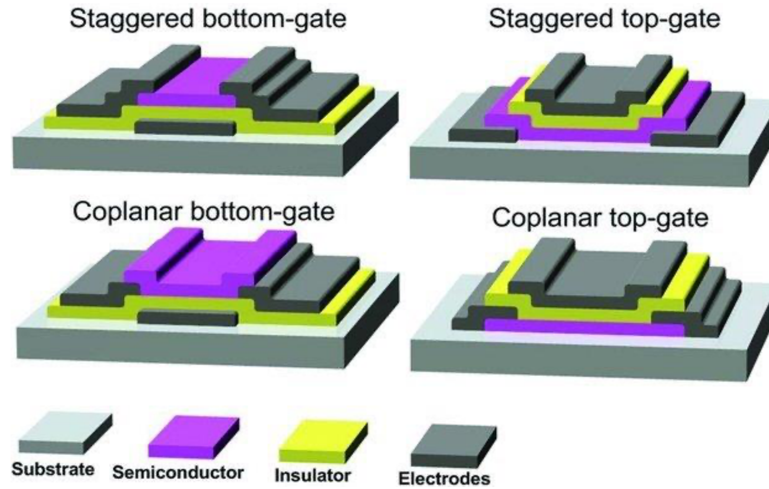

Figure 2- 14. Schematics showing some of the most conventional TFT structures, according to the position of the gate electrode and to the distribution of the electrodes relatively to the semiconductor [22].

The electrical characteristics of the TFT can be derived from its current-voltage relationship at the linear regime using gradual channel approximation [23].

$$I_D = \mu C_{ox}\frac{W}{L}\left(V_{GS} - V_T - \frac{V_{DS}}{2}\right)V_{DS}, \qquad for\ V_{GS} - V_T \geq\ V_{DS} \geq 0 \tag{2.15}$$

Where (W) and (L) are the channel width and length respectively, (C_{ox}) is the gate dielectric geometric capacitance, (μ) the charge carrier (hole or electron) mobility, (V_{GS}) the gate-source voltage, (V_T) the threshold voltage and (V_{DS}) the drain-source voltage. The current-voltage relationship at the saturation regime is:

$$I_D = \frac{\mu C_{ox}}{2}\frac{W}{L}(V_G - V_T)^2, \quad for\ V_{DS} \geq (V_{GS} - V_T) \geq 0 \tag{2.16}$$

From the transfer and output characteristics curves of a TFT, parameters such as mobility (μ), current modulation ratio (I_D^{On}/I_D^{Off}), subthreshold swing (SS) and turn-on voltage (V_{on}) could be extracted.

2.4.1 Mobility (μ)

The mobility (μ) is one of the main parameters that defines the performance of a TFT. It is associated with the efficiency of carrier transport in a material, affecting directly the maximum I_D and operating frequencies of the devices [22]. The μ of a given TFT is affected by several scattering mechanisms such as lattice vibrations, ionized impurities, grain boundaries and other structural defects [24]. Since the movement of carriers is constrained to a narrow region close to dielectric/semiconductor interface, additional sources of scattering should be considered such as Coulomb scattering from dielectric charges and from interface states or surface roughness scattering [25]. It is worth mentioning that the μ of a TFT is modulated by V_G, which makes scattering mechanisms less relevant for biasing conditions. The μ of a TFT can be extracted using different methodologies [22]. The widely used expression for μ extraction is obtained by given equations [26].

$$\mu_{lin} = \frac{L}{WC_{ox}} \cdot \frac{1}{V_D} \cdot \frac{\partial I_D}{\partial V_G} \tag{2.17}$$

For the linear region and

$$\mu_{sat} = \frac{L}{WC_{ox}} \cdot \frac{\partial^2 I_D}{\partial V_G^2} \tag{2.18}$$

For the saturation region.

2.4.2 Current modulation ratio

The current modulation ratio (I_D^{On}/I_D^{Off}) is the ratio between the maximum to the minimum drain current (I_D). The minimum I_D is associated with the noise level of the measurement equipment or the gate leakage current ((I_G), while the maximum I_D depends on the semiconductor material itself and on the effectiveness of capacitive injection by the field effect. In TFTs, a large I_D^{On}/I_D^{Off} typically above 10^6, is required for their successful implementation in devices. Figure 2-15 show a schematic of an output and transfer characteristics of an n-type oxide TFT.

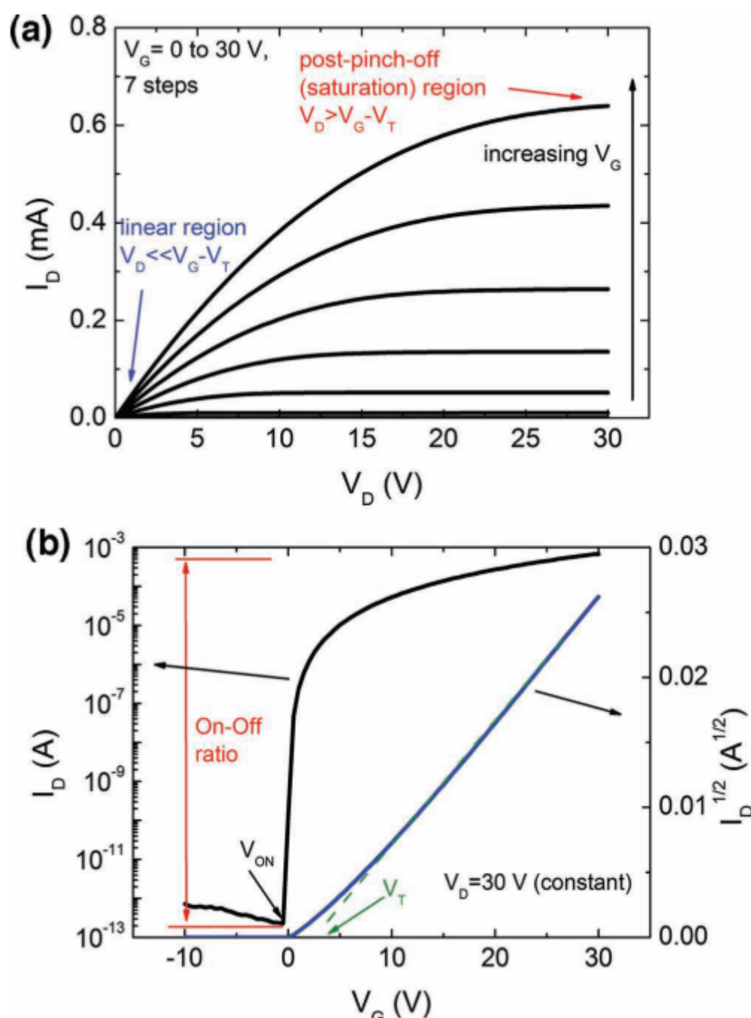

Figure 2- 15. Typical a) Output and b) transfer characteristics of a n-type oxide TFT [22].

2.4.3 Threshold/Turn on Voltage

The threshold/turn on voltage (V_T/V_{on}) is the V_G required for the transistor to turn on. An accumulation layer or conductive channel is formed closed to the dielectric/semiconductor interface between the source and drain electrodes (channel region). For an n-type TFT, regardless of the polarity of the V_T (i.e., whether positive or negative), the devices operate as enhancement or depletion mode. Both types are essential for circuit fabrications, however, enhancement mode is preferable as it does not require any V_G to turn off the transistor, contributing to the simplicity of the circuit design as well as minimizing power dissipation. V_T can be determined using different methodologies, such as linear extrapolation of the $I_D - V_G$ plot (for low V_D) or of the $I_D^{1/2} - V_G$ plot (for high V_D). The concept of V_{on} is often used in literature, simply corresponding to the V_G at which I_D starts to increase as seen in a log $I_D - V_G$ plot, or in other words, the V_G necessary to fully turn-off the transistor [27].

2.4.4 Subthreshold swing (SS)

The subthreshold swing (SS) is defined as the amount V_G needed to increase the I_D level by an order of magnitude. The equation used to determine the subthreshold swing is already given in equation (2.14). A typical SS value should be far less than 1, (i.e., 0.10 – 0.30 V/dec), and small values results in higher speeds and lower power consumption. From the SS value, the trap density per unit energy at the semiconductor/dielectric interface could be calculated as:

$$N_{SS}^{max} = C_{ox} \cdot \left(\frac{SS}{2.3eK_BT} - \frac{1}{e^2}\right) \tag{2.19}$$

Where (C_{ox}) is the geometric capacitance of the dielectric, (e) is the elementary charge, (K_B) is the Boltzmann constant, and T is the temperature [28].

2.5 References

[1] F.-C. Chiu, “A Review on Conduction Mechanisms in Dielectric Films,” *Adv. Mater. Sci. Eng.*, vol. 2014, no. 7, pp. 1–18, 2014.

[2] M. Q. Feng, G. Roqueta and L. Jofre, “Non-destructive evaluation (NDE) of composites: Microwave techniques,” in *Non-Destructive Evaluation (NDE) of Ploymer Matrix Composites*, 1st ed., V. M. Karbhari, Ed. 2013, pp. 574–616.

[3] J. Robertson, “High dielectric constant gate oxides for metal oxide Si transistors,” *Reports Prog. Phys.*, vol. 69, no. 2, pp. 327–396, 2006.

[4] P. W. P. and J. Robertson, “Band offsets and Schottky barrier heights of high dielectric constant oxides,” *J. Appl. Phys.*, vol. 92, no. 8, pp. 4712–4721, 2002.

[5] J. Robertson, “Band offsets of wide-band-gap oxides and implications for future electronic devices,” *J. Vac. Sci. Technol. B Microelectron. Nanom. Struct.*, vol. 18, no. 3, p. 1785, 2000.

[6] J. Robertson, “High K Dielectrics for Future CMOS Devices,” vol. 19, no. 2, pp. 579–591, 2009.

[7] C. Wenger, M. Lukosius, H. J. Müssig, G. Ruhl, S. Pasko, and C. Lohe, “Influence of the electrode material on Hf O2 metal-insulator-metal capacitors,” *J. Vac. Sci. Technol. B Microelectron. Nanom. Struct.*, vol. 27, no. 1, pp. 286–289, 2009.

[8] B. L. Yang, P. T. Lai, and H. Wong, “Conduction mechanisms in MOS gate dielectric films,” *Microelectron. Reliab.*, vol. 44, no. 5, pp. 709–718, May 2004.

[9] H. Wong, “The Current Conduction Issues in High-k Gate Dielectrics,” in *2007 IEEE Conference on Electron Devices and Solid-State Circuits*, 2007, no. CityU 121707, pp. 31–36.

[10] E. W. and Lim and R. Ismail, “Conduction mechanism of valence change resistive switching memory: A survey,” *Electron.*, vol. 4, no. 3, pp. 586–613, 2015.

[11] P. W. Peacock and J. Robertson, “Band offsets and Schottky barrier heights of high dielectric constant oxides,” *J. Appl. Phys.*, vol. 92, no. 8, pp. 4712–4721, 2002.

[12] J. G. Simmons, “Conduction in thin dielectric films,” *J. Phys. D. Appl. Phys.*, vol. 4, no. 5, pp. 613–657, 1971.

[13] J. G. Simmons, “Poole-Frenkel Effect and Schottky Effect in Metal- Insulator-Metal Systems,” *Phys. Rev.*, vol. 155, no. 3, 1967.

[14] F. C. Chiu, “Interface characterization and carrier transportation in metal/ HfO_2 /silicon structure,” *J. Appl. Phys.*, vol. 100, no. 11, 2006.

[15] F. C. Chiu, P. W. Li, and W. Y. Chang, “Reliability characteristics and conduction mechanisms in resistive switching memory devices using ZnO thin films,” *Nanoscale Res. Lett.*, vol. 7, pp. 1–9, 2012.

[16] Y. C. Yeo, T. J. King, and C. Hu, “Direct tunneling leakage current and scalability of alternative gate dielectrics,” *Appl. Phys. Lett.*, vol. 81, no. 11, pp. 2091–2093, 2002.

[17] H. Bentarzi, “The MOS Structure,” in *Transport in Metal-Oxide-Semiconductor Structures: Mobile Ions Effects on the Oxide Properties*, Berlin: Springer Berlin Heidelberg, 2011, pp. 5–16.

[18] S. Dimitrijev, “Metal-Semiconductor Contact and MOS Capacitor,” in *Principles of Semiconductor Devices*, 2nd ed., New York: Oxford University Press, Inc., 2012, pp. 252–295.

[19] A. Kiani, “Analysis of metal oxide thin film transistors with high-k dielectrics and source / drain contact metals,” University of Cambridge, 2013.

[20] S. M. Sze and Kwok K., “MOSFETs,” in *Physics of Semiconductor Devices*, Third., Hoboken, New Jersey: John Wiley & Sons, Ltd, 2006, pp. 293–373.

[21] D. Afouxenidis, R. Mazzocco, G. Vourlias, P. J. Livesley, A. Krier, W. I. Milne, O. Kolosov, and G. Adamopoulos, “ZnO-based thin film transistors employing aluminum titanate gate dielectrics deposited by spray pyrolysis at ambient air,” *ACS Appl. Mater. Interfaces*, vol. 7, no. 13, pp. 7334–7341, 2015.

[22] E. Fortunato, P. Barquinha, and R. Martins, “Oxide semiconductor thin-film transistors: A review of recent advances,” *Advanced Materials*, vol. 24, no. 22. pp. 2945–2986, 2012.

[23] R. C. Jaeger and T. N. Blalock, “Field-Effect Transistors,” in *Microelectronic Circuit Design*, 4th ed., and P. E. M. M. Lange, D. M. Schueller, Ed. New York: McGraw-Hill, 2011, pp. 145–204.

[24] E. S. Yang, *Microelectronic Devices*. Singapore: McGraw-Hill, 1988.

[25] D. K. Schroder, *Semiconductor Material and Device Characterization*, Third. New Jersey: John Wiley & Sons, Inc., 2006.

[26] D. Hong, G. Yerubandi, H. Q. Chiang, M. C. Spiegelberg, and J. F. Wager, “Electrical Modeling of Thin-Film Transistors,” *Crit. Rev. Solid State Mater. Sci.*, vol. 33, no. 2, pp. 101–132, May 2008.

[27] R. L. Hoffman, “ZnO-Channel thin-film transistors: Channel mobility,” *Appl. Phys.*, vol. 95, no. 10, pp. 5813–5819.

[28] M. A. M. and T. D. A. P. Pattanasattayavong, S. Thomas, G. Adamopoulos, “P-Channel thin-film transistors based on spray-coated CU_2O films,” *Appl. Phys. Lett.*, vol. 102, no. 2013, pp. 1–4, 2013.

3 Experimental: Deposition and Characterization

3.1 Introduction

In this chapter, the deposition and the characterization techniques used for thin film deposition are discussed. For the deposition, spray pyrolysis was used for deposition of thin films on substrates while thermal evaporation was employed for the deposition of top electrodes on the spray-coated films. The characterization of the spray-coated films was carried out using range of techniques including ellipsometry, x-ray diffraction (XRD), atomic force microscopy (AFM), ultraviolet-visible (UV-Vis) spectroscopy, impedance spectroscopy, fourier transform infrared (FTIR) spectroscopy and I – V measurements.

3.2 Experiment

3.2.1 Spray Pyrolysis

In the spray pyrolysis technique, films are typically deposited by an aerosol solution of the precursor which is spray coated onto pre-heated substrate where the constituents undergo chemical reaction to form a chemical compound [1].

Viguie and Spitz [2] described the four stages of reaction that may occur in the deposition process. In the first stage, the droplets reach the hot surface while the solvent evaporates leaving behind solids that further react in solid state. In the second stage, the solvents evaporate before the droplets approaches the hot surface and the dry solid impinges on the surface by decomposition. In the third process, the solvents are vaporized as the droplets approach the hot surface, the solid then melt and vaporizes, and the vapour diffuses to the hot surface to undergo heterogeneous reaction (typical CVD process). The last stage involves the entire reaction to take place in a vapour state [1]. The most important parameters in all the stages mentioned are the substrate temperature, solution concentration and solution flow rate, carrier gas flow rate, nozzle-to-substrate distance and droplet radius [1].

The substrate temperature is the most important parameter of spray pyrolysis technique because it determines the film morphology and the properties of the deposited material [3]. By increasing the substrate temperature, the films morphology changes from a cracked to porous microstructure. The properties of the films can also be influenced by varying the substrate temperature. For instance, it has already been reported in the literature [4] that the zinc oxide (ZnO) films deposited at 490 °C from aqueous solution of zinc acetate ($ZnC_4H_6O_4$), showed better crystallinity and thicker films than the one deposited at 420 °C. Another instance is that of terbia-doped yttria-stabilized zirconia thin films [5], where It was reported that the surface morphology was influenced by increasing substrate temperature resulting from a dense to a highly porous structure.

The solution concentration is considered as second most important parameter when employing spray pyrolysis technique. Usually, a metal salt precursor is dissolved in a solvent at solution concentration between 0.001 – 0.1 M which when deposited, leads to formation of thin films [1]. The thickness of the films can be controlled by varying the molarity of the solution concentration.

The carrier gas flow rate is another important parameter employed for spray pyrolysis technique. Here, a non-reactive gas such as noble gases are required to transport the solutions onto the substrate. It can also determine the growth rate of the film thickness. By increasing the carrier gas flow rate, the formation of films on the substrate becomes rapid. The carrier gas flow rate can be controlled by regulating the pressure pump.

The nozzle-to-substrate distance is critical in spray pyrolysis technique as it determines the formation of film thickness on the substrate. The formation of the film thickness also depends on the substrate temperature, volume of the solution and solution concentration.

Finally, the droplet radius is obtained from the droplet as it strikes the pre-heated substrate. The process undergoes chemical reactions that further results to the formation of thin film onto the substrate. An ideal deposition condition is when the droplets approach the substrate just as the solvent is completely removed.

For many years, spray pyrolysis technique have been utilized mainly for deposition of oxides (especially transparent conductors such as SnO_x) on glass [1][3]. This method can be used to grow high quality dense films, porous films and even multi-layered films of any composition [3]. The film properties depend on the choice of precursor and solvent, spray rate, atmosphere, carrier gas, droplet size, substrate temperature and also cooling rate after deposition [6]. The substrate temperature plays an important role in producing high quality films. The substrate temperature is expected to be at least +50 °C of the decomposition temperature of the precursor. The idea of choosing a suitable substrate temperature is to prevent the occurrence of an undesirable phenomenon such as Leidenfrost effect. Leidenfrost effect [7] is a physical phenomenon that occur when a droplet splashes onto a very hot surface such that the temperature of that surface is much higher than that of the boiling point of the droplet. This generates an undesirable insulating vapour layer between the droplet and the hot surface thereby slowing down the evaporation process of the droplet [7]. A typical water boiling graph curve at 1 atmosphere is shown in Figure 3-1 to illustrate the Leidenfrost phenomenon.

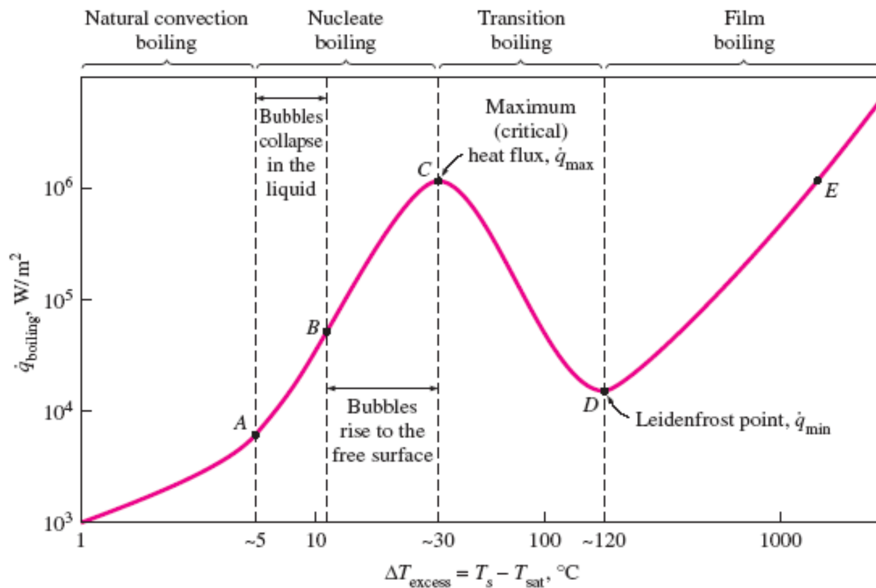

Figure 3- 1. A typical water boiling graph curve at 1 atmosphere [8].

The graph explains five stages of water boiling points between point A and E. In stage 1, also known as the natural convection boiling stage, there was no formation of water bubbles on the heating surface until after a few degrees above the saturation temperature (usually about 2 to 5 °C for water) as indicated at point A. In stage 2, there was formation of water bubbles between points A and C (nucleate boiling stage). At point A, the water bubbles start forming at various preferential sites on the heating surface. As the heating rate increases, the water bubbles keep increasing until the water boiling curves reaches point B. Again, with further increase in heating rate, more water bubbles are formed and the water boiling curve reaches point C where the maximum (critical) heat flux is obtained. When the heating rate further increases beyond point C, the heat flux starts to decrease due to the formation of vapour films on the heating surface that further act as an insulation due to low thermal conductivity relative to that of the liquid. This stage is also called the transition boiling stage and the point D which correspond to the minimum heat flux is called the Leidenfrost point. Beyond point D, the heater surface is completely covered by a continuous stable vapour film.

To that point, to avoid occurrence of such unwanted phenomenon, a moderate substrate temperature must be chosen. The decomposition temperature can be determined by running thermal analysis on the precursor.

Spray pyrolysis method offers several advantages compared to other methods of deposition because it is relatively very easy to adopt, it is cost-efficient compared to the vacuum-based techniques (MBE, ALD, MOCVD, sputtering etc.), uniform films can be deposited over large area, easy to dope materials, easy to control film growth rate and no vacuum chamber is required for the deposition. The parameters needed to adopt this technique includes the airbrush/atomizer, temperature controller, non-reactive carrier gas, pressure controller and substrate heater. Figure 3-2 illustrate the set-up of spray pyrolysis technique while Figure 3-3 show an image of a number of different substrates during spray coating process.

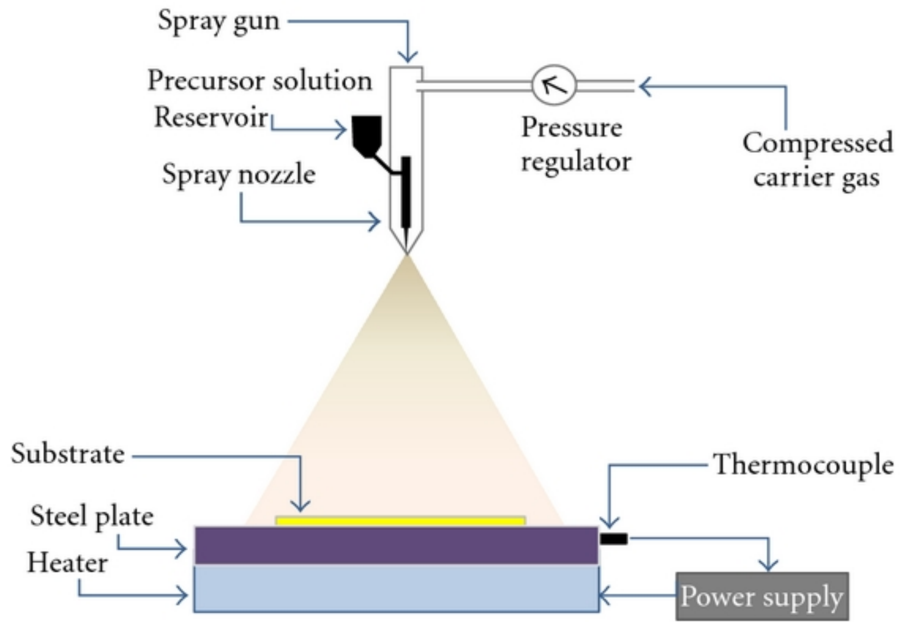

Figure 3- 2. Spray Pyrolysis technique for thin-film deposition [9].

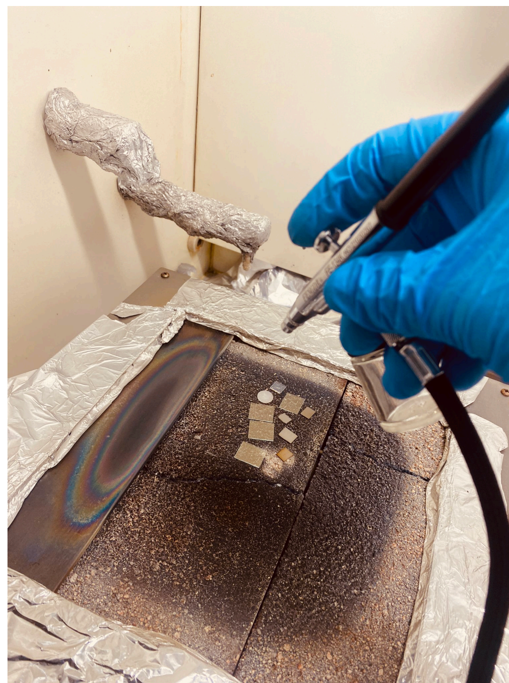

Figure 3- 3. An image showing variety of substrates during spray coating process on a preheated surface.

Table 3-1 presents examples of metal oxide thin films deposited by spray pyrolysis in recent years.

Table 3- 1. Selected previous works carried out by spray pyrolysis technique (Al_2O_3: aluminium (III) oxide, Al $(NO_3).9H_2O$: aluminium nitrate nonahydrate, Al $(C_5H_7O_2)_3$: aluminium acetylacetonate, $AlCl_3$: aluminium (III) chloride, 2-ME: 2-methoxyethanol, MeOH: methanol, DMF: dimethylformamide, DIW: deionized water, EtOH: ethanol, Acac: acetylacetone, HfO_2: hafnium oxide, $HfCl_4$: hafnium (IV) chloride, ZrO_2: zirconium oxide, Zr $(C_5H_7O_2)_4$: zirconium acetylacetonate, ZnO: zinc oxide, Zn (OAc). $2H_2O$: zinc acetate dilhydrate, In_2O_3: indium oxide, In $(NO_3)_3$. H_2O: indium (III) nitrate hydrate, In $(C_2H_3O_2)_3$: indium (III) acetate, SnO_2: tin oxide, Sn $(CH_3CO_2)_2$: tin (II) acetate, La_2O_3: lanthanum oxide, La $(NO_3)_3.6H_2O$: lanthanum (III) nitrate hexahydrate).

Films	Precursor	Solvent	Deposition temperature (°C)	Ref
Al_2O_3	Al $(NO_3).9H_2O$, Al $(C_5H_7O_2)_3$, $AlCl_3$,	2-ME & Acac, MeOH, MeOH & DMF, MeOH & Acac	350 400, 440 420	[10] [11][12] [13]
HfO_2	$HfCl_4$	MeOH & EtOH	450	[14]
ZrO_2	Zr $(C_5H_7O_2)_4$	MeOH	400	[15][16][17]
ZnO	Zn (OAc). $2H_2O$	MeOH 2-ME	400, 500 350	[18][19][20] [21][22] [23]
In_2O_3	In $(NO_3)_3$. H_2O In $(C_2H_3O_2)_3$	DIW	250 350-450	[24][21] [25]
SnO_2	Sn $(CH_3CO_2)_2$	DIW	350-450	[25]
La_2O_3	La $(NO_3)_3.6H_2O$	2-ME MeOH	350 500	[23] [22]

3.2.2 TGA/ DSC

The simultaneous thermal analysis generally refers to the simultaneous application of both thermogravimetric analysis (TGA) and differential scanning calorimetry (DSC) on a sample in a single instrument. The TGA measures the change in mass as a function of temperature or time of a sample while the DSC measures the amount of heat that is absorbed or released by the sample as a function of temperature or time. This measurement is carried out simultaneously by the STA. From the TGA curve, information about the decomposition profile of the sample could be revealed while from the DSC curve, information about the phase transition of the sample could also be revealed as illustrated in Figure 3-4.

In this thesis, the thermal analysis on tantalum chloride, aluminium acetylacetonate, hafnium chloride, titanium chloride, zirconium acetylacetonate and silicon chloride were ran using the simultaneous thermal analyser NETZSCH STA 449 F3 Jupiter® system, with alumina (Al_2O_3) crucible. All measurements were conducted in the range between 40 – 700 °C at a constant heating rate of 10 K/min under nitrogen atmosphere.

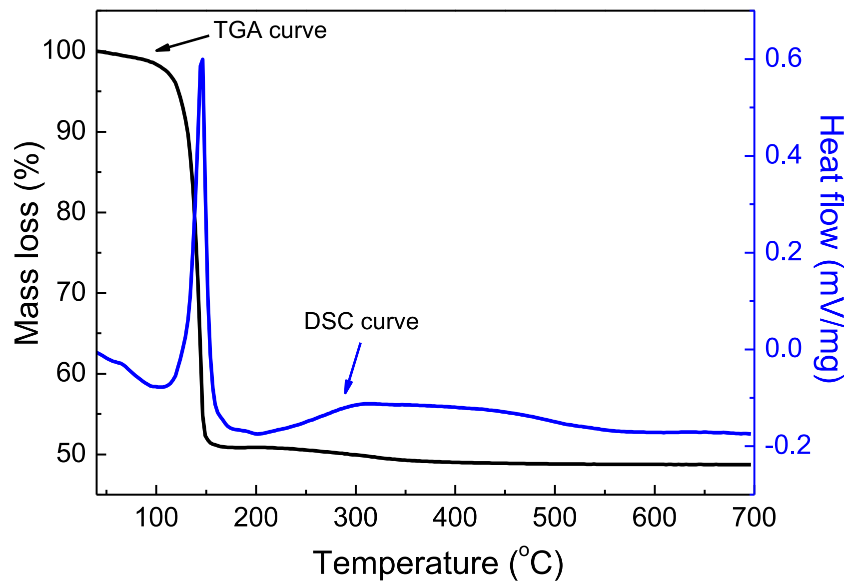

Figure 3- 4. Schematic of a typical TGA/DSC curve of titanium chloride liquid.

3.2.3 Thermal Evaporation

Thermal evaporation is among the oldest thin film deposition techniques specifically employed for deposition of metal and metal alloys. The process mainly consists of evaporation from the source and condensation at the substrate surface in a vacuum chamber (10^{-6} mbar). The principle of its operation requires a generated vapour by boiling or subliming a source material. This vapour is further transported onto the substrate where it will condense to produce solid film onto the substrate [26]. This technique can use two types of sources i.e. the resistive and electron beam source [27]. Figure 3-5 show a schematic of a typical electron beam source thermal evaporation system.

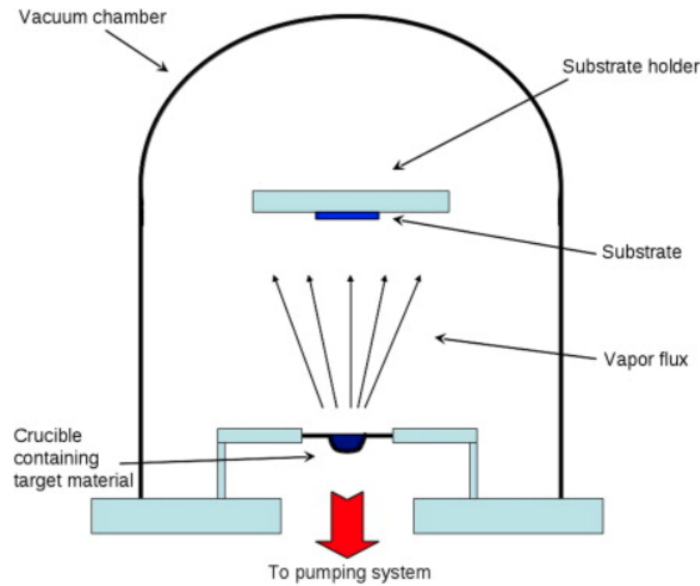

Figure 3- 5. A Schematic of a typical electron beam source thermal evaporation system [28].

In this thesis, thermal evaporation method was used for the deposition of top electrode contacts on the MIM and TFT devices. Aluminium metals were deposited through shadow masks, under high vacuum (10^{-6} mbar).

3.3 Characterization

3.3.1 Single Wavelength Ellipsometry

Ellipsometry is a powerful characterisation technique adopted for measurement of film thickness and optical parameters such as refractive index, angle of incidence and wavelength of the light source. Its principle is based on polarization of light interacting with the surface of the substrate by means of reflection, refraction and transmission of light. This means of interactions causes the change in the polarisation along with some other optical properties in the incident light beam. Figure 3-6 illustrate a single wavelength ellipsometry setup. It consists of a light source that produces a non-linear polarised light beam. This light beam is further linearized by a linear polariser and transmit to a compensator where it is elliptically polarised before hitting the surface of the sample. The polarised light on the film (still linearly polarised) is reflected off to the analyser and detected by a photodetector for data processing.

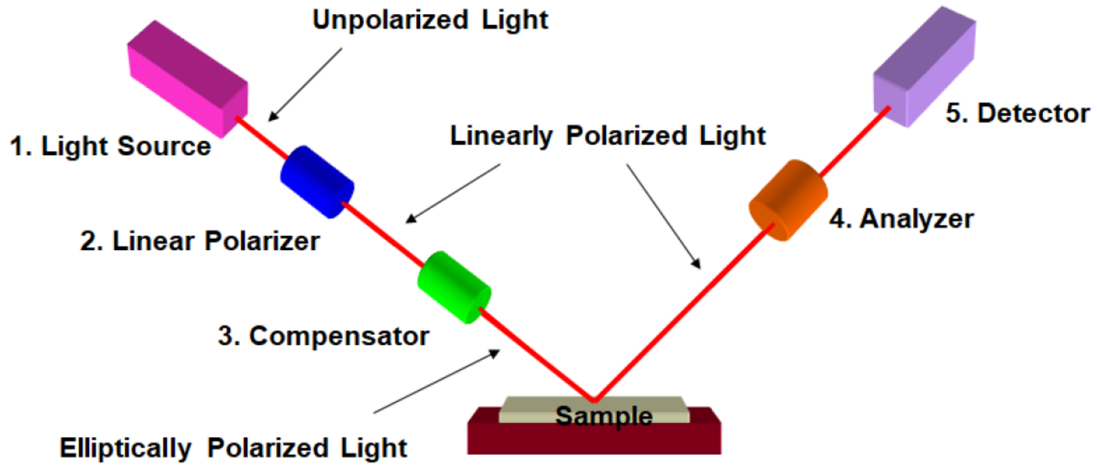

Figure 3- 6. Single wavelength ellipsometer setup [29].

The mathematical expression for describing the change of polarisation is given by the equation [30].

$$\rho = \frac{R_P}{R_S} = \tan(\Psi)e^{i\Delta} \tag{3.1}$$

Where, (ρ) is the change in polarisation, (R_P) is the component oscillating in the plane of the incident, (R_S) is the oscillating component perpendicular to the plane of the incidence, $(\tan(\Psi))$ is the amplitude ratio of the reflection and (Δ) is the phase shift.
In general, the ratio ρ is a function of several parameters [30].

$$\rho = \rho\,(d, N_0, N_1, N_2, \phi, \lambda) \tag{3.2}$$

Where (d) is the thickness of the film, N_0, N_1, and N_2 are the refractive indices of the ambient film, and substrate respectively, ϕ is the angle of incidence, and λ is the wavelength of the source.

In this thesis, a single wavelength ellipsometer (Rudolph AutoEL II) was used to estimate the thickness and the refractive index of the deposited metal oxides films. Rudolpg AutoEL II uses HeNe laser (632.8 nm) as a light source.

3.3.2 X-ray Diffraction (XRD)

The X-ray Diffraction (XRD) is a powerful technique for investigation of structural properties of solids. These structural properties can be investigated in terms of the crystal structure of a material, the preferred orientations (textured) and other parameters such as average grain size, crystallinity, strain, and crystal defects. The diffraction peak is produced by constructive interference of a monochromatic beam of X-rays scattered at specific angles from each set of lattice planes in a sample. The peak intensities are determined by the

distribution of atoms within the lattice [31]. Figure 3-7 show a schematic diagram of x-ray diffraction from a periodic atom structure.

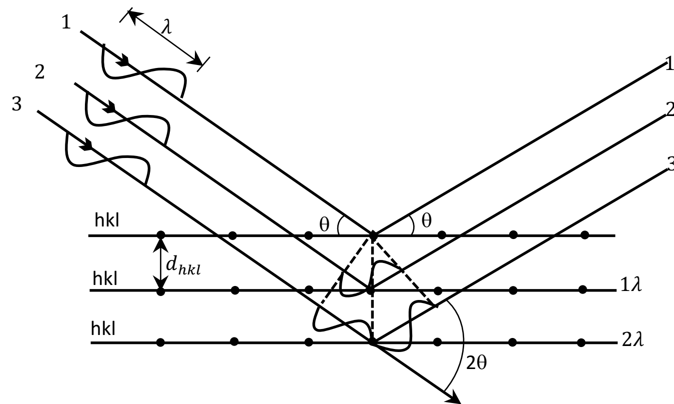

Figure 3- 7. Schematic of X-ray Diffraction from a periodic atomic structure.

The general relationship between wavelength of the incident X-rays, angle of incidence and spacing between crystal lattice planes of atoms is known as Bragg's Law, expressed as:

$$n\,.\,\lambda = 2d_{hkl}\,.\sin\theta \tag{3.3}$$

Where, (n) is the diffraction order, (λ) is the wavelength of the incident X-rays, (d_{hkl}) is the interplanar spacing of the crystal and (θ) is angle of incidence.

The diffraction peaks obtained from the XRD spectrum graph, can be analysed using the Scherrer's equation [32] to determine the average crystallite size $< d >$ of the atomic structure.

$$< d > = \frac{K\,.\,\lambda}{\beta_w\,.\cos\theta} \tag{3.4}$$

Where, (K) is the so-called Scherrer constant and is typically taken as 0.9, (λ) is the wavelength of the incident X-rays, (β_w) is the full width at the half maximum of the peak's intensity and (θ) is the Bragg angle. It is important to mention that the $< d >$ depends on the broadening of the XRD diffraction peak.

The equipment used to measure the XRD patterns of a material is the X-ray diffractometer. The X-ray diffractometer consists of three basic components: An X-ray tube, a sample holder and a detector. In the X-ray tube, current is applied to heat the filament that produces electrons. These electrons are accelerated towards a target by applying a voltage. The accelerated electrons bombard the target material and generates the X-rays. The X-rays are further directed onto the sample in a collimated way. The detector and the sample rotate in a circular path as the intensity of the X-ray is recorded at each point on the sample. Although, in some instruments, it is the X-ray tube that rotate while the sample is fixed. As

the geometry of incident X-rays impinges the sample, the Bragg's law [33] is satisfied causing constructive interference that appear as a peak in the intensity [31]. The detector then records and process this X-ray signal by converting the signal into a count rate that serve as an output to a device such as a computer. Figure 3-8 describes a typical X-ray diffractometer measurement using Bragg's geometry configuration.

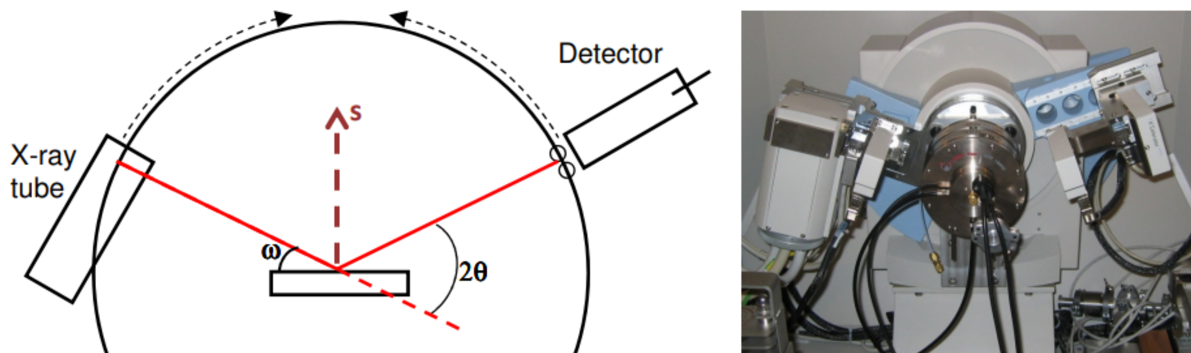

Figure 3- 8. Schematic of X-ray Diffractometer measurement [34].

Another geometry configuration suitable for measuring thin films is the grazing incidence x-ray diffraction (GIXRD). In GIXRD, the incident beam is fixed at a small angle (between 0.2 and 5 deg) [35] while the detector rotates across the sample (fixed) in a circular path for data collection as illustrated in Figure 3-9.

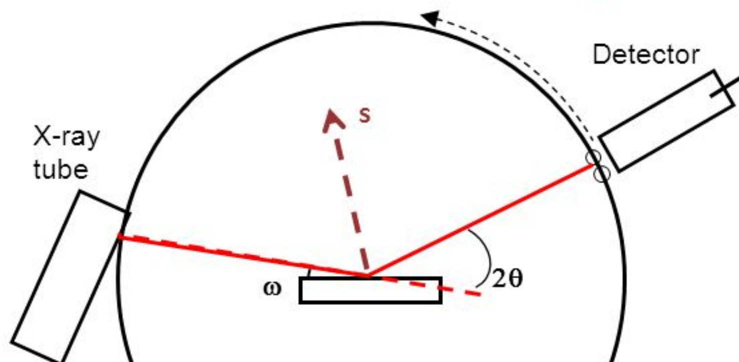

Figure 3- 9. Schematic of X-ray Diffractometer measurement [34].

Where, (ω) is the angle of incidence, defined as the angle between the X-ray source and the sample and (2θ) is the diffraction angle, defined as the angle between the incident beam and the detector.

One of the benefits of using smaller angle of incidence in GIXRD is to prevent high absorption of x-rays through the sample that may further caused signal loss and damage. Figure 3-10 show an illustration of GIXRD at high and low incident angle.

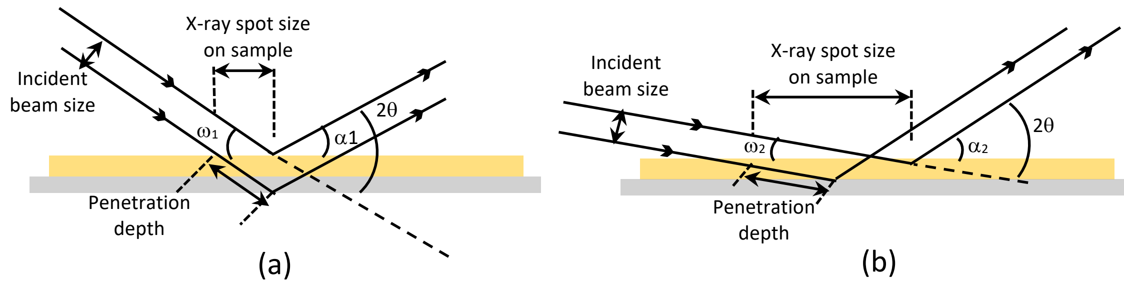

Figure 3- 10. Illustration of GIXRD at (a) high incident angle and, (b) at low incident angle [35].

At high incident angle ($\omega_1 > 5^0$), the incident x-ray is absorbed by the substrate as shown in Figure 3-10(a). The x-ray spot size narrows and may lead to x-ray penetration through the sample that may cause signal loss or damage to the sample. However, at low incident angle ($\omega_2 < 5^0$), the absorption of x-rays is focussed on the bulk sample and does not extend to the substrate as shown in Figure 3-10(b). In this case, the x-ray spot size widens and less penetration through the sample resulting to higher signal and reduced background noise.

In this thesis, the grazing incidence x-ray diffraction measurements were performed using a Rigaku Ultima$^+$ diffractometer, with CuKa radiation operating at 40 kV and 30 mA.

3.3.3 Atomic Force Microscopy (AFM)

The atomic force microscopy (AFM) is a powerful tool that provides information on surface morphology of thin films in terms of surface roughness at nano level. The surface roughness of the films is obtained by calculating the root mean square (RMS) of the AFM images.

The working principle of this technique is based on interaction force between the probe and the surface of the sample. There are basically six components that describe the working principle of this technique. These components include a photodetector, a light source, feedback loop, a cantilever, a probe and a sample. The probe is mounted at the apex of flexible cantilever which is usually made of Si or Si_3N_4. The light source is focussed on the rear side of the cantilever and reflects off to the four-quadrant photodiode. The photodiode detects and measure the bending of the cantilever as the tip is scanned over the surface of the sample. This bending is caused by the interaction force between the tip and the surface of the sample. The detected signals are further transmitted to the feedback electronics where it is processed and converted into a voltage and further extends to the piezo. The piezo allows free movement of the positions of the cantilever while the sample is fixed or vice-versa. This

depends on the actual type of the AFM configuration. Figure 3-11 illustrate the schematic of AFM setup.

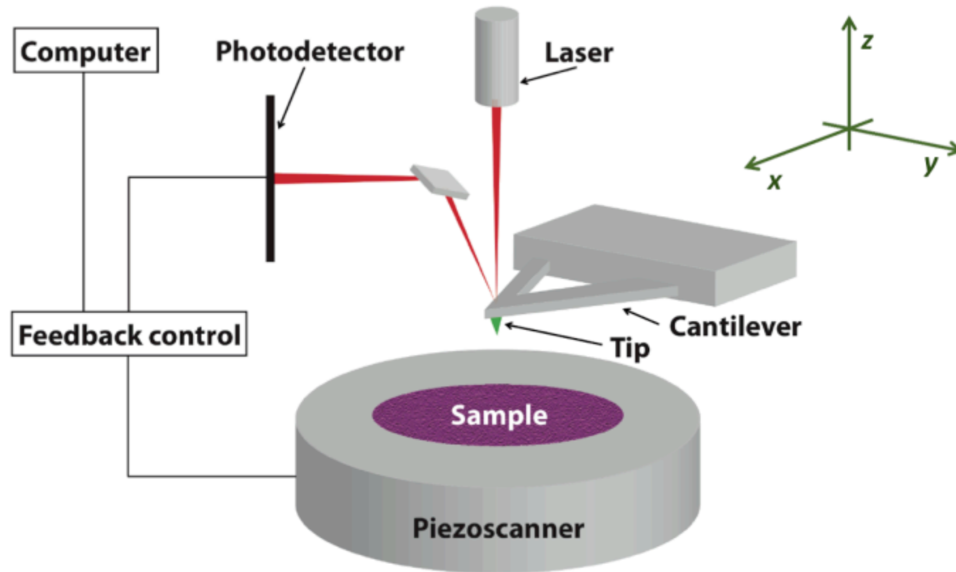

Figure 3- 11. A schematic of AFM setup [36].

There are basically two major scanning modes of AFM operation [37], namely the contact mode and tapping mode. In the contact mode (also known as repulsive force), the tip is always in contact with the sample surface during measurement while in the tapping mode (also known as attractive force), the tip is not in contact with the sample's surface however, it oscillates in a very close proximity to the sample's surface. The contact mode has an advantage of obtaining very high-resolution images of the surface of the sample [37]. However, with constant contact between the tip and the surface of the sample, the surface of the sample could damage due to high lateral force exerted on the sample.

In this thesis, AFM images were taken in contact mode under ambient conditions using a MultiMode probe microscope (MM-SPM) fitted to a Nanoscope IIIa controller unit employing a silicon tip of radius < 10 nm.

3.3.4 Ultraviolet Visible (UV-Vis) spectroscopy

The UV-Vis is a technique for the investigation of the optical properties of films. In this technique, measurements of the samples are taken in %transmittance spectra in a wavelength range between 190 and 1000 nm on fused silica substrate. From these measurements, parameters such as optical band gap (E_G) and Urbarch tail energy (E_U) [38] of the material could be obtained.

The E_G is defined as the energy difference between the conduction band and the valence band in the energy band diagram and it can be extrapolated from the Tauc plot [39]. Generally, the E_G can be calculated by the given mathematical expression [38]:

$$(\alpha hv)^n = \beta(hv - E_G) \tag{3.5}$$

Where, α is absorption coefficient, h is the Planck constant, v is the frequency of wavelength, β is a constant linked to the disorder degree of the structure and n is an exponent index taken as ½ or 2 for direct and indirect transition E_G respectively. The Tauc plot can be obtained from the graph of $(\alpha hv)^n$ versus photon energy (hv) as illustrated in Figure 3-12.

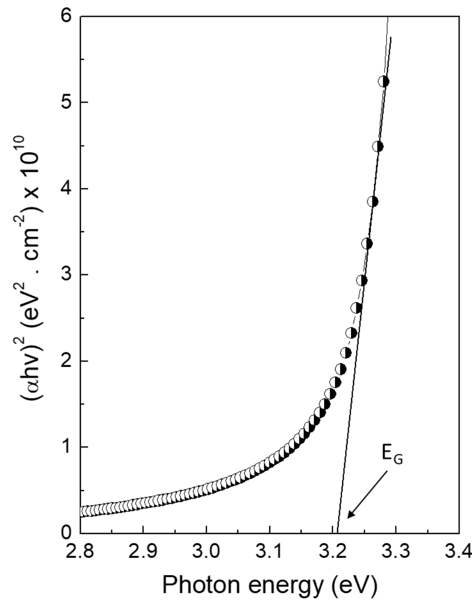

Figure 3- 12. The extrapolation of a linear curve of a Tauc plot to determine the direct E_G of ZnO thin films.

The E_U on the other hand, is an exponential tail that appears along the absorption coefficient curve near optical band edge in the absorption coefficient versus photon energy plot. E_U characterizes local defects which create localized states in the E_G. it is associated with disordered degree in amorphous materials which leads to extension of density of states in band tails [40]. E_U can be obtained by the given equation [38]:

$$\alpha = \alpha_0 exp\left({hv}/{E_U}\right) \tag{3.6}$$

Where,(α_0) is a constant and (E_U) can be determined from the inverse slope of $ln\alpha$ versus (hv) plot as illustrated in Figure 3-13.

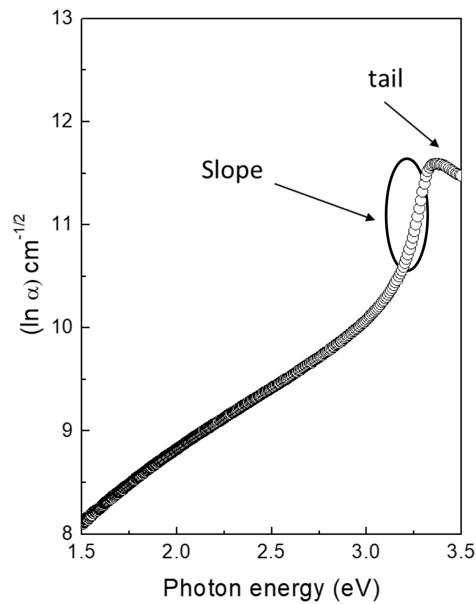

Figure 3- 13. The E_U plot of ZnO thin films.

The optical path of a UV-Vis lambda 35 spectrometer is described in Figure 3-14. It has two independent radiation sources (deuterium lamp and halogen lamp source) that generates the wavelength range of the spectrometer. The radiation from the halogen lamp is used for operation in the visible region while the radiation from the deuterium source is used for operation in ultraviolet region. For operation in visible region, the radiation from the halogen lamp is transmitted to the mirror M1 and reflects off to mirror M2. Because the operation is in visible region, the radiation from the deuterium lamp is blocked by mirror M1. Subsequently, for operation in ultraviolet region, the radiation from the deuterium lamp passes through mirror M1 and extends to mirror M2 for further reflection. The reflected light on mirror M2 is transmitted to the grating (monochromator) via optical filter on the filter wheel assembly. The radiation at the monochromator further reflects off to the mirror M3 and again reflects off to the beam splitter. The beam splitter splits the radiation into two, transmitting only 50 % of each to mirror M4 and mirror M5. Both mirror M4 and mirror M5 are focused on the sample and the reference cell respectively. Finally, the beam extends to the detector via the convex lens for data processing.

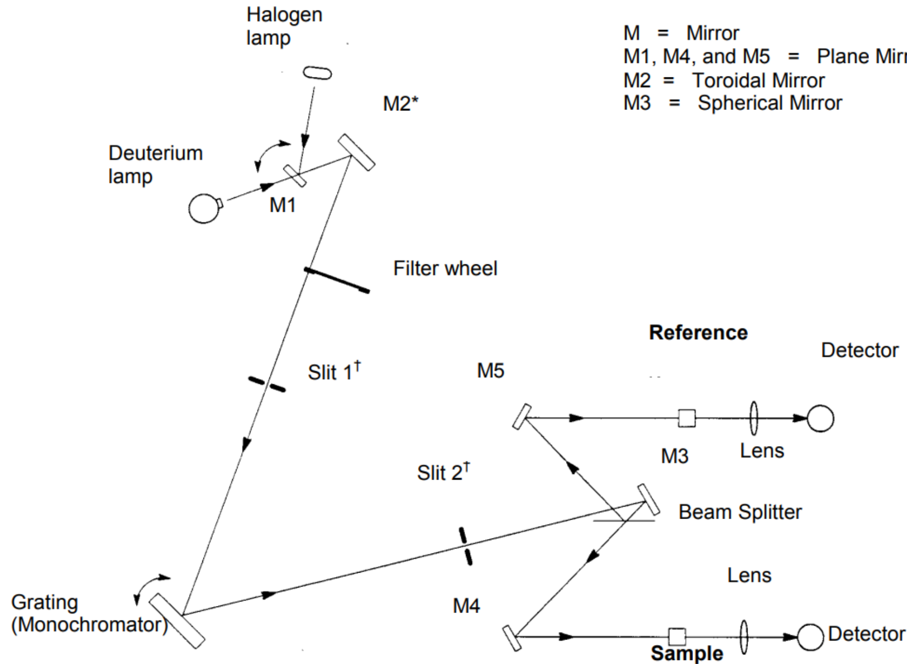

Figure 3- 14. Optical path of a UV-Vis spectrometer [41].

In this thesis, the UV Vis lambda 35 spectrometer was used to investigate the optical properties of deposited thin films.

3.3.5 Impedance spectroscopy

The impedance spectroscopy is a characterization technique employed to investigate the dielectric properties of films in MIM structure. In this technique, characterization on MIM devices on glass/ITO substrates were conducted in the probe station under high vacuum (10^{-2} mbar) using the Wayne Kerr 6500B impedance analyser. The impedance analyser characterises the component using range of AC functions over range of frequencies (1 kHz – 10 MHz). These AC functions include capacitance, inductance, resistance, reactance, conductance, susceptance, dissipation factor, quality factor, impedance, admittance and phase angle. The impedance spectrometer displays two simultaneous measurements of selected AC functions which can be exported to the computer via USB or GPIB for data processing. The mathematical expression of a geometric capacitance (C_{ox}) of a MIM capacitor is given as:

$$C_{ox} = \frac{1}{2\pi f.A} \tag{3.7}$$

Where, (f) is the frequency and (A) is the area of the top electrode in cm^2. Figure 3-15 show an example of a geometric capacitance as a function of frequency of Ta_2O_5 films.

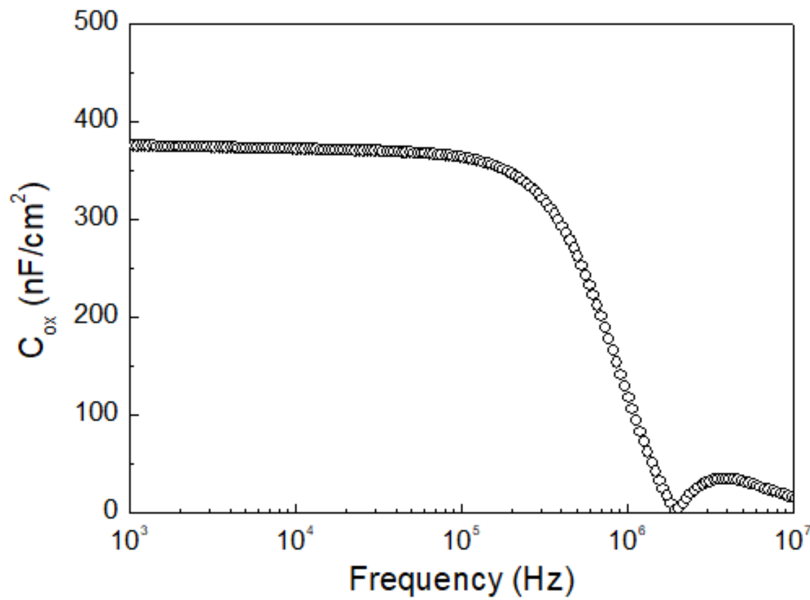

Figure 3- 15. An example of geometric capacitance as a function of frequency of Ta_2O_5 films.

The dielectric constant (k) is related to the geometric capacitance and can mathematically be expressed as:

$$k = \frac{C_{ox} \cdot t}{\varepsilon_o \cdot A} \tag{3.8}$$

Where, (t) is thickness of the film and $(\varepsilon_o) = 8.85 \times 10^{-12}\ F/m$ is the permittivity of free space.

3.3.6 Fourier Transform Infrared Spectroscopy (FTIR)

FTIR is an infrared spectroscopy technique used for the identification of chemical bonds including solids, liquid and gases in infrared region. This identification of chemical bonds is achieved through means of interactions between the infrared radiation and the matter. In traditional IR spectroscopy, when light interacts with matter, the matter absorbs the light, and the absorption causes vibration within the atoms or molecules of that matter. This vibration occurs at a specific frequency corresponding to a chemical bond in the atoms. The FTIR differs from traditional IR spectroscopy as it offers the advantage of simultaneous measurements of all infrared frequencies rather than individually.

The working principle of the FTIR is based on optical interferometry [42]. Figure 3-16 show a schematic of interferometer used in FTIR. In the optical interferometry, a beam splitter takes an incoming infrared beam and splits it into two optical beams. One of the beams reflects to a flat optical fixed mirror and the other reflects to the other flat optical movable mirror that is very few millimetres away from the beam splitter. The two beams are further reflected from their respective mirrors and recombined. It is important to note that as one path of the beam travels in fixed length, the other path is constantly changing (in length) due

to the movement of the mirror. Consequently, the signal that exits the interferometry is a signal comprising of two beams interfering with each other. This resulting signal is called an interferogram, which is a unique type of signal comprising of encoded infrared frequencies. In other words, as the interferogram is measured, so also the infrared frequencies simultaneously. Finally, the resulting interferogram signals are converted into frequency spectrum by a computer using a well-known mathematical technique called Fourier transformation.

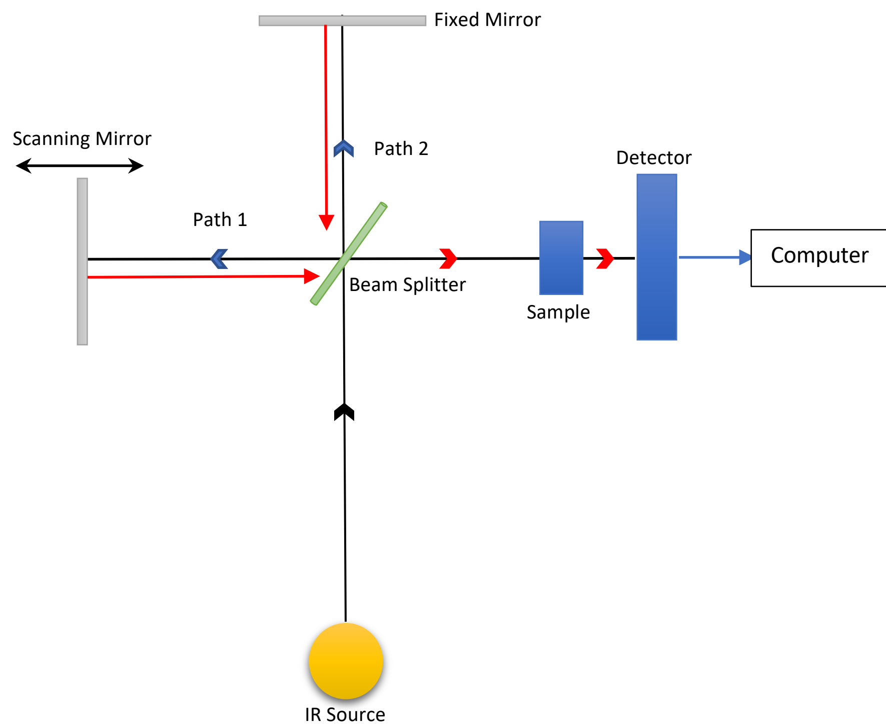

Figure 3- 16. Schematic of interferometer used in FTIR [43].

3.3.7 I – V measurement

The I – V measurement is used to investigate the electrical properties of thin films. In this technique, characterization on MIM devices on glass/ITO substrates were conducted in the probe station under high vacuum (10^{-2} mbar) using B5100 Parameter analyser. From this technique, parameters such as current density – electric field (J – E) characteristics and dielectric strength of the MIM device could be extracted. Additionally, the current conduction mechanism could also be investigated from the J – E characteristics to further reveal the nature of the current leakage in the dielectric. A more detailed review on conduction mechanism has already been discussed in chapter 2 of this thesis.

3.4 References

[1] J. B. Mooney and S. B. Radding, “Spray Pyrolysis Processing,” *Annu. Rev. Mater. Sci.*, vol. 12, pp. 81–101, 1982.

[2] J. C. Vigui and J. Spitz, “Chemical Vapor Deposition at Low Tempertures,” *J. Electrochem. Soc.*, vol. 268, no. 4, pp. 2–5, 1971.

[3] D. Perednis and L. J. Gauckler, “Thin film deposition using spray pyrolysis,” *J. Electroceramics*, vol. 14, pp. 103–111, 2005.

[4] H. H. Afify, S. A. Nasser, and S. E. Demian, “Influence of substrate temperature on the structural, optical and electrical properties of ZnO thin films prepared by spray pyrolysis,” *J. Mater. Sci. Mater. Electron.*, vol. 2, no. 3, pp. 152–156, 1991.

[5] N. H. J. Stelzer and J. Schoonman, “Synthesis of terbia-doped yttria-stabilized zirconia thin films by electrostatic spray deposition (ESD),” *J. Mater. Synth. Process.*, vol. 4, no. 6, 1996.

[6] P. S. Patil, “Versatility of chemical spray pyrolysis technique,” *Mater. Chem. Phys.*, vol. 59, no. 3, pp. 185–198, 1999.

[7] V. Talari, P. Behar, Y. Lu, E. Haryadi, and D. Liu, “Leidenfrost drops on micro/nanostructured surfaces,” *Front. Energy*, vol. 12, no. 1, pp. 22–42, 2018.

[8] “Water Boiling Graph Curve at 1 Atmosphere,” *Engineers Edge*, 2021. [Online]. Available: https://www.engineersedge.com/heat_transfer/water_boiling_graph_curve_13825.htm. [Accessed: 07-Oct-2021].

[9] G. E. Patil, D. D. Kajale, V. B. Gaikwad, and G. H. Jain, “Spray Pyrolysis Deposition of Nanostructured Tin Oxide Thin Films,” *ISRN Nanotechnol.*, vol. 2012, pp. 1–5, 2012.

[10] B. Wang, X. Yu, P. Guo, W. Huang, L. Zeng, N. Zhou, L. Chi, M. J. Bedzyk, R. P. H. Chang, T. J. Marks, and A. Facchetti, “Solution-Processed All-Oxide Transparent High-Performance Transistors Fabricated by Spray-Combustion Synthesis,” *Adv. Electron. Mater.*, vol. 2, no. 4, 2016.

[11] G. Adamopoulos, S. Thomas, D. D. C. Bradley, M. A. McLachlan, and T. D. Anthopoulos, “Low-voltage ZnO thin-film transistors based on Y_2O_3 and Al_2O_3 high-k dielectrics deposited by spray pyrolysis in air,” *Appl. Phys. Lett.*, vol. 98, no. 12, pp. 1–4, 2011.

[12] M. Esro, R. Mazzocco, G. Vourlias, O. Kolosov, A. Krier, W. I. Milne, and G. Adamopoulos, “Solution processed lanthanum aluminate gate dielectrics for use in metal oxide-based thin film transistors,” *Appl. Phys. Lett.*, vol. 106, no. 20, 2015.

[13] D. Afouxenidis, R. Mazzocco, G. Vourlias, P. J. Livesley, A. Krier, W. I. Milne, O. Kolosov,

and G. Adamopoulos, "ZnO-based thin film transistors employing aluminum titanate gate dielectrics deposited by spray pyrolysis at ambient air," *ACS Appl. Mater. Interfaces*, vol. 7, no. 13, pp. 7334–7341, 2015.

[14] M. Esro, G. Vourlias, C. Somerton, W. I. Milne, and G. Adamopoulos, "High-mobility ZnO thin film transistors based on solution-processed hafnium oxide gate dielectrics," *Adv. Funct. Mater.*, vol. 25, no. 1, pp. 134–141, 2015.

[15] G. Adamopoulos, S. Thomas, P. H. Wobkenberg, D. D. C. Bradley, M. A. McLachlan, and T. D. Anthopoulos, "High-mobility low-voltage ZnO and Li-doped ZnO transistors based on ZrO_2 high-k dielectric grown by spray pyrolysis in ambient air," *Adv. Mater.*, vol. 23, no. 16, pp. 1894–1898, 2011.

[16] H. Faber, B. Burtz, C. Dicker, E. Spiecker, and M. Halik, "Fully patterned low-voltage transparent metal oxide transistors deposited solely by chemical spray pyrolysis," *Adv. Funct. Mater.*, vol. 23, no. 22, pp. 2828–2834, 2013.

[17] A. T. Oluwabi, A. Katerski, E. Carlos, R. Branquinho, A. Mere, M. Krunks, E. Fortunato, L. Pereira, and I. O. Acik, "Application of ultrasonic sprayed zirconium oxide dielectric in zinc tin oxide-based thin film transistor," *J. Mater. Chem. C*, vol. 8, no. 11, pp. 3730–3739, 2020.

[18] G. Adamopoulos, A. Bashir, P. H. Wöbkenberg, D. D. C. Bradley, and T. D. Anthopoulos, "Electronic properties of ZnO field-effect transistors fabricated by spray pyrolysis in ambient air," *Appl. Phys. Lett.*, vol. 95, no. 13, pp. 2007–2010, 2009.

[19] G. Adamopoulos, A. Bashir, S. Thomas, W. P. Gillin, S. Georgakopoulos, M. Shkunov, M. A. Baklar, N. Stingelin, R. C. Maher, L. F. Cohen, D. D. C. Bradley, and T. D. Anthopoulos, "Spray-deposited Li-doped ZnO transistors with electron mobility exceeding 50 cm2/Vs," *Adv. Mater.*, vol. 22, no. 42, pp. 4764–4769, 2010.

[20] G. Adamopoulos, A. Bashir, W. P. Gillin, S. Georgakopoulos, M. Shkunov, M. A. Baklar, N. Stingelin, D. D. C. Bradley, and T. D. Anthopoulos, "Structural and electrical characterization of ZnO films grown by spray pyrolysis and their application in thin-film transistors," *Adv. Funct. Mater.*, vol. 21, no. 3, pp. 525–531, 2011.

[21] L. Castaneda, A. Maldonado, A. E-Morales, M. A-Alejo, H. Gomez, J. V-Perez, and M. D. L. L. Olvera, "Indium doped zinc oxide thin films deposited by ultrasonic spray pyrolysis technique: Effect of the substrate temperature on the physical properties," *Mater. Sci. Semicond. Process.*, vol. 14, no. 2, pp. 114–119, 2011.

[22] Y. Bouznit, Y. Beggah, and F. Ynineb, "Sprayed lanthanum doped zinc oxide thin films," *Appl. Surf. Sci.*, vol. 258, no. 7, pp. 2967–2971, 2012.

[23] R. N. Bukke, J. K. Saha, N. N. Mude, Y. Kim, S. Ldd, and J. Jang, "Lanthanum Doping in Zinc Oxide for Highly Reliable Thin-Film Transistors on Flexible Substrates by Spray Pyrolysis," *ACS Appl. Mater. Interfaces*, vol. 12, no. 31, pp. 35164–35174, 2020.

[24] L. Petti, H. Faber, N. Munzenrieder, G. Cantarella, P. A. Patsalas, G. Troster, and T. D. Anthopoulos, "Low-temperature spray-deposited indium oxide for flexible thin-film transistors and integrated circuits," *Appl. Phys. Lett.*, vol. 106, no. 9, pp. 10–14, 2015.

[25] S. Marikkannu, M. Kashif, N. Sethupathy, V. S. Vidhya, S. Piraman, A. Ayeshamariam, M. Bououdina, N. M. Ahmed, and M. Jayachandran, "Effect of substrate temperature on indium tin oxide (ITO) thin films deposited by jet nebulizer spray pyrolysis and solar cell application," *Mater. Sci. Semicond. Process.*, vol. 27, no. 1, pp. 562–568, 2014.

[26] W. Kern and K. Schuergraf, "Deposition technologies and applications: introduction and overview," in *Handbook of Thin-Film Deposition Processes and Techniques*, 2nd ed., K. Seshan, Ed. New York: Noyes Publications, 2002, pp. 11–43.

[27] D. A. Jameel, "Thin Film Deposition Processes," *Int. J. Mod. Phys. Appl.*, vol. 1, no. 4, pp. 193–199, 2015.

[28] R. J. Martin-Palma and A. Lakhtakia, "Vapor-Deposition Techniques," in *Engineered Biomimicry*, Kindle., Pennsylvania: Elsevier Inc., 2013, pp. 383–398.

[29] D. Afouxenidis, "Solution-Processed Metal Oxide Dielectrics and Semiconductors for Thin Film Transistor Applications," 2018.

[30] P. Durgapal, "Thin film ellipsometry metrology Thin Film Ellipsometry Metrology," in *AIP Conference Proceedings*, 1998, vol. 449, no. 121, pp. 121–131.

[31] A. A. Bunaciu, E. G. Udristioiu, and H. Y. Aboul-Enein, "X-Ray Diffraction: Instrumentation and Applications," *Crit. Rev. Anal. Chem.*, vol. 45, pp. 289–299, 2015.

[32] A. L. Patternson, "The Scherrer Formula for X-Ray Particle Size Determination," *Physical review*, vol. 56. pp. 978–982, 1939.

[33] C. J. Humphreys, "The significance of Bragg's law in electron diffraction and microscopy, and Bragg's second law," *Acta Crystallogr. Sect. A*, vol. 69, no. 1, pp. 45–50, 2012.

[34] S. A. Speakman, "Basics of X-Ray Powder Diffraction," *Massachusette Institute of Technology*. [Online]. Available: http://prism.mit.edu/xray/documents/1 Basics of X-Ray Powder Diffraction.pdf. [Accessed: 07-Oct-2021].

[35] N. Widjonarko, "Introduction to Advanced X-ray Diffraction Techniques for Polymeric Thin Films," *Coatings*, vol. 6, no. 4, p. 54, 2016.

[36] F. M. M. Facchini, M. V. Filho, S. A. S. Vedovello, F. A. Cotrim, A. Cotrim-Ferreira, and C. A. M. Tubei, "Wire Roughness Assessment of 0.016" × 0.022" the Technique Lingual Orthodontics," *Contemp. Dent. Pract.*, vol. 18, no. 4, pp. 295–299, 2017.

[37] C. P. and Melissa and H. R. Wouter, "Atomic Force Microscopy: An Introduction," *Single*

Molecule Analysis, Second. Amsterdam: Humana Press, 2018.

[38] M. F. and L. T. F. Rebib, N. Laidani, G. Gottardi, V. Micheli, R. Bartali, Y. Jestin, E. Tomasella, "Investigation of structural and optical properties of sputtered Zirconia thin films," *Eur. Phys. JournalApplied Phys.*, vol. 43, pp. 363–368, 2008.

[39] J. Tauc, "Optical properties and electronic structure of amorphous Ge and Si," *Mater. Res. Bull.*, vol. 3, no. 1, pp. 37–46, 1968.

[40] V. R. Akshay, B. Arun, G. Mandal, and M. Vasundhara, "Visible range optical absorption, Urbach energy estimation and paramagnetic response in Cr-doped TiO_2 nanocrystals derived by a sol-gel method," *Phys. Chem. Chem. Phys.*, vol. 21, no. 24, pp. 12991–13004, 2019.

[41] L. K. Muthén and B. O. Muthén, "UV Vis Spectrometer User ' S Guide," *Perkin Elmer*, no. 888, 2000.

[42] M. A. Ganzoury, N. K. Allam, T. Nicolet, and C. All, "Introduction to Fourier Transform Infrared Spectrometry," *Renew. Sustain. Energy Rev.*, vol. 50, pp. 1–8, 2015.

[43] A. Clayborne and V. Morris, "Fourier Transform Infrared Spectroscopy (FTIR)," in *Fall 2017*, 2017, pp. 2–5.

4 Tantalum Aluminate $Ta_{1-x}Al_xO_y$ Thin Films

In this chapter, the deposition and characterization of Tantalum Aluminate ($Ta_{1-x}Al_xO_y$) thin films as a function of the Ta to Al atomic ratio (in the precursor solution) and their implementation as gate dielectrics in TFTs employing ZnO semiconducting channels are investigated. The films were deposited by spray coating in ambient atmosphere and characterized by UV-Vis spectroscopy, GIXRD, AFM, Impedance spectroscopy, I – V and field effect measurements. The results showed amorphous $Ta_{1-x}Al_xO_y$ films with low surface roughness (< 1 nm), with dielectric constant that ranges between 7 and 24, and optical bandgap between 4.9 and 8.8 eV. The leakage current density at 2 MV/cm showed decrease between 10^{-3} and 10^{-8} A/cm^2 with increasing Al atomic ratio. Finally, the ZnO-based TFTs on $Ta_{50}Al_{50}O_x$ high-k gate dielectrics showed excellent performance such as high electron mobility of 16 cm^2/Vs, high on/off current modulation ratio of 10^5, threshold voltage of -3.2 V, subthreshold swing of 0.56 V/dec, interface trap density of 7.7 x 10^{12} cm^{-2}, low operation voltage of 4 V and negligible hysteresis.

4.1 Introduction

The continuous scaling of MOSFETs have attracted interest in realization of potential high k (k > 3.9) metal oxides as alternative candidates to replace the conventional silicon dioxide (SiO_2) gate dielectric. Among these high k metal oxides, the transition metal oxide Tantalum oxide (Ta_2O_5), have been given much consideration due to its promising application as a storage capacitor in memories [1]–[7].

Ta_2O_5 exhibit high dielectric constant of (k > 20) depending on its manufacturing processes, high refractive index (n = 2.18 at λ = 550 nm) [8]. It is highly transparent in visible spectrum (400 – 700 nm) and exhibit a wide energy gap 4.4 eV [9]. Such properties of Ta_2O_5 made it suitable to be utilized in other areas of application such as in optoelectronics [10], silicon solar cells [11] and thin-film transistor (TFT) applications [12].

Ta_2O_5 films have already been deposited by several techniques including RF sputtering [13], atomic layer deposition (ALD) [14][15], metal organic chemical vapour deposition (MOCVD) [2], pulsed laser deposition (PLD) [3], spin and dip coating [16] and ultrasonic spray pyrolysis [7].

Its atomic structure can exist in amorphous or crystalline phase depending on the deposition conditions. It has been reported that as-deposited tantalum oxide films at moderate temperatures (< 600 °C) are amorphous. Salaun et al. [14], reported that as-deposited Ta_2O_5 films deposited by ALD were amorphous even after annealed at 600 °C. Similarly, Kukli et al.[15], reported that Ta_2O_5 films grown by ALD were found to be amorphous after deposition at 300 °C. Furthermore, Nowak et al. [17], also reported that sputtered Ta_2O_5 films at 300 °C were amorphous. However, in the listed references, Ta_2O_5 films crystallizes after post-deposition treatment above 600 °C. There are several reports on the atomic structure of Ta_2O_5 films [3][7][13][17][18][21]–[24].

Amorphous high-k metal oxides are preferable than the crystalline metal oxides. This is due to the absence of grain boundaries that act as diffusion pathways that promotes current leakage within the dielectrics and as a result, leads to poor performance of the device [23]. Additionally, amorphous metal oxides have better quality interface with the semiconductor than the crystalline ones because of its smoother surfaces that results to better interface properties [23][24].

The crystallinity of Ta_2O_5 occurs in two phases namely: low temperature phase (L-Ta_2O_5) and high temperature phase (H- Ta_2O_5) [26][27]. The transition point between them is ∼1360 °C, it is slow and reversible. However, the exact crystal structure of these phases are yet to be fully known due to difficulty in growing stable crystals of Ta_2O_5 even when stabilized with other metal oxides [27]–[30]. Recent works on the crystal structure of L-Ta_2O_5 suggested an orthorhombic arrangement form (β-Ta_2O_5) and a less common phase consisting of hexagonal (δ-Ta_2O_5) unit cell [31]–[35]. An orthorhombic and hexagonal crystal structure Ta_2O_5 is shown in Figure 4-1 and Figure 4-2 respectively.

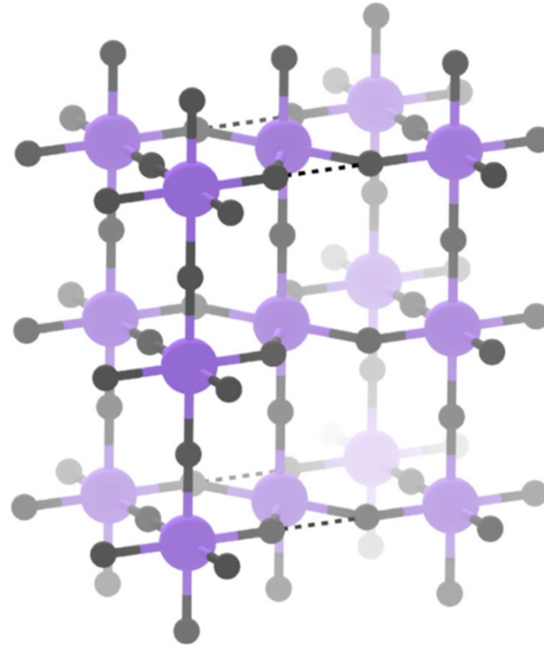

Figure 4- 1. Unit cell of β-Ta_2O_5 (space group Pccm). Ta: purple and O: dark grey. The unit cell boundaries are displayed as dashed lines [27].

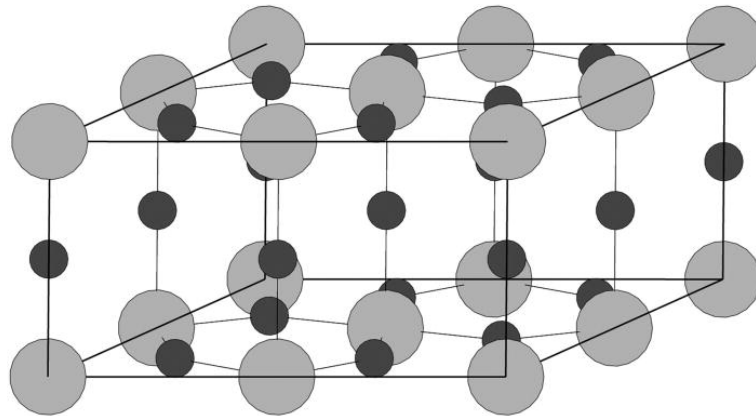

Figure 4- 2. Crystal structure of δ-Ta_2O_5. Light balls correspond to Ta atoms while dark circles correspond to O atoms [35].

There have been few reports on solution processed Ta_2O_5 gate dielectrics mostly deposited by spin coating using tantalum (V) ethoxide. Table 4-1 summarize the properties of Ta_2O_5 gate dielectrics and their TFT characteristics.

Table 4- 1. Selected previous work on Ta_2O_5 gate dielectric and their TFT characteristics (T_{dep}: deposition temperature, k: dielectric constant, J_{leak}: leakage current density, μ : electron mobility, SS: subthreshold swing, $I_{on/off}$: current modulation ratio, V_{th}: threshold voltage).

Deposition Techniques	**T_{dep} (°C)**	**k**	**J_{leak} (A/cm^2)**	**Semiconductor**	**μ (cm^2/Vs)**	**SS (V/dec)**	**$I_{on/off}$**	**V_{th} (V)**	**Ref**
Sputtering	400	12.7	-	IGZO	6.4	0.17	10^4	1.1	[36]
Electron beam	-	21	-	P3HT	0.02	-	10^1	0.26	[37]
Sputtering	RT	-		ZnO	1.35	0.5	10^6		[38]
Sputtering	RT	-		ZnO	60.4	0.23	10^7		[39]
Electron beam	400	25	-	IGZO	1.36	2.56	10^5	2.32	[40]
ALD		16.8	10^{-5} @ 20 V	ZnO	0.1	2.15	10^5	-0.3	[41]
Sputtering	RT	26	10^{-7} @ 1.6 MV/cm	IZO	17	0.14	10^7	1.6	[42]
Sputtering	RT	16.5	10^{-7} @ -4 V	HD	70.1	-	10^3	-	[43]
Sputtering	-	-	-	P-OFET	0.45	-	10^2	0.56	[44]
Sputtering	150	-	10^{-5} @ 20 V	IGZO	2.3	0.09	10^5	0.4	[45]
Electron beam	RT	29.5	10^{-5} @ 2V	IGZO	61.5	0.61	10^5	0.25	[46]
Dip coating	UV 184 nm	28	-	-	-	-	-		[47]
Spin coating	200	26	10^{-7} @ 3 V	CdS	2.97	-	10^3	1	[48]
Spin coating	400	27	10^{-5} @ 3 V	-	-	-	-	-	[49]
Spin coating	300	-	-	In_2O_3	23.1	0.14	10^5	0.84	[50]
Sputtering	120	-	10^{-7} @ 1 V	DPPDTT-PMMA	0.22	0.12	10^3	-0.55	[51]

Tepehan et al. [18], reported on the optical properties of dip coated Ta_2O_5 films for electrochromic applications. Their results showed amorphous Ta_2O_5 films with high optical transmittance, high refractive index 1.706 at 500 nm, and wide bandgap of 3.75 eV.

Heo et al. [48], investigated a CdS-based TFT employing solution processed Ta_2O_5 gate dielectric. Their results showed that Ta_2O_5 exhibited a dielectric constant of 26, bandgap of 4.67 eV and leakage current density of 10^{-7} A/cm^2 at 3 V. The performance of CdS – based TFTs showed low voltage operation of 3 V, current modulation ratio of 10^4 and electron mobility of 2.97 cm^2/Vs.

Park et al. [50], reported that spin coated tantalum pentoxide films were found to be amorphous and exhibited excellent performance as gate dielectric for indium – based TFTs such as low voltage operation of 3.5 V, high current modulation ratio of 10^5 and electron mobility of 23.1 cm^2/Vs.

Frunza et al. [49], investigated a Ta_2O_5-based high-k dielectric thin films from solution processed at low temperatures. Ta_2O_5 films annealed at 400 °C exhibited a dielectric constant of 27 and a leakage current density of 10^{-5} A/cm^2 at 3V.

To this point, there are no reports on solution processed Ta_2O_5 gate dielectric deposited by spray pyrolysis which is one of the objectives of this chapter.

Despite its high dielectric constant ($k \sim 20$), there is issue with conduction and valence band offsets when integrated in TFTs especially when employing wide bandgap materials such as ZnO ($E_g \sim 3.4$ eV) as active channel. There is a trade-off between dielectric constant (k) and bandgap of metal oxide dielectrics. Figure 4-3 show the relationship between optical bandgap and dielectric constant of some metal oxides.

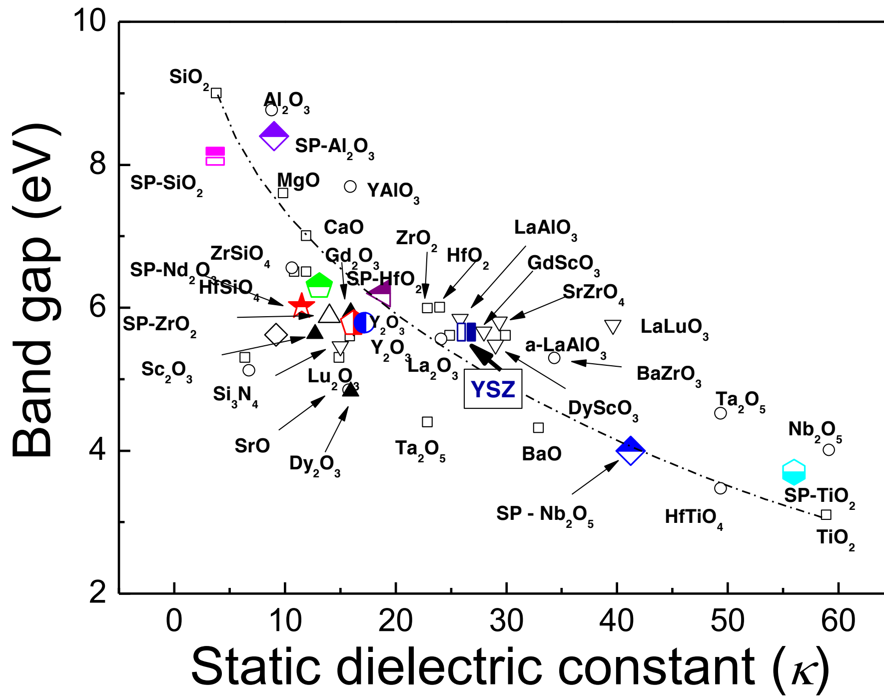

Figure 4- 3. Bandgap and dielectric constant of selected metal oxides [52].

The optical bandgap varies inversely with the dielectric constant (k), which means oxides with wide bandgap exhibit low dielectric constant while oxides with high dielectric constant exhibit narrower optical bandgap. According to Robertson's criteria [53], a high-k oxide must act as an insulator, by having a band offsets of at least 1 eV between the oxide dielectric and the semiconductor in order to minimise carrier injection into oxide bands. For this reason, Ta_2O_5 does not satisfy the criterion due to its low bandgap ($E_g \sim 4.4$ eV). An alternative solution is to incorporate a wide bandgap metal oxide such as Al_2O_3. Figure 4-4 show some calculated conduction band offsets (CBO) of metal oxides with the values normalised to the valence band maximum (VBM) of ZnO.

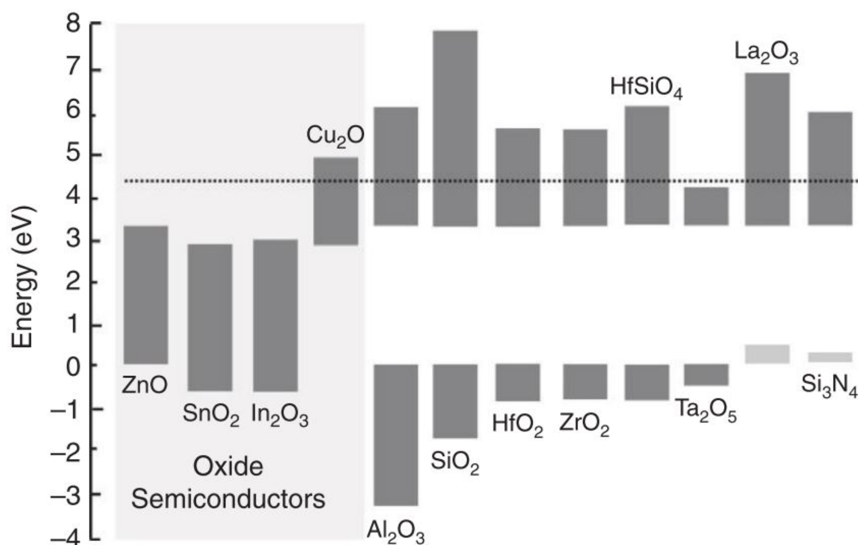

Figure 4- 4. Calculated band offsets of selected dielectrics. The values are normalised to the VBM of ZnO. The dotted line indicates the minimum of 1 eV for CBO [23].

Aluminium oxide (Al_2O_3) is another well-studied transition metal oxide that exhibit a wide bandgap ($E_g \sim 9$ eV) and higher dielectric constant ($k \sim 9$) than conventional SiO_2 [54][55]. Its films are highly transparent in visible spectrum and has high refractive index ($n \sim 1.7$). Additionally, it is thermodynamically stable at high temperatures and forms a good interface with silicon. These remarkable characteristics made it a suitable gate dielectric for implementation in TFTs [54].

Al_2O_3 thin films are amorphous when deposited at moderate temperature (< 600 °C) [55]. However, above 600 °C, Al_2O_3 thin films exhibit several crystalline phases, e.g., α-Al_2O_3, γ-Al_2O_3, or θ-Al_2O_3 [56]. The α-Al_2O_3 is the most stable crystalline Al_2O_3 while the others are metastable. According to Trunov et al. [57], crystalline Al_2O_3 films undergo phase transitions at 910 K with increasing temperature, starting from γ-Al_2O_3 to θ-Al_2O_3 and finally α-Al_2O_3. Figure 4-5 show the crystalline structure of α-Al_2O_3 films.

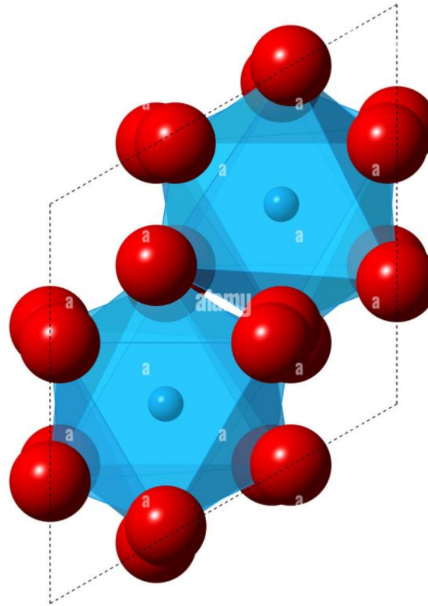

Figure 4- 5. The crystalline structure of α-Al_2O_3. Blue balls: Al atoms, Red balls: O atoms [58].

Al_2O_3 films have also been deposited by several deposition techniques including sputtering [59]–[61], spin coating [62][63], atomic layer deposition (ALD) [64]–[66], pulsed laser deposition (PLD) [67] and spray pyrolysis [54][55][68]. There are several reports on solution processed Al_2O_3 gate dielectrics and their implementation in TFTs. Table 4-2 present a review of solution processed Al_2O_3 gate dielectric. The vast majority of the works were deposited by spin coating technique using aluminium nitrate nonahydrate [$Al(NO_3)_3 \cdot 9H_2O$] and 2-methoxyethanol (2-ME) as the solvent.

Table 4- 2. Selected previous work on solution processed Al_2O_3 gate dielectric and their TFT characteristics.

Deposition technique	T_{dep} (°C)	k	J_{leak} (A/cm²)	Semiconductor	μ (cm²/Vs)	SS (V/dec)	$I_{on/off}$	V_{th} (V)	ref
Spin coating	400	-	-	ZTO	17.36 & 39.18	0.14	10^6 & 10^5	1.67	[69]
Spin coating	350	7	-	IGZO	30	0.14	10^6	1.72	[70]
Spin coating	300	-	-	IBO	11.3	0.17	10^5	0.6	[71]
Spin coating	180	8.81	-	IGZO	69.2	0.86	10^8	1.3	[72]
Spin coating	170	7	10^{-8} @ 3V	P-OFT	2.7	0.107	10^6	-0.9	[73]
Spray pyrolysis	440	7.5	20 n @ 1 MV/cm	ZnO	10	1	10^5	-	[74]
Spin coating	350	7.4	10n @ 7 V	NiO_x	25	0.7	10^5	-	[75]
Spin coating	350	7	0.4n @ 1 MV/cm	IWO	15.3	0.068	10^7	0.15	[76]
Spin coating	200	7.2	10^{-6} @ -4 V	P-OFT	0.65	0.45	10^3	-0.6	[77]
Spin coating	200	7.5	10^{-7} @ 5V	P-OFT	0.51	-	10^4	-2.1	[78]
Spin coating	250	5.8	-	In_2O_3	23.1	0.35	10^5	-	[79]
Spin coating	250	-	10^{-8} @ 2MV/cm	NiO_x	4.4	0.25	10^5	-1.3	[80]
Spray pyrolysis	350	7.07	94 n@ 1MV/cm	IGZO	5.5	-	10^5	-0.8	[81]
Spin coating	350	7.1	10^{-5} @ 1 MV/cm	GZTO	1.3	0.3	10^5	0.8	[62]

Wang et al. [82], investigated a gallium oxide based TFTs employing Al_2O_3 gate dielectric using spin coating. Their results showed low voltage operation of 4 V, current modulation ratio of 10^4, subthreshold swing of 0.13 V/dec and high electron mobility of 40.87 cm^2/Vs.

Similarly, Xu et al. [83], investigated an indium oxide based TFTs employing Al_2O_3 gate dielectric using spin coating. Al_2O_3 films were processed at different annealing temperatures between 200 °C and 500 °C, which showed a decreasing dielectric constant (from 15.2 for 200 °C to 8.7 for 500 °C) and leakage current density at 1 MV/cm (from 1.4 x 10^{-6} to 4.1 x 10^{-7} A/cm^2). Further implementation of Al_2O_3 after annealing at 300 °C as gate dielectric for In_2O_3 and InZnO-based TFTs showed a low voltage operation of 4 V (for both cases), current modulation ratio of 10^5 (for both cases), subthreshold swing (0.22 V/dec for In_2O_3 and 0.17 V/dec for InZnO-based TFTs) and high electron mobility (57.21 cm^2/Vs for In_2O_3 and 10.13 cm^2/Vs for InZnO-based TFTs).

Tan et al. [84], investigated the annealing effects on the properties of spin coated alumina thin films using aluminium chloride. The samples were processed at different annealing temperatures between 250 °C and 550 °C. Their results showed that Al_2O_3 films annealed at 550 °C exhibited the lowest leakage current density of 2.69 x 10^{-9} A/cm^2 at 3V. The indium-titanium-zinc oxide (ITZO) based TFTs employing annealed 550 °C Al_2O_3 gate dielectric showed a low voltage operation of 5 V, high current modulation ratio of 10^6, subthreshold swing of 0.22 V/dec and high electron mobility of 23.7 cm^2/Vs.

Wang et al. [85], investigated a spin coated Al_2O_3 films processed at different annealing temperatures between 220 °C and 300 °C. Their results showed a leakage current density of approximately 10^{-6} A/cm^2 at 3V regardless of the annealing conditions. They further investigated its implementation as gate dielectric after annealing at 260 °C for IGZO-based TFTs and their results showed a low voltage operation of 3 V, current modulation ratio of 10^4, subthreshold swing of 0.186 V/dec and electron mobility of 2.26 cm^2/Vs.

Adamopoulos et al. [54], investigated a spray coated Al_2O_3 films using blends of aluminium (III) acetylacetonate [$Al(C_5H_7O_2)_3$] and methanol. Their results showed a dielectric constant of 9.2 and leakage current density of 10^{-6} A/cm^2 at 1.8 MV/cm. Further investigation on the ZnO – based TFTs employing Al_2O_3 gate dielectric showed a low voltage operation of 4 V, current modulation ratio of 10^5 and electron mobility of 7 cm^2/Vs.

Evidently, Al_2O_3 gate dielectric exhibits promising characteristics for high performance TFT applications due to its amorphous nature, low leakage current density (J_{leak} < 100 nA/cm^2 at 1 MV/cm) and high dielectric constant ($k \sim 7$) depending on the deposition conditions.

However, with the low bandgap of Ta_2O_5 (4.4 eV) and dielectric constant of Al_2O_3 (7), the combination of the two oxides will produce an optimised properties of the gate dielectric for better implementation in TFTs. Such combination yields tantalum aluminate ($Ta_{1-x}Al_xO_y$) films, that can exhibit a high dielectric constant ($k > Al_2O_3$) and wide energy bandgap ($E_g > Ta_2O_5$) and also satisfy the band offset conditions [53].

There are few reports on solution processed metal aluminate gate dielectrics. Table 4-3 present a review on solution processed metal aluminate gate dielectrics and their properties. These works were deposited by mainly spin coating and spray pyrolysis.

Table 4- 3. Selected previous work on solution processed metal aluminate gate dielectric and their TFT characteristics (LAO: lanthanum aluminate, HAO: hafnium aluminate, TAO: titanium aluminate, NAO: niobium aluminate, ZAO: zirconium aluminate, Ta-AO: tantalum aluminate).

Deposition Technique	Dielectric	T_{dep} (°C)	K	E_g	J_{leak} (A/cm^2)	Semiconductor	μ (cm^2/Vs)	SS (V/dec)	$I_{on/off}$	Ref
Spray pyrolysis	LAO	440	16	6.18	<6 x 10^{-9} @ 3 MV/cm	ZnO	12	0.65	10^6	[74]
Spin coating	HAO	600	11.3	-	-	ITZO	13.5	0.087	10^7	[86]
Spin coating	LAO	350	10.5	-	1 x 10^{-8} @ 2 MV/cm	IZO	17	0.38	10^5	[87]
Spray pyrolysis	TAO	420	13	4.5	<5 x 10^{-9} @ 3 MV/cm	ZnO	10	0.55	10^6	[68]
Spray pyrolysis	NAO	400	13.5	5.15	<10 x 10^{-9} @ 1 MV/cm	ZnO	1	-	10^5	[88]
Spin coating	ZAO	500	10	-	10^{-8}@ 1 MV/cm	-	-	-	-	[89]
Spray pyrolysis	Ta-AO	250	15	4.53	10^{-7} @ 1.2 MV/cm	-	-	-	-	[7]
Spin coating	ZAO	350	11.8	-	-	IZO	53	0.12	10^6	[90]
Spin coating	ZAO	150	7.35	-	10^{-9} @ 2 MV/cm	IGZO	7.71	0.153	10^9	[91]

In this chapter, the properties of $Ta_{1-x}Al_xO_y$ films and their implementation as gate dielectric for ZnO-based TFTs are investigated. The films were deposited by spray pyrolysis in ambient air using a conventional airbrush and by varying the tantalum (Ta) to aluminium (Al) atomic ratio, by physical blending of the soluble precursors in alcohol-based precursors [68].

4.2 Precursors

The precursors used were tantalum (V) chloride [($TaCl_5$), 99.99%], aluminium acetylacetonate [($Al(C_5H_7O_2)_3$, 99%] and zinc acetate dilhydrate [($Zn(O_2C_2H_3)2.\ 2H_2O$), 99.9%]. The tantalum and zinc precursors were purchased from Alfa Aesar while the aluminium precursor from Sigma Aldrich. All precursors were used without any further purification.

The tantalum aluminate solutions were prepared by the blends of methanol and ethanol (ratio 1:3) solution of $TaCl_5$ and methanol solution of $Al(C_5H_7O_2)_3$. Both solutions were prepared at a total concentration of 0.1 M.

Additionally, 1 mL of Acetylacetone (Acac) was added to the tantalum solution to increase the thickness of the deposited films. The solutions were kept under continuous stirring for at least an hour prior to the deposition to ensure complete dissolution.

The tantalum (Ta) to aluminium (Al) atomic ratio was controlled by simple blending of the amount of each of the precursor's solution.

Finally, for the deposition of zinc oxide, zinc acetate dilhydrate [($Zn(O_2C_2H_3)2.\ 2H_2O$), 99.9%] was dissolved in methanol at a concentration of 0.1 M [92].

4.2.1 Thermal Properties of Precursors

Thermogravimetric analysis (TGA) and differential scanning calorimetry (DSC) measurements were conducted on all precursors to determine their decomposition temperatures that plays an important role in the film's deposition.

All measurements were carried out using a simultaneous thermal analyser NRTZSCH STA 449 F3 Jupiter®. The measurements were carried out under a N_2 atmosphere at constant heating rate of 10 K/min in the temperature range between 40 – 700 °C.

Figure 4-6 illustrate the TGA and DSC measurements of a 4 mg $TaCl_5$ powder.

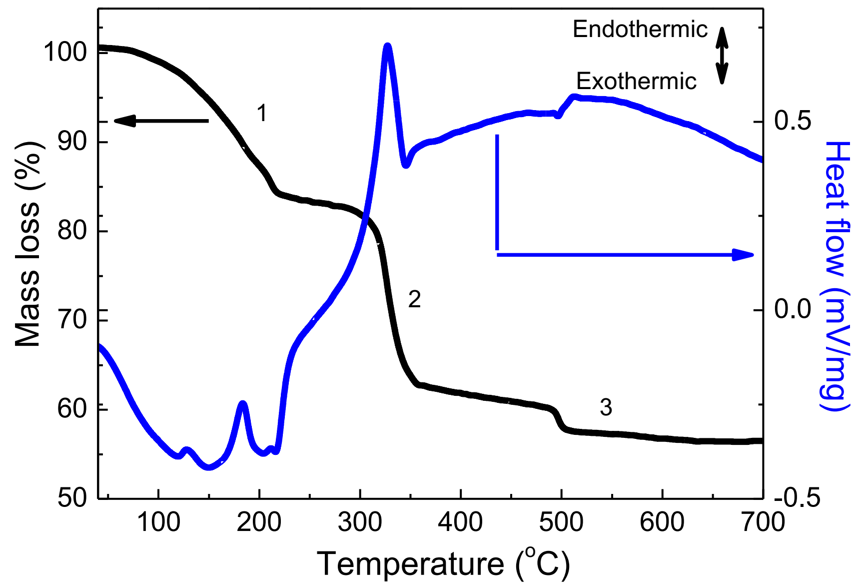

Figure 4- 6. Thermogravimetric analysis (black line) and differential scanning calorimetry (blue line) of 4 mg $TaCl_5$ powder.

The TGA curve showed three stages of mass loss; in stage 1, the continuous rapid decrease of the mass loss from 63 – 228 °C was due to the dehydration of $TaCl_5$ (absorbed water molecules from the atmosphere during the process of mounting the sample onto the TGA holder). In stage 2, the sharp decrease of mass loss from 240 – 368 °C was due to the decomposition of some chloride matrix [93].

$$TaCl_5 \rightarrow TaCl_2 + \frac{3}{2}Cl_2 \quad (4.1)$$

In stage 3, the mass loss from 470 – 520 °C was due to decomposition of tantalum dichloride with Ta metal as final product above 520 °C.

$$TaCl_2 \rightarrow Ta + Cl_2 \quad (4.2)$$

The DSC curve on the other hand showed some peaks which were related to either released (exothermic) or absorbed (endothermic) heat energy. The weak endothermic peak observed at 127 °C is due to the sublimation of $TaCl_5$ powder which reaches maximum at 182 °C. These peaks were close to the ones observed by Kim et. al [94], (150 °C and 180 °C). The strong endothermic peak observed at 326 °C shows the evidence of the decomposed amount of chloride matrix mentioned in the stage 2 of the TGA curve. Finally, the weak exothermic peak observed at 496 °C shows the evidence of the decomposed $TaCl_2$ and the formation of Ta metal as the final product.

Figure 4-7 illustrate the TGA and DSC of a 9 mg $Al(acac)_3$ powder.

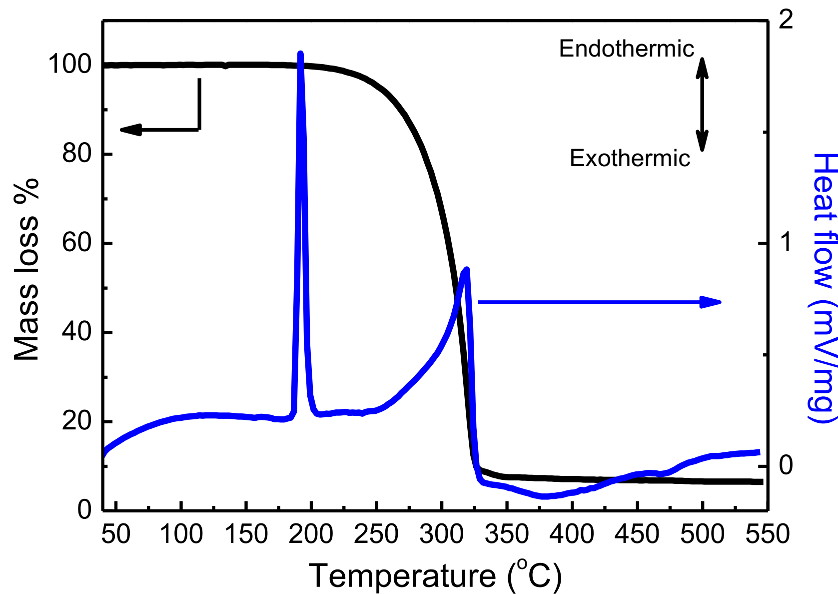

Figure 4- 7. Thermogravimetric analysis (black line) and differential scanning calorimetry (blue line) of 9 mg Al(acac)$_3$ powder.

The TGA curve shown in Figure 4-7 showed almost a negligible mass loss up to 174 °C, however, the sharp endothermic peak of the DSC observed at 195 °C is due to sublimation of heated Al(acac)$_3$ powder. It has already been reported by Kovarik et al. [95], that heated Al(acac)$_3$ powder sublimes between 150 and 225 °C without decomposition. The major mass loss observed at about 320 °C is attributed to the complete decomposition of Al(acac)$_3$ precursor and the formation of amorphous Al_2O_3.

4.3 Thin Film Deposition & Characterisation

Aerosols of 0.1 M solutions containing $TaCl_5$ in methanol and ethanol (1:3) and $Al(C_5H_7O_2)_3$ solution in methanol were spray coated at 500 °C on different substrates employing a pneumatic airbrush, held at a vertical distance of about 30 cm. The tantalum-aluminate composites ($Ta_{1-x}Al_xO_y$) were deposited by blending $TaCl_5$ and $Al(C_5H_7O_2)_3$ solutions so that the desired [Al] to [Ta] ratio in the solution could be obtained. Aerosols of the blends were spray coated for 10 s spray and interrupted for another 50 s to allow the vapours to settle onto the sample. The cycle was repeated until films of typical thickness of > 50 nm were obtained.

Furthermore, the films were characterized by some range of techniques. The optical properties of $Ta_{1-x}Al_xO_y$ films on fused silica were studied by the UV-Vis spectroscopy. The structural and morphological properties on silicon were studied by grazing incidence x-ray diffraction (GIXRD) and atomic force microscopy (AFM) respectively. Also, metal-insulator-metal (MIM) devices were fabricated by employing Al metal contacts that were thermally evaporated under high vacuum (10^{-6} mbar) through a shadow mask onto the glass/ITO/Ta_{1-}

$_xAl_xO_y$ stacks. Finally, the dielectric and electrical properties on $Ta_{1-x}Al_xO_y$ films were studied by impedance spectroscopy (dielectric) and current – voltage (I – V) and TFT measurements.

Figure 4-8 show a schematic of a MIM stack of glass/ITO/ $Ta_{1-x}Al_xO_y$/Al gate dielectric.

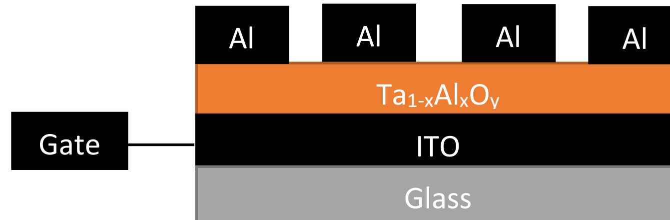

Figure 4- 8. A schematic of a metal-insulator-metal (MIM) stack of glass/ITO/ $Ta_{1-x}Al_xO_y$/Al gate dielectric.

4.4 UV-Vis Spectroscopy

The optical properties of $Ta_{1-x}Al_xO_y$ films were studied by UV-Vis spectroscopy. The measurements were recorded in transmission mode in the wavelength range between 190 and 1000 nm. Figure 4-9 show the transmittance (T%) spectra of $Ta_{1-x}Al_xO_y$ films with different [Al] to [Ta] ratios.

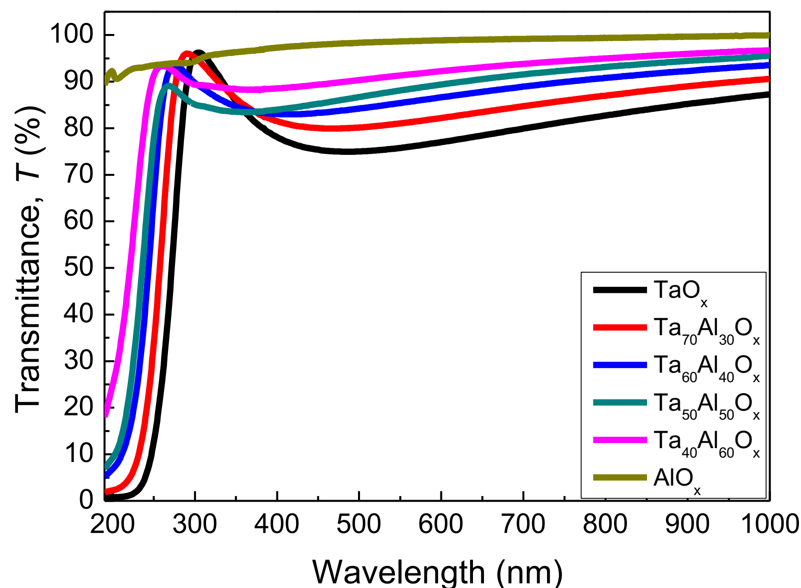

Figure 4- 9. Transmittance (%T) spectra of $Ta_{1-x}Al_xO_y$ films for different [Al] to [Ta] ratios.

The average %T in visible region (400 – 700 nm) is in the range between 70 % and 80 % indicating highly transparent $Ta_{1-x}Al_xO_y$ films. The optical bandgaps were calculated from the linearly extrapolated Taucs plot [96] that are shown in Figure 4-10.

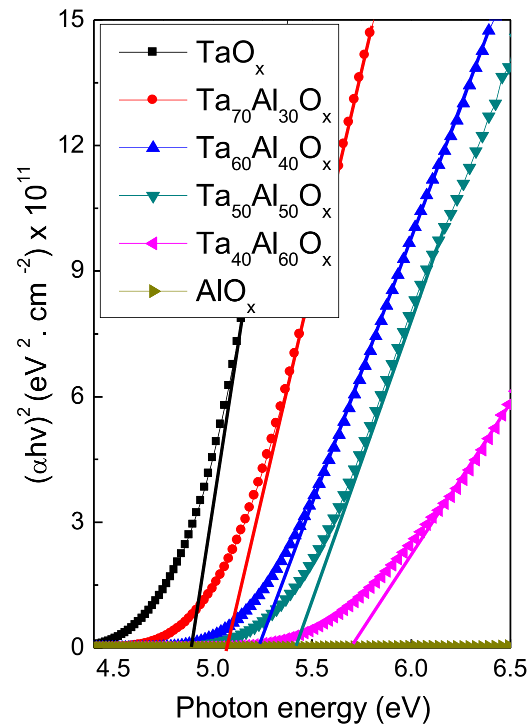

Figure 4- 10. Tauc plots of as-deposited $Ta_{1-x}Al_xO_y$ films with different [Al] to [Ta] ratios.

The evolution of the bandgaps as a function of [Al]/ [Al + Ta] atomic ratio is shown in Figure 4-11.

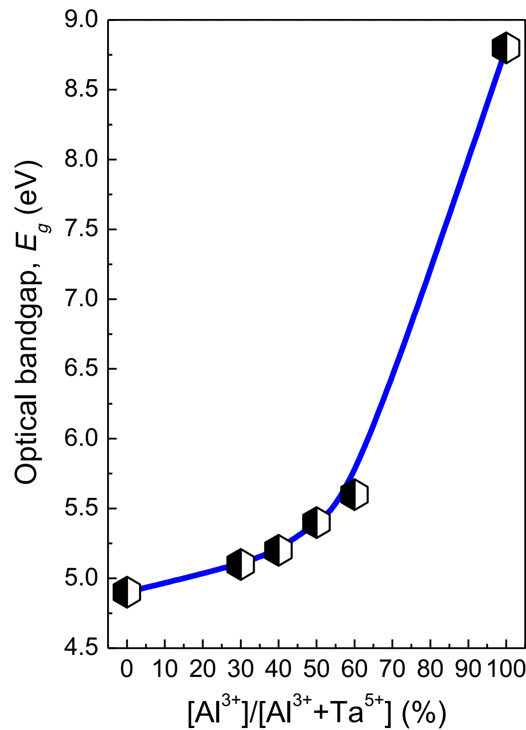

Figure 4- 11. Optical bandgap of $Ta_{1-x}Al_xO_y$ films as a function of the [Al]/ [Al+Ta] atomic ratio. The solid line is a guide to the eye.

The optical bandgap increases with increasing [Al]/ [Al + Ta] atomic ratio. In Figure 4-10, one can observe the Tauc plot of AlO_x appearing as a flat line due to inability of the UV-Vis spectrometer to characterize wide bandgap (E_g > 6.5 eV) materials such as AlO_x films. As a result, the optical bandgap of AlO_x was taken as 8.8 eV as widely reported in the literature [53][97]–[99]. The optical bandgap (Figure 4-11) varies between 4.9 eV for TaO_x and 8.8 eV for AlO_x. Such trend was expected for ternary oxides where wide bandgap dielectrics such as AlO_x combine with low bandgap oxides such as TaO_x. Afouxenidis et al. [68], and Esro et al. [74], reported similar trends on titanium aluminate and lanthanum aluminate films respectively. In comparison with the previously reported bandgap [7][9][18][48] of TaO_x, the calculated bandgap ($E_g \sim$ 4.9 eV) emerged as the highest ever recorded and promising for future implementation in TFTs.

Furthermore, the Urbach tail energy (E_u) was investigated to determine the material disorder in $Ta_{1-x}Al_xO_y$ films. The E_u plots of $Ta_{1-x}Al_xO_y$ films with different [Al] to [Ta] ratios are shown in Figure 4-12 while the calculated values as a function of [Al]/ [Al + Ta] atomic ratio is shown in Figure 4-13.

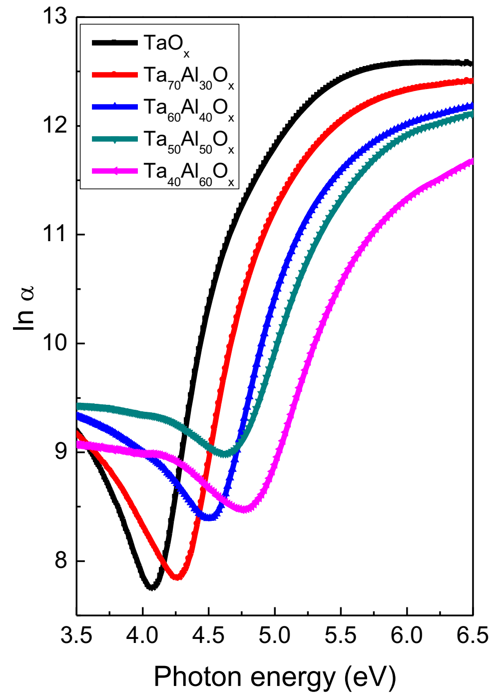

Figure 4- 12. Absorption coefficient spectra of $Ta_{1-x}Al_xO_y$ films with different [Al] to [Ta] ratios.

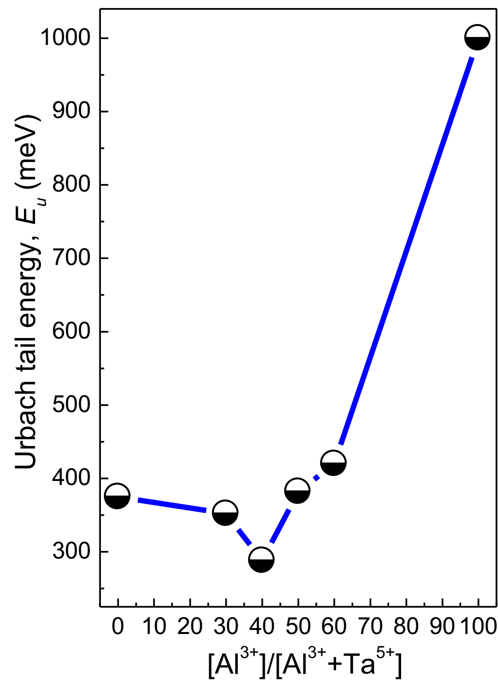

Figure 4- 13. Urbach tail energy, E_u of $Ta_{1-x}Al_xO_y$ films as function of the [Al]/ [Al + Ta] atomic ratio. The solid line is a guide to the eye.

The E_u increases with increasing [Al]/ [Al + Ta] atomic ratio. Generally, the E_u identifies localized states extended in the optical bandgap of poor crystalline materials through means of defects or disorder. For a non-crystalline material, it has already been reported that amorphous AlO_x films exhibit high E_u value of about 1000 meV [68][74][88]. As a result, with the increasing content of [Al], the E_u values are expected to increase and contribute to the disordering of $Ta_{1-x}Al_xO_y$ films.

4.5 Structural/Surface Properties

The structural properties of $Ta_{1-x}Al_xO_y$ films were studied by grazing incidence x-ray diffraction (GIXRD) and the surface morphologies by atomic force microscopy (AFM).

4.5.1 Grazing Incidence X-Ray Diffraction (GIXRD)

To investigate the structure of $Ta_{1-x}Al_xO_y$ films, grazing incidence XRD (GIXRD) experiments were carried out using a Rigaku Ultima⁺ diffractometer with Cu Kα radiation operating at 40 kV, 30 mA. Figure 4-14 show the GIXRD patterns of $Ta_{1-x}Al_xO_y$ films.

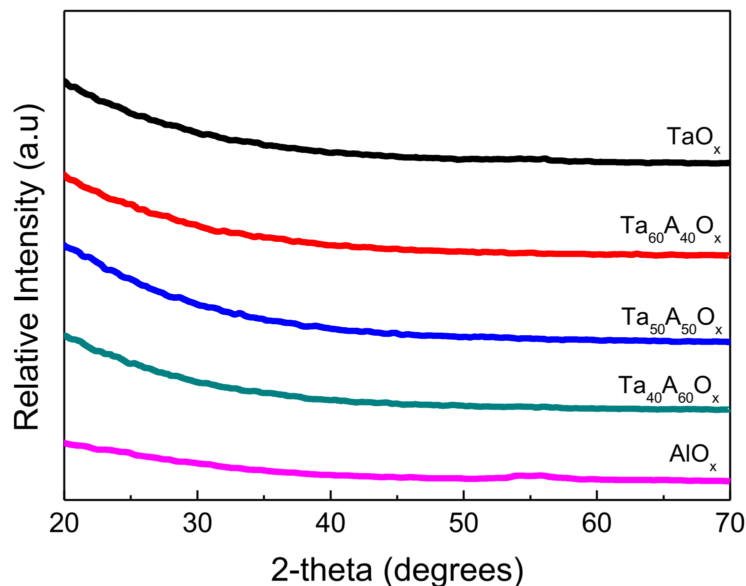

Figure 4- 14. GIXRD patterns of selected $Ta_{1-x}Al_xO_y$ films deposited by spray pyrolysis on silicon substrates.

The absence of diffraction peaks from the GIXRD patterns of $Ta_{1-x}Al_xO_y$ indicates amorphous films. The amorphous nature of the selected $Ta_{1-x}Al_xO_y$ films were expected considering the fact that both TaO_x and AlO_x films are amorphous in nature at moderate temperatures (< 500 °C) [14][15][17][54][68][74].

4.5.2 Atomic Force Microscopy

The surface morphologies of $Ta_{1-x}Al_xO_y$ films were investigated by atomic force microscopy (AFM). AFM images were taken in contact mode under ambient conditions using a Multimode scanning probe microscope (MM-SPM) fitted to a Nanoscope IIIa controller unit employing a silicon tip of a radius < 10 nm. The images presented are the raw images after they have been flattened out.

In Figure 4-15, the AFM images of $Ta_{1-x}Al_xO_y$ films on silicon substrates are illustrated.

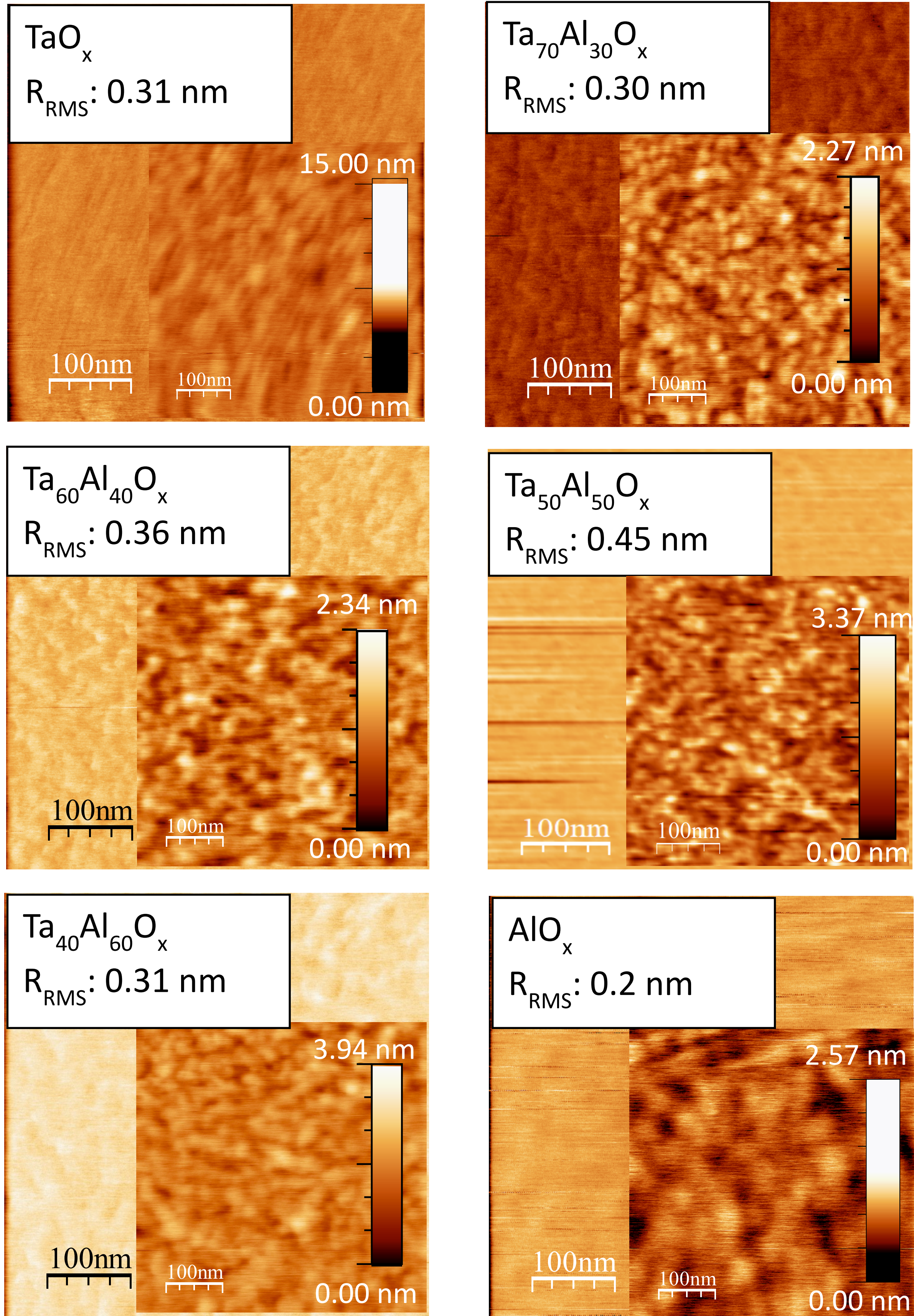

Figure 4- 15. AFM friction and topography images of $Ta_{1-x}Al_xO_y$ films on silicon substrates.

The topographical images of $Ta_{1-x}Al_xO_y$ films showed smooth and low surface roughness as evidenced from the root mean square (R_{RMS} < 1 nm) measurements shown in Figure 4-15 (inset). Such smooth dielectrics providing good interface properties between the dielectric and the semiconducting channel are promising for the implementation of $Ta_{1-x}Al_xO_y$ films in TFTs.

4.6 Electrical Properties

The dielectric properties of the $Ta_{1-x}Al_xO_y$ films were investigated by impedance spectroscopy and I – V measurements.

4.6.1 Impedance Spectroscopy

The impedance dispersions of the $Ta_{1-x}Al_xO_y$ films were measured with MIM (glass/ITO/ $Ta_{1-x}Al_xO_y$/Al), using a Wayne Kerr 6550B Precision impedance analyser in the frequency range of 1 kHz – 10 MHz applying 50 mV AC voltage. The static dielectric constant dispersions of $Ta_{1-x}Al_xO_y$ films are shown in Figure 4-16.

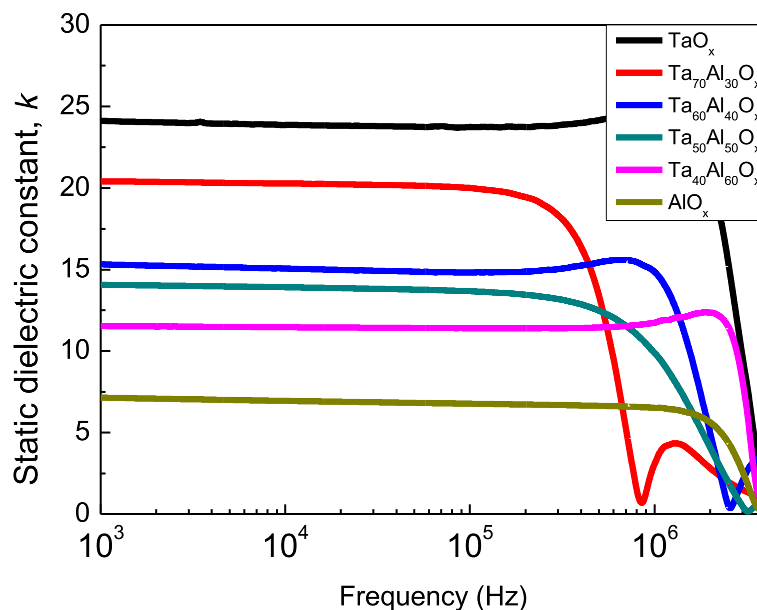

Figure 4- 16. Static dielectric constant dispersions of $Ta_{1-x}Al_xO_y$ films in the frequency range of 1kHz – 4 MHz.

The static dielectric constant of $Ta_{1-x}Al_xO_y$ films were calculated at 1 kHz and the values were further plotted in Figure 4-17 as a function of [Al]/ [Al + Ta] atomic ratio. The appearance of the band at the high frequency side of the dispersion (TaO_x, $Ta_{60}Al_{40}O_x$ and $Ta_{40}Al_{60}O_x$) was probably due to parasitic inductance caused by the analyser, cables or probe station adaptors.

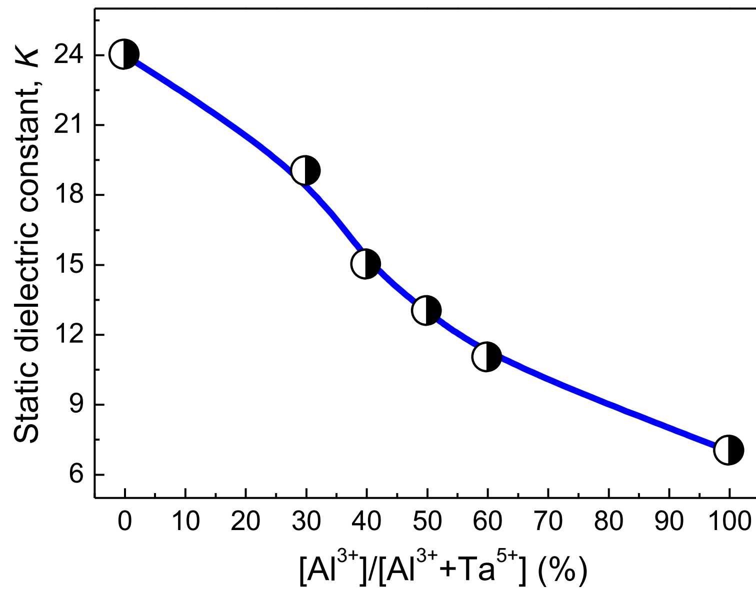

Figure 4- 17. Static dielectric constant of $Ta_{1-x}Al_xO_y$ films as a function of [Al]/ [Al + Ta] atomic ratio calculated at 1 kHz. The solid line is guide to the eye.

The static dielectric constant shows a decrease with increasing [Al]/ ([Al] + [Ta] atomic ratio and varies between 24 for TaO_x and 7 for AlO_x. Such trend was expected for high-k metal oxides composites when combining the low and high-k dielectrics. Afouxenidis et al. [68], reported similar trend for titanium aluminate gate dielectric films. Esro et al. [74], also reported similar trends for lanthanum aluminate gate dielectrics. Furthermore, the stability of $Ta_{1-x}Al_xO_y$ films were investigated by the Nyquist plots shown in Figure 4-18.

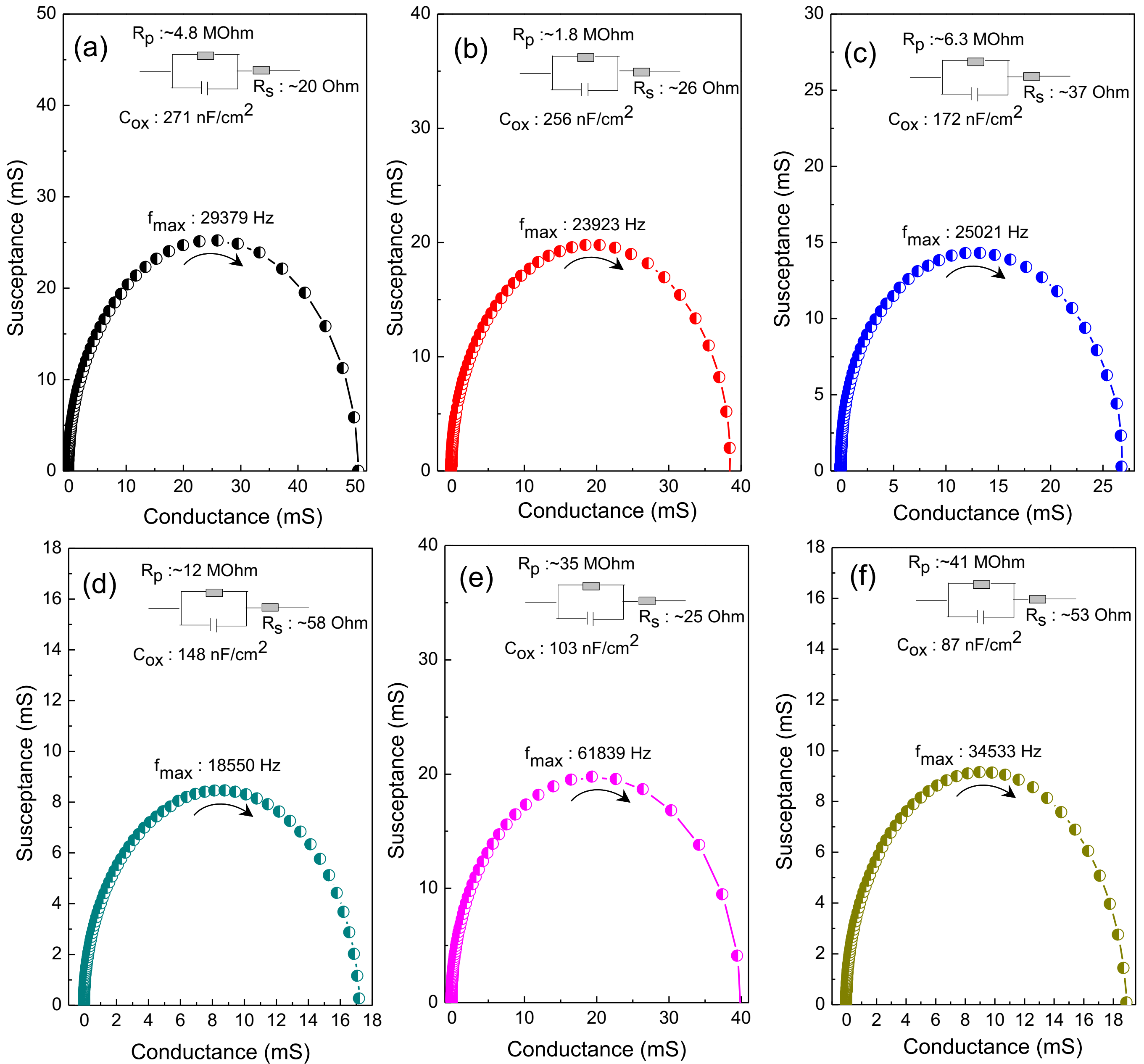

Figure 4- 18 Nyquist plots and equivalent circuit (inset) of (a) TaO_x (b) $Ta_{70}Al_{30}O_x$ (c) $Ta_{60}Al_{40}O_x$ (d) $Ta_{50}Al_{50}O_x$ (e) $Ta_{40}Al_{60}O_x$ and (e) AlO_x devices.

The Nyquist plots reveal the stable $Ta_{1-x}Al_xO_y$ dielectrics as seen in Figure 4-18(a)-(f). The stability of the stacks can be observed by the parabolic behaviour of the plot starting from the origin. Additionally, the stacks demonstrate excellent capacitive properties as evidenced from the equivalent circuits (insets) that consist of large shunt and low series resistance.

4.6.2 I – V characterization

The current – voltage measurements of $Ta_{1-x}Al_xO_y$ films were conducted on MIM devices (glass/ITO/$Ta_{1-x}Al_xO_y$/Al), using the Agilent B1500A semiconductor parameter analyser. All measurements were conducted under dark conditions at room temperature (300 K). Figure 4-19 show the leakage current density (J) versus electric field (MV/cm) of $Ta_{1-x}Al_xO_y$ films.

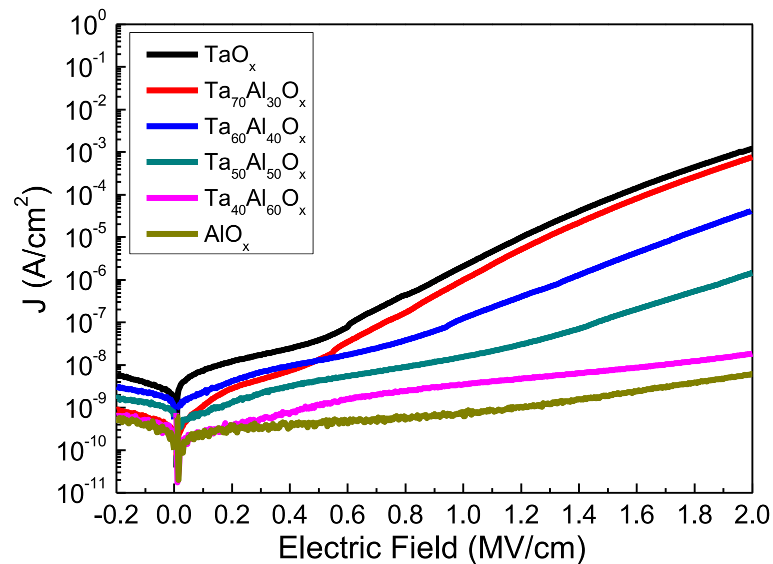

Figure 4- 19. Leakage current density (J) of $Ta_{1-x}Al_xO_y$ MIMs with different [Al] to [Ta] ratios.

Figure 4-20 depict the leakage current densities recorded at electric field of 1 and 2 MV/cm as a function of [Al]/ [Al +Ta] atomic ratio.

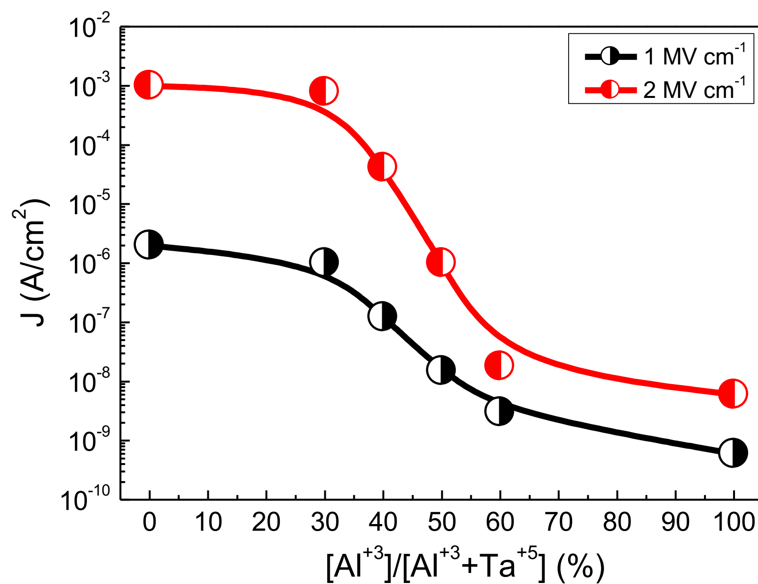

Figure 4- 20. Leakage current density (J) of $Ta_{1-x}Al_xO_y$ films at 1 and 2 MV/cm as a function of [Al]/ [Al + Ta] atomic ratio.

The leakage current density decreases with increasing [Al]/ [Al + Ta] atomic ratio as expected. Such decrease can be associated with the wide bandgap ($E_g \sim$ 8.8 eV) of AlO_x films that complements the low bandgap of TaO_x. Afouxenidis et al. [88], and Esro et al. [74], reported similar trends in their work on $Ti_{1-x}Al_xO_y$ and $La_{1-x}Al_xO_y$ films respectively. Figure 4-21 show the relationship between the leakage current density and the optical bandgap of $Ta_{1-x}Al_xO_y$ films.

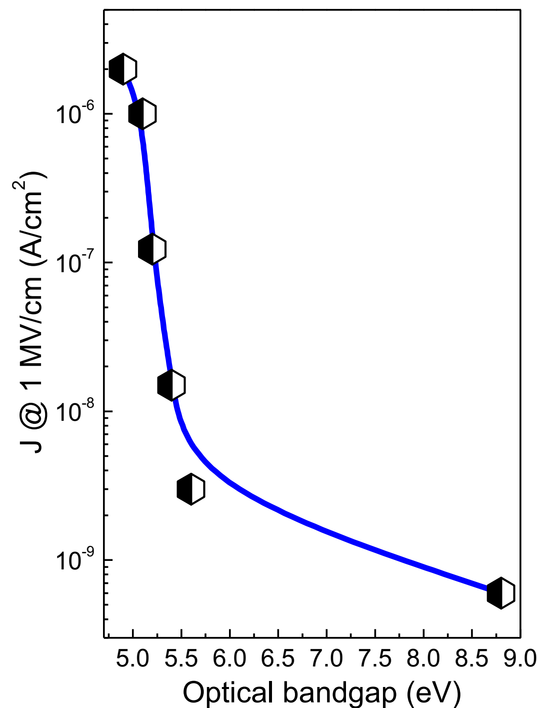

Figure 4- 21. Leakage current density (J) versus optical bandgap of $Ta_{1-x}Al_xO_y$ films with different [Al] to [Ta] ratios.

Evidently, it can be seen that the leakage current density drastically reduces with increasing optical bandgap of $Ta_{1-x}Al_xO_y$ films. Such decrease could potentially be promising for implementation in TFTs as will later be investigated.

The origin of current leakages in dielectrics may be associated by some factors such as material composition, film thickness, and trap density in the films [100]. To elaborate more on the leakage currents in the $Ta_{1-x}Al_xO_y$ MIMs, the current conduction mechanisms were investigated. The current conduction mechanisms can be categorized in two classes: the electrode-limited and the bulk-limited current conduction mechanism. The electrode-limited mechanism depends on the electrical characterization at interface between the electrode and the dielectric film while the bulk-limited depends on the electrical characterization of the bulk material itself. The electrode-limited conduction mechanisms include: Schottky emission (SE), Fowler Nordheim (FN), Direct tunneling (DT) and Thermionic-field emission (TE) conduction mechanism while the bulk-limited conduction mechanisms include Poole Frenkel (PF),

hopping, Ohmic, space-charge-limited, ionic and grain boundary-limited conduction mechanism [100]–[105].

In electrode-limited, parameters such as effective mass of electron and barrier hight could be determined while in bulk limited parameters such as trap density, trap levels, trap spacing, and carrier drift mobility could be determined. More detailed review on current conduction mechanisms have previously been discussed in chapter 2 of this thesis.

The current conduction in insulators have been widely reported to be governed by one of the three mechanisms: SE (electrode-limited), FN (electrode-limited) and PF (bulk-limited) [101].

Figure 4-22 – Figure 4-24 show the SE, FN and PF plots of $Ta_{1-x}Al_xO_y$ films respectively.

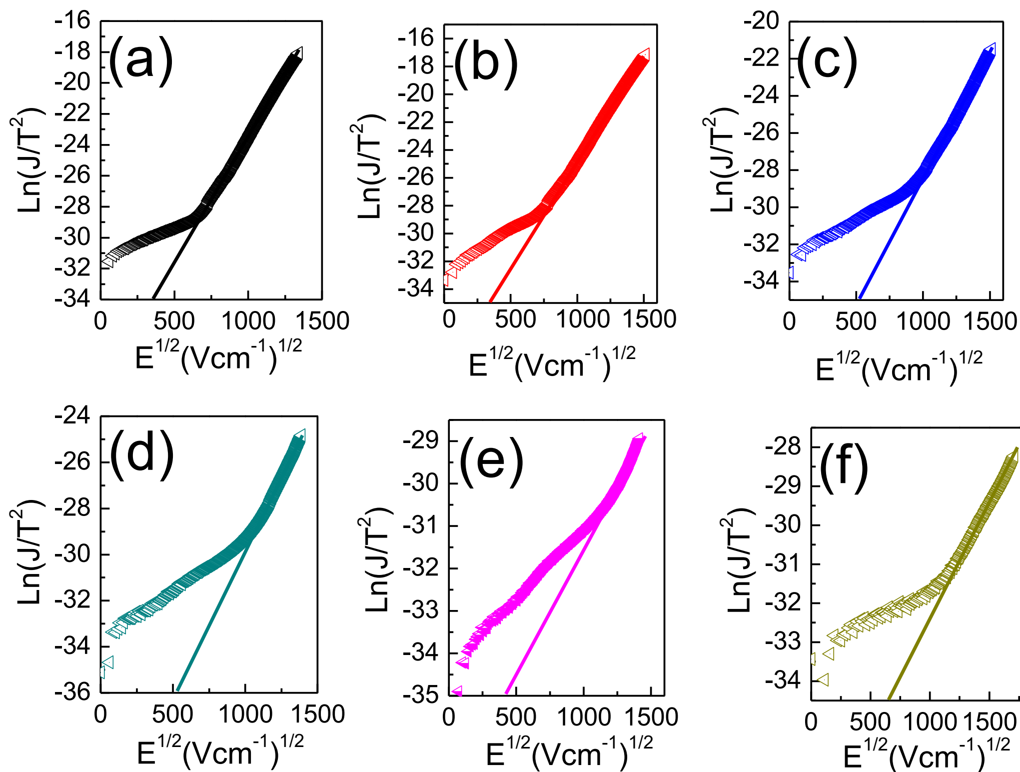

Figure 4- 22. Schottky emission plots of (a) TaO_x (b) $Ta_{70}Al_{30}O_x$ (c) $Ta_{60}Al_{40}O_x$ (d) $Ta_{50}Al_{50}O_x$ (e) $Ta_{40}Al_{60}O_x$ and (e) AlO_x films.

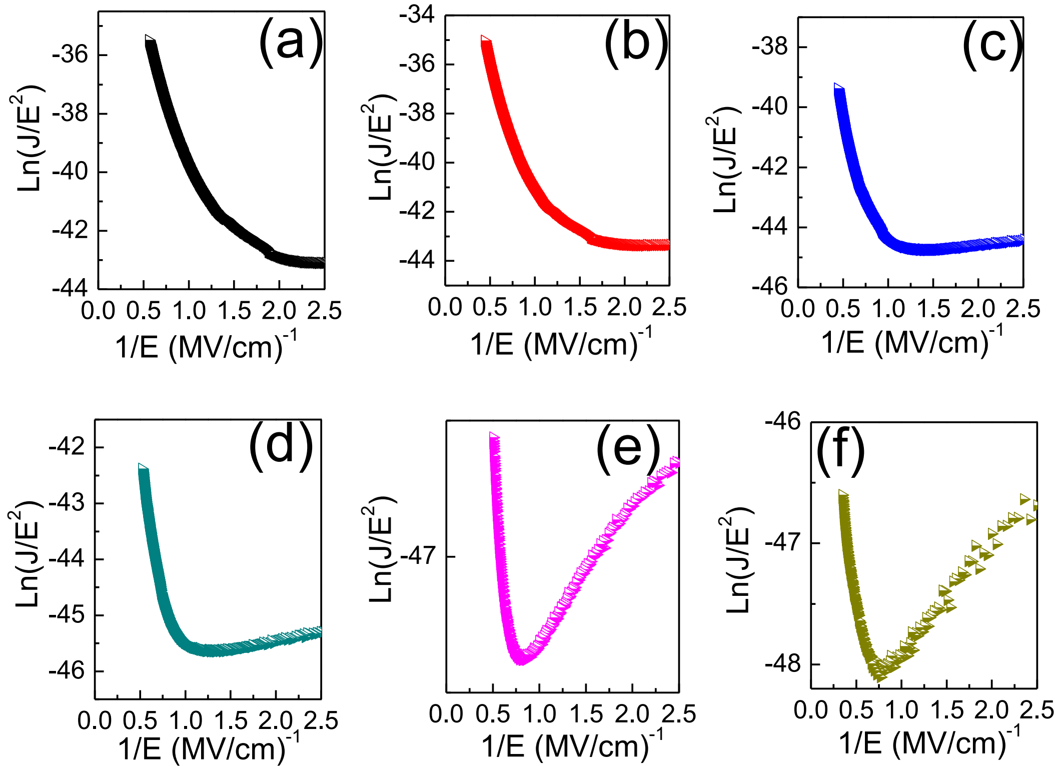

Figure 4- 23. Fowler-Nordheim plots of (a) TaO_x (b) $Ta_{70}Al_{30}O_x$ (c) $Ta_{60}Al_{40}O_x$ (d) $Ta_{50}Al_{50}O_x$ (e) $Ta_{40}Al_{60}O_x$ and (e) AlO_x films.

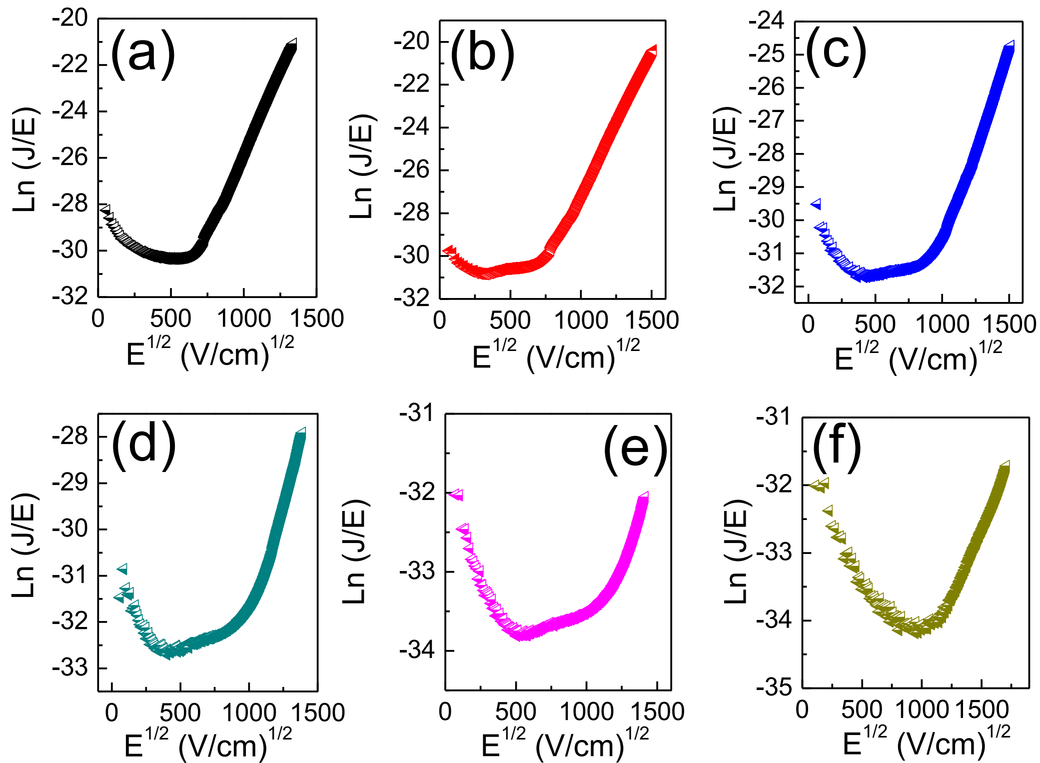

Figure 4- 24. Poole-Frenkel plots of (a) TaO_x (b) $Ta_{70}Al_{30}O_x$ (c) $Ta_{60}Al_{40}O_x$ (d) $Ta_{50}Al_{50}O_x$ (e) $Ta_{40}Al_{60}O_x$ and (e) AlO_x films.

At high electric field, the SE plots shown in Figure 4-22, exhibited linear characteristics, indicating that SE could potentially govern the charge transport in $Ta_{1-x}Al_xO_y$ films since the characterization was performed at room temperature (300 K). At room temperature, there is sufficient energy for the electrons to be thermally excited and overcome the potential barrier at the metal-dielectric interface that further diffuses into the dielectric.

Similarly, the linear part (at high electric field) of the FN plots shown in Figure 4-23, show the dominant conduction mechanism for all $Ta_{1-x}Al_xO_y$ films. In FN mechanism, electrons penetrate the potential barrier height due to large electric field applied at the metal-dielectric interface. An electric field of 2 MV/cm was used to characterize the $Ta_{1-x}Al_xO_y$ films.

Also, the linear part (at high electric field) of the PF plots shown in Figure 4-24, show dominant conduction mechanism for all $Ta_{1-x}Al_xO_y$ films. This is due to trapped electrons at the dielectric that further require large electric field to excite the electron out of its trapping centres and jump into the dielectric conduction band. According to Robertson et al. [106], oxide dielectrics have a high density of charge carrier trap levels. These trap levels are significant to the conduction of the dielectrics which explains the conduction in $Ta_{1-x}Al_xO_y$ films.

In all cases, the above-mentioned mechanisms (SE, FN, and PF) show nonlinear behaviour at the low electric field. Based on the findings, one cannot safely decide on the dominant conduction mechanisms in $Ta_{1-x}Al_xO_y$ films. Similar observation was made for solution-processed SiO_2 films reported by Esro et al. [107], where both FN and PF plots showed linear behaviour at high electric field indicating dominant conduction mechanisms.

Further analysis on the effective mass of electron and barrier height of $Ta_{1-x}Al_xO_y$ films is calculated from equation 3.17 and 3.18.

The calculated effective mass of electron and barrier height of $Ta_{1-x}Al_xO_y$ films as a function of [Al]/ [Al + Ta] atomic ratio is shown in Figure 4-25.

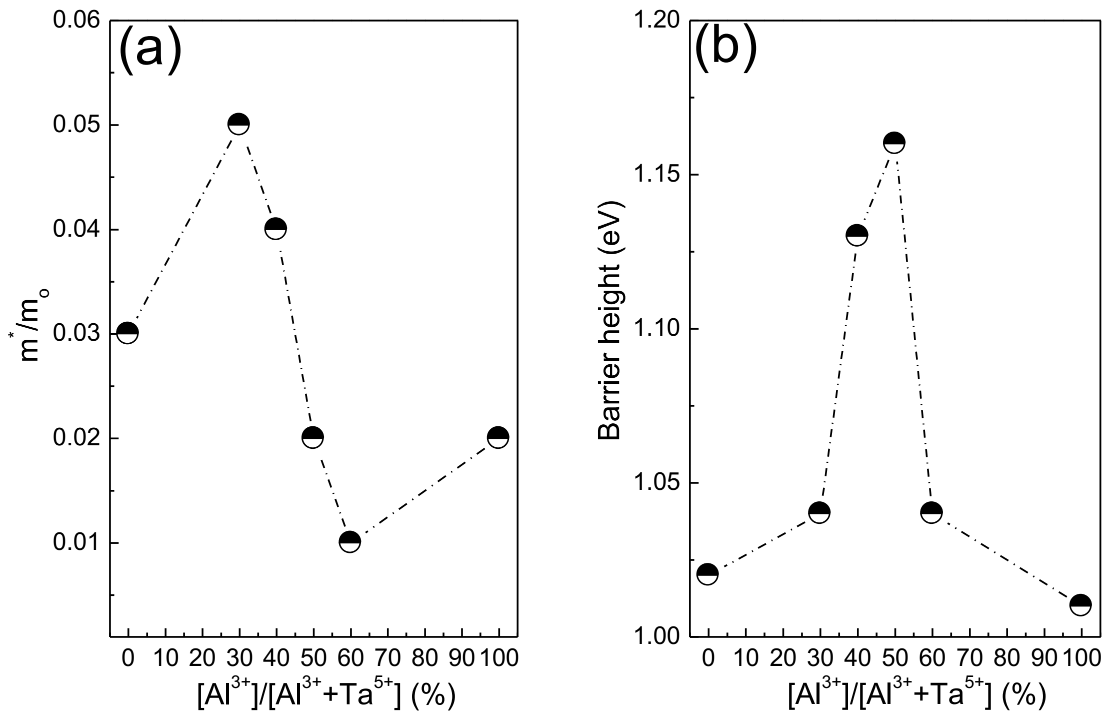

Figure 4- 25. (a) effective mass of the electron and (b) barrier height of $Ta_{1-x}Al_xO_y$ films as a function of [Al]/ [Al + Ta] atomic ratio.

The effective mass of electron (m^*) varies between 0.03m_o for TaO_x and 0.02m_o for AlO_x, however, the non-pure $Ta_{1-x}Al_xO_y$ film (i.e., x = 0.3 - 0.6) show decreasing trend as a function of [Al]/ [Al + Ta] atomic ratio as shown in Figure 4-25(a). The barrier height (ϕ_b) plot on the other hand, increases and reaches maximum (1.16 eV) for $Ta_{50}Al_{50}O_x$ films as shown in Figure 4-25(b). The ϕ_b value varies between 1.02 eV for TaO_x and 1.01 eV for AlO_x. it is important to note that a reliable dielectric should exhibit a low effective electron mass and a high barrier to prevent transport of charges within the dielectric. Such parameters play a significant role in leakage current of $Ta_{1-x}Al_xO_y$ films.

4.6.3 Field Effect Measurement

The implementation of the $Ta_{1-x}Al_xO_y$ films as gate dielectrics for ZnO – based TFTs were investigated by employing the bottom-gate top-contact (BG – TC) TFT architecture. ZnO semiconducting channels were sequentially deposited onto spray coated $Ta_{1-x}Al_xO_y$ films and Al source and drain (S/D) contacts were thermally evaporated onto the ZnO films through shadow masks, under high vacuum (10^{-6} mbar).

Figure 4-26 show a schematic of the BG – TC ZnO – based TFT architecture while Figure 4-27 to Figure 4-32 show a representative set of transfer and output characteristics obtained from a ZnO TFT (L = 50 um, W = 1000 um) based on a > 50 nm thick $Ta_{1-x}Al_xO_y$ gate dielectric.

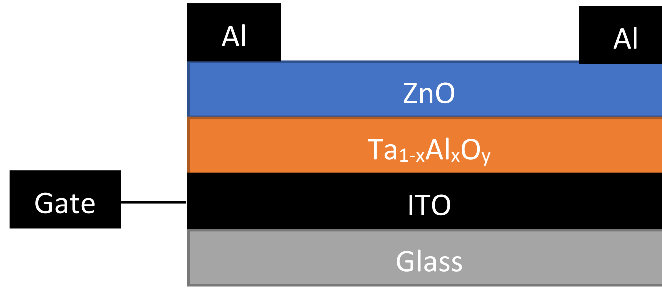

Figure 4- 26. A schematic of deposited BG – TC ZnO – based TFT architecture employing $Ta_{1-x}Al_xO_y$ gate dielectric.

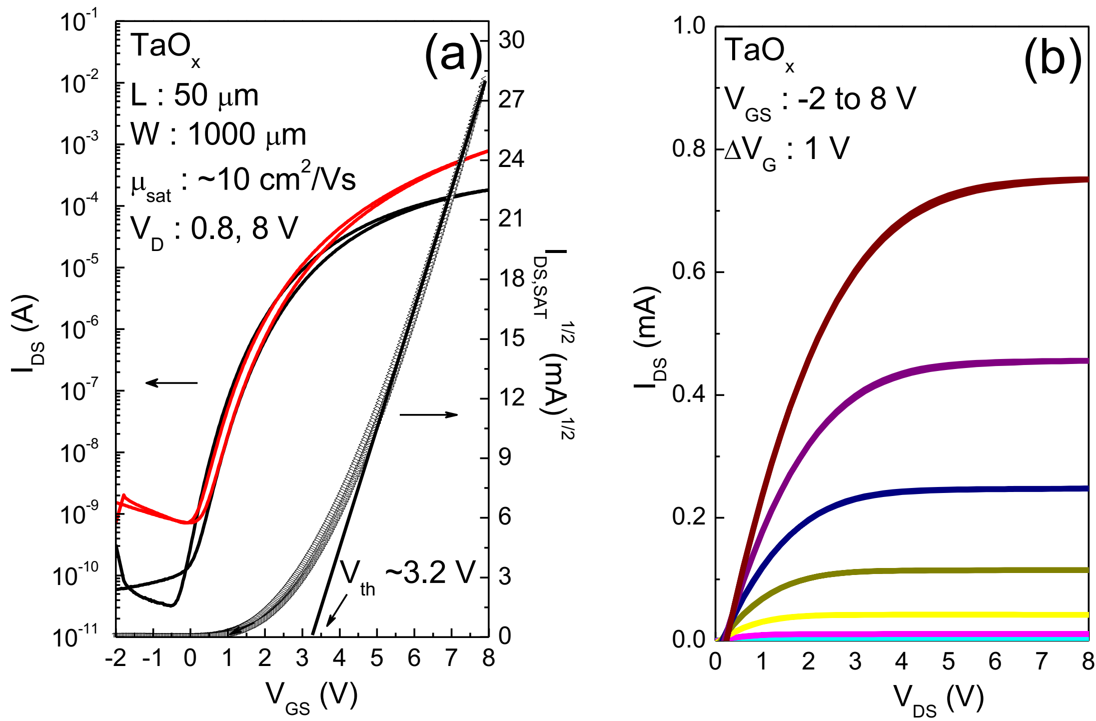

Figure 4- 27. (a) Transfer and (b) output characteristics of ZnO – based TFTs employing TaO_x gate dielectric.

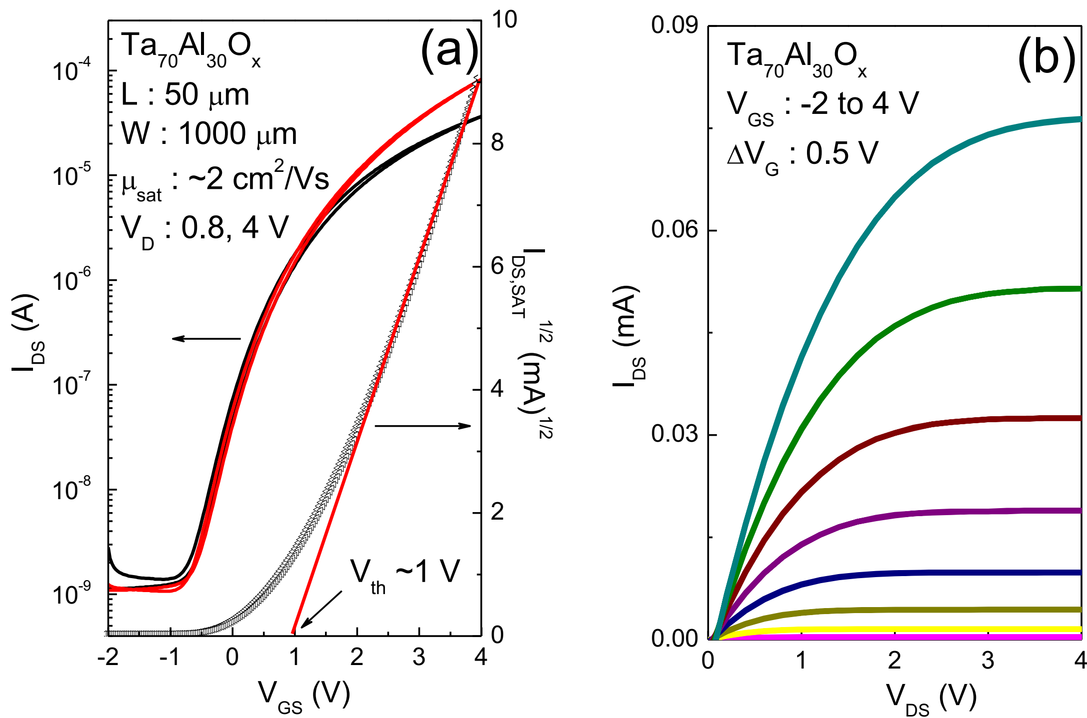

Figure 4- 28. (a) Transfer and (b) output characteristics of ZnO – based TFTs employing $Ta_{70}Al_{30}O_y$ gate dielectric.

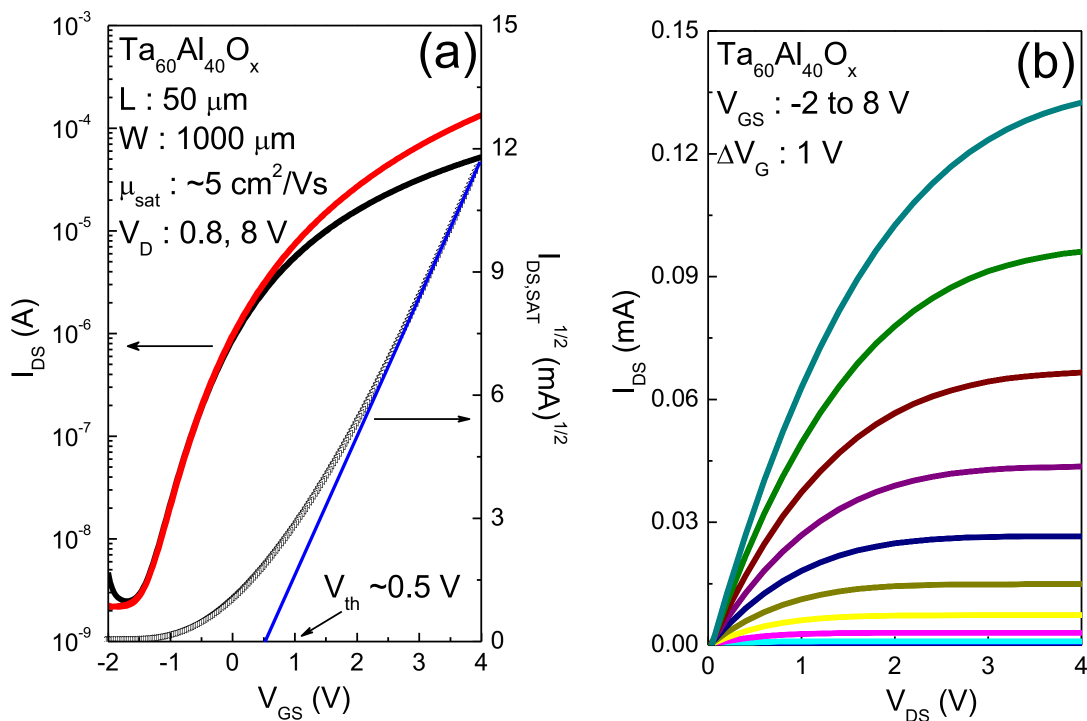

Figure 4- 29. (a) Transfer and (b) output characteristics of ZnO – based TFTs employing $Ta_{60}Al_{40}O_x$ gate dielectric.

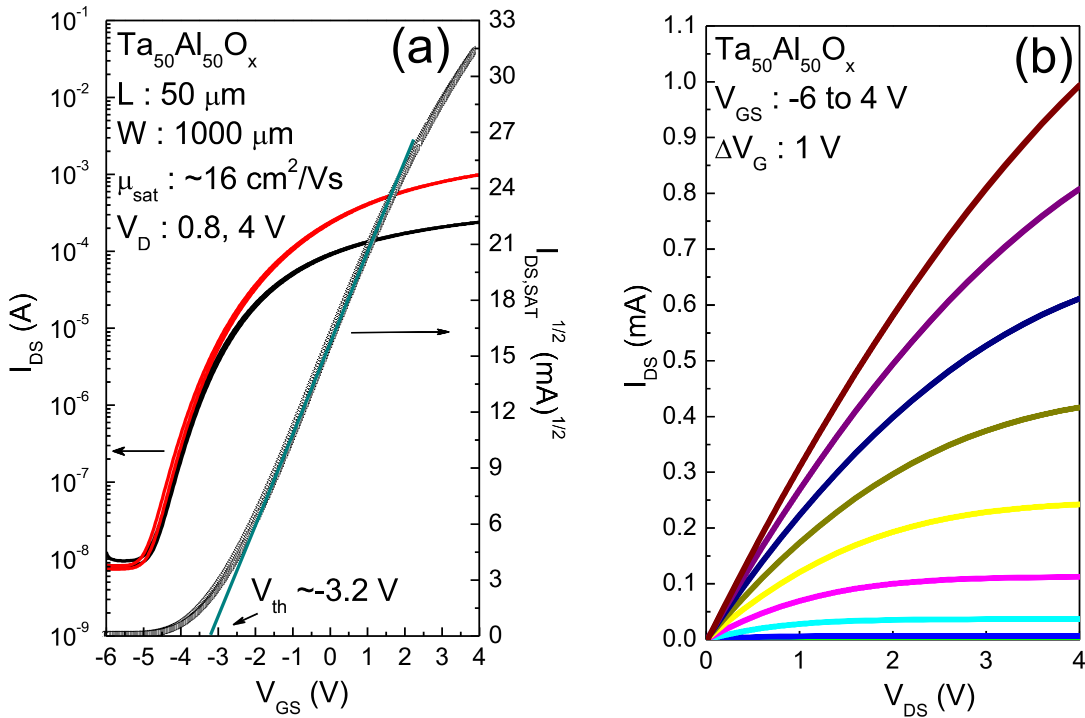

Figure 4- 30. (a) Transfer and (b) output characteristics of ZnO – based TFTs employing $Ta_{50}Al_{50}O_x$ gate dielectric.

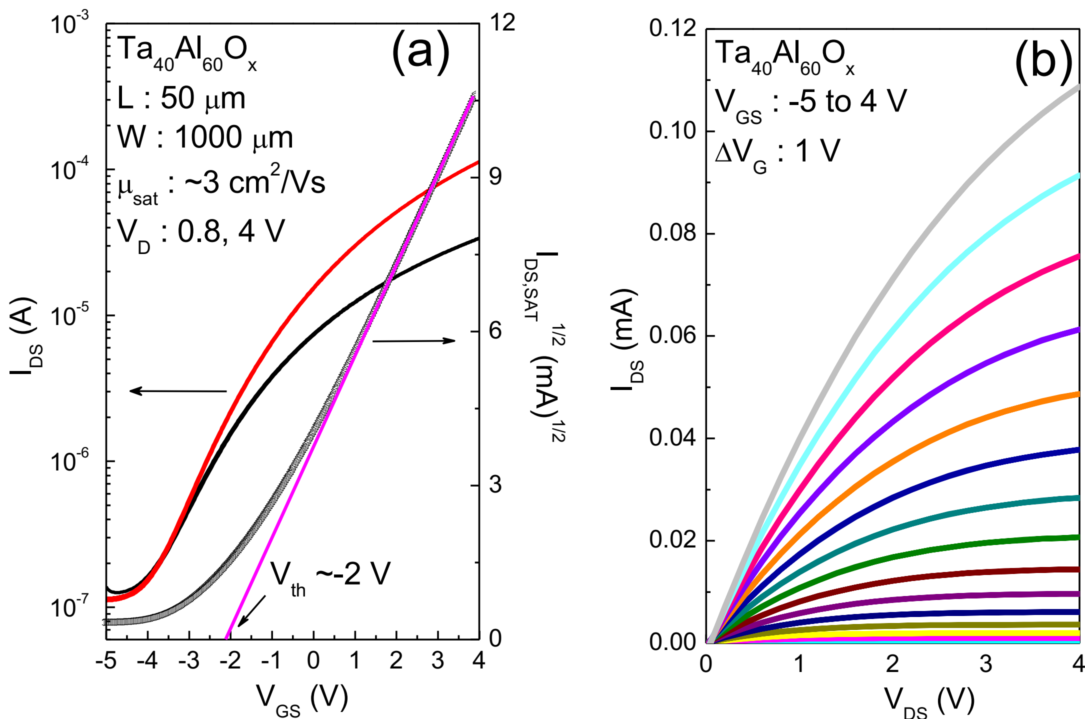

Figure 4- 31. (a) Transfer and (b) output characteristics of ZnO – based TFTs employing $Ta_{40}Al_{60}O_x$ gate dielectric.

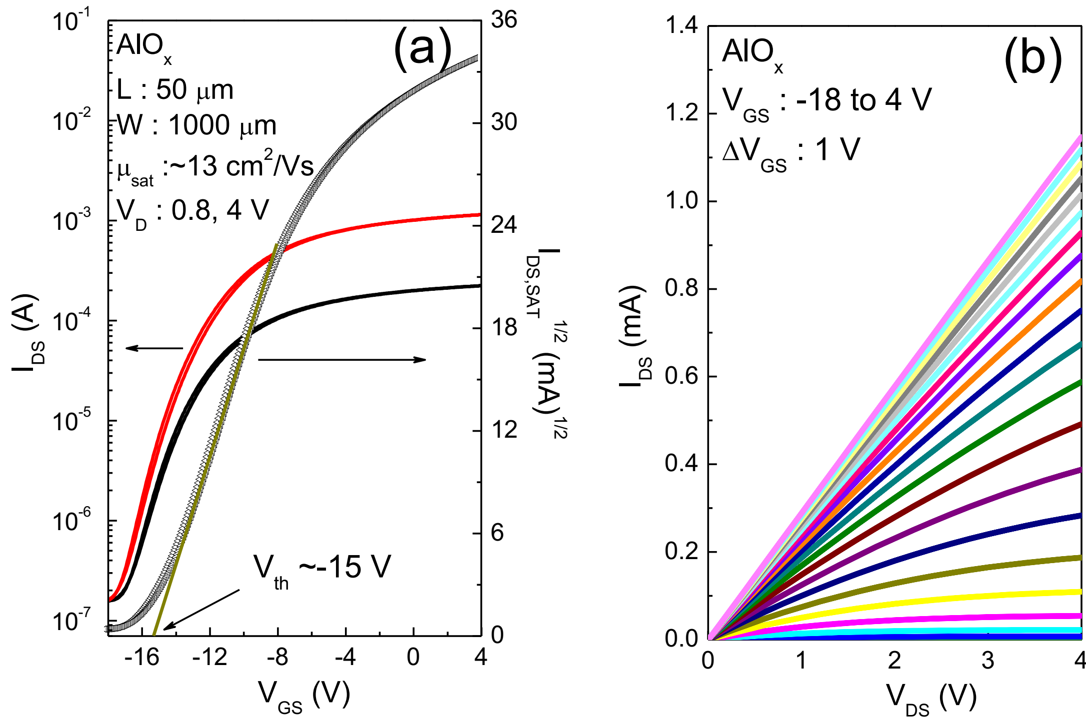

Figure 4- 32. (a) Transfer and (b) output characteristics of ZnO – based TFTs employing as-deposited AlO_x gate dielectric.

For better interpretation of the results, Figure 4-33 show the evolution of the properties of the ZnO – based TFTs employing $Ta_{1-x}Al_xO_y$ gate dielectric in terms of electron mobility (μ), current modulation ratio ($I_{on/off}$), threshold voltage (V_{th}), subthreshold swing (SS) and interface trap density (D_{it}) as a function of [Al]/ [Al + Ta] atomic ratio.

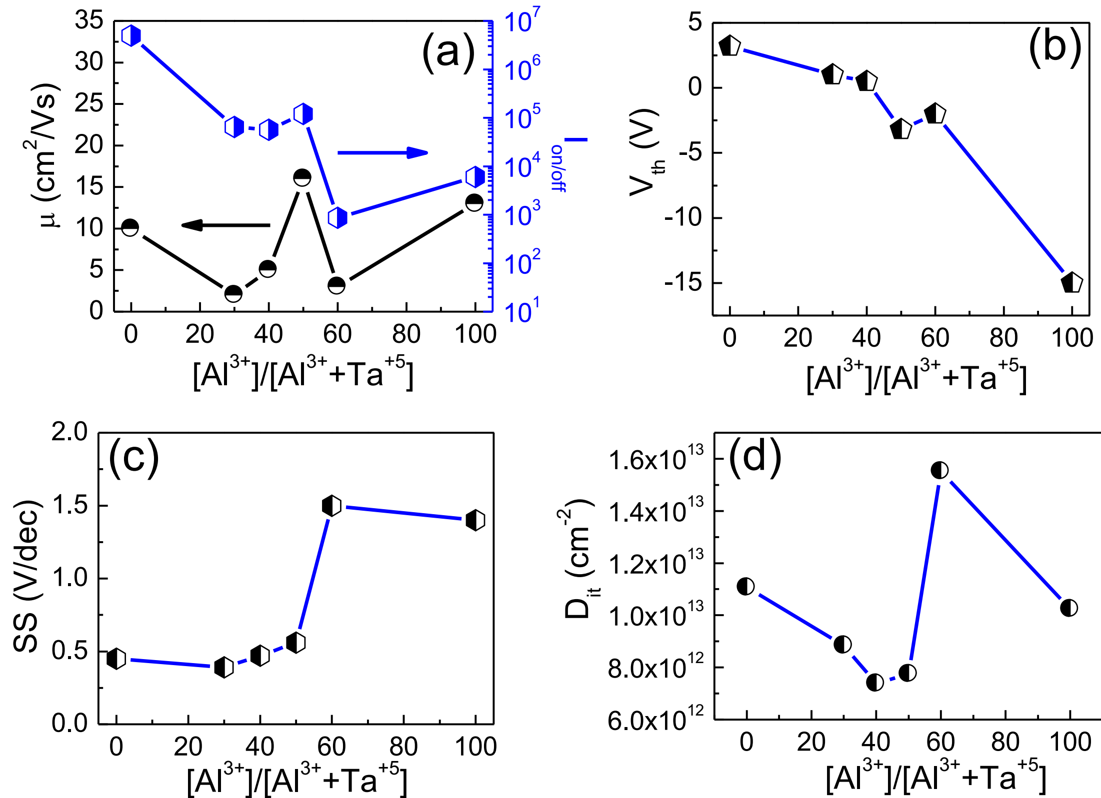

Figure 4- 33. (a) Electron mobility (left axis) and current modulation ratio (right axis), (b) Threshold voltage (V_{th}), (c) Subthreshold swing (SS) and (d) Interface trap density of ZnO – based TFTs employing $Ta_{1-x}Al_xO_y$ gate dielectric.

The dependence of the electron mobility (μ) and the current modulation ratio ($I_{on/off}$) as a function of the [Al] / [Al + Ta] TFTs is shown in Figure 4-33(a). The highest μ recorded was ~16 cm^2/Vs for ZnO – based TFT employing $Ta_{50}Al_{50}O_x$ gate dielectric. Interestingly, the μ showed slight improvement compared to the device fabricated with pure TaO_x (μ ~ 10 cm^2/Vs) and AlO_x (μ ~ 13 cm^2/Vs). The $I_{on/off}$ value of ~10^5 was obtained for ZnO – based TFT employing $Ta_{50}Al_{50}O_x$ gate dielectric. Additionally, TFTs with tantalum-rich compositions showed improved $I_{on/off}$ by an order of magnitude (from 10^4 to 10^5) compared to the aluminium-rich ones. Afouxenidis [88] reported similar observations when he fabricated ZnO – based TFT employing stoichiometric niobium aluminate gate dielectric.

The dependence of V_{th} as a function of the [Al] / [Al + Ta] TFTs is shown in Figure 4-33(b). The results show decreasing trend up to negative V_{th} (from 3.2 V for TaO_x to -15 V for AlO_x) with increasing [Al]/ [Al + Ta] atomic ratio. Such decrease may probably be associated with the decreased dielectric constant of $Ta_{1-x}Al_xO_y$ films (Figure 4-17) as a function of [Al]/ [Al + Ta] atomic ratio. The higher the dielectric constant the positive the V_{th} and vice-versa.

The dependence of SS as a function of the [Al] / [Al + Ta] TFTs is shown in Figure 4-33(c). The SS values increased from 0.45 V/dec for TaO_x to 1.4 V/dec for AlO_x as a function of [Al]/ [Al + Ta] atomic ratio. In comparison with the previous works done by Esro et al. [74], and Afouxenidis et al. [68], they reported the SS value of ZnO – based TFTs employing AlO_x gate dielectric as 1 V/dec and 0.99 V/dec respectively. These values were decreased to 0.6

V/dec and 0.549 V/dec for stochiometric $La_{1-x}Al_xO_y$ and $Ti_{1-x}Al_xO_y$ gate dielectric respectively, which clearly agrees with the value obtained for $Ta_{50}Al_{50}O_x$ gate dielectric (SS ~ 0.56 V/dec). On that basis, such increase can be attributed to the low dielectric constant of AlO_x (k ~ 7).

The dependence of D_{it} as a function of the [Al] / [Al + Ta] TFTs is shown in Figure 4-33(d). The D_{it} dependence was averaged around $\sim 10^{13}$ cm^{-2} and such values are quite acceptable for an oxide/oxide interface or an interface using high-k materials [108].

4.7 Conclusion

In conclusion, the properties of solution processed $Ta_{1-x}Al_xO_y$ films as a function [Al]/ [Al + Ta] atomic ratio was investigated. The optical bandgap values were varied between 4.9 – 8.8 eV with increasing [Al]/ [Al + Ta] atomic ratio. The $Ta_{50}Al_{50}O_x$ films exhibited an optical bandgap of 5.4 eV, which satisfies the band offset conditions and suitable for implementation in TFTs. $Ta_{1-x}Al_xO_y$ films were found to be amorphous and the surface morphology of the films showed low surface roughness with $R_{RMS} < 1$ nm. The static dielectric constant was varied between 24 and 7 with increasing Al content. The $Ta_{50}Al_{50}O_x$ films exhibited a dielectric constant of 13, which is reasonably enough for future TFTs application. The I – V measurements decreased with increasing [Al]/ [Al + Ta] atomic ratio. A current density of 15 nA/cm^2 at 1 MV/cm was obtained for $Ta_{50}Al_{50}O_x$ films.

Further investigation on the origin of the charge transport in $Ta_{1-x}Al_xO_y$ films showed that it could not be dominated by Schottky emission, Fowler Nordhiem and Poole-Frenkel mechanism, because all mechanisms exhibited linear behaviour at high electric fields. However, other potential mechanisms could be investigated for future study. Analysis on the effective mass of electron and barrier height showed that $Ta_{50}Al_{50}O_x$ films exhibited the effective electron mass of $0.02m_o$ and highest barrier height of 1.16 eV. Such parameters play a significant role for the leakage current in $Ta_{1-x}Al_xO_y$ films.

Finally, $Ta_{1-x}Al_xO_y$ films with different [Al] to [Ta] ratios were implemented as gate dielectric for ZnO – based TFTs. Based on the results, the performance of ZnO – based TFTs employing $Ta_{50}Al_{50}O_x$ gate dielectric exhibited the best properties in terms of highest electron mobility of ~ 16 cm^2/Vs, high on/off current modulation ratio 10^5, threshold voltage of -3.2 V, subthreshold swing of 0.56 V/dec, interface trap density of 7.7×10^{12} cm^{-2}, low operation voltage of 4 V and negligible hysteresis.

4.8 References

[1] J. Kristóf, A. De Battisti, G. Keresztury, E. Horváth, and T. Szilágyi, "Investigation of Ta_2O_5 Thin Film Evolution," *Langmuir*, vol. 17, no. 5, pp. 1637–1640, 2001.

[2] N. O. and H. F. H. Chiba, K. Tada, T. Furukawa, T. Yamamoto, T. Yotsuya, "Low temperature MOCVD of Ta_2O_5 dielectric thin films from $Ta[NC(CH_3)_3][OC(CH_3)_3]_3$ and O_2," *J. Ceram. Soc. Japan*, vol. 124, no. 5, pp. 510–514, 2016.

[3] J.-Y. Zhang and I. W. Boyd, "Pulsed laser deposition of tantalum pentoxide film," *Appl. Phys. A Mater. Sci. Process.*, vol. 70, no. 6, pp. 657–661, 2000.

[4] O. A. Azim, M. M. Abdel-Aziz, and I. S. Yahia, "Structure and optical analysis of Ta_2O_5 deposited on infrasil substrate," *Appl. Surf. Sci.*, vol. 255, no. 9, pp. 4829–4835, 2009.

[5] H. Koyama, S. Tanimoto, K. Kuroiwa, and Y. Tarui, "Thermal properties of various Ta precursors used in chemical vapor deposition of tantalum pentoxide," *Jpn. J. Appl. Phys.*, vol. 33, no. 11R, pp. 629–628, 1994.

[6] J.-Y. Zhang, B. Lim, and I. W. Boyd, "Thin tantalum pentoxide films deposited by photo-induced CVD," *Thin Solid Films*, vol. 336, no. 1–2, pp. 340–343, 1998.

[7] O. Rico-Fuentes, J. C. Alonso, G. Santana, and A. Ortiz, "Ultrasonic Spray Pyrolysis Deposition and Characterization of Tantalum–Aluminum Oxide Thin Films," *J. Electrochem. Soc.*, vol. 154, no. 12, p. G277, 2007.

[8] S. M. Edlou, "Optical properties of tantalum pentoxide coatings deposited using ion beam processes," vol. 209, pp. 223–229, 1992.

[9] J. Robertson, "Band offsets of wide-band-gap oxides and implications for future electronic devices," *J. Vac. Sci. Technol. B Microelectron. Nanom. Struct.*, vol. 18, no. 3, p. 1785, 2000.

[10] W. M. Paulson, F. S. Hickernell, and R. L. Davis, "Effects of deposition parameters on optical loss for rf-sputtered Ta_2O_5 and Si_3N_4 waveguides," *J. Vac. Sci. Technol.*, vol. 16, no. 2, pp. 307–310, 1979.

[11] M. Cid, N. Stem, C. Brunetti, A. F. Beloto, and C. A. S. Ramos, "Improvements in anti-reflection coatings for high-efficiency silicon solar cells," *Surf. Coatings Technol.*, vol. 106, no. 2, pp. 117–120, 1998.

[12] R. Engel-Herbert, Y. Hwang, J. Cagnon, and S. Stemmer, "Metal-oxide-semiconductor capacitors with ZrO_2 dielectrics grown on In 0.53 Ga 0.47 As by chemical beam deposition," *Appl. Phys. Lett.*, vol. 95, no. 6, pp. 62903–62908, 2009.

[13] S. jeh J. Wu, B. Houng, and B. sen Huang, "Effect of growth and annealing temperatures on crystallization of tantalum pentoxide thin film prepared by RF magnetron sputtering

method," *J. Alloys Compd.*, vol. 475, no. 1–2, pp. 488–493, 2009.

[14] A. L. Salaün, A. Mantoux, E. Blanquet, and E. Djurado, "ESD and ALD Depositions of Ta_2O_5 Thin Films Investigated as Barriers to Copper Diffusion for Advanced Metallization," *J. Electrochem. Soc.*, vol. 156, no. 5, p. H311, 2009.

[15] K. Kukli, M. Kemell, M. Vehkamaki, M. J. Heikkila, K. Mizohata, K. Kalam, M. Ritala, M. Leskela, I. Kundrata, and K. Frohlich, "Atomic layer deposition and properties of mixed Ta_2O_5 and ZrO_2 films," *AIP Adv.*, vol. 7, no. 2, p. 025001, 2017.

[16] F. Z. Tepehan, F. E. Ghodsi, N. Ozer, and G. G. Tepehan, "Determination of optical properties of amorphous Ta_2O_5 films deposited by spin- and dip-coating methods," *Sol. Energy Mater. Sol. Cells*, vol. 46, no. 4, pp. 311–321, 1997.

[17] J. S. and K. S. A. Nowak, J. Persson, B. Schmeizer, "Low temperature reduction in Ta-O and Nb-O thin films," *J. Phys. D. Appl. Phys.*, vol. 47, no. 13, 2014.

[18] F. Z. Tepehan, F. E. Ghodsi, N. Ozer, and G. G. Tepehan, "Optical properties of sol–gel dip-coated Ta_2O_5 films for electrochromic applications," *Sol. Energy Mater. Sol. Cells*, vol. 59, no. 3, pp. 265–275, 1999.

[19] F. Z. and D. C. L. Wang, H. Liu, Y. Jiang, X. Yang, D. Liu, Y. Ji, "Effects of hot-isostatic pressing and annealing post-treatment on HfO_2 and Ta_2O_5 films prepared by ion beam sputtering," *Optik (Stuttg).*, vol. 142, pp. 33–41, 2017.

[20] S. V. J. Chandra, S. Uthanna, and G. M. Rao, "Effect of substrate temperature on the structural, optical and electrical properties of dc magnetron sputtered tantalum oxide films," *Appl. Surf. Sci.*, vol. 254, no. 7, pp. 1953–1960, 2008.

[21] P. C. Joshi and M. W. Cole, "Influence of postdeposition annealing on the enhanced structural and electrical properties of amorphous and crystalline thin films for dynamic random access memory applications Influence of postdeposition annealing on the enhanced structural and electrical," vol. 5243, no. 2001, 2000.

[22] T. Ōishi, T. Nakazawa, and A. Katou, "Preparation and properties of tantalum oxide films by sol-gel method," *Electron. Commun. Japan (Part II Electron.*, vol. 76, no. 9, pp. 50–60, 1993.

[23] P. Barqiunha, R. Martins, E. Fortunato, and L. P.ereira, "Gate Dielectrics in Oxide Electronics," in *Transparent Oxide Electronics*, First., John Wiley & Sons. Ltd, 2012, pp. 101–153.

[24] G. D. Wilk, R. M. Wallace, and J. M. Anthony, "High-κ gate dielectrics: Current status and materials properties considerations," *J. Appl. Phys.*, vol. 89, no. 10, pp. 5243–5275, 2001.

[25] J. Robertson, "E lectronic Structure and Band Offsets of High-Dielectric- Constant Gate

Oxides," no. March 2002, pp. 217–221, 2020.

[26] S. Lagergren and A. Magneli, "On the Tantalum-Oxygen System," *Acta Chemica Scandinavica*, vol. 6, no. 3. pp. 444–446, 1952.

[27] S. Sathasivam, B. A. D. Williamson, A. Kafizas, S. A. Althabaiti, A. Y. Obaid, S. N. Basahel, D. O. Scanion, C. J. Carmalt, and I. P. Parkin, "Computational and experimental study of Ta_2O_5 thin films," *J. Phys. Chem. C*, vol. 121, no. 1, pp. 202–210, 2017.

[28] R. J. Bondi, M. P. Desjarlais, A. P. Thompson, G. L. Brennecka, and M. J. Marinella, "Electrical conductivity in oxygen-deficient phases of tantalum pentoxide from first-principles calculations," *J. Appl. Phys.*, vol. 114, no. 20, 2013.

[29] E. Stavrou, J. M. Zaug, S. Bastea, and M. Kunz, "A study of tantalum pentoxide Ta_2O_5 structures up to 28 GPa," *J. Appl. Phys.*, vol. 121, no. 17, 2017.

[30] Yong Yang and Yoshiyuki Kawazoe, "Prediction of New Ground State Crystal Structure of Ta_2O_5," vol. 3, no. iv, pp. 3–6.

[31] K. Lehovec, "Lattice structure of β-Ta_2O_5," *J. Less-Common Met.*, vol. 7, no. 6, pp. 397–410, 1964.

[32] C. Askeljung, B. O. Marinder, and M. Sundberg, "Effect of heat treatment on the structure of L-Ta_2O_5: A study by XRPD and HRTEM methods," *J. Solid State Chem.*, vol. 176, no. 1, pp. 250–258, 2003.

[33] M. Hiratani, S. Kimura, T. Hamada, S. Iijima, and N. Nakanishi, "Hexagonal polymorph of tantalum-pentoxide with enhanced dielectric constant," *Appl. Phys. Lett.*, vol. 81, no. 13, pp. 2433–2435, 2002.

[34] F. M. d'Heurle and R. G. S. Oehrlein, "Some properties of crystallized tantalum pentoxide thin films on silicon," *J. Appl. Phys.*, vol. 55, no. 10, pp. 3715–3725, 1984.

[35] M. V. Ivanov, T. V. Perevalov, V. S. Aliev, V. A. Gritsenko, and V. V. Kaichev, "Electronic structure of δ -Ta_2O_5 with oxygen vacancy: ab initio calculations and comparison with experiment," *J. Appl. Phys.*, vol. 110, no. 2, 2011.

[36] L. X. Qian, X. Z. Liu, C. Y. Han, and P. T. Lai, "Improved performance of amorphous InGaZnO thin-film transistor with Ta_2O_5 gate dielectric by using la incorporation," *IEEE Trans. Device Mater. Reliab.*, vol. 14, no. 4, pp. 1056–1060, 2014.

[37] C. Bartic, H. Jansen, A. Campitelli, and S. Borghs, "Ta_2O_5 as gate dielectric material for low-voltage organic thin-film transistors," *Org. Electron.*, vol. 3, no. 2, pp. 65–72, 2002.

[38] H.-C. P. and J.-S. C. H.J.H. Chen, B.B.L Yeh, "ZnO transparent thin-film transistors with HfO_2/Ta_2O_5 stacking gate dielectrics," *Electron. Lett.*, vol. 44, no. 3, 2008.

[39] L. Zhang, J. Li, X. W. Zhang, X. Y. Jiang, and Z. L. Zhang, “High performance ZnO-thin-film transistor with Ta_2O_5 dielectrics fabricated at room temperature,” *Appl. Phys. Lett.*, vol. 95, no. 7, 2009.

[40] N. Kumar, M. Sutradhar, J. Kumar, and S. Panda, “Role of deposition and annealing of the top gate dielectric in a-IGZO TFT-based dual-gate ion-sensitive field-effect transistors,” *Semicond. Sci. Technol.*, vol. 32, no. 3, 2017.

[41] F. H. Alshammari, P. K. Nayak, Z. Wang, and H. N. Alshareef, “Enhanced ZnO thin-film transistor performance using bilayer gate dielectrics,” *ACS Appl. Mater. Interfaces*, vol. 8, no. 35, pp. 22751–22755, 2016.

[42] W. Xu, M. Dai, L. Liang, Z. Liu, X. Sun, Q. Wan, and H. Cao, “Anomalous bias-stress-induced unstable phenomena of InZnO thin-film transistors using Ta_2O_5 gate dielectric,” *J. Phys. D. Appl. Phys.*, vol. 45, no. 20, 2012.

[43] J. W. Liu, M. Y. Liao, M. Imura, E. Watanabe, H. Oosato, and Y. Koide, “Diamond field effect transistors with a high-dielectric constant Ta_2O_5 as gate material,” *J. Phys. D. Appl. Phys.*, vol. 47, no. 24, 2014.

[44] Y. T. Jeong and A. Dodabalapur, “Pentacene-based low voltage organic field-effect transistors with anodized Ta_2O_5 gate dielectric,” *Appl. Phys. Lett.*, vol. 91, no. 19, pp. 2005–2008, 2007.

[45] N. Mohammadian, B. C. Das, and L. A. Majewski, “Low-Voltage IGZO TFTs Using Solution-Deposited OTS-Modified Ta_2O_5 Dielectric,” *IEEE Trans. Electron Devices*, vol. 67, no. 4, pp. 1625–1631, 2020.

[46] C. J. Chiu, S. P. Chang, and S. J. Chang, “High-Performance a-IGZO Thin-Film Transistor Using Ta_2O_5 Gate Dielectric,” vol. 31, no. 11, pp. 1245–1247, 2010.

[47] T. Ohishi, S. Maekawa, and A. Katoh, “Synthesis and properties of tantalum oxide films prepared by the sol-gel method using photo-irradiation,” *J. Non. Cryst. Solids*, vol. 147–148, no. C, pp. 493–498, 1992.

[48] J. Heo, S. Y. Park, J. W. Kim, S. Song, Y. J. Yoon, J. Jeong, H. Jang, K. T. Lee, J. H. Seo, B. Walker, and J. Y. Kim, “Implementation of Low-Power Electronic Devices Using Solution-Processed Tantalum Pentoxide Dielectric,” *Adv. Funct. Mater.*, vol. 28, no. 28, pp. 1–8, 2018.

[49] R. C. Frunză, B. Kmet, M. Jankovec, M. Topič, and B. Malič, “Ta_2O_5-based high-K dielectric thin films from solution processed at low temperatures,” *Mater. Res. Bull.*, vol. 50, pp. 323–328, 2014.

[50] S. Y. Park, J. Heo, Y. J. Yoon, J. W. Kim, H. Jang, B. Walker, and J. Y. Kim, “Synergistic combination of amorphous indium oxide with tantalum pentoxide for efficient electron transport in low-power electronics,” *J. Mater. Chem. C*, vol. 7, no. 15, pp. 4559–4566,

2019.

[51] N. Mohammadian, S. Faraji, S. Sagar, and B. C. Das, “One-Volt , Solution-Processed Organic Transistors,” *Materials (Basel).*, vol. 12, p. 2563, 2019.

[52] J. Robertson, “Band offsets of high dielectric constant gate oxides on silicon,” *J. Non. Cryst. Solids*, vol. 303, no. 1, pp. 94–100, 2002.

[53] J. Robertson, “High dielectric constant gate oxides for metal oxide Si transistors,” *Reports Prog. Phys.*, vol. 69, no. 2, pp. 327–396, 2006.

[54] G. Adamopoulos, S. Thomas, D. D. C. Bradley, M. A. McLachlan, and T. D. Anthopoulos, “Low-voltage ZnO thin-film transistors based on Y_2O_3 and Al_2O_3 high- k dielectrics deposited by spray pyrolysis in air,” *Appl. Phys. Lett.*, vol. 98, no. 12, pp. 1–4, 2011.

[55] S. Carmona-Tellez, J. Guzman-Mendoza, M. Aguilar-Frutis, G. Alarcon-Flores, M. Garcia-Hipolito, M. A. Canseco, and C. Falcony, “Electrical, optical, and structural characteristics of Al_2O_3 thin films prepared by pulsed ultrasonic sprayed pyrolysis,” *J. Appl. Phys.*, vol. 103, no. 3, 2008.

[56] C. Pflitsch, D. Viefhaus, U. Bergmann, and B. Atakan, “Organometallic vapour deposition of crystalline aluminium oxide films on stainless steel substrates,” *Thin Solid Films*, vol. 515, no. 7–8, pp. 3653–3660, 2007.

[57] M. A. Trunov, M. Schoenitz, and E. L. Dreizin, “Ignition of aluminum powders under different experimental conditions,” *Propellants, Explos. Pyrotech.*, vol. 30, no. 1, pp. 36–43, 2005.

[58] Alamy, “Corundum Aluminium Oxide.” [Online]. Available: https://www.dreamstime.com/corundum-aluminium-oxide-crystal-structure-ruby-gems-consist-red-transparent-sapphire-other-color-varieties-oxygen-shown-image187046166. [Accessed: 03-Nov-2021].

[59] D. H. Kuo and K. H. Tzeng, “Growth and properties of titania and aluminum titanate thin films obtained by r.f. magnetron sputtering,” *Thin Solid Films*, vol. 420–421, no. 1, pp. 497–502, 2002.

[60] P. K. Nayak, J. A. Caraveo-Frescas, Z. Wang, M. N. Hedhili, Q. X. Wang, and H. N. Alshareef, “Thin film complementary metal oxide semiconductor (CMOS) device using a single-step deposition of the channel layer,” *Sci. Rep.*, vol. 4, pp. 1–7, 2014.

[61] S. Sellner, A. Gerlach, S. Kowarik, F. Schreiber, H. Dosch, S. Meyer, J. Pflaum, and G. Ulbricht, “Comparative study of the growth of sputtered aluminum oxide films on organic and inorganic substrates,” *Thin Solid Films*, vol. 516, no. 18, pp. 6377–6381, 2008.

[62] R. Branquinho, D. Salgueiro, L. Santos, P. Barquinha, L. Pereira, R. Martins, and E.

Fortunato, "Aqueous combustion synthesis of aluminum oxide thin films and application as gate dielectric in GZTO solution-based TFTs," *ACS Appl. Mater. Interfaces*, vol. 6, no. 22, pp. 19592–19599, 2014.

[63] G. Huang, L. Duan, G. Dong, D. Zhang, and Y. Qiu, "High-mobility solution-processed tin oxide thin-film transistors with high-κ alumina dielectric working in enhancement mode," *ACS Appl. Mater. Interfaces*, vol. 6, no. 23, pp. 20786–20794, 2014.

[64] S. K. Kim and C. S. Hwang, "Atomic-layer-deposited Al_2O_3 thin films with thin SiO_2 layers grown by in situ O_3 oxidation," *J. Appl. Phys.*, vol. 96, no. 4, pp. 2323–2329, 2004.

[65] P. D. Ye, B. Yang, K. K. Ng, and J. Bude, "GaN metal-oxide-semiconductor high-electron-mobility-transistor with atomic layer deposited Al_2O_3 as gate dielectric," *Appl. Phys. Lett.*, vol. 86, no. 6, pp. 1–3, 2005.

[66] M. S. Oh, K. Lee, J. H. Song, B. H. Lee, M. M. Sung, D. K. Hwang, and S. Im, "Improving the gate stability of ZnO thin-film transistors with aluminum oxide dielectric layers," *J. Electrochem. Soc.*, vol. 155, no. 12, pp. 1009–1014, 2008.

[67] P. Katiyar, C. Jin, and R. J. Narayan, "Electrical properties of amorphous aluminum oxide thin films," *Acta Mater.*, vol. 53, no. 9, pp. 2617–2622, 2005.

[68] D. Afouxenidis, R. Mazzocco, G. Vourlias, P. J. Livesley, A. Krier, W. I. Milne, O. Kolosov, and G. Adamopoulos, "ZnO-based thin film transistors employing aluminum titanate gate dielectrics deposited by spray pyrolysis at ambient air," *ACS Appl. Mater. Interfaces*, vol. 7, no. 13, pp. 7334–7341, 2015.

[69] W. S. Choi and Y. Kim, "Inkjet-printed ZTO TFT with a combustion-processed aluminum oxide (Al_2O_3) gate dielectric," *Mol. Cryst. Liq. Cryst.*, vol. 679, no. 1, pp. 111–118, 2019.

[70] S. Choi, K. T. Kim, S. K. Park, and Y. H. Kim, "High-mobility inkjet-printed indium-gallium-zinc-oxide thin-film transistors using sr-doped Al_2O_3 gate dielectric," *Materials (Basel).*, vol. 16, no. 6, 2019.

[71] X. Zhang, B. Wang, W. Huang, Y. Chen, G. Wang, L. Zeng, W. Zhu, M. J. Bedzyk, W. Zhang, J. E. Medvedeva, A. Facchetti, and T. J Marks, "Synergistic Boron Doping of Semiconductor and Dielectric Layers for High-Performance Metal Oxide Transistors: Interplay of Experiment and Theory," *J. Am. Chem. Soc.*, vol. 140, no. 39, pp. 12501–12510, 2018.

[72] M.-S. K. and W.-J. Cho, "High-performance amorphous indium gallium zinc oxide thin-film transistors with sol-gel processed gate dielectric and channel layer fabricated using microwave irradiation," *Curr. Appl. Phys.*, vol. 18, no. 9, pp. 1080–1086, 2018.

[73] A. Lui', G. Liu', H. Zhu, B. Shin, E. Fortunato, R. Martins, and F. Shan', "Low-power organic field-effect transistors and complementary inverter based on low-temperature processed Al_2O_3 dielectric," *Org. Electron.*, vol. 34, pp. 118–123, 2016.

[74] M. Esro, R. Mazzocco, G. Vourlias, O. Kolosov, A. Krier, W. I. Milne, and G. Adamopoulos, “Solution processed lanthanum aluminate gate dielectrics for use in metal oxide-based thin film transistors,” *Appl. Phys. Lett.*, vol. 106, no. 20, 2015.

[75] F. Shan, A. Liu, H. Zhu, W. Kong, J. Liu, B. Shin, E. Fortunato, R. Martins, and G. Liu, “High-mobility p-type NiO_x thin-film transistors processed at low temperatures with Al_2O_3 high-k dielectric,” *J. Mater. Chem. C*, vol. 4, no. 40, pp. 9438–9444, 2016.

[76] A. Liu, G. Liu, H. Zhu, B. Shin, E. Fortunato, R. Martins, and F. Shan, “Eco-friendly, solution-processed In-W-O thin films and their applications in low-voltage, high-performance transistors,” *J. Mater. Chem. C*, vol. 4, no. 20, pp. 4478–4484, 2016.

[77] X. Ye, H. Lin, X. Yu, S. Han, M. Shang, L. Zhang, Q. Jiang, and J. Zhong, “High performance low-voltage organic field-effect transistors enabled by solution processed alumina and polymer bilayer dielectrics,” *Synth. Met.*, vol. 209, pp. 337–342, 2015.

[78] L. Zhang, Q. Zhang, G. Xia, J. Zhou, and S. Wang, “Low-temperature solution-processed alumina dielectric films for low-voltage organic thin film transistors,” *J. Mater. Sci. Mater. Electron.*, vol. 26, no. 9, pp. 6639–6646, 2015.

[79] H. Park, Y. Nam, J. Jin, and B. S. Bae, “Space charge-induced unusually-high mobility of a solution-processed indium oxide thin film transistor with an ethylene glycol incorporated aluminum oxide gate dielectric,” *RSC Adv.*, vol. 5, no. 124, pp. 102362–102366, 2015.

[80] A. Liu, G. Liu, H. Zhu, B. Shin, E. Fortunato, R. Martins, and F. Shan, “Hole mobility modulation of solution-processed nickel oxide thin-film transistor based on high-k dielectric,” *Appl. Phys. Lett.*, vol. 108, no. 23, 2016.

[81] B. Wang, X. Yu, P. Guo, W. Huang, L. Zeng, N. Zhou, L. Chi, M. J. Bedzyk, R. P. H. Chang, T. J. Marks, and A. Facchetti, “Solution-Processed All-Oxide Transparent High-Performance Transistors Fabricated by Spray-Combustion Synthesis,” *Adv. Electron. Mater.*, vol. 2, no. 4, 2016.

[82] Y. Wang, Z. Wang, K. Huang, X. Liang, C. Liu, C. Chen, and C. Liu, “Solution-processed ITO thin-film transistors with doping of gallium oxide show high on-off ratios and work at 1 mV drain voltage,” *Appl. Phys. Lett.*, vol. 116, no. 14, 2020.

[83] J. Bin Xu, Wangying Wang, Han Xie, Fangyan Chen, Jian Cao, Hongtao Xu, “Facile and Environmentally Friendly Solution-Processed Aluminum Oxide Dielectric for Low-Temperature, High-Performance Oxide Thin-Film Transistors,” *ACS Appl. Mater. Interfaces*, vol. 7, no. 10, pp. 5803–5810, 2015.

[84] B. S. and F. S. H. Tan, G. Liu, A. Liu, “The annealing effects on the properties of solution-processed alumina thin film and its application in TFTs,” *Ceram. Int.*, vol. 41, no. S1, pp. S349–S355, 2015.

[85] J. C. and J. X. H. Wang, T. Sun, W. Xu, F. Xie, Y. Xiao, Y. Wang, "Low-temperature facile solution-processed gate dielectric for combustion derived oxide thin film transistors," *RSC Adv.*, vol. 4, no. 97, pp. 54729–54739, 2014.

[86] X. Li, L. Zhu, Y. Gao, and J. Zhang, "Solution-Processed Low-Operating-Voltage Thin-Film Transistors With Bottom-Gate," *IEEE Trans. Electron Devices*, vol. 62, no. 3, pp. 875–881, 2015.

[87] J. Kim, S. Choi, J. Jo, S. K. Park, and Y. Kim, "Solution-processed lanthanum-doped Al_2O_3 gate dielectrics for high-mobility metal-oxide thin-film transistors," *Thin Solid Films*, vol. 660, no. December 2017, pp. 814–818, 2018.

[88] D. Afouxenidis and G. Adamopoulos, "ZnO-based Thin Tilm Transistor employing Niobium Aluminate Gate Dielectrics Deposited by Spray Pyrolysis at Ambient air," 2018.

[89] K. N. Woods, E. C. Waddington, C. A. Crump, E. A. Bryan, T. S. Gleckler, M. R. Nellist, B. A. Duell, D. P. Nguyen, S. W. Boettcher, and C. J. Page, "Tunable high-κ $Zr_xAl_{1-x}O_y$ thin film dielectrics from all-inorganic aqueous precursor solutions," *RSC Adv.*, vol. 7, no. 62, pp. 39147–39152, 2017.

[90] W. Yang, K. Song, Y. Jung, S. Jeong, and J. Moon, "Solution-deposited Zr-doped AlO_x gate dielectrics enabling high-performance flexible transparent thin film transistors," *J. Mater. Chem. C*, vol. 1, no. 27, pp. 4275–4282, 2013.

[91] J. Jo, J. Kim, K. Kim, J. Kang, M. Kim, K. Kim, H. Ko, Y. Kim, and S. Park, "Highly stable and imperceptible electronics utilizing photoactivated heterogeneous sol-gel metal-oxide dielectrics and semiconductors," *Adv. Mater.*, vol. 27, no. 7, pp. 1182–1188, 2015.

[92] M. Esro, G. Vourlias, C. Somerton, W. I. Milne, and G. Adamopoulos, "High-mobility ZnO thin film transistors based on solution-processed hafnium oxide gate dielectrics," *Adv. Funct. Mater.*, vol. 25, no. 1, pp. 134–141, 2015.

[93] J. M. Hu, J. Q. Zhang, and C. N. Cao, "Thermolytic formation and microstructure of IrO_2 + Ta_2O_5 mixed oxide anodes from chloride precursors," *Thermochim. Acta*, vol. 403, no. 2, pp. 257–266, 2003.

[94] D. Kim, S. M. Jeong, S. G. Yoon, C. H. Woo, J. I. Kim, H-G. Lee, J. Y. Park, and W-J. Kim, "Chemical vapor deposition of tantalum carbide from $TaCl_5$-C_3H_6-Ar-H_2 system," *J. Korean Ceram. Soc.*, vol. 53, no. 6, pp. 597–603, 2016.

[95] T. Kovarik, D. Pokorna, M. Urbanova, P. Bedica, Z. Bastl, J. Kupcik, T. Krenek, M. Pola, L. Kullova, and J. Pola, "Formation of TiO/Al_2O_3/C composite in thermal co-decomposition of aluminium(III)acetylacetonate and titanium(IV) oxyacetylacetonate," *J. Anal. Appl. Pyrolysis*, vol. 117, pp. 182–190, 2016.

[96] J. Tauc, "Optical properties and electronic structure of amorphous Ge and Si," *Mater. Res. Bull.*, vol. 3, no. 1, pp. 37–46, 1968.

[97] J. Robertson, "High K Dielectrics for Future CMOS Devices," vol. 19, no. 2, pp. 579–591, 2009.

[98] J. Robertson and R. M. Wallace, "High-K materials and metal gates for CMOS applications," *Mater. Sci. Eng. R Reports*, vol. 88, pp. 1–41, 2015.

[99] Y. H. Kim, K. H. Kim, and S. K. Park, "Effects of annealing conditions on the dielectric properties of solution-processed Al_2O_3 layers for indium-zinc-tin-oxide thin-film transistors," *J. Nanosci. Nanotechnol.*, vol. 13, no. 11, pp. 7779–7782, 2013.

[100] B. L. Yang, P. T. Lai, and H. Wong, "Conduction mechanisms in MOS gate dielectric films," *Microelectron. Reliab.*, vol. 44, no. 5, pp. 709–718, May 2004.

[101] H. Wong, "The Current Conduction Issues in High-k Gate Dielectrics," in *2007 IEEE Conference on Electron Devices and Solid-State Circuits*, 2007, no. CityU 121707, pp. 31–36.

[102] F.-C. Chiu, "A Review on Conduction Mechanisms in Dielectric Films," *Adv. Mater. Sci. Eng.*, vol. 2014, no. 7, pp. 1–18, 2014.

[103] P. W. Peacock and J. Robertson, "Band offsets and Schottky barrier heights of high dielectric constant oxides," *J. Appl. Phys.*, vol. 92, no. 8, pp. 4712–4721, 2002.

[104] J. G. Simmons, "Conduction in thin dielectric films," *J. Phys. D. Appl. Phys.*, vol. 4, no. 5, pp. 613–657, 1971.

[105] F. C. Chiu, P. W. Li, and W. Y. Chang, "Reliability characteristics and conduction mechanisms in resistive switching memory devices using ZnO thin films," *Nanoscale Res. Lett.*, vol. 7, pp. 1–9, 2012.

[106] J. Robertson and R. M. Wallace, "High-K materials and Metal Gates for CMOS applications," pp. 1–77.

[107] M. Esro, O. Kolosov, P. J. Jones, W. I. Milne, and G. Adamopoulos, "Structural and electrical characterization of SiO_2 gate dielectrics deposited from solutions at moderate temperatures in air," *ACS Appl. Mater. Interfaces*, vol. 9, no. 1, pp. 529–536, 2017.

[108] R. Martins, P. Barquinha, I. Ferreira, L. Pereira, G. Goņalves, and E. Fortunato, "Role of order and disorder on the electronic performances of oxide semiconductor thin film transistors," *J. Appl. Phys.*, vol. 101, no. 4, 2007.

5 Hafnium Titanate $Hf_{1-x}Ti_xO_y$ Thin Films

This chapter discusses the deposition and characterization of Hafnium Titanate ($Hf_{1-x}Ti_xO_y$) thin films as a function of the Hf to Ti atomic ratio and their implementation as gate dielectrics in TFTs employing ZnO semiconducting channels. $Hf_{1-x}Ti_xO_y$ thin films were deposited by spray pyrolysis in air and were characterized by range of techniques including UV-Vis spectroscopy, FTIR, XRD, AFM, Impedance spectroscopy, current – voltage and field effect measurements. The structure of $Hf_{1-x}Ti_xO_y$ films were found to be amorphous except for HfO_x and TiO_x films while the morphology showed a surface roughness of about 1 nm. The optical bandgap, dielectric constant and current density at 1 MV/cm of as-deposited $Hf_{1-x}Ti_xO_y$ films varies between 3.7 eV and 5.8 eV, 14 and 60 and 10^{-7} A/cm^2 and 10 A/cm^2 respectively. *Further investigation on the conduction mechanism showed that the Poole Frenkel conduction mechanism dominates the current transport in $Hf_{1-x}Ti_xO_y$ films. Finally, the performance of $Hf_{1-x}Ti_xO_y$ as gate dielectrics for ZnO – based TFTs showed high electron mobility of 7 cm^2/Vs, high current modulation ratio (>10^6), threshold voltage of 0.6 V, subthreshold swing of 0.17 V/dec and low operation voltage (3 V).*

The $Hf_{1-x}Ti_xO_y$ films were further annealed at 800 °C for 30 minutes in air to investigate the effects of post-deposition annealing. Analyses showed the formation of stochiometric orthorhombic phase $Hf_{1-x}Ti_xO_y$ films with a surface roughness of 1.95 nm, bandgap of 4.35 eV, dielectric constant of 38 and a current density of 5 mA/cm^2 at 1 MV/cm. Finally, the stochiometric $Hf_{1-x}Ti_xO_y$ films showed dominant conduction governed by Fowler-Nordhiem mechanism having the parameters of 0.003 m_o and 0.49 eV representing the effective mass of the electron and the barrier heigh at the interface respectively.

5.1 Introduction

Hafnium (IV) oxide (HfO_2) and Titanium oxide (TiO_2) are among the most researched high-k metal oxides as alternatives to SiO_2 gate dielectric due to their high dielectric constant ($k_{HfO2, TiO2} > k_{SiO2} \sim 3.9$).

HfO_2 has a high dielectric constant of between 14 – 25 depending on its deposition method. It is of a high refractive index (n ~ 1.9 at λ = 550 nm), high transparency in visible spectrum (400 – 700 nm) and exhibit a wide energy gap ~5.7 eV. Additionally, HfO_2 films are thermodynamically and chemically stable with oxide semiconductors [1]. These remarkable properties makes HfO_2 suitable for integration in electronic devices such as in memories, capacitors, optoelectronics [2], silicon solar cells [3] and thin-film transistors (TFTs) [4].

HfO_2 thin films can exist in one of the three polymorphs [5]: monoclinic, tetragonal and cubic phase. At room temperature, HfO_2 films crystallizes into monoclinic phase and can be transformed into tetragonal and cubic phase at 1726 °C and above 2596 °C respectively [6]. Among the three phases, the monoclinic phase is regarded as the most stable and exhibit a dielectric constant of ~22 while other metastable structures such as tetragonal and cubic exhibit a dielectric constant of ~30 [7]. In Figure 5-1, the unit cell of the polymorphs of HfO_2 films is shown.

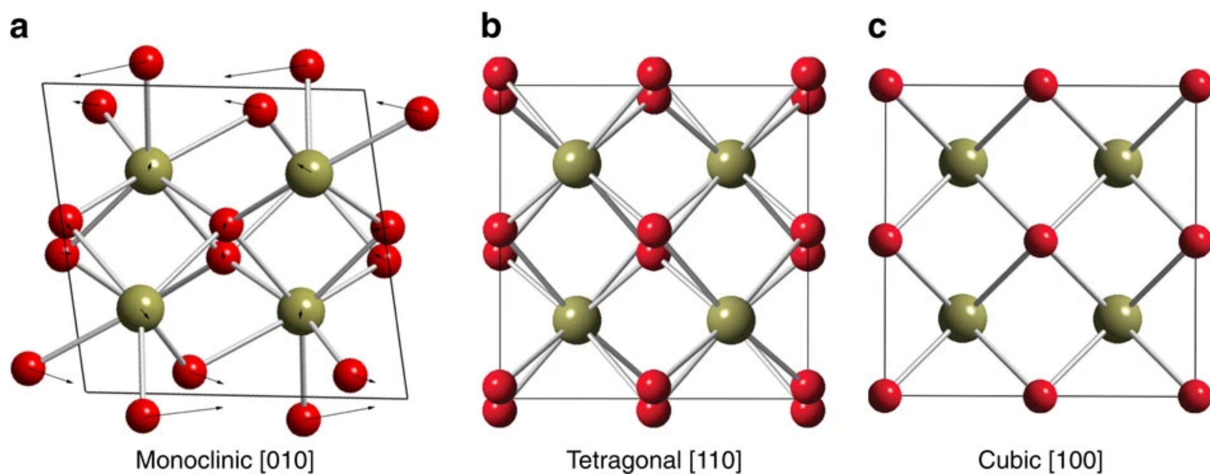

Figure 5- 1. The unit cells of three phases of HfO_2, showing the small atomic displacements, and presentation of the coordination environments during the transformation between the phases. The dark yellow circles represents Hf atoms while the red ones represents O atoms [5].

HfO_2 thin films have been deposited by several techniques including the vacuum-based such as atomic layer deposition (ALD) [8], chemical vapour deposition (CVD) [9][10], magnetron sputtering [11]–[13], pulsed laser deposition (PLD) [14], molecular beam epitaxy (MBE) [15] and from solutions such as spin coating [1][16]–[22] and spray pyrolysis [23]–[29].

One of the major issues of HfO_2 is that it crystallizes at relatively low temperatures (<450 °C) and produces grain boundaries [18][30]. The latter leads to increased gate leakage current which may further result to high off-state current, low on/off current ratios and

increased power consumption [31]. Additionally, grain boundaries affect uniformity of the crystalline high-k oxides films and may induce variations in device-to-device performance.

There are several reports on solution processed HfO_2 gate dielectric for TFTs applications. Table 5-1 present some selected works on properties of solution processed HfO_2 gate dielectrics mostly deposited by spin coating process using hafnium chloride ($HfCl_4$) as the precursor.

Esro et al. [29], investigated a high-mobility ZnO thin film transistors based on solution-processed hafnium oxide gate dielectric deposited by spray pyrolysis using hafnium chloride ($HfCl_4$). They reported a monoclinic HfO_2 structure, dielectric constant of 18.8, wide bandgap of 5.7 eV, and low leakage current (<74 nA/cm^2 at 6 V). Furthermore, ZnO-based TFTs employing HfO_2 gate dielectrics showed excellent characteristics such as low voltage operation of 6 V, high current modulation ratio (10^7), and high electron mobility of 40 cm^2/Vs.

Similarly, Chung et al. [16], investigated a spin coated HfO_2 films that exhibited a high dielectric constant of ∼10.23 and low leakage current density of ∼10^{-9} A/cm^2 at 4 MV/cm. Furthermore, the In_2O_3-based TFTs showed low voltage operation of 10 V, high current modulation ratio of 10^6, subthreshold swing of 0.18 V/dec, and high electron mobility of 3.67 cm^2/Vs.

Also, Zhang et al. [17], reported a spin coated HfO_2 films that showed a dielectric constant of 12.4, wide bandgap of 5.82 eV, and very low leakage current of 1 nA/cm^2 at 4.5 MV/cm, with IZO-based TFT performance such as low voltage operation of 3 V, high current modulation ratio of 10^9, subthreshold swing of 0.38 V/dec, and high electron mobility of 36.9 cm^2/Vs.

Table 5- 1. Selected previous work on solution processed HfO_2 gate dielectric and their TFT characteristics. (T_{dep}: deposition temperature, k: dielectric constant, J_{leak}: leakage current density, μ : electron mobility, SS: subthreshold swing, $I_{on/off}$: current modulation ratio, V_{th}: threshold voltage).

Deposition technique	T_{dep} (°C)	k	J_{leak} (A/cm^2)	Semiconductor	μ (cm^2/Vs)	SS (V/dec)	$I_{on/off}$	V_{th} (V)	ref
Spin coating	350	10.23	10^{-9} @ 4 MV/cm	In_2O_3	3.67	0.18	10^6	-	[16]
Spin coating	300	14.2	5.8 x 10^{-8} @ 100 MV/cm	-	-	-	-	-	[19]
Spin coating	500	25	5 x 10^{-7} @ 4 V	P-OFTs	0.36	0.37	4 x 10^4	-1.1	[20]
Spin coating	300	14	-	ZTO	1.05	0.15	-	1.18	[32]
Spin coating	500	12.4	10^{-9} @ 4.5 MV/cm	IZO	36.9	0.38	10^9	1.8	[17]
Spray pyrolysis	450	18.8	74 x 10^{-9} @ 6V	ZnO	40	-	10^7	2	[29]
Spin coating	500	13.1	10^{-7} @ 2.5 MV/cm	HIZO	3.64	1.1	2.94 x 10^4	0.51	[22]
Spin coating	500	18.5	10^{-6} @ 3 MV/cm	ZnO	1.6	-	10^7	0.0015	[1]
Spin coating	400	12.4	2.8 x 10^{-8} @ 1 MV/cm	ZnO	1.17	-	10^6	5.87	[18]
Spin coating	230	-	-	ZTO	3.84	0.117	-	0.84	[21]

TiO_2 on the other hand, is another well-studied high-k oxide due to its high dielectric constant k ~ 60 – 80. TiO_2 films are highly transparent in visible region (400 – 800 nm) and has high refractive index (n ~ 2 at λ = 550 nm). It has been used in many applications such as optical filters [33], gas sensors [34], ceramic membranes [35], waveguides [36], photocatalysts [37], and antireflection coatings [38].

TiO_2 exhibits a crystalline structure at low deposition temperature (<450 °C) and can exist in any of the three polymorphs: anatase, rutile and brookite and are strongly dependent on the growth conditions [39]–[42]. The anatase and brookite phases are metastable while rutile is regarded as the most thermodynamically stable. The transformation of anatase to rutile phase have been reported to undergo above 600 °C and can be influenced by some parameters such as particle size, impurities, heating rate, volume of the samples etc [42]–[44]. Figure 5-2 show the unit cell of the polymorphs of TiO_2.

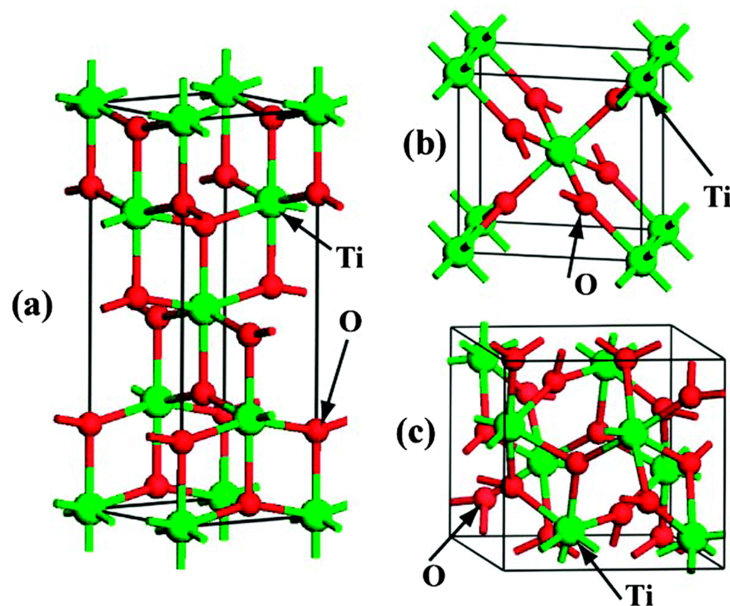

Figure 5- 2. The unit cells of three polymorphs of TiO_2. (a) anatase, (b) rutile, and (c) brookite. The green spheres represent Ti atoms and the small red spheres represents O atoms [45].

Despite its promising properties, TiO_2 is a low band gap (E_g ~ 3.8 eV) material. Such low bandgap limits its application as gate dielectrics for TFTs especially when wide band gap semiconductor such as ZnO (E_g ~ 3.3 eV) is employed as active channel. Such low bandgap can be improved by incorporation of another wide bandgap oxide such as HfO_2 to produce hafnium titanate ($HfTiO_4$) films.

$HfTiO_4$ or HTO is a potential multicomponent oxide alternative to the conventional SiO_2 gate dielectric due to its high dielectric constant and wide bandgap. The former is presumed to be greater than the HfO_2 ($k_{HTO} > k_{HfO2}$) while the latter is greater than TiO_2 ($E_{g\text{-}HTO} > E_{g\text{-}TiO2}$ eV).

HTO films exhibit a dielectric constant between 15 – 50 and a bandgap between 3.5 – 4.5 eV depending on the composition and manufacturing process [46]–[52]. Its atomic

structure is amorphous due to addition of Ti content that further deteriorates crystallinity of HfO_2 [53]. However, upon annealing above 700 °C, HTO films exhibit an orthorhombic-like crystalline structure.

For instance, Chen et al. [46], reported an orthorhombic HTO phase after annealing between 700 – 1000 °C deposited by CVD. Similarly, Popovici et al. [51], also reported an orthorhombic phase HTO films after annealing at 700 °C. In other literatures, Triyoso et al. [47], Wang et al. [48], and Jin et al. [49], all reported an amorphous structure for as-deposited HTO films by different techniques.

HTO films have been deposited by mainly costly vacuum-based techniques. Table 5-2 present some selected works on properties of HTO films deposited by vacuum-based techniques.

Table 5- 2. Selected previous works on properties of HTO gate dielectric.

Deposition Techniques	T_{dep} (°C)	k	E_g (eV)	J_{leak} (A/cm^2)	Ref
CVD	250	50	-	-	[46]
ALD	300	38		1 @ 5 V	[47]
ALD	300	-	3.4	0.001 @ 0.5 V	[52]
Sputtering	RT	31.3	4.58	0.001 @ 3V	[48]
Sputtering	RT	15.04 – 26.12	4. 03 – 4.21	10^{-6} @ 1 V	[49]
CVD	400	50	-	10^{-5} @ 1 MV/cm	[54]
Sputtering	600	45.9	-	3.1 x 10^{-6} @ -1 V	[50]
ALD	300	36	-	10 @ 5 V	[51]

To this point, most of the reports suggested that an orthorhombic HTO phase could be obtained upon annealing at 700 °C or higher. Furthermore, the reported dielectric constant was obtained between 15.04 – 50 and the lowest current density obtained was 10^{-6} A/cm^2 at 1 V deposited by sputtering technique. In this chapter and for the first time, HTO thin films will be deposited by a solution processed technique and its properties as gate dielectric for ZnO-based TFTs will also be investigated.

The properties of $Hf_{1-x}Ti_xO_y$ films such as optical, structural, surface, dielectric and electrical properties of $Hf_{1-x}Ti_xO_y$ films are studied as well as their implementation as gate dielectrics in ZnO – based TFTs.

5.2 Precursors

Hafnium (IV) chloride ($HfCl_4$, 99.9%), titanium (IV) chloride ($TiCl_4$,) and zinc acetate dilhydrate ($Zn(O_2C_2H_3)2.\ 2H_2O$, 99.9%) precursors were purchased from Alfa Aesar and used without any further purification. The hafnium titanate solutions were prepared from the mixture of the blends of the hafnium chloride in 2,4 pentanedione and methanol (1:2) and titanium chloride in absolute ethanol at a total concentration of 0.1 M. The atomic ratio of the hafnium (Hf) to titanium (Ti) was controlled by simple blending of the amount of each of the precursor's solution.

Finally, the zinc oxide solution was prepared by dissolving zinc acetate dilhydrate ($Zn(O_2C_2H_3)2.\ 2H_2O$, 99.9%) in methanol at a concentration of 0.1 M [29].

5.2.1 Thermal Properties of Precursors

The thermogravimetric analysis (TGA) and differential scanning calorimetry (DSC) measurements of the precursors were investigated to determine their decomposition profiles. The measurements were taken under N_2 atmosphere at a constant heating rate of 10 K/min in the temperature range between 40 – 700 °C, by employing a simultaneous thermal analyser NRTZSCH STA 449 F3 Jupiter® equipment.

Figure 5-3 and Figure 5-4 illustrate the TGA and DSC measurements of hafnium (IV) chloride and titanium (IV) chloride respectively.

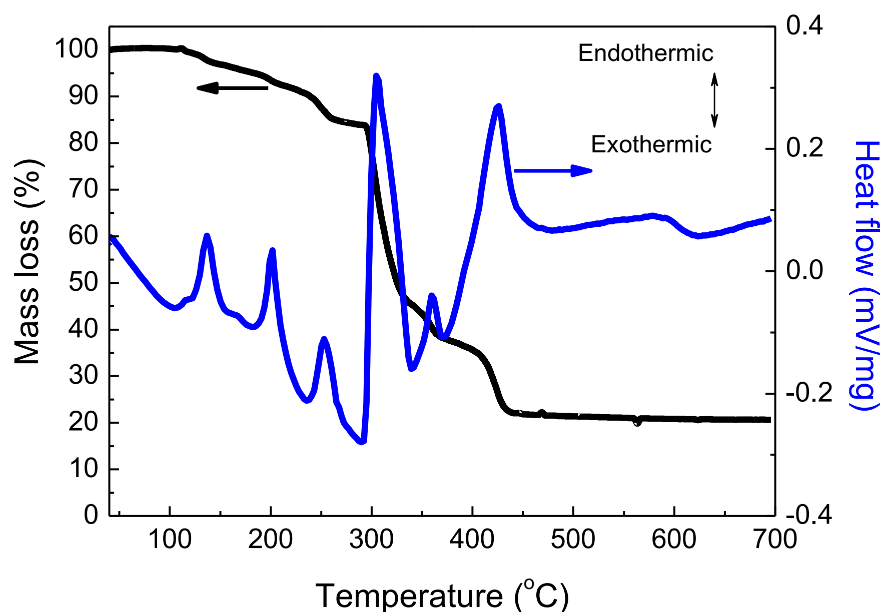

Figure 5- 3. TGA (black line) DSC (blue line) of 19 mg hafnium chloride powder.

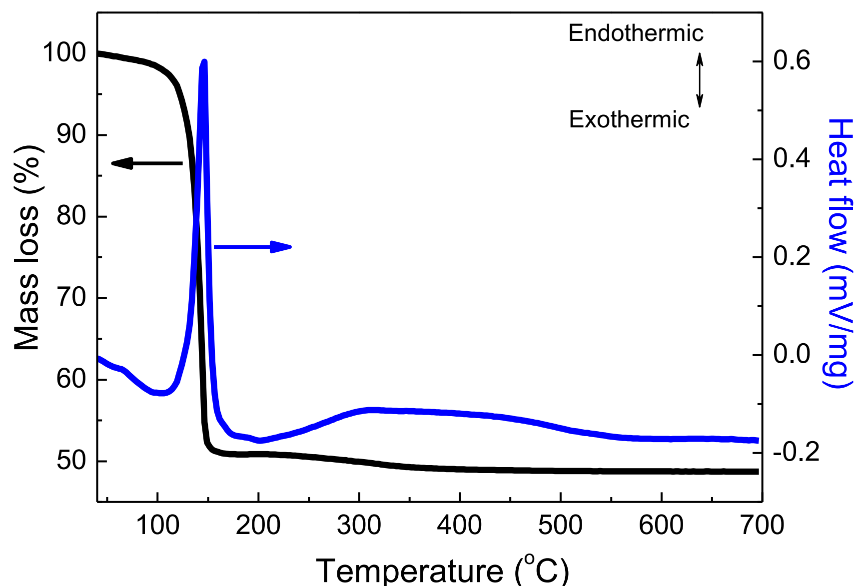

Figure 5- 4. TGA (black line) and DSC (blue line) of 84 mg titanium chloride liquid.

As shown in Figure 5-3, there was a progressive mass loss of about 16 % from 100 – 270 °C which can be related to loss of water molecules absorbed from the atmosphere and beginning of sublimation of $HfCl_4$ powder. The three sharp peaks of the DSC were the corresponding endothermic reactions for the mass loss observed between 100 – 270 °C. From 272 – 390 °C the sublimation reaches its maximum at an endothermic peak of 304 °C while some chloride matrixes are decomposed. Finally, after 450 °C, the complete decomposition of the precursor occurs leading to the formation of a monoclinic HfO_2 films as the final product. These findings were in agreement with the ones reported by Barraud et al.[55],for partially hydrated $HfCl_4$ precursor.

Similarly, the TGA shown in Figure 5-4, shows a pronounced mass loss of about 48 % that was related to the decomposition of the precursor leaving behind Ti or TiN cation as the final product as evidenced by the strong endothermic peak centred about 145 °C.

5.3 Thin Film Deposition & Characterization

The solutions of Hafnium (IV) chloride ($HfCl_4$) in 2,4 pentanedione and methanol (1:2) and Titanium (IV) chloride ($TiCl_4$) in ethanol were spray coated at 500 °C on different substrates using a pneumatic airbrush, held at a vertical distance of about 30 cm. The hafnium-titanate films were deposited by blending $HfCl_4$ and $TiCl_4$ solutions so that the desired [Ti] to [Hf] ratio in the solution could be obtained. Aerosols of the precursor's blends were spray coated for 10 s spray and interrupted for another 50 s to allow the vapours to settle onto the sample. The cycle was repeated until films of typical thickness between 60 - 80 nm were obtained.

For the characterization, the optical properties of the as-deposited $Hf_{1-x}Ti_xO_y$ films on fused silica were studied by the UV-Vis spectroscopy. Fourier transform infrared spectroscopy (FTIR) measurements on potassium bromide (KBr) were studied to investigate the chemical bonding between the metal and the oxide. The structural and morphological properties on silicon were investigated by grazing incidence x-ray diffraction (GIXRD) and atomic force microscopy (AFM) respectively. Furthermore, metal-insulator-metal (MIM) devices were fabricated by employing Al metal contacts that were thermally evaporated under high vacuum (10^{-6} mbar) through a shadow mask onto the glass/ITO/$Hf_{1-x}Ti_xO_y$ stacks (Figure 5-5). Finally, the dielectric and electrical properties on MIMs were studied by impedance spectroscopy and I – V measurements respectively while the performance of the TFTs were characterized by the field effect measurements.

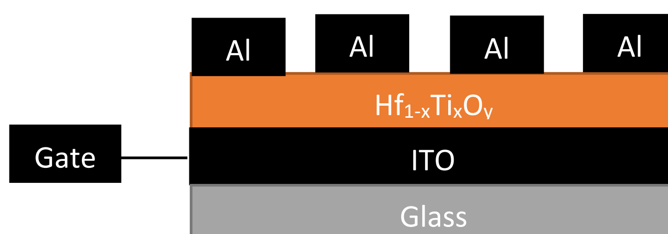

Figure 5- 5. A schematic of a metal-insulator-metal (MIM) stack of glass/ITO/ $Hf_{1-x}Ti_xO_y$/Al gate dielectric.

5.4 UV-Vis Spectroscopy

The optical properties of as-deposited $Hf_{1-x}Ti_xO_y$ films were investigated by the UV-Vis spectroscopy measurements in the transmission spectra between 190 and 1000 nm wavelength range. The transmittance (%T) spectra of the as-deposited $Hf_{1-x}Ti_xO_y$ films with different [Ti] to [Hf] ratios are shown in Figure 5-6.

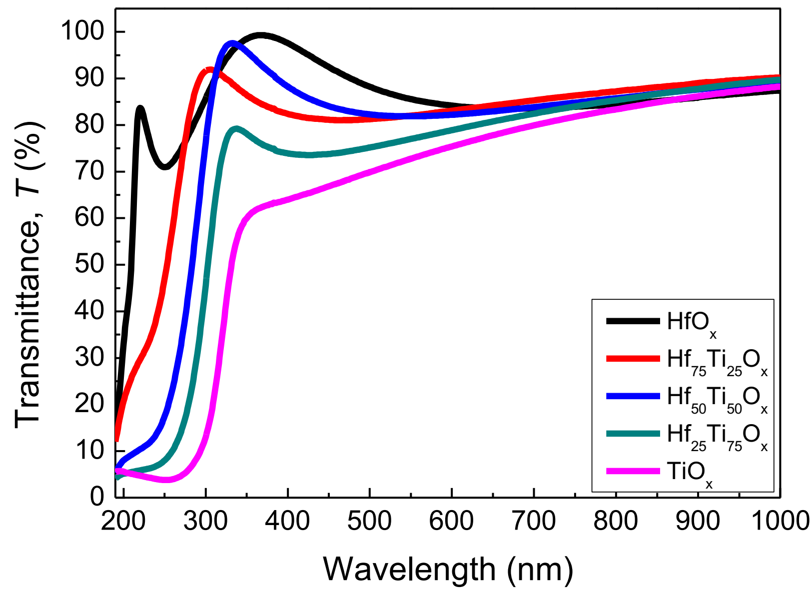

Figure 5- 6. Transmittance %T spectra of as-deposited $Hf_{1-x}Ti_xO_y$ films for different [Ti] to [Hf] ratios.

The average %T in visible region (400 – 700 nm) operates in the range between 70 % and 80 %, indicating high transparent as-deposited $Hf_{1-x}Ti_xO_y$ films. From the Tauc [56] plots, the optical bandgap of as-deposited $Hf_{1-x}Ti_xO_y$ films were calculated as shown in Figure 5-7.

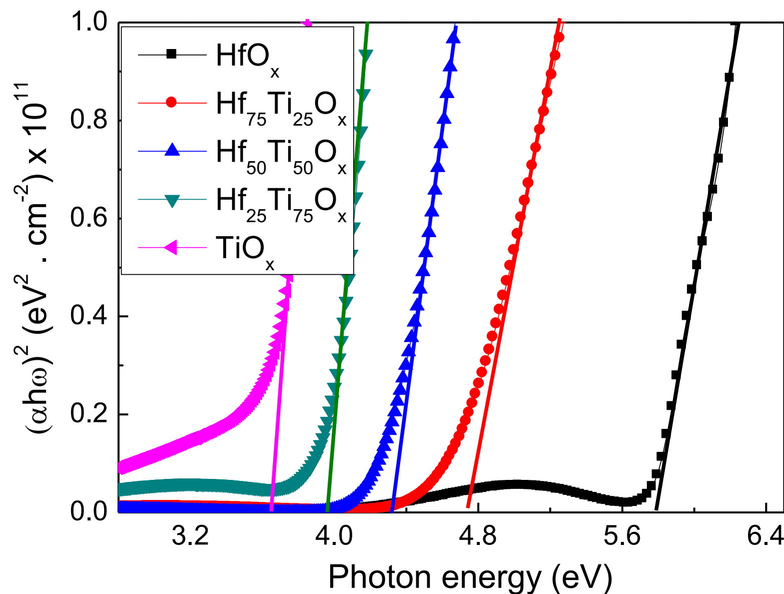

Figure 5- 7. Tauc plots of as-deposited $Hf_{1-x}Ti_xO_y$ films with different [Ti] to [Hf] ratios.

The linear extrapolation along the photon energy axis of Tauc plot shown in Figure 5-7 estimates the optical bandgap of as-deposited $Hf_{1-x}Ti_xO_y$ films with different [Ti] to [Hf]

ratios. The Tauc gaps were further illustrated as a function of [Ti]/ [Ti + Hf] atomic ratio in Figure 5-8.

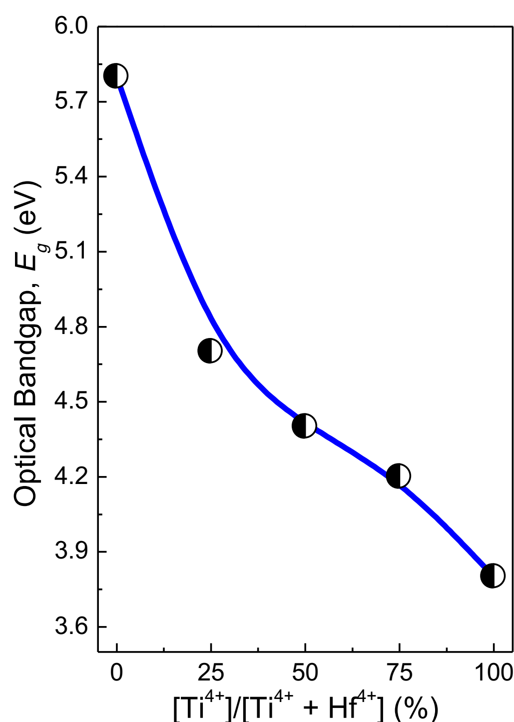

Figure 5- 8. Optical bandgap of as-deposited $Hf_{1-x}Ti_xO_y$ films as a function of the [Ti]/ [Ti + Hf] atomic ratio. The solid line is a guide to the eye.

The optical bandgap varies between 5.8 eV for HfO_x and 3.8 eV for TiO_x with increasing $[Ti^{4+}]/ [Ti^{4+} + Hf^{4+}]$ atomic ratio. Similar trend was observed in our previous study on $Ta_{1-x}Al_xO_y$ films (chapter 4) and such trend was expected for wide bandgap oxides combining with low bandgap ones as already reported by Afouxenidis et al. [57], and Esro et al. [58], for $Ti_{1-x}Al_xO_y$ and $La_{1-x}Al_xO_y$ films respectively.

Furthermore, the Urbach tail energy (E_u) of as-deposited $Hf_{1-x}Ti_xO_y$ films as function of $[Ti^{4+}]/ [Ti^{4+} + Hf^{4+}]$ atomic ratio was investigated to expose material disorder. Generally, E_u characterizes the extent of the absorption edge smearing due to disordering caused by the structural features as well as induced external factors [59]. The structural disordering maybe caused by oxygen vacancies or dislocations while the induced external factors may probably be caused by non-stoichiometry or doping [59]. Figure 5-9 and Figure 5-10 show absorption coefficient spectra of as-deposited $Hf_{1-x}Ti_xO_y$ films with different [Ti] to [Hf] ratios and the calculated E_u values plotted as a function of [Ti] / [Ti + Hf] atomic ratio respectively.

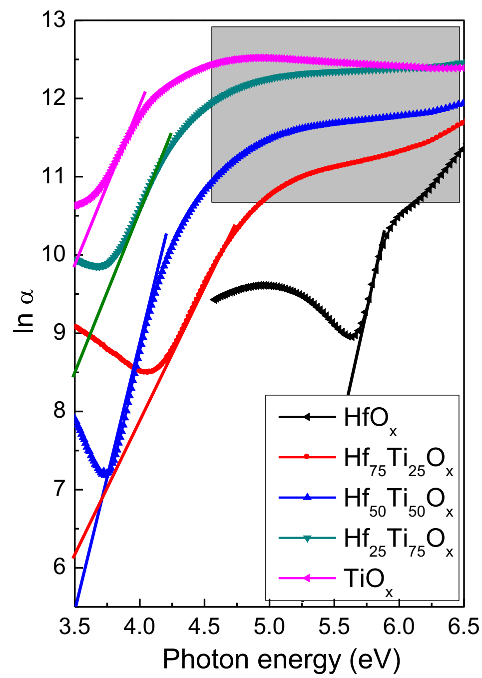

Figure 5- 9. Absorption coefficient spectra of as-deposited $Hf_{1-x}Ti_xO_y$ films with different [Ti] to [Hf] ratios.

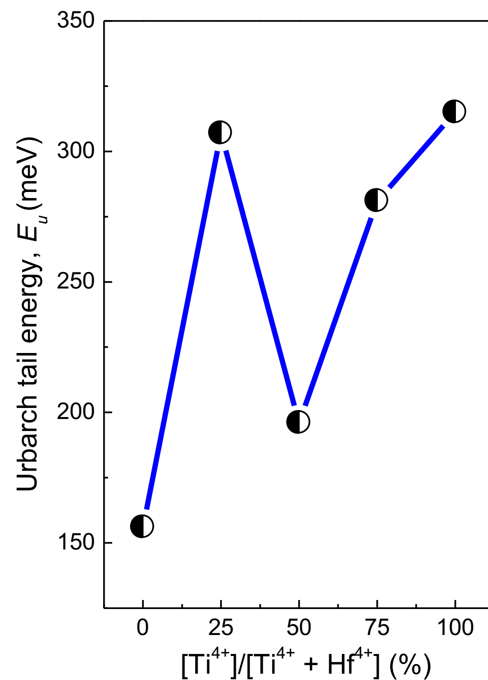

Figure 5- 10. Urbarch tail energy (E_u) of as-deposited $Hf_{1-x}Ti_xO_y$ films as a function of the [Ti]/ [Ti + Hf] atomic ratio. The solid line is a guide to the eye.

In Figure 5-9, the shaded region illustrates the tail of the absorption coefficient edge while fitted lines are the slope that determines the E_u of as-deposited $Hf_{1-x}Ti_xO_y$ films. The calculated E_u values varies between 156 meV for HfO_x and 315 meV for TiO_x as a function of [Ti]/ [Ti + Hf] atomic ratio. The $Hf_{50}Ti_{50}O_y$ films shows an E_u of 199 meV, which is close to the value (250 meV) reported by Mazur et al. [60], for magnetron sputtered hafnium titanate films.

5.5 Fourier Transform Infrared Spectroscopy (FTIR)

Figure 5-11 illustrate the FTIR transmission spectra of as-deposited $Hf_{1-x}Ti_xO_y$ films deposited on KBr substrates with different [Ti] to [Hf] ratios.

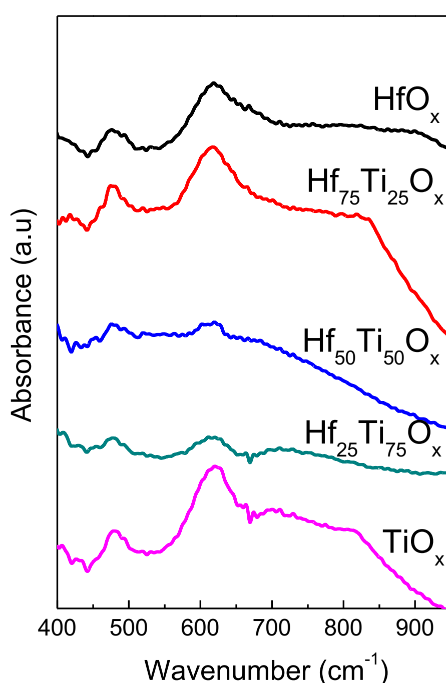

Figure 5- 11. Absorbance spectra of as-deposited $Hf_{1-x}Ti_xO_y$ *films with different [Ti] to [Hf] ratios.*

As shown in Figure 5-11, the absorbance peaks between 400 cm^{-1} and 700 cm^{-1} conforms the characteristics feature of monoclinic HfO_2 and tetragonal TiO_2 films. Contributions to the bands are associated to Hf-O and Ti-O vibrations. Cartier et al. [61], reported that the characteristics peaks of 512 and 635 cm^{-1} are associated to Hf-O vibrations. Arhin et al. [62], also reported the characteristics peaks of Ti-O vibrations lie between 414 and 800 cm^{-1}. Ba-abbad et al. [63], similarly reported that the peaks between 450 and 800 cm^{-1} are due to Ti-O vibrations.

It is safe to say that the characteristic peaks centred at 474 and 615 cm^{-1} are in good agreement with the ones mentioned in the literatures. One can observe that the

stochiometric $Hf_{1-x}Ti_xO_y$ films exhibited a weak absorbance band and may probably be due to poor crystallinity of the films as will be investigated later by the GIXRD.

5.6 Structural and Surface Properties

The atomic structure of the as-deposited $Hf_{1-x}Ti_xO_y$ films were investigated by the grazing incidence x-ray diffraction (GIXRD) while the surface morphologies by the atomic force microscopy (AFM).

5.6.1 Grazing Incidence X-Ray Diffraction (GIXRD)

Figure 5.12 illustrate the GIXRD patterns of as-deposited $Hf_{1-x}Ti_xO_y$ films.

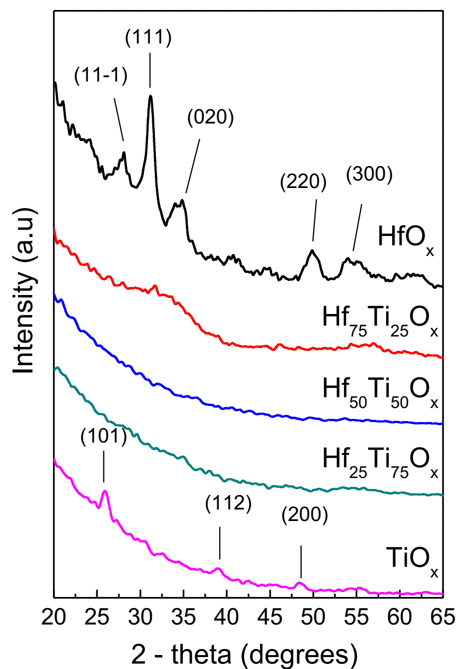

Figure 5- 12. GIXRD patterns of as-deposited $Hf_{1-x}Ti_xO_y$ films deposited by spray pyrolysis on silicon substrates.

From Figure 5-12, one can observe the diffraction peaks for as-deposited HfO_x and TiO_x films. According to the standard XRD pattern database, such peaks confirm the presence of monoclinic phase (ICCD 43 – 1017 and 65 – 1142, space group *P 1 21/c*) HfO_x films and tetragonal phase [ICCD 21 – 1272, space group (*I 41/amd*)] anatase TiO_x films. Further analysis on the diffraction peaks were carried out to determine the average crystallite size ($< d >$) using Debye – Scherrer formula [64].

$$< d > = \frac{K \, . \lambda}{\beta_w \, . \cos\theta} \tag{5.1}$$

Where, (K) is the constant factor, usually taken as 0.9, (λ) is the wavelength of the incident X-rays in nm, (β_w) is the full width at the half maximum of the peak's intensity in radians and (θ) is the Bragg angle in degrees.

For HfO_x films, the analysis on diffraction peak (111) at $\sim$31° yields an average crystallite size of 8.2 nm and lattice parameters a = 5.1156 Å, b = 5.1722 Å, c = 2.2948 Å and beta 99.180°. These parameters are similar to the ones reported by Esro et al. [29], for monoclinic HfO_x films deposited by spray pyrolysis. Similarly for TiO_x, the analysis on diffraction peak (101) at $\sim$25° yields an average crystallite size of 10 nm and lattice parameters a = 3.7534 Å and c = 9.4736 Å, which were close to the values reported by Afouxenidis et al. [57], for $Ti_{1-x}Al_xO_y$ films also deposited by spray pyrolysis.

However, as-deposited $Hf_{1-x}Ti_xO_y$ films showed no diffraction peak indicating amorphous films. The absence of diffraction peaks suggested that the crystallization temperature of HfO_x films increased with addition of Ti content. Triyoso et al. [53], Jin et al. [49], Popovici et al. [51], and Zhang et al. [54], all reported that as-deposited hafnium titanate films were amorphous. Such amorphous phase may probably be connected to the weak absorbance peak observed in the FTIR (Figure 5-11). Amorphous $Hf_{1-x}Ti_xO_y$ films are preferable for TFTs integration compared to crystalline ones because it prevents flow of electron within the gate dielectric thus reduces leakage current.

5.6.2 Atomic Force Microscopy (AFM)

The AFM images of as-deposited $Hf_{1-x}Ti_xO_y$ films on silicon were taken in contact mode and the images presented are the raw images after they have been flattened out as illustrated in Figure 5.13.

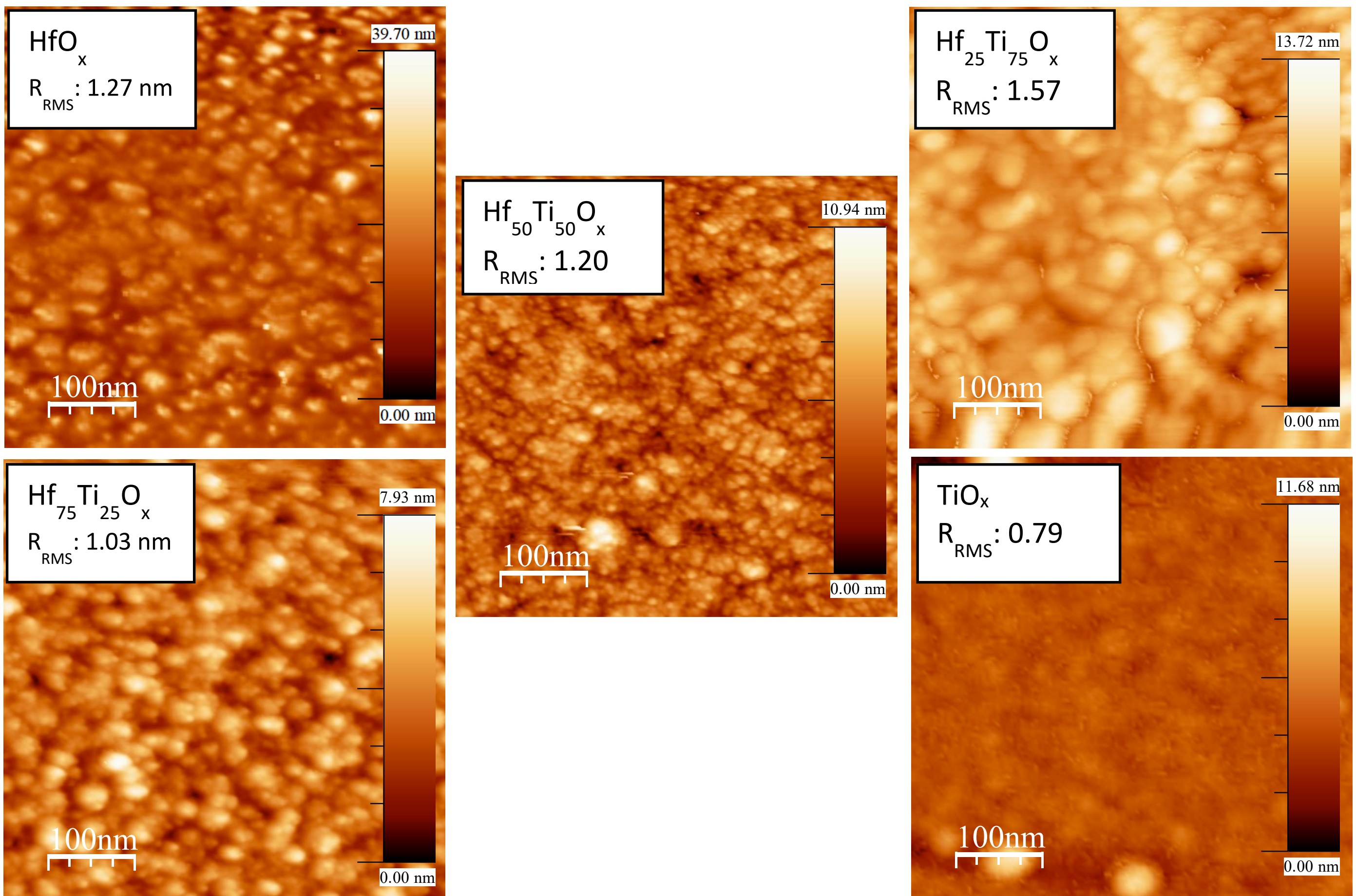

Figure 5- 13. AFM topography images (RMS roughness inset) of as-deposited $Hf_{1-x}Ti_xO_y$ with different [Ti] to [Hf] ratios.

From Figure 5-13, the topographical images showed surface roughness of ~1 nm with increasing [Ti] content, which is reasonably good enough for high-performance optoelectronics devices. Interestingly, the $Hf_{50}Ti_{50}O_y$ films shows negligible grain-like structure compared to other samples, which may further explain its amorphous nature as already observed in the GIXRD (Figure 5-12). A possible reason for that may be associated to the crystallinity of as-deposited HfO_x and TiO_x films at moderate temperature (< 500 °C). Since the as-deposited $Hf_{1-x}Ti_xO_y$ films were deposited at same temperature, there may be some existence of nano-crystalline structures in the films that may not be detected by the GIXRD equipment used in this chapter.

5.7 Electrical Properties

The dielectric constant and the leakage current density are the most important parameters of evaluating the performance of $Hf_{1-x}Ti_xO_y$ films as gate dielectric. In this study, the dielectric constant is calculated from the impedance spectroscopy dispersions in the frequency range of 1 kHz – 50 MHz while the leakage current density is from the I – V measurements.

5.7.1 Impedance Spectroscopy

The static dielectric dispersions of the as-deposited $Hf_{1-x}Ti_xO_y$ films are shown in Figure 5-14.

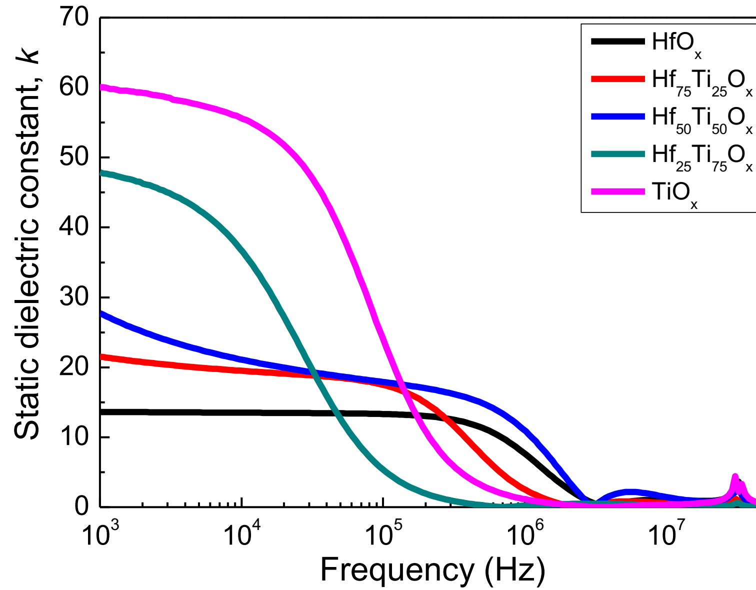

Figure 5- 14. Static dielectric constant dispersions of as-deposited $Hf_{1-x}Ti_xO_y$ films in the frequency range between 1 kHz and 50 MHz.

It can be observed that apart from the HfO_x films, the dispersions of other $Hf_{1-x}Ti_xO_y$ films shows that the dielectric constant values are higher at low frequency side (<10 kHz) than at high frequency side. Zhang et al.[65], explained that such behaviour can be attributed to the dielectric polarization.

In Figure 5-15, the calculated static dielectric constant at 1 kHz is further plotted as a function of [Ti]/ [Ti + Hf] atomic ratio.

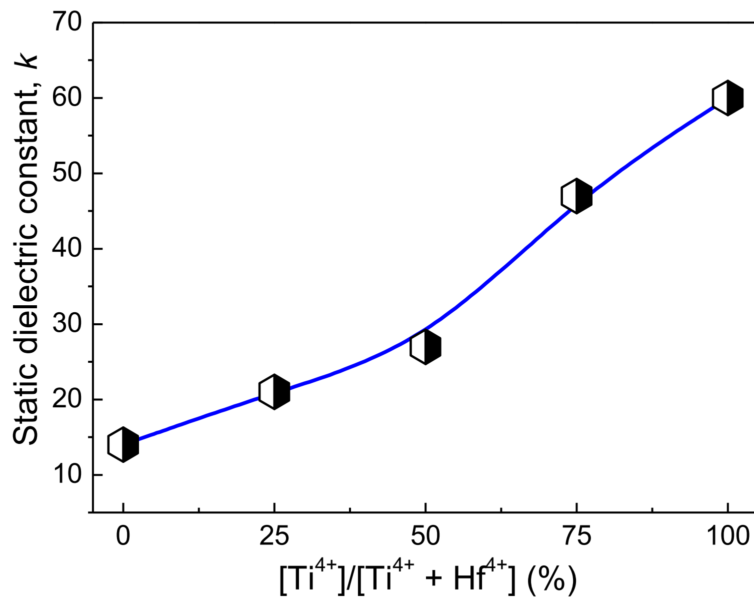

Figure 5- 15. Static dielectric constant of as-deposited $Hf_{1-x}Ti_xO_y$ films as a function of [Ti]/ [Ti + Hf] atomic ratio calculated at 1 kHz. The solid line is a guide to the eye.

With the addition of the Ti content, the static dielectric constant increases linearly as a function of [Ti]/ [Ti + Hf] atomic ratio and varies between 14 and 60. Such trend was consistent with the previous work on $Ta_{1-x}Al_xO_y$ (chapter 4) and other related works [57][58]. It is important to mention that the stochiometric $Hf_{1-x}Ti_xO_y$ films exhibited a static dielectric constant of 30, which agrees with the value 31.3 reported by Wang et al.[48], for sputtered $Hf_{1-x}Ti_xO_y$ films.

The stability of as-deposited $Hf_{1-x}Ti_xO_y$ films were investigated by the Nyquist plots shown in Figure 5-16.

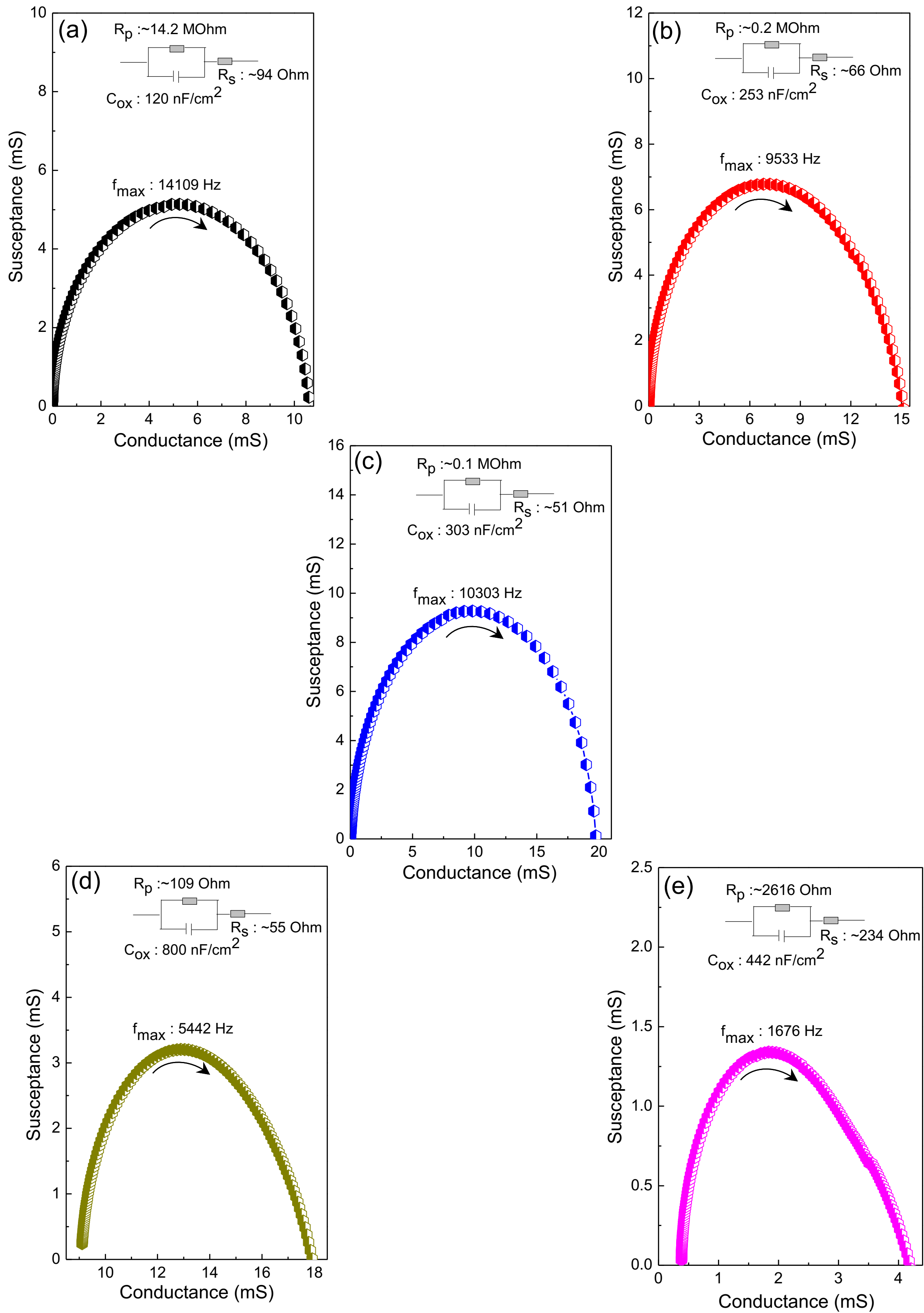

Figure 5- 16. Nyquist plots and equivalent circuit (inset) of as-deposited (a) HfO_x (b) $Hf_{75}Ti_{25}O_x$ (c) $Hf_{50}Ti_{50}O_x$ (d) $Hf_{25}Ti_{75}O_x$ and (e) TiO_x capacitors.

The parabolic behaviour of the Nyquist plots starting from origin describes the stability of the as-deposited films. Here, the stability occurs for Hf rich films ($x \leq 0.5$) and supported by the equivalent circuit exhibiting a large shunt and low series resistance as shown in the inset of Figure 5-16 (a-c). The non-stability in Ti^{4+} ($x > 0.5$) rich MIMs may be probably due to high leakage current which will be investigated by the I – V characterization.

5.7.2 I – V Characterization

The I – V measurements provide insight on the electrical behaviour of the as-deposited $Hf_{1-x}Ti_xO_y$ films under applied field. In Figure 5-17, the leakage current density (J) (at 1 MV/cm) as a function of [Ti]/ [Ti + Hf] atomic ratio is shown.

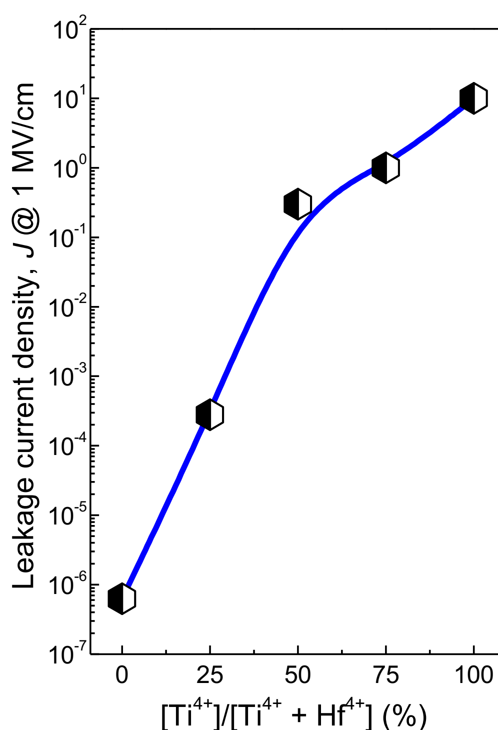

Figure 5- 17. Leakage current density (J) of as-deposited $Hf_{1-x}Ti_xO_y$ films at 1 MV/cm as a function of [Ti]/ [Ti + Hf] atomic ratio. The solid line is a guide to the eye.

As seen in Figure 5-17, the leakage current shows a drastic increase from $\sim 10^{-7}$ A/cm^2 for HfO_x to 10 A/cm^2 for TiO_x with increasing [Ti]/ [Ti + Hf] atomic ratio. Such increase was expected due to the increased Ti content that exhibited poor insulating properties. As evidently confirmed by the bandgap plot shown in Figure 5-8, $Hf_{1-x}Ti_xO_y$ films exhibited a lower bandgap than HfO_x, which can result to a reduced barrier height for electron injection into the oxide bands, resulting to an increase in the leakage current density.

Further investigation on the current conduction in $Hf_{1-x}Ti_xO_y$ films were investigated by Schottky emission (SE), Fowler-Nordheim (FN) and Poole-Frenkel (PF) conduction mechanism [66]. In Figure 5-18 – Figure 5-20, the SE, FN & PF conduction mechanism plots of as-deposited $Hf_{1-x}Ti_xO_y$ films are shown respectively.

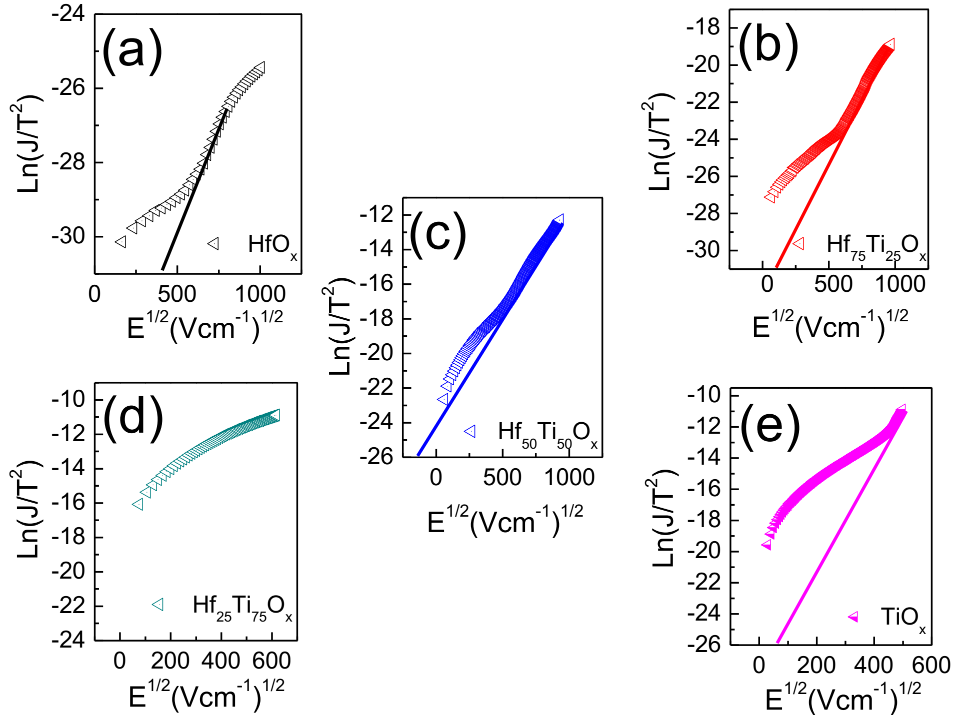

Figure 5- 18. Schottky emission plots of (a) HfO_x (b) $Hf_{75}Ti_{25}O_x$ (c) $Hf_{50}Ti_{50}O_x$ (d) $Hf_{25}Ti_{75}O_x$ and (e) TiO_x films.

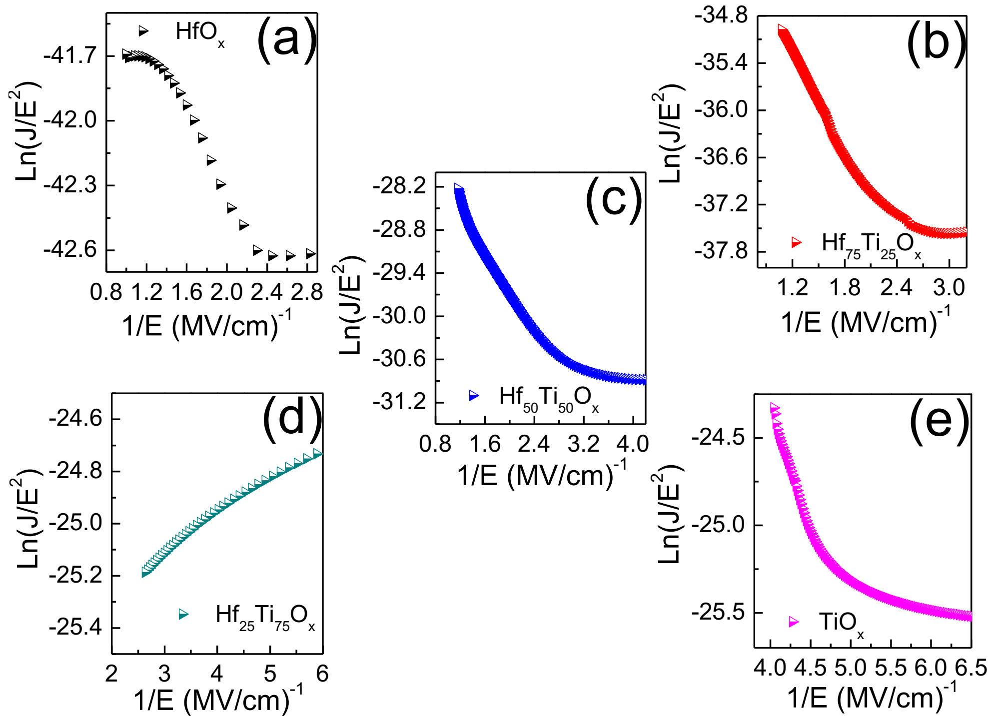

Figure 5- 19. Fowler-Nordheim plots of (a) HfO_x (b) $Hf_{75}Ti_{25}O_x$ (c) $Hf_{50}Ti_{50}O_x$ (d) $Hf_{25}Ti_{75}O_x$ and (e) TiO_x films.

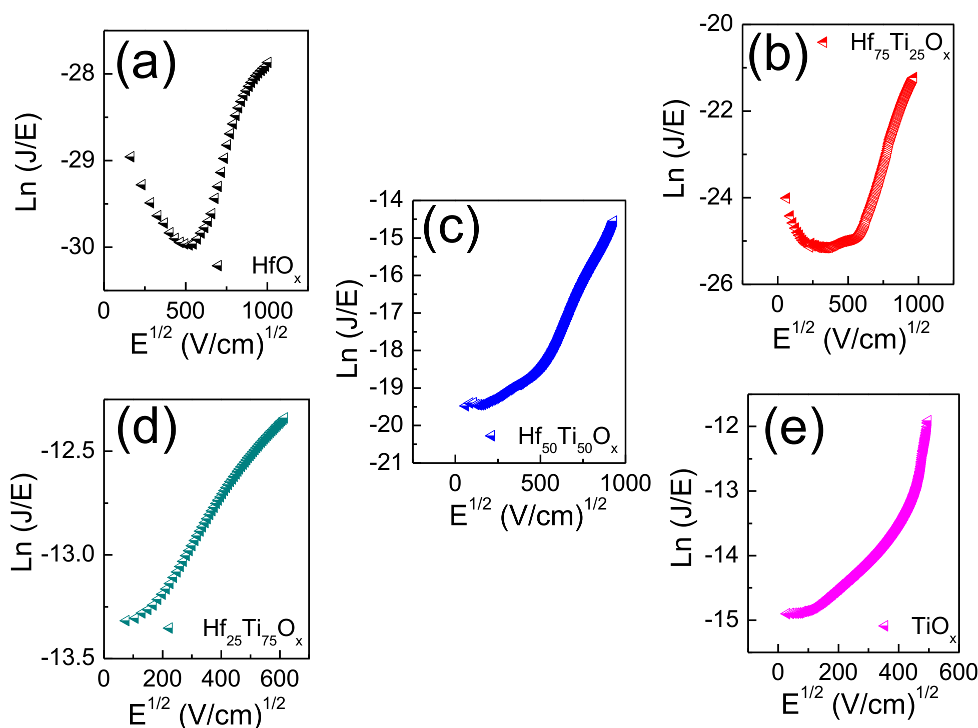

Figure 5- 20. Poole-Frenkel plots of (a) HfO_x (b) $Hf_{75}Ti_{25}O_x$ (c) $Hf_{50}Ti_{50}O_x$ (d) $Hf_{25}Ti_{75}O_x$ and (e) TiO_x films.

In the SE plots shown in Figure 5-18, only $Hf_{25}Ti_{75}O_y$ films exhibited a non-linear behaviour over wide range of $E^{1/2}$ and could therefore not be considered as dominant conduction mechanism that governs the current transport in the oxide. Similarly, in the FN plots shown in Figure 5-19, the linearity occurs for HfO_x and $Hf_{75}Ti_{25}O_y$ films, indicating not dominant conduction mechanism for other $Hf_{1-x}Ti_xO_y$ films. Finally, the PF plots shown in Figure 5-20 shows linearity over wide range of $E^{1/2}$ and therefore could be considered as dominant conduction mechanism for all $Hf_{1-x}Ti_xO_y$ films. This means that there are trapped electrons at the bulk of $Hf_{1-x}Ti_xO_y$ films, thus explains the leakage current in the films. Zhang et al.[54], reported that PF mechanism dominates electron transport in $Hf_{1-x}Ti_xO_y$ films deposited by CVD. Their investigations suggested that PF mechanism is dominant in $Hf_{1-x}Ti_xO_y$ films when the voltages are larger than 0.5 V. it can be concluded that PF mechanism is the dominant conduction mechanism in $Hf_{1-x}Ti_xO_y$ films because all samples were characterized at high electric fields and exhibited linearity at high electric field.

5.7.3 Field Effect Measurement

To investigate the applicability of as-deposited $Hf_{1-x}Ti_xO_y$ as gate dielectric, ZnO – based TFTs were investigated by employing the bottom-gate top-contact (BG – TC) TFT architecture as illustrated in Figure 5-21.

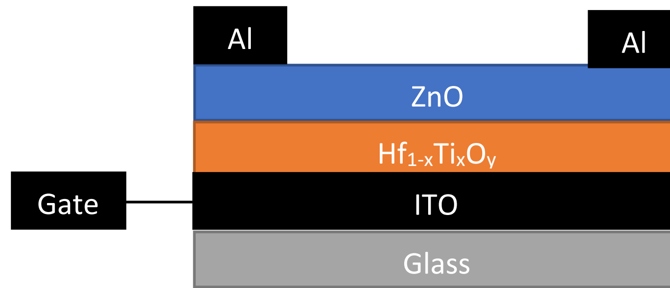

Figure 5- 21. BG – TC ZnO-based TFT architecture employing $Hf_{1-x}Ti_xO_y$ gate dielectric.

Figure 5-22 and Figure 5-23 show a representative set of transfer and output characteristics obtained from ZnO TFT (L = 20 um, W = 1000 um) based on a ~80 nm thick $Hf_{1-x}Ti_xO_y$ gate dielectrics.

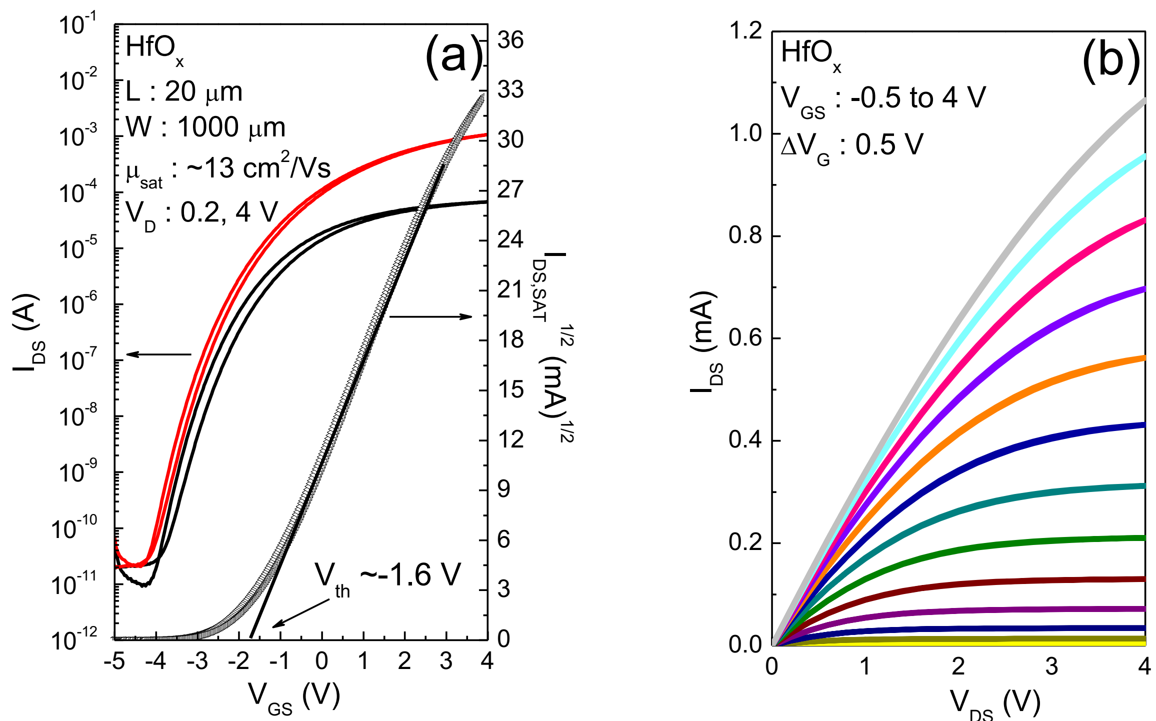

Figure 5- 22. (a) Transfer and (b) output characteristics of ZnO – based TFTs employing as-deposited HfO_x gate dielectric.

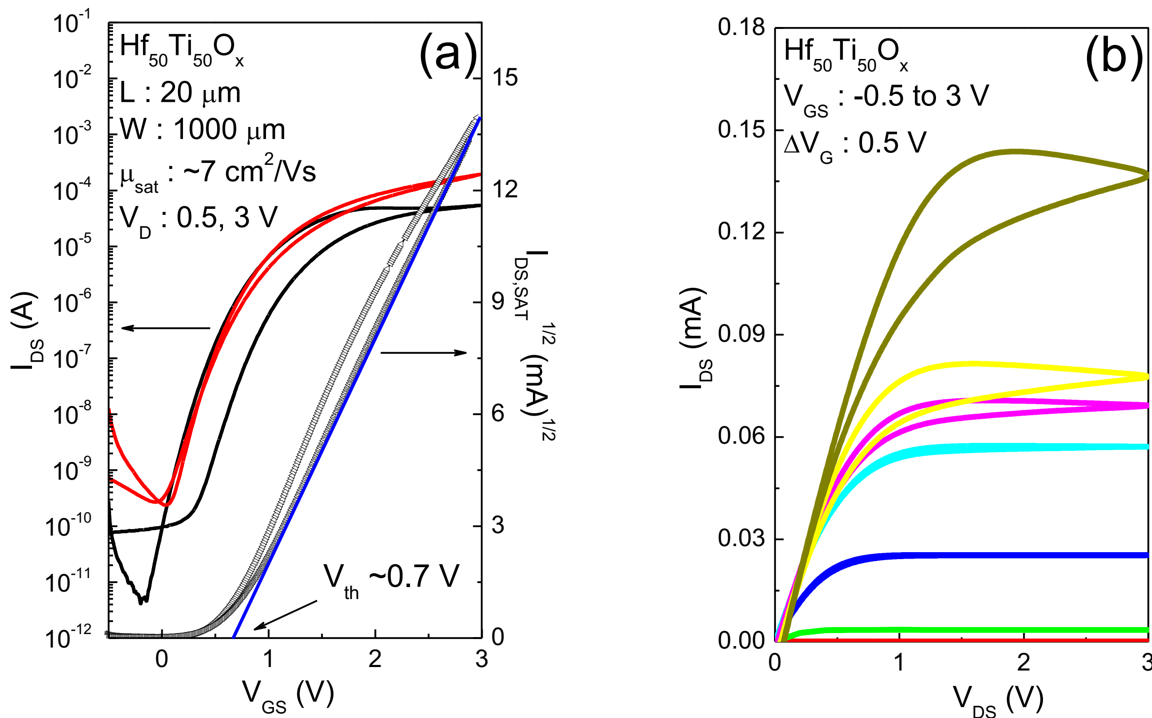

Figure 5- 23. (a) Transfer and (b) output characteristics of ZnO – based TFTs employing as-deposited stoichiometric $Hf_{1-x}Ti_xO_y$ gate dielectric.

As shown in Figure 5-22(a) and (b), ZnO – based TFT employing as-deposited HfO_x gate dielectrics exhibited excellent characteristics such as low voltage operation (4 V), high current modulation ratio ($I_{on/off} \sim 10^6$), threshold voltage ($V_{th} \sim$ -1.6 V) negligible hysteresis and high electron mobility (μ_{sat}) of ~13 cm^2/Vs. Additionally, the subthreshold swing (SS) and interface trap density (D_{it}) values were calculated from the transfer curve and found to be ~0.29 V/dec and ~2.9 x 10^{12} cm^{-2} respectively.

Similarly, the ZnO – based TFT employing as-deposited $Hf_{50}Ti_{50}O_x$ gate dielectrics shown in Figure 5-23(a) and (b) also showed promising characteristics such as low voltage operation (3 V), $I_{on/off}$ ~10^7, V_{th} ~0.6 V and electron mobility of ~7 cm^2/Vs. The SS and D_{it} values were calculated as ~0.17 V/dec and ~2.1 x 10^{12} cm^{-2} respectively.

Comparing the above, one can observe the increase in $I_{on/off}$ by an order of magnitude (~10^6 for HfO_x to ~10^7 for stochiometric $Hf_{1-x}Ti_xO_y$ gate dielectric). Additionally, there was a decrease in the SS, D_{it} and μ_{sat} values which reduces from 0.29 V/dec, 2.9 x 10^{12} cm^{-2} and ~13 cm^2/Vs for HfO_x to 0.17 V/dec, 2.1 x 10^{12} cm^{-2} and ~7 cm^2/Vs for $Hf_{50}Ti_{50}O_x$ gate dielectric respectively. The decrease in the SS and D_{it} values demonstrate improvement in the switching characteristics and level of density traps in the TFT device respectively while deteriorating its performance in terms of μ_{sat}. The deterioration of the μ_{sat} may be hindered by the gate leakage current of $Hf_{50}Ti_{50}O_x$ gate dielectrics as evidently seen by its large hysteresis characteristics shown in Figure 5-23(a) and (b).

To our knowledge, this was the first successful TFT employing $Hf_{50}Ti_{50}O_x$ gate dielectric, and it has shown promising performance for future application. Unfortunately,

there was no working device on other TFTs employing different compositions of $Hf_{1-x}Ti_xO_y$ gate dielectric especially TiO_x dielectric. The latter was expected due to influence of negative band offsets between TiO_x and ZnO that plays crucial role in the performance of the TFTs [57]. In Figure 5-24, the energy band diagram of ZnO, HfO_2, $Hf_{50}Ti_{50}O_x$ and TiO_2 as well as their estimated conduction and valence band offsets on ZnO is illustrated.

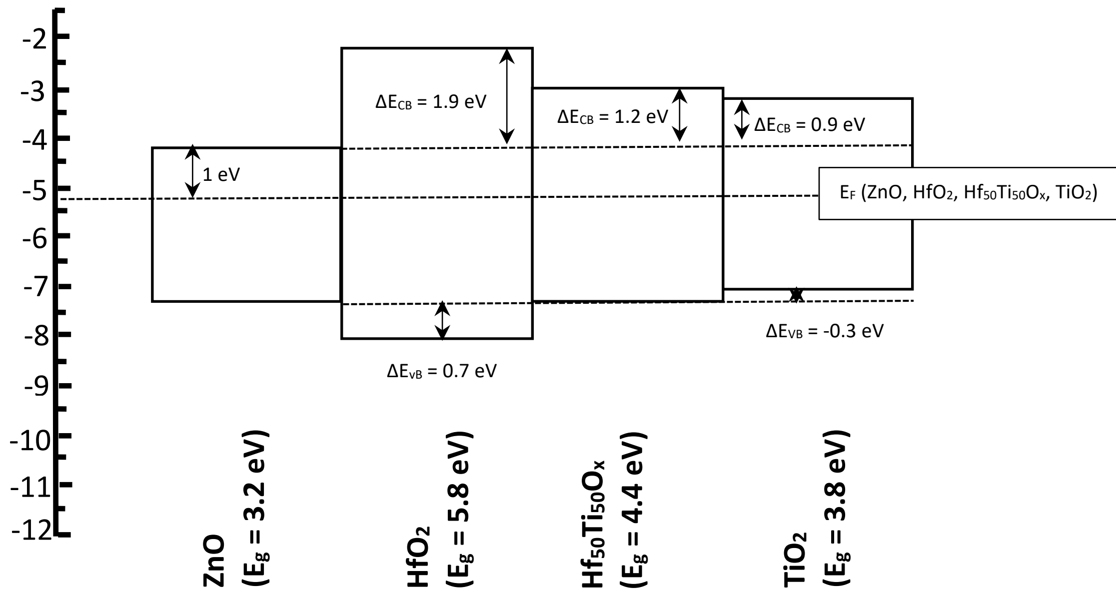

Figure 5- 24. Band diagrams of ZnO, HfO_2, $Hf_{50}Ti_{50}O_x$ and TiO_2 and estimated conduction and valence band offsets on ZnO.

The conduction band minimum (E_{CB}) of ZnO was taken as the electron affinity (χ_e) of ZnO (4.2 eV) [67] while the work function i.e., the position of the Fermi energy level (E_F) has been previously estimated to be 5.2 eV according to Zhang et al.[68], and Zheng et al.[69],. Similarly, the conduction band minimum (E_{CB}) and the valence band maximum (E_{VB}) of the other oxides were estimated based on their calculated energy bandgaps. The calculated bandgap of HfO_2, $Hf_{50}Ti_{50}O_x$ and TiO_x were 5.8, 4.4 and 3.8 eV respectively. The band alignment diagram was constructed with the assumption that the position of the Fermi energy level of the oxides are positioned in the middle of their calculated bandgaps and on same level with that of the ZnO. As seen in the band diagram, the calculated conduction band offsets (ΔE_{CB}) of HfO_2, stoichiometric $Hf_{50}Ti_{50}O_x$ and TiO_2 were 1.9, 1.2 and 0.9 eV respectively. These findings evidently suggests that TiO_2 does not satisfy the band offsets criterion.

5.8 Conclusion

To summarise on the properties of as-deposited $Hf_{1-x}Ti_xO_y$ films with different [Ti] to [Hf] ratios, The optical bandgap decreased from 5.8 – 3.8 eV with increasing $[Ti^{4+}]/[Ti^{4+} + Hf^{4+}]$ atomic ratio. Such decrease was attributed to the low bandgap of TiO_x films. Furthermore, the E_u varies between 156 and 315 meV with increasing $[Ti^{4+}]/[Ti^{4+} + Hf^{4+}]$ atomic ratio.

The structure of as-deposited $Hf_{1-x}Ti_xO_y$ films were found to be amorphous except for the HfO_x and TiO_x that are naturally crystalline at moderate temperatures. HfO_x films exhibited a monoclinic phase while TiO_x exhibited a tetragonal anatase phase as confirmed by the GIXRD. Its AFM images showed RMS of about 1 nm which demonstrated smooth films.

The static dielectric constant of as-deposited $Hf_{1-x}Ti_xO_y$ films was calculated at 1 kHz and varies between 14 and 60 with increasing Ti content. The leakage current density recorded at 1 MV/cm also varies between 10^7 and 10 A/cm^2. Such high leakages were further investigated by the SE, FN and PF conduction mechanism and it was observed that the PF mechanism dominates the charge transport in $Hf_{1-x}Ti_xO_y$ films.

Particularly, the stoichiometric $Hf_{1-x}Ti_xO_y$ films exhibited promising properties such as optical bandgap of 4.4 eV, Urbach energy of 173 meV, amorphous phase, RMS of 1.2 nm, static dielectric constant of 30 and leakage current density of 0.3 A/cm^2 at 1 MV/cm.

Finally, the performance of ZnO–based TFTs employing stochiometric $Hf_{1-x}Ti_xO_y$ gate dielectric showed promising characteristics such as low voltage operation (3 V), $I_{on/off}$ ~10^7, V_{th} ~0.6 V, SS~0.17 V/dec, D_{it}~2.1 x 10^{12} cm^{-2} and μ_{sat} of ~7 cm^2/Vs.

5.9 Effects of Post-deposition Annealing of $Hf_{1-x}Ti_xO_y$ Films

The as-deposited $Hf_{1-x}Ti_xO_y$ thin films were further annealed at 800 °C for 30 minutes in air. In this study, focus was given to the composites of $Hf_{1-x}Ti_xO_y$ thin films since both as-deposited HfO_x and TiO_x exhibit crystalline phase at substrate temperature of 500 °C.

5.10 UV-Vis Spectroscopy

In Figure 5-26, the Tauc plots of $Hf_{1-x}Ti_xO_y$ films is shown after annealing at 800 °C for 30 mins in air.

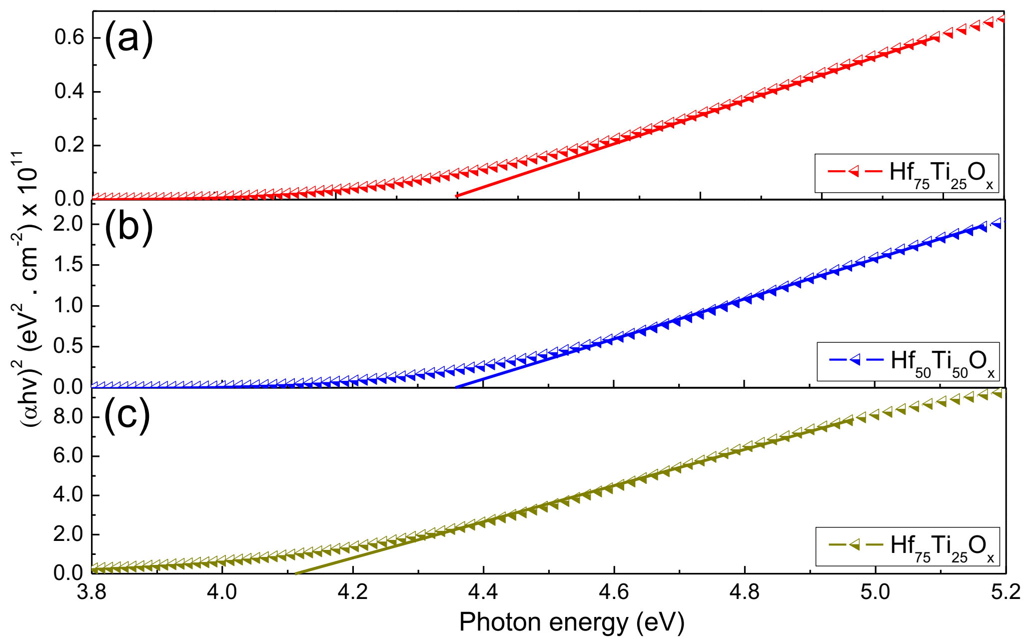

Figure 5- 25. Tauc plots of $Hf_{1-x}Ti_xO_y$ films with different [Ti] to [Hf] ratios after annealing at 800 °C for 30 mins in air.

The optical bandgap of the annealed $Hf_{1-x}Ti_xO_y$ films as a function of [Ti]/ [Ti + Hf] atomic ratio is illustrated in Figure 5-26.

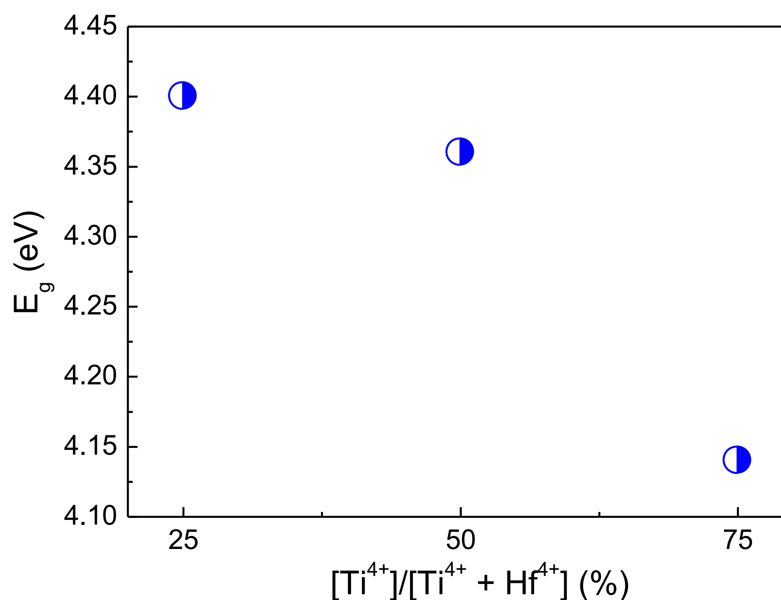

Figure 5- 26. Optical bandgap of $Hf_{1-x}Ti_xO_y$ films as a function of the [Ti]/ [Ti +Hf] atomic ratio after annealing at 800 °C for 30 mins in air.

The E_g appears to be decreasing with increasing [Ti]/ [Ti + Hf] atomic ratio. The E_g of the annealed $Hf_{1-x}Ti_xO_y$ films decreases from 4.4 eV for $Hf_{75}Ti_{25}O_y$ to 4.1 eV for $Hf_{25}Ti_{75}O_x$ films. These values were slightly lower than the ones previously obtained for as-deposited $Hf_{1-x}Ti_xO_y$ films, which can be attributed to effect of the annealing conditions. One possible reason for such decrease may probably be related to the phase transformation of the films i.e., from amorphous to crystalline phase as will be later be investigated by the GIXRD characterization.

Figure 5-27 illustrate the calculated Urbach energy values of annealed $Hf_{1-x}Ti_xO_y$ films as a function of [Ti]/ [Ti + Hf] atomic ratio.

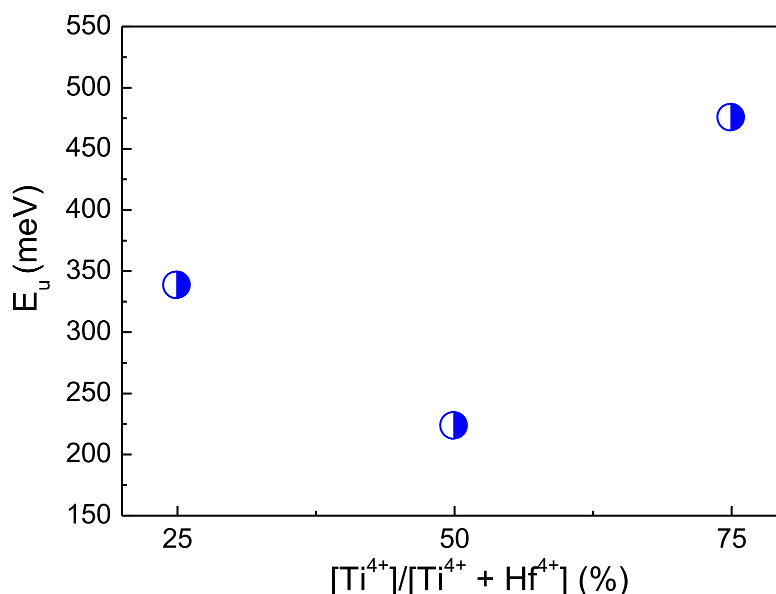

Figure 5- 27. Urbarch tail energy (E_u) of $Hf_{1-x}Ti_xO_y$ films as a function of the [Ti]/ [Ti + Hf] atomic ratio after annealing at 800 °C for 30 mins in air.

The calculated E_u values were found to be 338, 223 and 475 meV for $Hf_{75}Ti_{25}O_y$, $Hf_{50}Ti_{50}O_x$ and $Hf_{25}Ti_{75}O_x$ respectively. In comparison with as-deposited ones previously shown in Figure 5-10, one can observe the slight increase in the degree of disorder in $Hf_{1-x}Ti_xO_y$ films which may probably be due to oxygen vacancies caused by the defect of the TiO_x films. As already known that E_u is associated with degree of disorder in crystalline and amorphous materials [70]. This degree of disorder appears as defects to the materials that induces localized states extended to the bandgap of the material. Defects such as oxygen vacancies and interstitial, change in bond lengths and bond angle between atoms in crystal structure play a significant role in the structure of material.

5.11 Structural and Surface Properties

5.11.1 GIXRD

The GIXRD patterns of annealed $Hf_{1-x}Ti_xO_y$ films is shown in Figure 5-28.

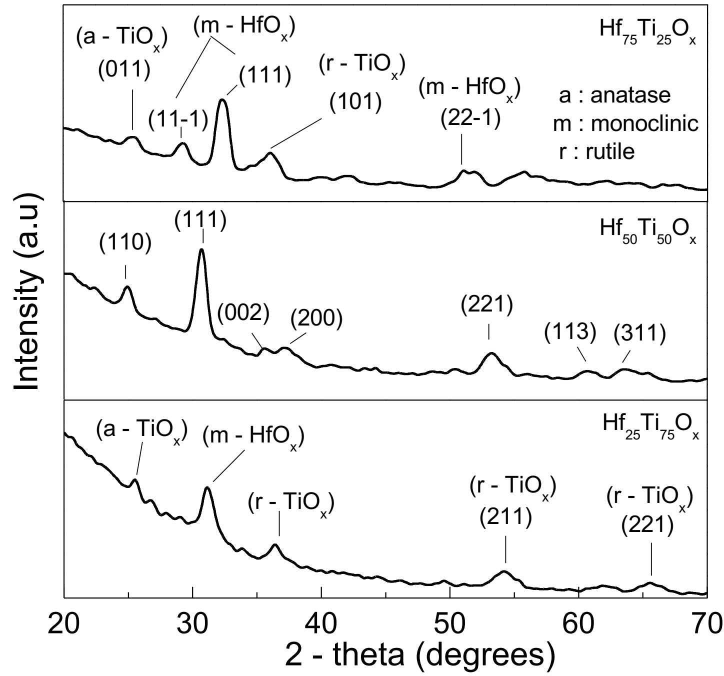

Figure 5- 28. GIXRD patterns of annealed $Hf_{1-x}Ti_xO_y$ films with different [Ti] to [Hf] ratios.

The annealed $Hf_{1-x}Ti_xO_y$ films shows diffraction peaks indicating a transformation of structure from amorphous to crystalline phase. For $Hf_{75}Ti_{25}O_x$ films, the exhibited diffraction peaks were the reflection of both m-HfO_x and a-TiO_x and r-TiO_x films. Based on the existence of both phases, it is safe to say that annealed $Hf_{75}Ti_{25}O_y$ films did not form stochiometric $Hf_{1-x}Ti_xO_y$ films rather, it could be considered as more of m-HfO_x films. Similarly, the diffraction peaks observed for annealed $Hf_{25}Ti_{75}O_x$ films were the reflection of tetragonal TiO_x and m-HfO_x films, thus, does not form stoichiometric $Hf_{1-x}Ti_xO_y$ films. The TiO_x films undergo phase transitions from a-TiO_x to r-TiO_x. Finally, the diffraction peaks observed for annealed $Hf_{50}Ti_{50}O_y$ films, were the reflection of an orthorhombic $Hf_{1-x}Ti_xO_y$ with the space group (*Pbcn*). This observation agrees with the report in literatures. Popovic et al [51], reported a sharp peak of O-$HfTiO_4$ films deposited by ALD after annealing at ~700 °C. Also, Chen et al. [46], reported an O-$HfTiO_4$ films deposited by CVD after annealing between 700 - 1000 °C. Comparing both observations with that of the present study, one can confirm the formation of the stoichiometric $Hf_{1-x}Ti_xO_y$ films. Further analysis on the diffraction peak (111) at ~30.6° yields an average crystallite size of 8.2 nm and the lattice parameters a = 4.82861 Å, b = 5.29627 Å and c = 5.0425 Å. The lattice parameters were calculated by the following Miller indices equation:

$$\frac{1}{d^2} = \frac{h^2}{a^2} + \frac{k^2}{b^2} + \frac{l^2}{c^2} \tag{5.1}$$

Where, h, k and l are the integers denoting the Miller indices, d is the interplanar spacing between the planes of the atoms and a, b and c are the lattice parameters in Å.

5.11.2 AFM

Figure 5-29 show the AFM images of annealed $Hf_{1-x}Ti_xO_y$ films.

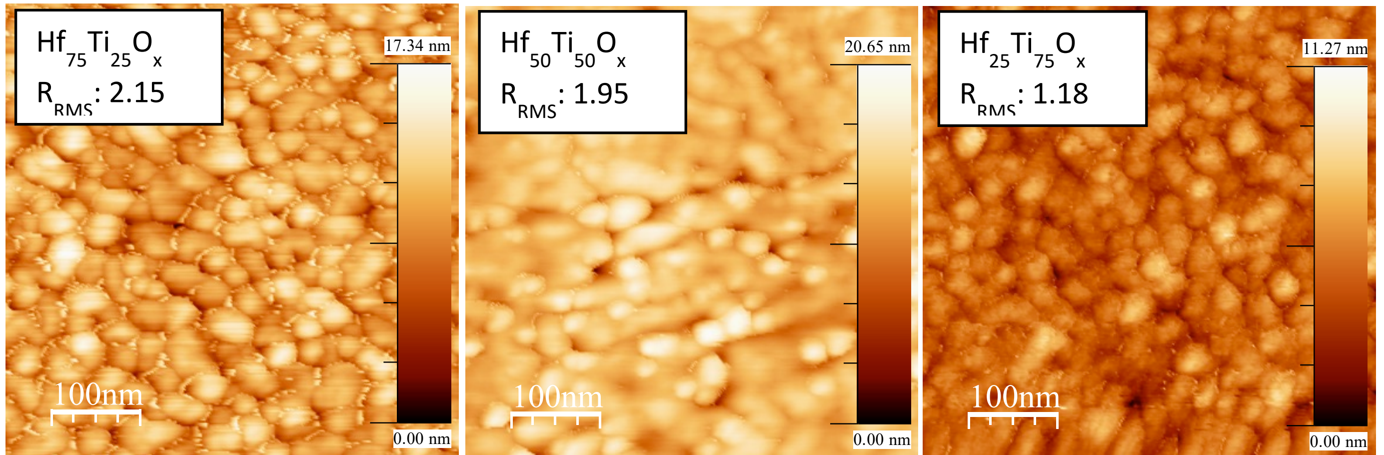

Figure 5- 29. AFM topography images (RMS roughness inset) of $Hf_{1-x}Ti_xO_y$ films with different [Ti] to [Hf] ratios after annealing at 800 °C for 30 mins in air.

The AFM images of annealed $Hf_{1-x}Ti_xO_y$ films shows a pronounced grain-like structures compared to the as-deposited ones. The surface roughness varies between 2.15 nm for $Hf_{75}Ti_{25}O_x$ and 1.18 nm for $Hf_{25}Ti_{75}O_y$, indicating rougher films. Such increase in roughness was due to crystallization or grain growth caused by the effect of annealed $Hf_{1-x}Ti_xO_y$ films. Zhang et al. [71], reported that the surface roughness of hafnium titanate films increases after annealing at 700 °C deposited by CVD.

5.12 Electrical Properties

5.12.1 Impedance spectroscopy

Figure 5-30 show the dielectric constant dispersion of annealed $Hf_{1-x}Ti_xO_y$ films.

.

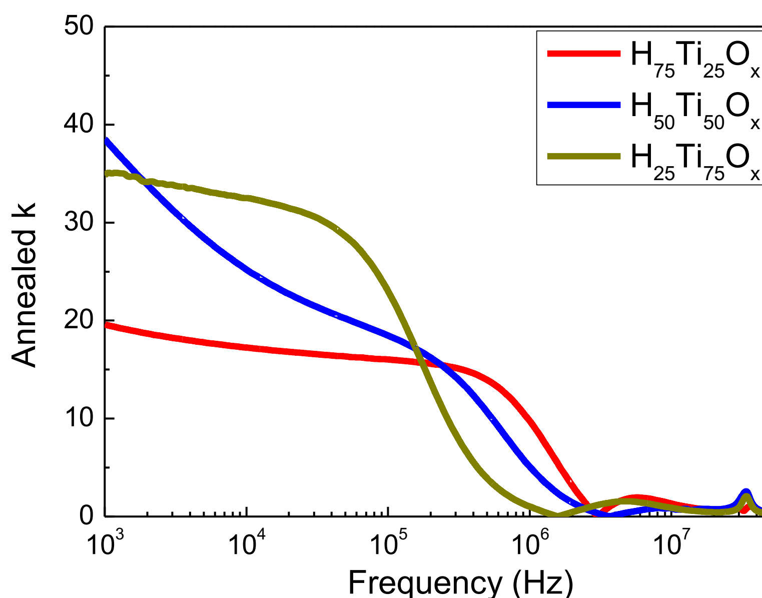

Figure 5- 30. Static dielectric constant dispersions of $Hf_{1-x}Ti_xO_y$ films in the frequency range of 1 kHz – 50 MHz after annealing at 800 °C for 30 mins in air.

The dispersions of annealed $Hf_{1-x}Ti_xO_y$ films over the range of frequencies shows rapid decrease for stochiometric $Hf_{1-x}Ti_xO_y$ films. This may be caused by the crystallization of $Hf_{1-x}Ti_xO_y$ films that further exhibit grain boundaries and creates diffusion pathways for leakage current. In Figure 5-31, the annealed k values estimated at 1 kHz were further plotted as a function of [Ti]/ [Ti + Hf] atomic ratio.

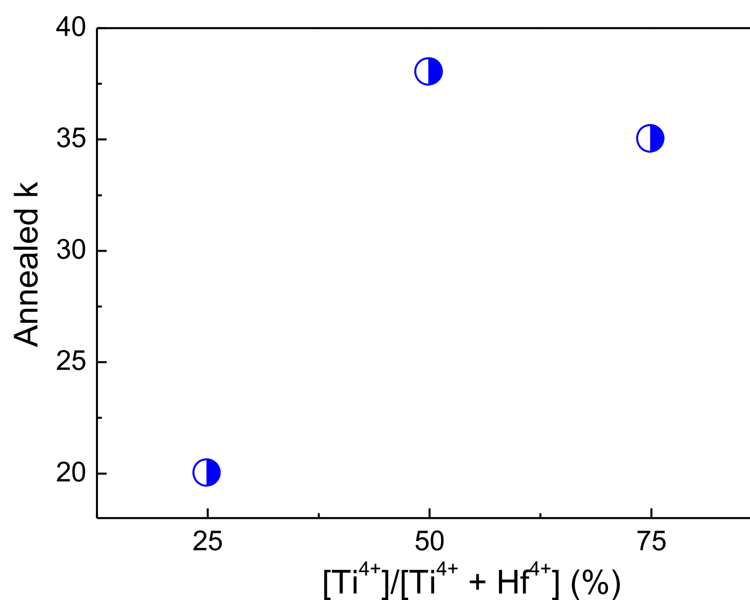

Figure 5- 31. Static dielectric constant of $Hf_{1-x}Ti_xO_y$ films as a function of [Ti]/ [Ti + Hf] atomic ratio after annealing at 800 °C for 30 mins in air.

The stochiometric $Hf_{1-x}Ti_xO_y$ films exhibited the highest dielectric constant value of 38 and is very close to the value 36, reported by Popovici et al. [51], for $Hf_{1-x}Ti_xO_y$ films deposited by ALD and annealed at 500 °C. Furthermore, the stability of annealed $Hf_{1-x}Ti_xO_y$ films were investigated by Nyquist plots as shown in Figure 5-32.

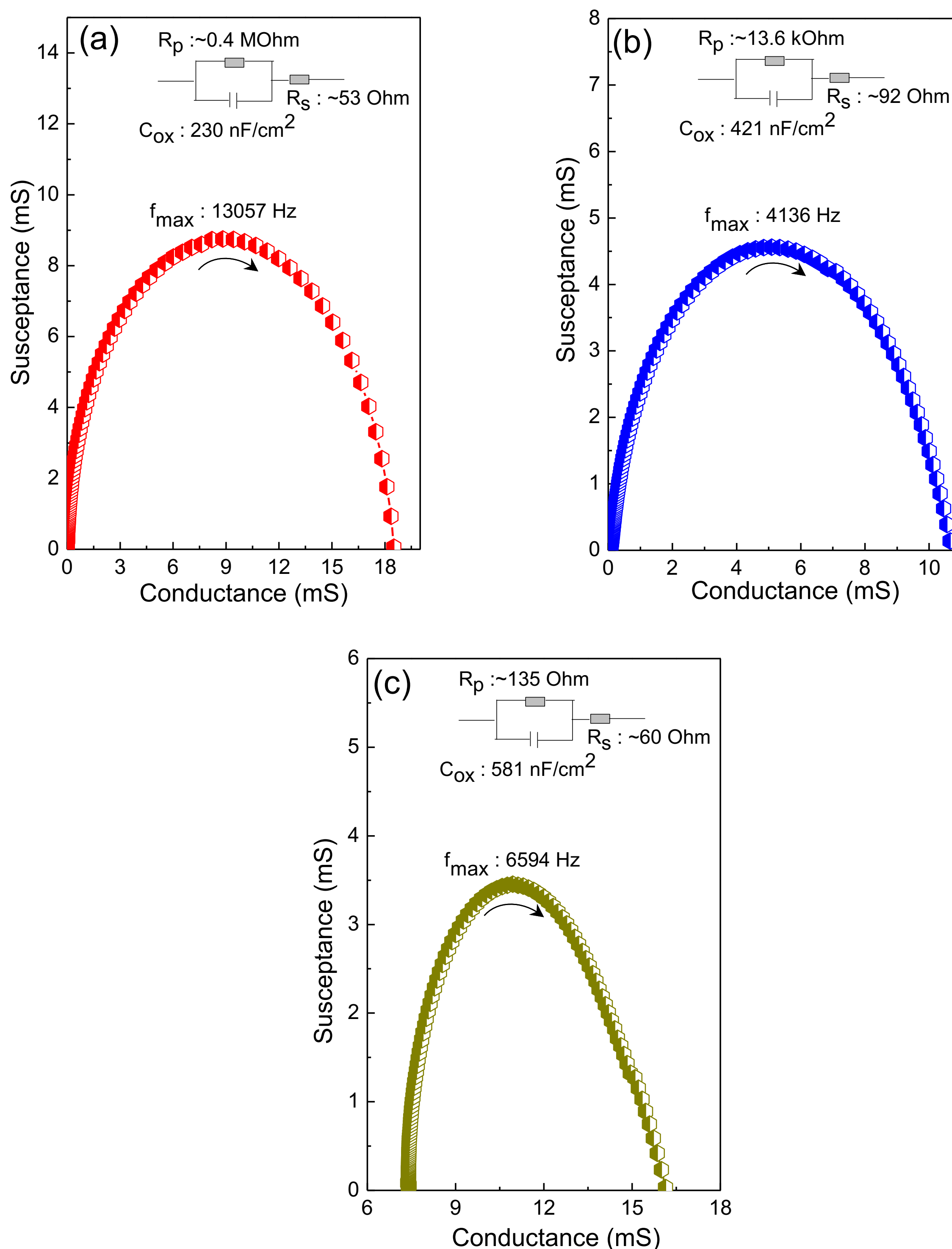

Figure 5- 32. Nyquist plots and equivalent circuit (inset) of annealed (a) $Hf_{75}Ti_{25}O_x$ (b) $Hf_{50}Ti_{50}O_x$ and (c) $Hf_{25}Ti_{75}O_x$ films.

$Hf_{1-x}Ti_xO_y$ films exhibited stability as evidently seen by the parabolic behaviour of the plots starting from the origin. However, the sample with $Hf_{25}Ti_{75}O_y$ films, despite exhibiting parabolic behaviour, however, did not start from the origin and thus not a stable system. Additionally, the equivalent circuit shown in the inset of the sample shows poor capacitive properties such as low shunt and low series resistance.

5.12.2 I – V measurements

In Figure 5-33, the leakage current density (at 1 MV/cm) of $Hf_{1-x}Ti_xO_y$ films is shown.

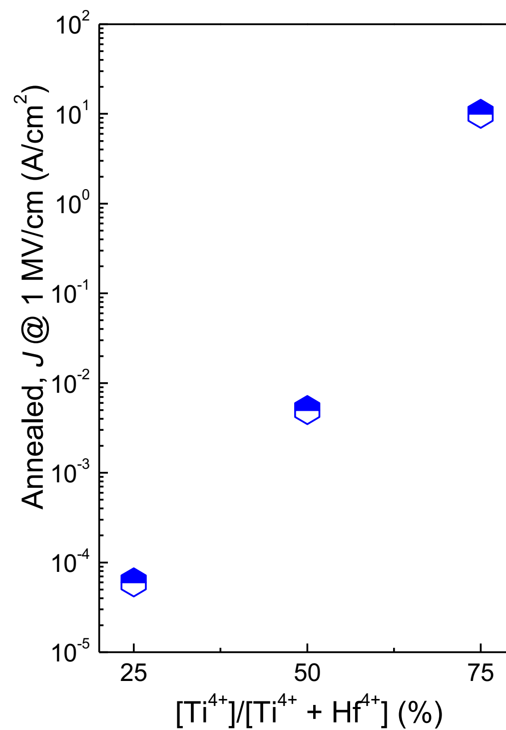

Figure 5- 33. Leakage current density (J) of $Hf_{1-x}Ti_xO_y$ films at 1 MV/cm as a function of [Ti]/ [Ti + Hf] atomic ratio after annealing at 800 °C for 30 mins in air.

The leakage current of annealed films at 1 MV/cm varies linearly between 6 x 10^{-5} A/cm^2 for $Hf_{75}Ti_{25}O_x$ and 10 A/cm^2 for $Hf_{25}Ti_{75}O_y$ films as shown in Figure 5-33. The stoichiometric $Hf_{1-x}Ti_xO_y$ films exhibited a value of 5 mA/cm^2 at 1 MV/cm. Popovici et at. [51], reported a current density of 10 A/cm^2 at 5 V for $Hf_{1-x}Ti_xO_y$ films deposited by ALD after annealing at 500 °C. Figure 5-35 illustrate the annealed stochiometric $Hf_{1-x}Ti_xO_y$ films I – V measurement.

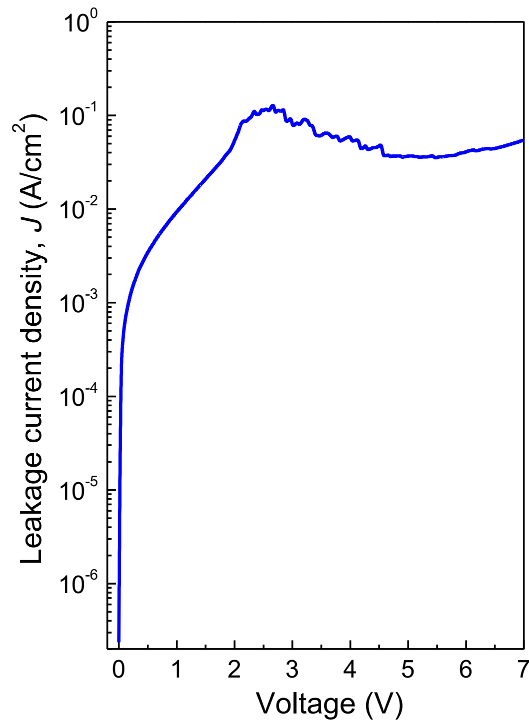

Figure 5- 34. Leakage current density versus voltage of stochiometric $Hf_{1-x}Ti_xO_y$ films after annealing at 800 ℃ for 30 mins in air.

As shown in Figure 5-34, the leakage current density at 5 V is 3 mA/cm^2 and it is slightly lower than the value reported by Popovici et al. [51], at same voltage.

To further interpret the nature of the leakage current, the Schottky emission (SE), Fowler-Nordhiem (FN) and Poole-Frenkel conduction mechanisms were investigated.

In Figures 5-35 – Figure 5-37 the SE, FN & PF plots of annealed $Hf_{1-x}Ti_xO_y$ films are shown.

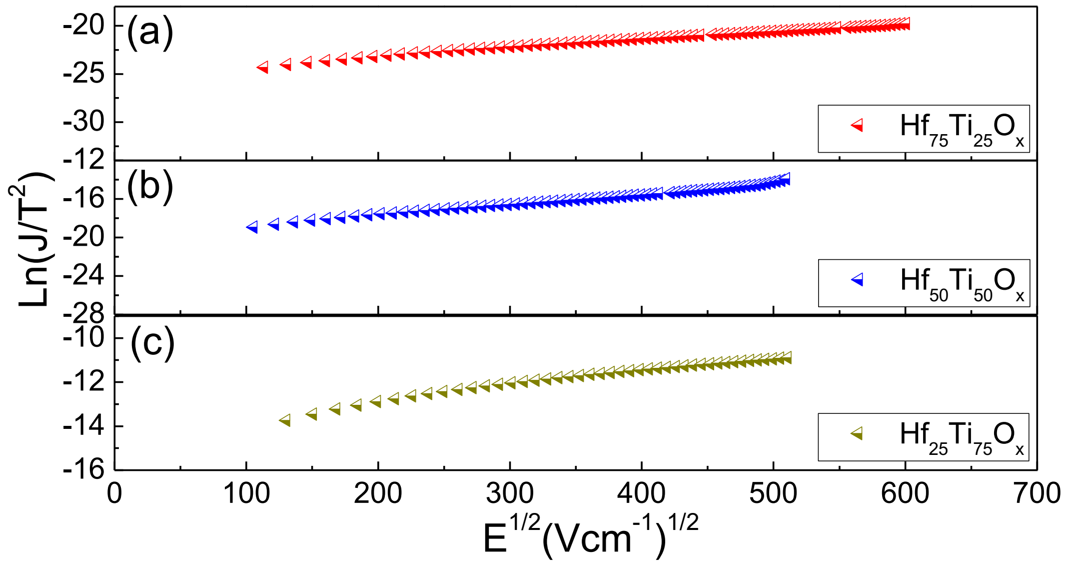

Figure 5- 35. Schottky plots of annealed (a) $Hf_{75}Ti_{25}O_x$ (b) $Hf_{50}Ti_{50}O_x$ and (c) $Hf_{25}Ti_{75}O_x$ films.

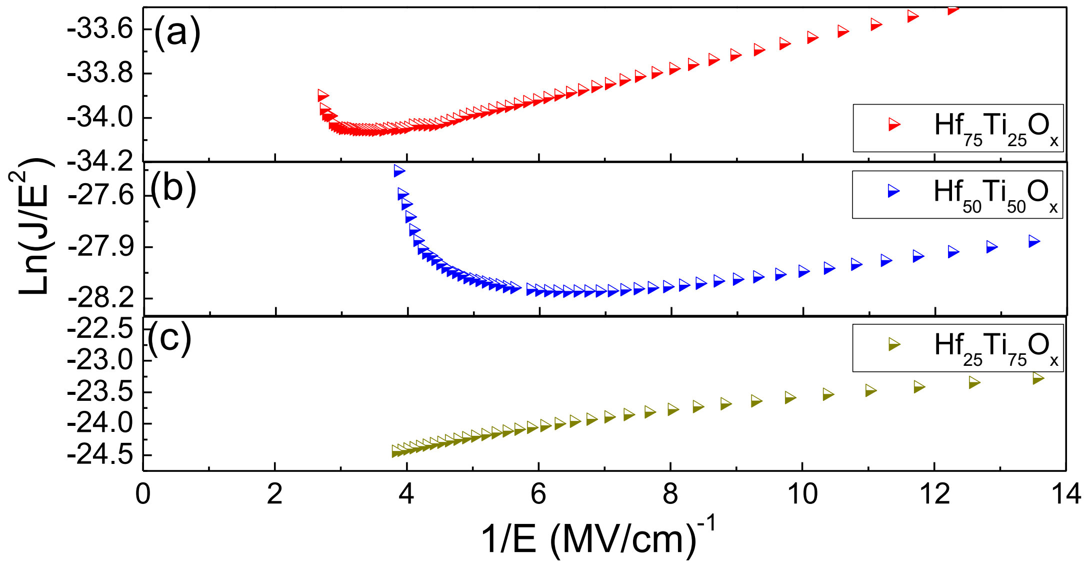

Figure 5- 36. Fowler-Nordheim plots of annealed (a) $Hf_{75}Ti_{25}O_x$ (b) $Hf_{50}Ti_{50}O_x$ and (c) $Hf_{25}Ti_{75}O_x$ films.

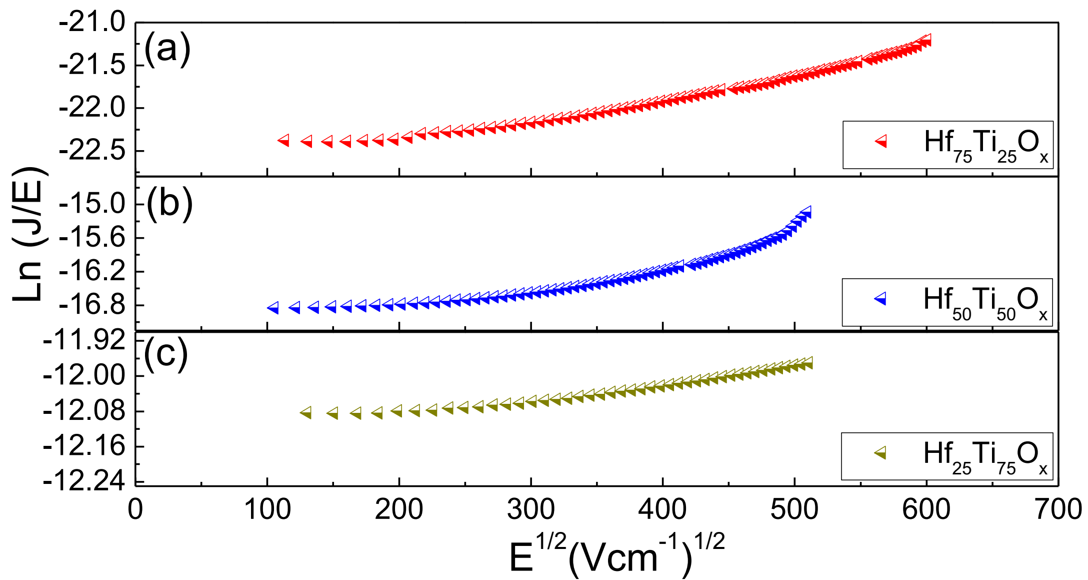

Figure 5- 37. Poole-Frenkel plots of annealed (a) $Hf_{75}Ti_{25}O_x$ (b) $Hf_{50}Ti_{50}O_x$ and (c) $Hf_{25}Ti_{75}O_x$ films.

At high electric fields, the SE and PE (Figures 5-35 & 5-37) plots shows linear behaviour that suggested that both mechanisms could act as dominant conduction mechanism of the annealed $Hf_{1-x}Ti_xO_y$ films and as result, one cannot simply decide on the dominant conduction mechanism. However, further investigation based on temperature dependence may clarify the actual conduction mechanism which is out of the scope of this study.

The FN plot on the other hand, suggests that only stochiometric $Hf_{1-x}Ti_xO_y$ films exhibited linearity at both high and low electric field, indicating an interface process as shown in Figure 5-36. Further analysis on the electron effective mass and potential barrier height of the stoichiometric $Hf_{1-x}Ti_xO_y$ films were calculated from the intercept of the SE and the slope of the FN plot and the values 0.003 m_o and 0.49 eV were obtained. Such parameters especially the low barrier height value explains the excessive leakage in the stochiometric $Hf_{1-x}Ti_xO_y$ films.

5.13 Conclusion

In summary, the effect of post-deposition annealing of $Hf_{1-x}Ti_xO_y$ films have been investigated.

The calculated optical bandgap of the annealed $Hf_{1-x}Ti_xO_y$ films were 4.4, 4.35 and 4.1 eV for $Hf_{75}Ti_{25}O_y$, $Hf_{50}Ti_{50}O_x$ and $Hf_{25}Ti_{75}O_x$ respectively. These values were slightly lower than the ones obtained for the as-deposited ones due to the annealing effect on the $Hf_{1-x}Ti_xO_y$ films. Additionally, the Urbach tail energy were also calculated and the values 338, 223 and

475 meV were obtained. In this case, the Urbach values were slightly higher than the as-deposited ones which may probably be due to the oxygen vacancies caused by the defect of TiO_x films.

The effect of the post-deposition annealing on the structure of $Hf_{1-x}Ti_xO_y$ films revealed the stoichiometry of $Hf_{50}Ti_{50}O_x$ films which exhibits an orthorhombic phase with average crystallite size of 8.2 nm and lattice parameters a = 4.82861 Å, b = 5.29627 Å and c = 5.0425 Å. The effect on the surface morphology showed increased roughness due to the crystallization of the $Hf_{1-x}Ti_xO_y$ films.

As for the dielectric properties, the stochiometric $Hf_{1-x}Ti_xO_y$ films exhibited a static dielectric constant of 38 and a current density of 5 mA/cm^2 at 1 MV/cm. Further investigation on the dominant conduction mechanism revealed that the Schottky emission and Poole-Frenkel mechanism could not be dominant in governing the charge transport of $Hf_{1-x}Ti_xO_y$ films as both mechanisms showed linearity over the extended electric fields. However, in the Fowler-Nordhiem plots, only stochiometric $Hf_{1-x}Ti_xO_y$ showed linear behaviour both at high and low electric fields indicating an interface process. Finally further analysis on the effective mass of electron and barrier height of the stochiometric $Hf_{1-x}Ti_xO_y$ films exhibited the values of 0.003 m_o and 0.49 eV respectively. The low barrier height value is a characteristic feature of excessive leakage current in stochiometric $Hf_{1-x}Ti_xO_y$ films and as result, no working TFT device could be achieved.

5.14 References

[1] J. Ko, J. Kim, S. Y. Park, E. Lee, K. Kim, K. H. Lim, and Y. S. Kim, "Solution-processed amorphous hafnium-lanthanum oxide gate insulator for oxide thin-film transistors," *J. Mater. Chem. C*, vol. 2, no. 6, pp. 1050–1056, 2014.

[2] W. M. Paulson, F. S. Hickernell, and R. L. Davis, "Effects of deposition parameters on optical loss for rf-sputtered Ta_2O_5 and Si_3N_4 waveguides," *J. Vac. Sci. Technol.*, vol. 16, no. 2, pp. 307–310, 1979.

[3] M. Cid, N. Stem, C. Brunetti, A. F. Beloto, and C. A. S. Ramos, "Improvements in anti-reflection coatings for high-efficiency silicon solar cells," *Surf. Coatings Technol.*, vol. 106, no. 2, pp. 117–120, 1998.

[4] R. Engel-Herbert, Y. Hwang, J. Cagnon, and S. Stemmer, "Metal-oxide-semiconductor capacitors with ZrO_2 dielectrics grown on $In_{0.53}Ga_{0.47}$ As by chemical beam deposition," *Appl. Phys. Lett.*, vol. 95, no. 6, pp. 62903–62908, 2009.

[5] B. M. Hudak, S. W. Depner, G. R. Waetzig, A. Talapatra, R. Arroyave, S. Banerjee, and B. S. Guiton, "Real-time atomistic observation of structural phase transformations in individual hafnia nanorods," *Nat. Commun.*, vol. 8, no. May, pp. 1–9, 2017.

[6] H. Shin, A. Benali, Y. Luo, E. Crabb, A. Lopez-Bezanilla, L. E. Ratcliff, A. M. Jokisaari, and O. Heinonen, "Zirconia and hafnia polymorphs: Ground-state structural properties from diffusion Monte Carlo," *Phys. Rev. Mater.*, vol. 2, no. 7, 2018.

[7] E. Laudadio, P. Stipa, L. Pierantoni, and D. Mencarelli, "Phase Properties of Different HfO_2 Polymorphs: A DFT-Based Study," *Crystals*, vol. 12, no. 1, 2022.

[8] M. Ritala, K. Kukli, A. Rahtu, P. I. Raisanen, M. Leskela, T. Sajavaara, and J. Keinonen, "Atomic layer deposition of oxide thin films with metal alkoxides as oxygen sources," *Science*, vol. 288, no. 5464, pp. 319–321, 2000.

[9] R. Pothiraja, A. P. Milanov, D. Barreca, A. Gasparotto, H-W. Becker, M. Winter, R. A. Fischer, and A. Devi, "Hafnium carbamates and ureates: New class of precursors for low-temperature growth of HfO_2 thin films," *Chem. Commun.*, no. 15, pp. 1978–1980, 2009.

[10] U. Patil, R. Thomas, A. Milanov, R. Bhakta, P. Ehrhart, R. Waser, R. Becker, H-W. Becker, M. Winter, K. Merz, R. A. Fischer, and A. Devi, "MOCVD of ZrO_2 and HfO_2 thin films from modified monomeric precursors," *Chem. Vap. Depos.*, vol. 12, no. 2–3, pp. 172–180, 2006.

[11] F. M. Li, B. C. Bayer, S. Hofmann, S. P. Speakman, C. Ducati, W. I. Milne, and A. J. Flewitt, "High-density remote plasma sputtering of high-dielectric-constant amorphous hafnium oxide films," *Phys. Status Solidi Basic Res.*, vol. 250, no. 5, pp. 957–967, 2013.

[12] A. J. Flewitt, A. J. Flewitt, F. M. Li, B. C. Bayer, S. Hofmann, and W. I. Milne, "Cubic-like Amorphous Hafnium Oxide : A New Dielectric for Active Matrix Backplanes," no. 1, pp. 1–2, 2012.

[13] P. Yang, Y. J-Noh, Y-J. Baek, H. Zheng, C-J. Kang, H-H. Lee, and T-S. Yoon, "Memcapacitive characteristics in reactive-metal (Mo, Al)/HfO_X/n-Si structures through migration of oxygen by applied voltage," *Appl. Phys. Lett.*, vol. 108, no. 5, pp. 6–11, 2016.

[14] S. S. Hullavarad, D. E. Pugel, E. B. Jones, R. D. Vispute, and T. Venkatesan, "Low leakage current transport and high breakdown strength of pulsed laser deposited HfO_2/SiC metal-insulator-semiconductor device structures," *J. Electron. Mater.*, vol. 36, no. 6, pp. 648–653, 2007.

[15] W. C. Lee, Y. J. Lee, Y. D. Wu, P. Chang, Y. L. Hsu, J. P. Mannaerts, R. L. Lo. F. R. Chen, S. Maikap, L. S. Lee, W. Y. Hsieh, M. J. Tsai, S. Y. Lin, T. Gustffson, M. Hong, and J. Kwo, "MBE-grown high κ gate dielectrics of HfO_2 and $(Hf\text{-}Al)O_2$ for Si and III-V semiconductors nano-electronics," *J. Cryst. Growth*, vol. 278, no. 1–4, pp. 619–623, 2005.

[16] J. Chung, Y. J. Tak, W. G. Kim, J. W. Park, T. S. Kim, J. H. Lim, and H. J Kim, "Low-temperature fabrication of solution-processed hafnium oxide gate insulator films using a thermally purified solution process," *J. Mater. Chem. C*, vol. 6, no. 18, pp. 4928–4935, 2018.

[17] F. Zheng, G. Liu, A. Liu, B. Shin, and F. Shan, "Solution-processed hafnium oxide dielectric thin films for thin-film transistors applications," *Ceram. Int.*, vol. 41, no. 10, pp. 13218–13223, 2015.

[18] Y. B. Yoo, J. H. Park, K. H. Lee, H. W. Lee, K. M. Song, S. J. Lee, and H. K. Baik, "Solution-processed high-k HfO_2 gate dielectric processed under softening temperature of polymer substrates," *J. Mater. Chem. C*, vol. 1, no. 8, pp. 1651–1658, 2013.

[19] J. Weng, W. Chen, W. Xia, J. Zhang, Y. Jiang, and G. Zhu, "Low-temperature solution-based fabrication of high-k HfO_2 dielectric thin films via combustion process," *J. Sol-Gel Sci. Technol.*, vol. 81, no. 3, pp. 662–668, 2017.

[20] J. D. Oh, J. W. Kim, D. K. Kim, and J. H. Choi and J. H. Choi, "Low-voltage organic transistors and inverters using HfO_x dielectrics," *Org. Electron.*, vol. 30, pp. 131–135, 2016.

[21] Y. G. Kim, C. Avis, and J. Jang, "Low voltage driven, stable solution-processed zinc-tin-oxide TFT with HfO_y and AlO_x stack gate dielectric," *ECS Solid State Lett.*, vol. 1, no. 2, pp. 23–26, 2012.

[22] Y. N. Gao, Y. L. Xu, J. G. Lu, J. H. Zhang, and X. F. Li, "Solution processable amorphous hafnium silicate dielectrics and their application in oxide thin film transistors," *J. Mater.*

Chem. C, vol. 3, no. 43, pp. 11497–11504, 2015.

[23] M. García-Hipólito, O. Alvarez-Fregoso, J. Guzmán, E. Martínez, and C. Falcony, "Characterization of HfO_2:Mn luminescent coatings deposited by spray pyrolysis," *Phys. Status Solidi Appl. Res.*, vol. 201, no. 15, pp. 127–130, 2004.

[24] J. Guzmán-Mendoza, D. Albarrán-Arreguín, O. Alvarez-Fragoso, M. A. Alvarez-Perez, C. Falcony, and M. García-Hipólito, "Photoluminescent characteristics of hafnium oxide layers activated with trivalent terbium (HfO_2:Tb^{+3})," *Radiat. Eff. Defects Solids*, vol. 162, no. 10–11, pp. 723–729, 2007.

[25] A. Avila-García and M. García-Hipólito, "Characterization of gas sensing HfO_2 coatings synthesized by spray pyrolysis technique," *Sensors Actuators, B Chem.*, vol. 133, no. 1, pp. 302–307, 2008.

[26] J. G. Mendoza, M. A. A. Frutis, G. A. Flores, M. G. Hipolito, A. M. Cerda, J. A. Nieto, T. R. Montalvo, and C. Falcony, "Synthesis and characterization of hafnium oxide films for thermo and photoluminescence applications," *Appl. Radiat. Isot.*, vol. 68, no. 4–5, pp. 696–699, 2010.

[27] R. R. Manriquez, J. A. I. Gongora, J. G-Mendoza, T. R. Montalvo, J. C. G. Olguin, P. V. C. Ramirez, M. G-Hipolito, and C. Falcony, "Photo-, cathodo- and thermoluminescent properties of dysprosium-doped HfO_2 films deposited by ultrasonic spray pyrolysis," *Appl. Radiat. Isot.*, vol. 92, pp. 91–95, 2014.

[28] I. M-Merlin, J. G-Mendoza, M. G-Hipolito, V. M. S-Resendiz, L. L-Rojas, R. J. Fragoso, and C. Falcony, "Transparent and low surface roughness HfO_2: Tb^{3+}, Eu^{3+} luminescent thin films deposited by USP technique," *Ceram. Int.*, vol. 42, no. 2, pp. 2446–2455, 2016.

[29] M. Esro, G. Vourlias, C. Somerton, W. I. Milne, and G. Adamopoulos, "High-mobility ZnO thin film transistors based on solution-processed hafnium oxide gate dielectrics," *Adv. Funct. Mater.*, vol. 25, no. 1, pp. 134–141, 2015.

[30] L. Xifeng, X. Enlong, and Z. Jianhua, "Low-temperature solution-processed zirconium oxide gate insulators for thin-film transistors," *IEEE Trans. Electron Devices*, vol. 60, no. 10, pp. 3413–3416, 2013.

[31] J. F. M. Hardigree, T. J. Dawidczyk, R. M. Ireland, G. L. Johns, B.-J. Jung, M. Nyman, R. Osterbacka, N. Markovic, and H. E. Katz, "Through Thick and Thin: Tuning the Threshold Voltage in Organic Field-Effect Transistors," *ACS Appl. Mater. Interfaces*, vol. 5, pp. 7025–7032, 2013.

[32] C. Avis, Y. G. Kim, and J. Jang, "Solution processed hafnium oxide as a gate insulator for low-voltage oxide thin-film transistors," *J. Mater. Chem.*, vol. 22, no. 34, pp. 17415–17420, 2012.

[33] H. Kostlin, G. Frank, G. Hebbinghaus, H. Auding, and K. Denissen, "Optical filters on linear haloge n-lamps prepared by dip-coating," *J. Non. Cryst. Solids,* vol. 218, pp. 1–7, 1997.

[34] H. T. and W. R. Hu, "Effects of high frequency vibration on critical Marangoni number," *Adv. Sp. Res.*, vol. 16, no. 7, pp. 71–74, 1995.

[35] Y. Yan, S. R. Chaudhuri, and A. Sarkar, "Synthesis, characterizations, and optical properties of stacked porous thin films derived from sol-gel process," *J. Am. Ceram. Soc.*, vol. 79, no. 4, pp. 1061–1065, 1996.

[36] Z. Jiwei, Y. Tao, Z. Liangying, and Y. Xi, "The optical waveguiding properties of TiO_2 -SiO_2 composite films prepared by the sol - gel process," *Ceram. Int.,* vol. 25, pp. 667–670, 1999.

[37] J. Yu, X. Zhao, and Q. Zhao, "Photocatalytic activity of nanometer TiO_2 thin films prepared by the sol-gel method," *Mater. Chem. Phys.*, vol. 69, no. 1–3, pp. 25–29, 2001.

[38] K. Bange, C. R. Ottermann, O. Anderson, and U. Jeschkowski, "Investigations of TiO_2 films deposited by different techniques," *Thin Solid Films*, vol. 197, pp. 279–285, 1991.

[39] I. Oja, A. Mere, M. Krunks, C. H. Solterbeck, and M. Es-Souni, "Properties of TiO_2 films prepared by the spray pyrolysis method," *Solid State Phenom.*, vol. 99–100, pp. 259–262, 2004.

[40] I. Oja, A. Mere, M. Krunks, R. Nisumaa, C. H. Solterbeck, and M. Es-Souni, "Structural and electrical characterization of TiO_2 films grown by spray pyrolysis," *Thin Solid Films*, vol. 515, no. 2, pp. 674–677, 2006.

[41] P. S. Shinde, P. S. Patil, P. N. Bhosale, and C. H. Bhosale, "Structural, optical, and photoelectrochemical properties of sprayed TiO_2 thin films: Effect of precursor concentration," *J. Am. Ceram. Soc.*, vol. 91, no. 4, pp. 1266–1272, 2008.

[42] A. Nakaruk, D. Ragazzon, and C. C. Sorrell, "Anatase-rutile transformation through high-temperature annealing of titania films produced by ultrasonic spray pyrolysis," *Thin Solid Films*, vol. 518, no. 14, pp. 3735–3742, 2010.

[43] M. Hirano. C. Nakahara, K. Ota, O. Tanaike, and M. Inagaki, "Photoactivity and phase stability of ZrO2-doped anatase-type TiO_2 directly formed as nanometer-sized particles by hydrolysis under hydrothermal conditions," *J. Solid State Chem.*, vol. 170, no. 1, pp. 39–47, 2003.

[44] O. Carp, C. L. Huisman, and A. Reller, "Photoinduced reactivity of titanium dioxide," *Prog. Solid State Chem.*, vol. 32, no. 1–2, pp. 33–177, 2004.

[45] J. Zhang, J. Zhou, P. Liu, J. And Yu, "New understanding of the difference of photocatalytic activity among anatase, rutile and brookite TiO_2," *Phys. Chem. Chem.*

Phys., vol. 16, no. 38, pp. 20382–20386, 2014.

[46] F. Chen, X. Bin, C. Hella, X. Shi, W. L. Gladfelter, and S. A. Campbell, "A study of mixtures of HfO_2 and TiO_2 as high-k gate dielectrics," *Microelectron. Eng.*, vol. 72, no. 1–4, pp. 263–266, 2004.

[47] D. H. Triyoso, R. I. Hegde, X.-D. Wang, M. W. Stoker, R. Rai, M. E. Ramon, B. E. White, and P. J. Tobin, "Characteristics of Mixed Oxides and Nanolaminates of Atomic Layer Deposited HfO_2–TiO_2 Gate Dielectrics," *J. Electrochem. Soc.*, vol. 153, no. 9, p. G834, 2006.

[48] Y. H. Wang, J. Zhang, Y. Ye, Y. Wang, B. Wang, and Y. Jin, "Composition dependence of band alignment and dielectric constant for $Hf_{1-x}Ti_xO_2$ thin films on Si (100)," *J. Appl. Phys.*, vol. 107, no. 10, 2010.

[49] P. Jin, G. He, M. Liu, D. Q. Xiao, J. Gao, X. F. Chen, R. Ma, J. W. Zhang, M. Zhang, Z. Q. Sun, and Y. M. Liu, "Deposition-power-modulated optical and electrical properties of sputtering-derived $HfTiO_x$ gate dielectrics," *J. Alloys Compd.*, vol. 649, pp. 128–134, 2015.

[50] C. Ye, Y. Wang, J. Zhang, J. Zhang, H. Wang, and Y. Jiang, "Evidence of interface conversion and electrical characteristics improvement of ultra-thin HfTiO films upon rapid thermal annealing," *Appl. Phys. Lett.*, vol. 99, no. 18, pp. 1–4, 2011.

[51] M. Popovici, A. Delabie, S. V. Elshoct, S. Clima, G. Pourtois, L. Nyns, K. Tomida, N. Menou, K. Opsomer, J. Swerts, C. Detavernier, D. Wouters, and J. A. Kittl, "Growth and Material Characterization of Hafnium Titanates Deposited by Atomic Layer Deposition," *J. Electrochem. Soc.*, vol. 156, no. 10, p. G145, 2009.

[52] Q. Lu, Y. Mu, J. W. Roberts, M. Althobaiti, V. R. Dhanak, J. Wu, C. Zhao, C. Z. Zhao, Q. Zhang, L. Yang, I. Z. Mitrovic, S. Taylor, and P. R. Chalker, "Electrical properties and interfacial studies of $Hf_xTi_{1-x}O_2$ high permittivity gate insulators deposited on germanium substrates," *Materials (Basel).*, vol. 8, no. 12, pp. 8169–8182, 2015.

[53] D. H. Triyoso, R. I. Hegde, S. Zollner, M. E. Ramon, S. Kalpat, R. Gregory, X-D. Wang, J. Jiang, M. Raymond, R. Rai, D. Werho, D. Roan, B. E. White, and P. J. Tobin, "Impact of titanium addition on film characteristics of HfO_2 gate dielectrics deposited by atomic layer deposition," *J. Appl. Phys.*, vol. 98, no. 5, 2005.

[54] M. Li, Z. Zhang, S. A. Campbell, H. J. Li, and J. J. Peterson, "Hafnium titanate as a high permittivity gate insulator: Electrical and physical characteristics and thermodynamic stability," *J. Appl. Phys.*, vol. 101, no. 4, 2007.

[55] E. Barraud, S. Begin-Colin, G. L. Caer, F. Villieras, and O. Barres, "Thermal decomposition of $HfCl_4$ as a function of its hydration state," *J. Solid State Chem.*, vol. 179, no. 6, pp. 1842–1851, 2006.

[56] J. Tauc, “Optical properties and electronic structure of amorphous Ge and Si,” *Mater. Res. Bull.*, vol. 3, no. 1, pp. 37–46, 1968.

[57] D. Afouxenidis, R. Mazzocco, G. Vourlias, P. J. Livesley, A. Krier, W. I. Milne, O. Kolosov, and G. Adamopoulos, “ZnO-based thin film transistors employing aluminum titanate gate dielectrics deposited by spray pyrolysis at ambient air,” *ACS Appl. Mater. Interfaces*, vol. 7, no. 13, pp. 7334–7341, 2015.

[58] M. Esro, R. Mazzocco, G. Vourlias, O. Kolosov, A. Krier, W. I. Milne, and G. Adamopoulos, “Solution processed lanthanum aluminate gate dielectrics for use in metal oxide-based thin film transistors,” *Appl. Phys. Lett.*, vol. 106, no. 20, 2015.

[59] M. Kranjčec, I. P. Studenyak, and M. V. Kurik, “On the Urbach rule in non-crystalline solids,” *J. Non. Cryst. Solids*, vol. 355, no. 1, pp. 54–57, 2009.

[60] M. Mazur, D. Wojcieszak, J. Domaradzki, D. Kaczmarek, A. Poniedzialek, and P. Domanowski, “Investigation of microstructure, micro-mechanical and optical properties of $HfTiO_4$ thin films prepared by magnetron co-sputtering,” *Mater. Res. Bull.*, vol. 72, pp. 116–122, 2015.

[61] D. A. N. and E. Cartier, “Materials characterization of and binary oxides deposited by chemical solution deposition,” vol. 1801, no. 2001, 2015.

[62] D. D-Arhin, F. P. Buabeng, J. M. Mwabora, P. N. Amaniampong, H. Agbe, E. Nyankson, D. O. Obada, and N. Y. Asiedu, “The effect of titanium dioxide synthesis technique and its photocatalytic degradation of organic dye pollutants,” *Heliyon*, vol. 4, no. 7, p. e00681, 2018.

[63] M. M. Ba-Abbad, A. A. H. Kadhum, A. B. Mohamad, M. S. Takriff, and K. Sopian, “Synthesis and Catalytic Activity of TiO_2 Nanoparticles for Photochemical Oxidation of Concentrated Chlorophenols under Direct Solar Radiation,” *Int. J. Electrochem. Sci.*, vol. 7, pp. 4871–4888, 2012.

[64] A. L. Patternson, “The Scherrer Formula for X-Ray Particle Size Determination,” *Physical review*, vol. 56. pp. 978–982, 1939.

[65] X. Zhang, S. Zhang, H. Zhu, X. Pan, C. Cheng, T. Yu, X. Li, Y. Cheng, G. Xing, D. Zhang, X. Luo, and B. Chen, “Frequency dispersion analysis of thin dielectric MOS capacitor in a five-element model,” *J. Phys. D. Appl. Phys.*, vol. 51, no. 5, pp. 1–9, 2018.

[66] F.-C. Chiu, “A Review on Conduction Mechanisms in Dielectric Films,” *Adv. Mater. Sci. Eng.*, vol. 2014, no. 7, pp. 1–18, 2014.

[67] K. Ellmer, A. Klein, and B. Rech, A. Klein, *Transparent Conductive Zinc Oxide*, vol. 104. 2008.

[68] Z. Zhang, C, Shao, X. Li, L. Zhang, H. Xue, C. Wang, and Y. Liu, “Electrospun nanofibers

of ZnO-SnO_2 heterojunction with high photocatalytic activity," *J. Phys. Chem. C*, vol. 114, no. 17, pp. 7920–7925, 2010.

[69] L. Zheng, Y. Zheng, C. Chen, Y. Zhan, X. Lin, Q. Zheng, K. Wei, and J. Zhu, "Network structured SnO_2/ZnO heterojunction nanocatalyst with high photocatalytic activity," *Inorg. Chem.*, vol. 48, no. 5, pp. 1819–1825, 2009.

[70] D. J. Dunstan, "Evidence for a common origin of the Urbach tails in amorphous and crystalline semiconductors," *J. Phys. C Solid State Phys.*, vol. 15, no. 13, 1982.

[71] M. Li, Z. Zhang, and S. A. Campbell, "Electrical and material characterizations of high-permittivity $Hf_xTi_{1-x}O_2$ gate insulators," *J. Appl. Phys.*, vol. 98, no. 5, 2005.

6 Zirconium Silicate $Zr_{1-x}Si_xO_y$ Thin Films

Zirconium Silicate ($Zr_{1-x}Si_xO_y$) is one of the emerging high-k metal oxide as alternative to the conventional SiO_2 as gate dielectrics for TFTs application. There were several reports on the properties of $Zr_{1-x}Si_xO_y$ films that have been deposited by mostly costly vacuum-based techniques. In this chapter, the properties of $Zr_{1-x}Si_xO_y$ films as a function of [Si] to [Zr] ratios were investigated by a simple and low-cost spray pyrolysis technique. The samples were deposited on different substrate for characterization, and it was observed that its optical bandgap varies between 5.8 and 8 eV with increasing Si content. The structure of $Zr_{1-x}Si_xO_y$ films were amorphous except for pure ZrO_x that showed the presence of both cubic and tetragonal phase. The latter demonstrate the natural state of ZrO_2 films at low deposition temperature. AFM images were taken and $Zr_{1-x}Si_xO_y$ films showed decreasing surface roughness with increasing Si content. The RMS values vary between 6.59 and 0.31 nm as a function of [Si]/ [Si + Zr] atomic ratio. As a gate dielectric, $Zr_{1-x}Si_xO_y$ films exhibited a high dielectric constant that varies between 23 and 4.2. Its leakage current density was measured at 1 MV/cm and it was observed that stochiometric $Zr_{1-x}Si_xO_y$ films ($J \sim 10^{-7}$ A/cm^2) exhibited the lowest leakage current density at 1 MV/cm. Further analysis on the current transport in $Zr_{1-x}Si_xO_y$ films showed that the current transport is dominated by Poole-Frenkel mechanism. Finally, the performance of the ZnO-based TFTs employing stochiometric $Zr_{1-x}Si_xO_y$ films showed high electron mobility of 57 cm^2/Vs, current modulation ratio of 10^6, threshold voltage of 0.1 V, subthreshold swing of 0.28 V/dec, interface trap density of 5×10^{12} cm^{-2}, low voltage operation of 4 V and negligible hysteresis.

6.1 Introduction

For many years, the fabrication of metal oxide field effect transistors (MOSFETs) has mostly been dominated by the conventional silicon (Si) based technologies due to the abundance of Si in the earth crust. Silicon dioxide (SiO_2) has been the most reliable metal oxide employed as gate dielectric for MOSFETs due to its thermal stability and excellent quality interface on Si. It has a wide energy gap of 10 eV and high dielectric strength of 10 MV/cm [1]. Despite its extraordinary properties, its low dielectric constant (k $\sim$ 3.9) is a concern for future generation of MOSFETs. The problem with tunneling current that leads to high power consumption causes degradation in the reliability of the devices and such issues must be addressed. The emergence of high-k metal oxides as alternatives to SiO_2 have shown promising attributes since it can decrease the tunneling current by increasing the layer thickness of the oxides, while maintaining same capacitance or equivalent SiO_2 thickness [2]. Among the various high-k metal oxides, zirconium oxide (ZrO_2) emerged as one of the most extensively studied oxide as alternative to SiO_2 due to its high dielectric constant, good thermal stability and wide band gap.

ZrO_2 exhibit excellent optical and dielectric characteristics as a gate dielectric. It is highly transparent in visible spectrum (400 – 700 nm), it has a high refractive index (n $\sim$ 2.1 at $\lambda = 550\ nm$) and has a wide energy gap $\sim$5.7 eV. Also, ZrO_2 has a high dielectric constant of 25 and all these properties are strongly dependent on the deposition technique.

ZrO_2 films have been used in different areas of electronic applications including storage capacitors in dynamic random access memories (DRAMs) [1][2], optical filters [3] and thin-film transistor (TFT) applications [4]–[15].

Depending on the deposition conditions, ZrO_2 thin films can exist in three polymorphs [16]; monoclinic, tetragonal and cubic phase. These polymorphs are strongly dependent on the deposition temperature. The monoclinic phase ZrO_2 can be thermodynamically stable between room temperature and 1170 °C, tetragonal phase between 1170 and 2370 °C and the cubic phase above 2370 °C. Additionally, both tetragonal and cubic phase ZrO_2 can be stabilised at room temperature through the means of doping by materials such as Y_2O_3, Al_2O_3 and CeO_2 etc. The stabilisation of the tetragonal and cubic phase ZrO_2 strongly depend on the concentration of the dopant. It is important to mention that different polymorphs of ZrO_2 thin films may exhibit different dielectric properties [16][17]. For instance, it has already been reported by Zhou et al. [18], that amorphous and monoclinic phase ZrO_2 exhibit a dielectric constant of $\sim$27 while the tetragonal and cubic phase exhibit 35 – 50. Sayan et al. [19], also reported that tetragonal phase ZrO_2 exhibit higher dielectric constant, wider bandgap and lower leakage current than the amorphous and monoclinic phase. Figure 6-1 illustrate different polymorphs of ZrO_2 thin films.

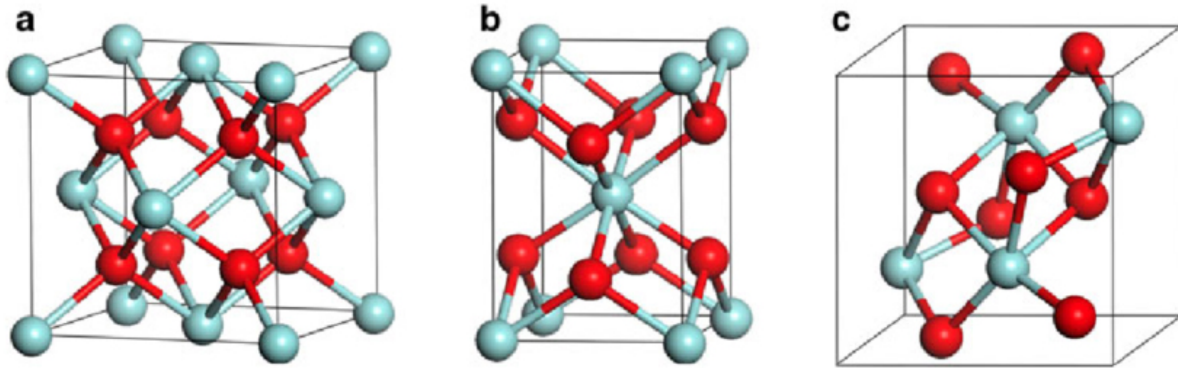

Figure 6- 1. The three polymorphs of ZrO_2: (a) cubic, (b) tetragonal and (c) monoclinic [20].

ZrO_2 films have already been manufactured by several deposition techniques such as pulsed laser deposition (PLD) [21], sputtering [22]–[24], electron beam evaporation [25], spin coating [26]–[32] and spray pyrolysis [17][31].

For thin film deposition, it has already been reported that ZrO_2 thin films exhibits crystalline phase at moderate temperatures (< 550 °C) in solution processable techniques [17]. As a gate dielectric for TFTs, table 6-1, summarizes some selected reports on solution processed ZrO_2 gate dielectric, which has mostly been deposited by spin coating technique using various zirconium precursors.

Table 6- 1. Selected previous work on solution processed ZrO_2 gate dielectric and their TFT characteristics (T_{dep}: deposition temperature, k: dielectric constant, J_{leak}: leakage current density, μ : electron mobility, SS: subthreshold swing, $I_{on/off}$: current modulation ratio, V_{th}: threshold voltage).

Deposition technique	T_{dep} (°C)	k	J_{leak} (A/cm^2)	Semiconductor	μ (cm^2/Vs)	SS (V/dec)	$I_{on/off}$	V_{th} (V)	ref
Spray pyrolysis	400	22.7	3.56×10^{-6} @ 1V	ZTO	4.61	0.25	10^6	0.03	[4]
Spin coating	300	-	-	RIZO	2.54	-	10^6	0.65	[5]
Spin coating	UV	22.6	10^{-9} @ 4 MV/cm	T-OSC	0.4	-	10^6	-	[8]
Spin coating	200	14.4	-	In_2O_3	18.7	0.26	-	0.09	[9]
Spin coating	300	-	-	IZTO	15.42	0.087	10^9	-	[10]
Spin coating	-	8.71	4.68×10^{-9} @ 1 MV/cm	IGZO	4.2	-	10^6	-	[11]
Spin coating	300	10	5×10^{-8} @ 1 MV/cm	P-OFT	3.7	0.65	10^6	-2.7	[34]
Spin coating	400	17.3	4.5×10^{-8} @ 1 MV/cm	SnO	2.5	0.88	10^3	-	[35]
Spin coating	250	-	-	LIZO	12	-	10^6	0.19	[12]
Spin coating	350	16.5	-	ITZO	0.04	1.05	10^3	-0.75	[13]
Spin coating	350	25	-	OTFT	2.38		10^4	-3.3	[14]
Spin coating	350	-	-	IGZO	0.123	-	10^6	6.25	[15]
Spin coating	UV	10.57	10^{-7} @ 2 V	P-OFT	0.73	0.15	10^5	-1.35	[36]
Spin coating	250	-	-	LIO	59.8	0.18	10^8	2.02	[37]
Spin coating	250	-	-	IZTO	2.65	0.133	10^8	0.44	[6]
Spin coating	300	-	-	ZnO	20	-	-	-	[7]
Spin coating	300	21.8	2.8×10^{-4} @ 2 V	-	-	-	-	-	[38]
Spin coating	300	17.6	10^{-5} @ 0.8 MV/cm	IGZO	0.2	0.34	10^3	0.3	[26]
Spin coating	250	13	4.8×10^{-5} @ 2 MV/cm	IZO	75	-	10^5	0.22	[27]
Spin coating	300	12.5	1×10^{-9} @ 2 MV/cm	In_2O_3	29.5	0.39	10^4	-0.27	[28]
Spin coating	200	21.8	-	ITZO	9.8	2.3	10^3	-1.5	[29]
Spin coating	300	20.5	100×10^{-9} @ 1 V	IGZO	0.8	-	10^4	0.1	[30]

Spin coating	350	14.8	7.7×10^{-9} @ 2 MV/cm	IZO	7.21	0.257	10^{6}	3.22	[31]
Spin coating	UV	8.79	10^{-6} @ 7.5 MV/cm	ZnO	0.45	0.25	10^{5}	0.1	[32]
Spray pyrolysis	400	14	-	ZnO	0.18	-	-	-	[33]
Spray pyrolysis	400	14	$<0.5 \times 10^{-6}$ @ 6 V	LZO	85	-	10^{6}	-	[17]

Despite the extraordinary properties of ZrO_2 as a gate dielectric, there is a bottleneck of film crystallization at low temperatures that may lead to excessive gate leakage current. Such low crystallization temperature can be increased by incorporation of another metal oxide that exhibits an amorphous structure. There are potential candidates to address such issue such as Al_2O_3 and SiO_2. In this chapter, SiO_2 was chosen due to its high crystallization temperature (> 800 °C) and high dielectric strength. The incorporation of SiO_2 into ZrO_2 (in solutions) yields the formation of zirconium silicate ($Zr_{1-x}Si_xO_y$ or ZSO) thin films.

ZSO is a potential candidate as alternative to the conventional SiO_2 gate dielectric due to its higher dielectric constant than SiO_2 and wider bandgap than ZrO_2. It is thermodynamically stable when in contact with the semiconductor. There are very few up-to-date reports on properties of ZSO thin films deposited mainly by vacuum-based techniques such as CVD-based and sputtering. In fact, there is no single report on solution processed ZSO thin films. Table 6-2 show some reports on properties of ZSO films and are mostly deposited by the vacuum-based techniques.

Table 6- 2. Review on selected reports on ZSO gate dielectrics.

Deposition techniques	T_{dep} (°C)	k	J_{leak} (A/cm^2)	Ref
MOCVD	550	10.5 – 15	5 x 10^{-9} @ -3 V	[39]
MOCVD	550	15	5 x 10^{-9} @ -3 V	[40]
Sputtering	500	9.5	1 x 10^{-6} @ 1 V	[41]
Sputtering	500 - 1000	-	10^{-9} - 10^{-6} @ -1 V	[42]
ALD	162	3.8 – 11.1	-	[43]
ALD	300	7.5 – 13	10^{-3} @ 4 V	[44]
ALD	270	10	1 x 10^{-8} @ 1 V	[45]

Table 6-2 shows that, ZSO thin films could be obtained at low deposition temperature (< 550 °C) and exhibit high dielectric constant between 7.5 – 15 and a low current leakage density of ~10^{-8} A/cm^2 at 1 V.

In this chapter, the properties of $Zr_{1-x}Si_xO_y$ thin films and their implementation in ZnO – based TFTs will be investigated. $Zr_{1-x}Si_xO_y$ thin films will be characterized by the UV-Vis spectroscopy, FTIR, XRD, AFM, impedance spectroscopy, I – V measurements and field effect measurements for implementation in TFTs. The films were deposited by spray pyrolysis in an ambient air using a conventional airbrush and by varying the zirconium (Zr) to silicon (Si) atomic ratio, by physical blending of the soluble precursors in alcohol-based precursors [46].

6.2 Precursors

Zirconium (IV) acetylacetonate (Zr(acac)$_4$, 97%), silicon (IV) chloride ($SiCl_4$) and zinc acetate dilhydrate ($Zn(O_2C_2H_3)_2 \cdot 2H_2O$, 99.9%) were used as precursors. The Zr(acac)$_4$ and $SiCl_4$

precursors were purchased from Sigma Aldrich while $Zn(O_2C_2H_3)2.\ 2H_2O$ precursor was purchased from Alfa Aesar. All precursors were used without any further purification.

The zirconium and silicon precursors were dissolved in methanol and 2,4 pentanedione respectively at a total concentration of 0.1 M, for the deposition of zirconium silicate films.

The zirconium (Zr) to silicon (Si) atomic ratio was controlled by simple blending of the amount of each of the precursor's solution.

Finally, zinc acetate dilhydrate ($Zn(O_2C_2H_3)2.\ 2H_2O$) precursor was dissolved in methanol at a concentration of 0.1 M for the deposition of zinc oxide films [47].

6.3 Thermal Properties of Precursor

The decomposition profile of the precursors was investigated by the thermogravimetric analysis (TGA) and differential scanning calorimetry (DSC) measurements. The measurements were carried out under a N_2 atmosphere at constant heating rate of 10 K/min in the temperature range between 40 – 700 °C, using a simultaneous thermal analyser NRTZSCH STA 449 F3 Jupiter® equipment.

Figure 6-2 and Figure 6-3 illustrate the TGA and DSC measurements of zirconium acetylacetonate and silicon chloride respectively.

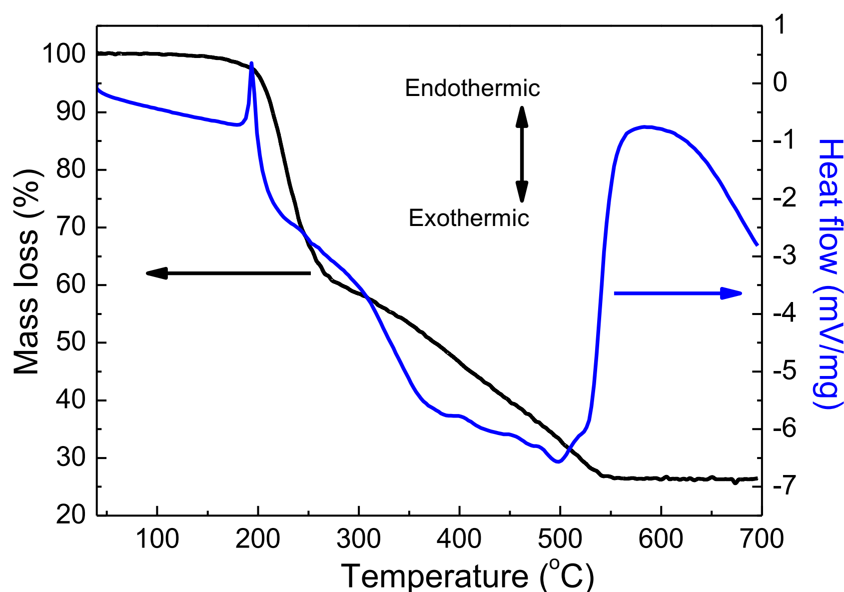

Figure 6- 2. TGA (black line) and DSC (blue line) of 6 mg zirconium acetylacetonate powder.

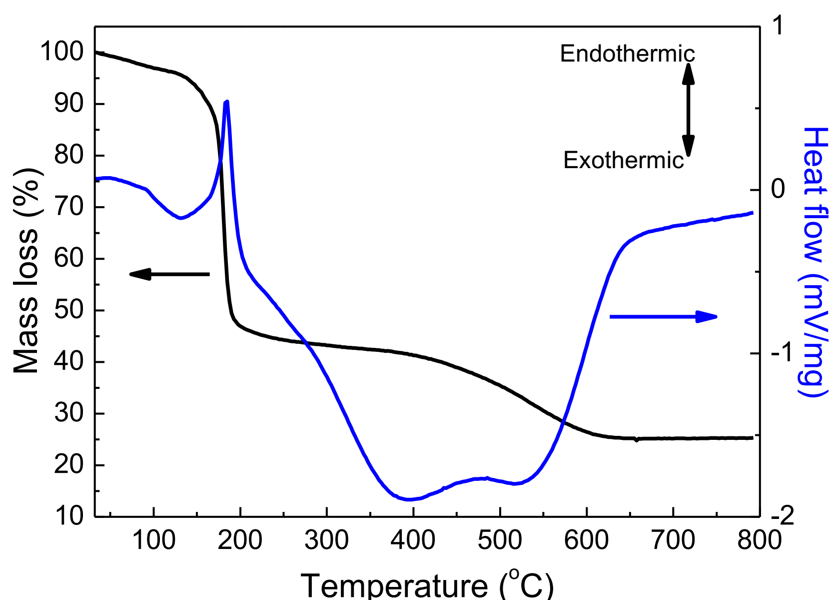

Figure 6- 3. TGA (black line) and DSC (blue line) of 10 mg silicon chloride solution.

The TGA curve in Figure 6-2 shows about ~40 % of the mass of zirconium acetylacetonate [Zr(acac)$_4$] powder was lost between 160 and 287 °C, followed by the progressive mass loss of ~31 % between 300 and 540 °C. In the first mass loss, the DSC curve shows a sharp endothermic peak centred at ~195 °C and is attributed to loss in water molecules and degradation of acetylacetonate ligand while in the second mass loss, the DSC curve shows a weak exothermic peak centred at ~496 °C and is due to the complete decomposition of acetylacetonate ligands and formation of crystalline ZrO_2 films as the final product. This finding is in good agreement with that of Perez-Tavares et al. [48].

Similarly, in Figure 6-3, there was a mass loss of 3 % and 51 % observed between 40 – 95 °C and 102 – 227 °C respectively. The former is due to dehydration of water molecules absorbed by the atmosphere while the latter may be due to decomposition of the chloride part of the precursor and formation of amorphous SiO_2 films as evidenced from the two endothermic peaks of the DSC curve centred at 87 (weak) and 182 °C (strong) respectively. Furthermore, the mass loss observed between 270 – 637 °C was 18.5 %, supported by the exothermic peak centred at 515 °C can be attributed to the beginning of the crystallization of SiO_2 films.

6.4 Thin Film Deposition & Characterization

The deposition process is similar to the ones described in the previous chapters (4&5). The blends of zirconium (IV) acetylacetonate [Zr(acac)$_4$] in methanol and Silicon (IV) chloride ($SiCl_4$) in 2,4 pentanedione were spray coated at 550 °C onto different substrates to obtain the desired zirconium-silicates ($Zr_{1-x}Si_xO_y$) films, until films of typical thickness between 60 – 80 nm were obtained.

The obtained $Zr_{1-x}Si_xO_y$ films were characterized by series of techniques including UV-Vis spectroscopy, XRD, AFM, FTIR, impedance spectroscopy and I – V measurements to measure their optical bandgap, realize the structure of the films, surface roughness, chemical bonding between the metal and the oxide, dielectric constant and leakage current density respectively.

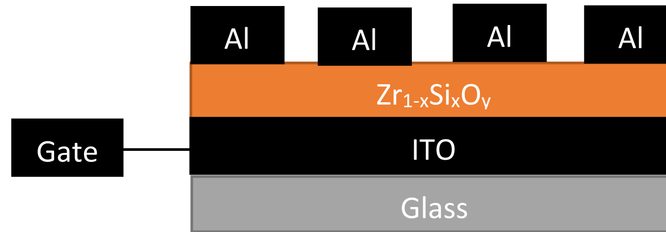

Figure 6- 4. A schematic of a metal-insulator-metal (MIM) stack of glass/ITO/ $Zr_{1-x}Si_xO_y$/Al gate dielectric.

6.5 UV-Vis Spectroscopy

The transmittance (T%) spectra of $Zr_{1-x}Si_xO_y$ films are shown in Figure 6-5. These spectra were used to investigate the optical properties of the $Zr_{1-x}Si_xO_y$ films using the UV-Vis spectroscopy.

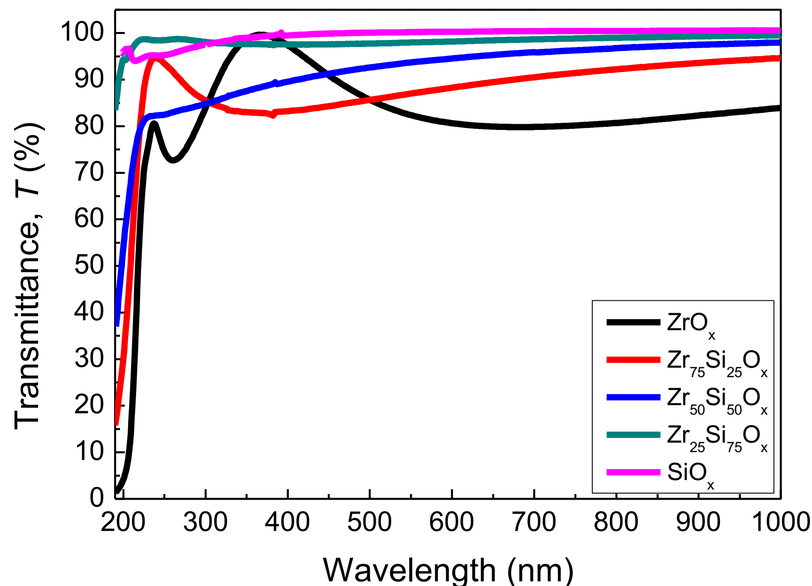

Figure 6- 5. Transmittance T% of spray coated $Zr_{1-x}Si_xO_y$ films with different [Si^{4+}] to [Zr^{4+}] ratios deposited by spray pyrolysis on fused silica substrates.

One can observe the average %transmittance in visible region (400 – 700 nm) that ranges between 80 % and 90 % which demonstrates high transparency of $Zr_{1-x}Si_xO_y$ films as

shown in Figure 6-5. The optical bandgap of $Zr_{1-x}Si_xO_y$ films was derived from the Tauc plots [49] and are shown in Figure 6-6.

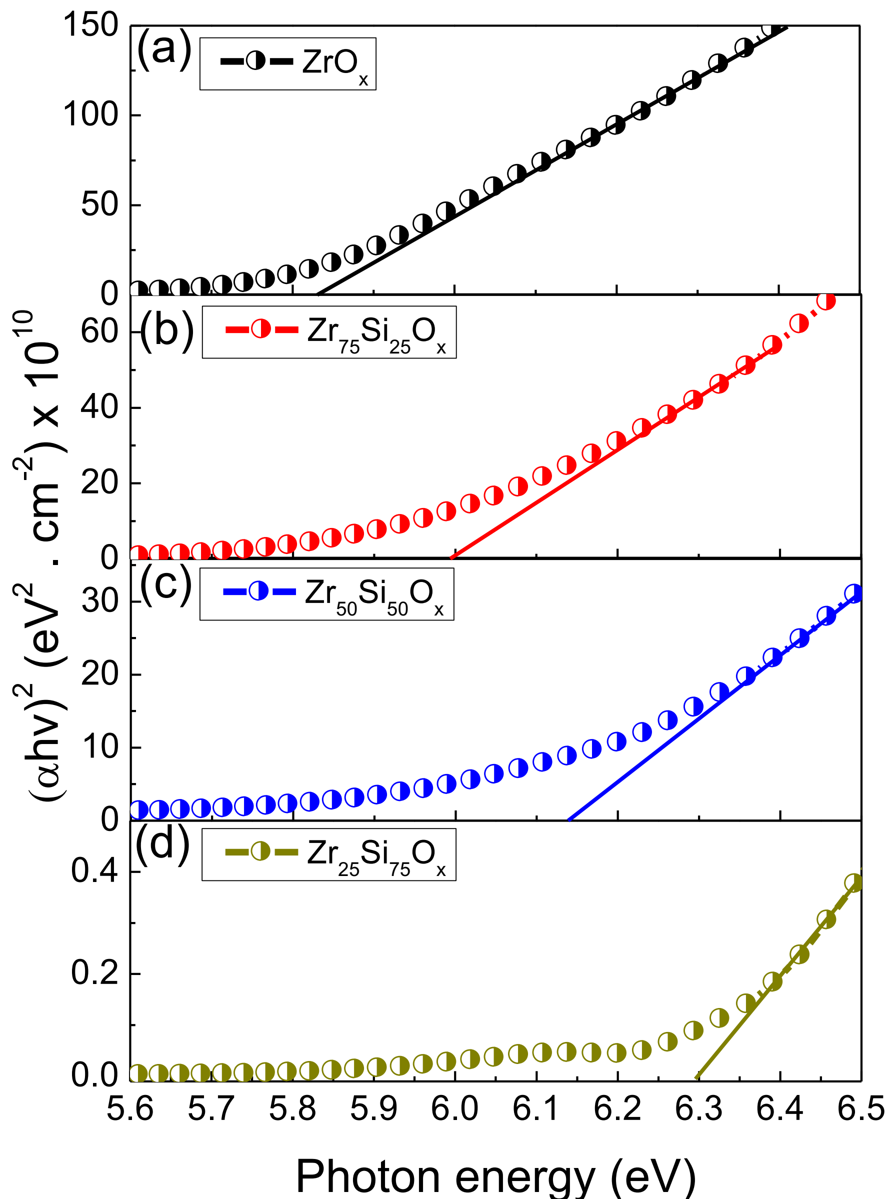

Figure 6- 6. Tauc plots of spray coated $Zr_{1-x}Si_xO_y$ films with different [Si] to [Zr] ratios.

It is important to mention that the Tauc plot of spray coated SiO_x film was not included due to equipment inability to characterize wide bandgap materials greater than 6.5 eV. However, in the recent work reported by Esro et al. [50], they calculated the optical bandgap of SiO_x as 8.11 eV using the spectroscopic ellipsometry model developed by Forouhi – Bloomer [55][56] and modified by Jellison and Modine [53]. On the basis of their work, the optical bandgap of SiO_x was taken as 8 eV and is consistent with the ones reported in the

literatures [58]–[60]. In Figure 6-7, the calculated optical bandgaps as a function of [Si]/[Si + Zr] atomic ratio are shown.

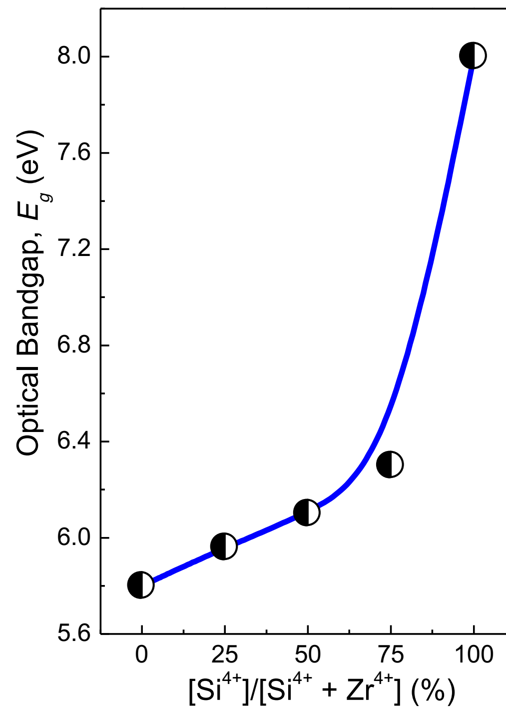

Figure 6- 7. Optical bandgap of $Zr_{1-x}Si_xO_y$ films as a function of the [Si]/ [Si + Zr] atomic ratio. The solid line is a guide to the eye.

The optical bandgap increases drastically from 5.8 eV for ZrO_x to 8 eV for SiO_x with increasing [Si] content as shown in Figure 6-8. In comparison with that of previous studies ($Ta_{1-x}Al_xO_y$ and $Hf_{1-x}Ti_xO_y$), such trend was expected due to the wide bandgap of SiO_x complementing the low bandgap of ZrO_x.

Furthermore, the Urbach tail energy (E_u) analysis was investigated to expose the degree of disorder in $Zr_{1-x}Si_xO_y$ films. Figure 6-8 show the E_u plots of $Zr_{1-x}Si_xO_y$ films.

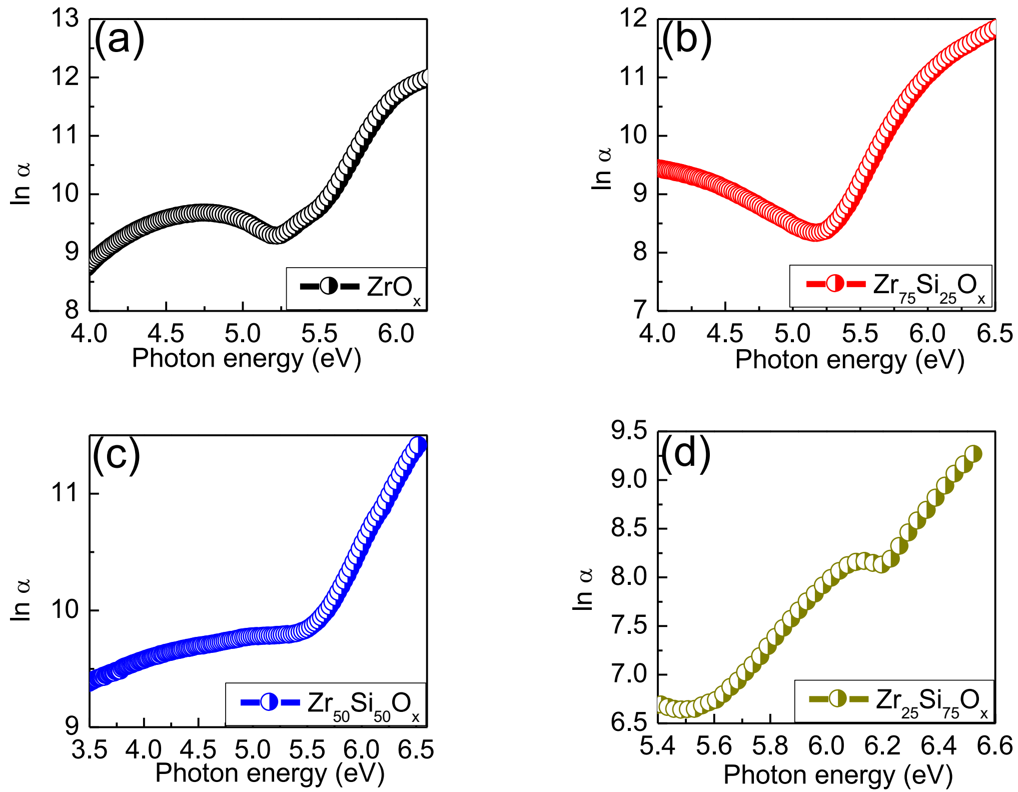

Figure 6- 8. Urbach plots of $Zr_{1-x}Si_xO_y$ films with different [Si] to [Zr] ratios.

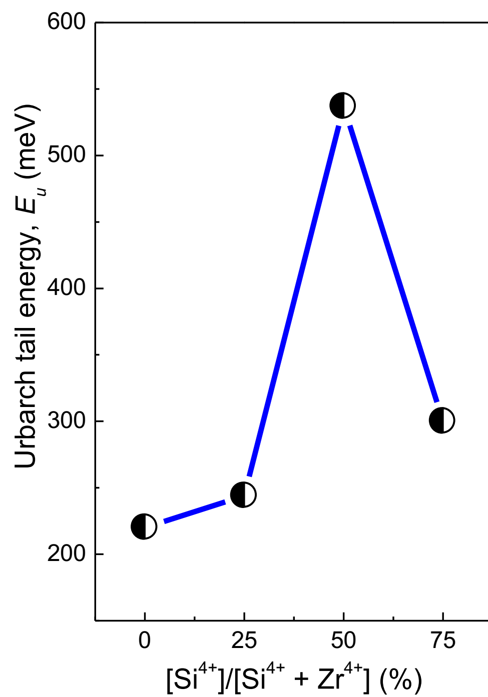

Figure 6- 9. Urbach tail energy (E_u) of $Zr_{1-x}Si_xO_y$ films as a function of [Si]/ [Si + Zr] atomic ratio. The solid line is a guide to the eye.

The calculated E_u values from the inverse slope of Figure 6-8 is further plotted in Figure 6-9 as a function of [Si]/ [Si + Zr] atomic ratio.

The E_u values increases with increasing Si content and reaches maximum (540 meV) for $Zr_{50}Si_{50}O_x$ films. Such high E_u may probably be associated with the formation of amorphous stochiometric $Zr_{1-x}Si_xO_y$ films.

6.6 Fourier Transform Infrared Spectroscopy (FTIR)

The FTIR measurements were performed to identify the chemical bonding of $Zr_{1-x}Si_xO_y$ films. In Figure 6-10, the FTIR absorbance spectra of $Zr_{1-x}Si_xO_y$ films deposited on KBr substrates with different [Si] to [Zr] ratios are shown.

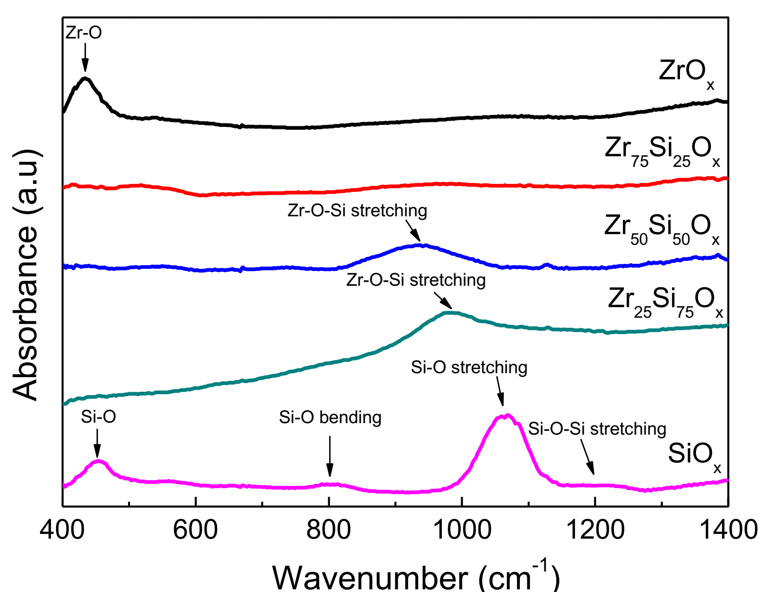

Figure 6- 10. FTIR spectra of as-deposited $Zr_{1-x}Si_xO_y$ films with different [Si^{4+}] to [Zr^{4+}] ratios.

For the ZrO_x spectrum, the dominant characteristic absorbance peak centred at 433 cm^{-1} is due to Zr-O stretching mode [57]. For the SiO_x spectrum, the characteristic peaks centred at 455 cm^{-1}, 800 cm^{-1}, 1060 cm^{-1} and 1200 cm^{-1} are due to out of plane deformation Si-O, Si-O bending, Si-O stretching and Si-O-Si stretching respectively [50]. Finally, the $Zr_{1-x}Si_xO_y$ spectrum showed some broad peaks centred at 930 cm^{-1} and 977 cm^{-1} and are due to stretching modes of Zr-O-Si [5][7]. These broad peaks are characteristics of poor crystalline materials and could explain the high E_u value of $Zr_{50}Si_{50}O_y$ films seen in Figure 6-9.

6.7 Structural and Surface Properties

The grazing incidence x-ray diffraction (GIXRD) and the atomic force microscopy (AFM) measurements were conducted to investigate the structural and surface properties of $Zr_{1-x}Si_xO_y$ films.

6.7.1 Grazing Incidence X-Ray Diffraction (GIXRD)

The GIXRD patterns of $Zr_{1-x}Si_xO_y$ films are illustrated In Figure 6-11.

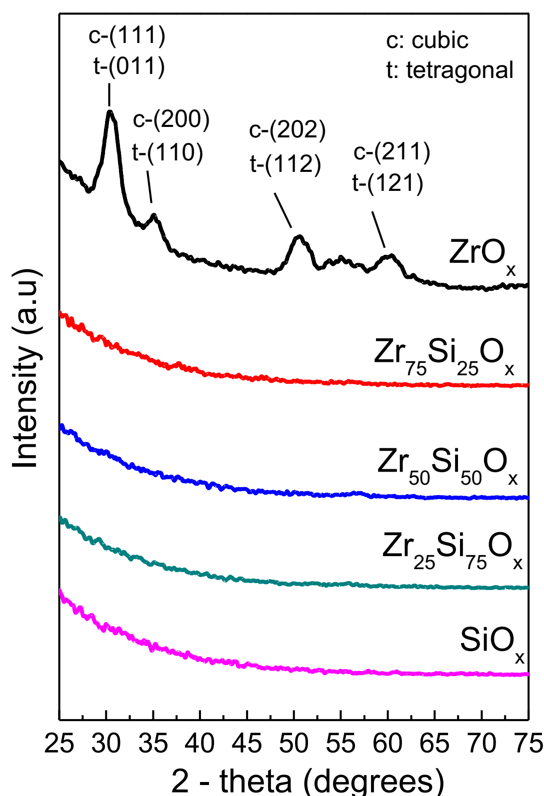

Figure 6- 11. GIXRD patterns of $Zr_{1-x}Si_xO_y$ films deposited by spray pyrolysis on silicon substrates.

The GIXRD patterns shows diffraction peaks on ZrO_x films that are attributed to the presence of either cubic (JCPDS CAS number 27 – 0997) or tetragonal (JCPDS CAS number 80 – 0965) phase ZrO_2. The diffraction peaks of (111), (200), (202) and (311) planes reveal the presence of the c-ZrO_2 while (011), (110), (112) and (121) for t-ZrO_2. These observations have also been reported by Basahel et al. [59], when they synthesized ZrO_2 films with different precursors.

Further indexing on the diffraction peak at ~30.4 ° was calculated using Debye – Scherrer formular [60] and the average crystallite size <d> of 4 nm and lattice constant of a = 5.0662 Å were obtained for c-ZrO_2 while 4 nm and a = 3.6194 Å and c = 4.9660 Å for t-ZrO_2.

However, the GIXRD patterns of $Zr_{1-x}Si_xO_y$ films showed no diffraction peaks, indicating amorphous films. This finding correlates well with that of Rittersma et al. [44] , and Zhong et al. [43], for as-deposited zirconium silicate films and even after annealing at 500 °C.

6.7.2 Atomic Force Microscopy (AFM)

To assess the interface quality of the $Zr_{1-x}Si_xO_y$ films, the AFM measurements on silicon substrates were performed and the images presented are the raw images after they have been flattened out. Figure 6-12 show the AFM images of spray coated $Zr_{1-x}Si_xO_y$ films.

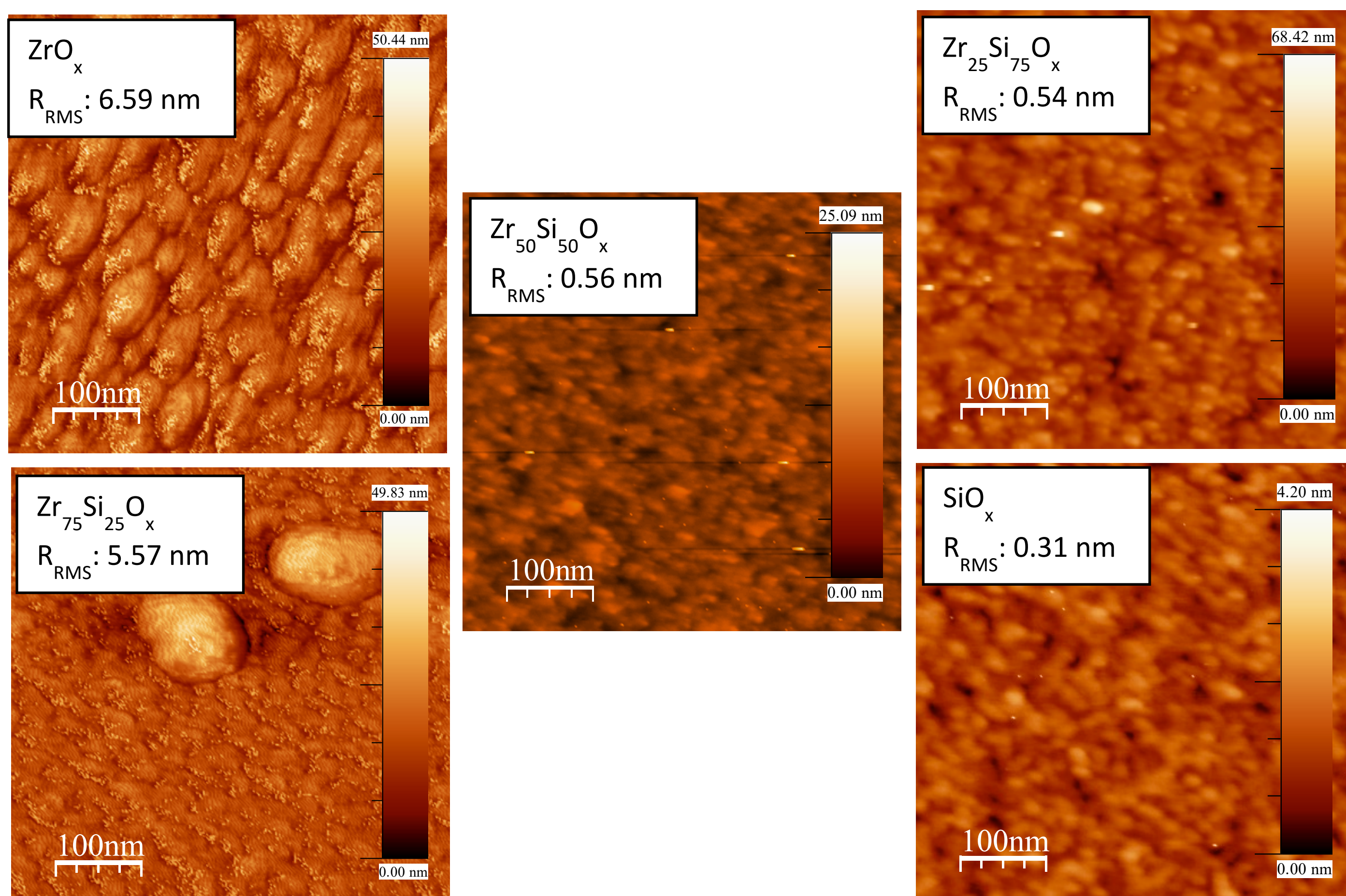

Figure 6- 12. AFM topography images (RMS roughness inset) of $Zr_{1-x}Si_xO_y$ films with different [Si] to [Zr] ratios on silicon substrates.

The surface roughness of $Zr_{1-x}Si_xO_y$ films varies from 6.59 nm for ZrO_x and 0.31 nm for SiO_x with different [Si] to [Zr] ratios as shown in the images (inset) presented in Figure 6-12. In Figure 6-13, the RMS values are plotted as a function of $[Si^{4+}]/ [Si^{4+} + Zr^{4+}]$ atomic ratio.

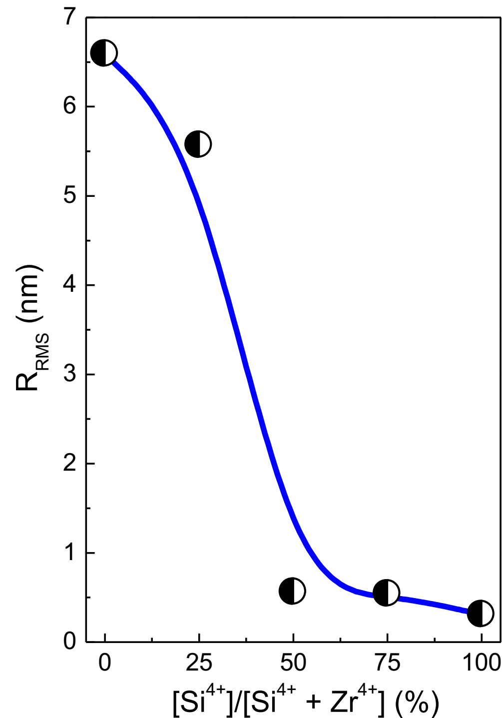

Figure 6- 13. RMS values of $Zr_{1-x}Si_xO_y$ films as a function of [Si]/ [Si + Zr] atomic ratio.

As evidence from the graph, the RMS values decreases with the addition of [Si] content. Such decrease is important for $Zr_{1-x}Si_xO_y$ films as it demonstrate smoothness and quality interface for future implementation as gate dielectric in TFTs.

6.8 Electrical Properties

One of the most important parameters of a dielectric material is its dielectric constant and leakage current density. The performance of $Zr_{1-x}Si_xO_y$ films as gate dielectric was investigated by impedance spectroscopy and I – V characterizations.

6.8.1 Impedance Spectroscopy

The static dielectric constant dispersion of $Zr_{1-x}Si_xO_y$ films obtained from the impedance analysis is shown in Figure 6-14.

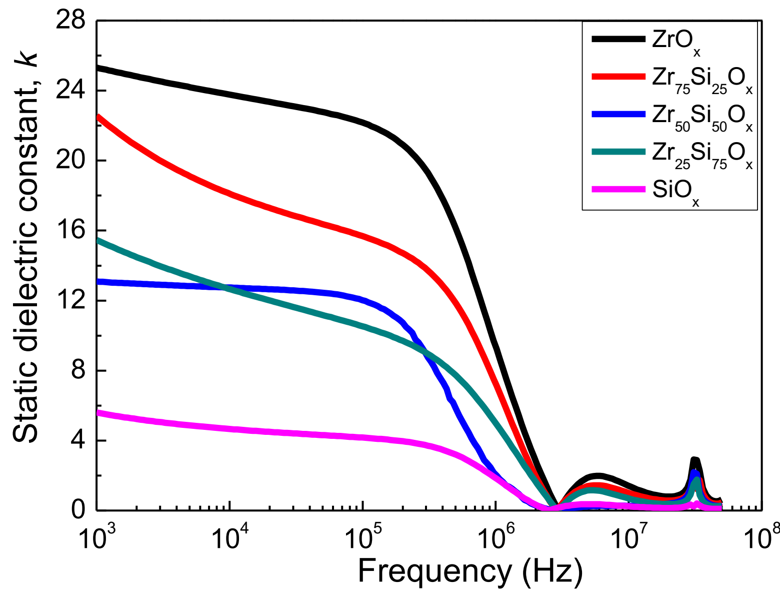

Figure 6- 14. Static dielectric constant dispersions of $Zr_{1-x}Si_xO_y$ films in the frequency range of 1 kHz – 50 MHz.

The dispersions of $Zr_{1-x}Si_xO_y$ films indicated that dielectric constant values are higher at low frequencies (1 kHz) compared to the high frequencies (>100 kHz). The change in the dispersion behaviour from high dielectric constant at low frequencies to low dielectric constant at high frequencies may be attributed to the dielectric polarization. This observation has also been reported by Zhang et al. [61], in their work on frequency dispersion analysis of thin dielectric MOS capacitor. In Figure 6-15, the calculated dielectric constant at 30 kHz were further plotted as a function of $[Si^{4+}]/ [Si^{4+} + Zr^{4+}]$ atomic ratio.

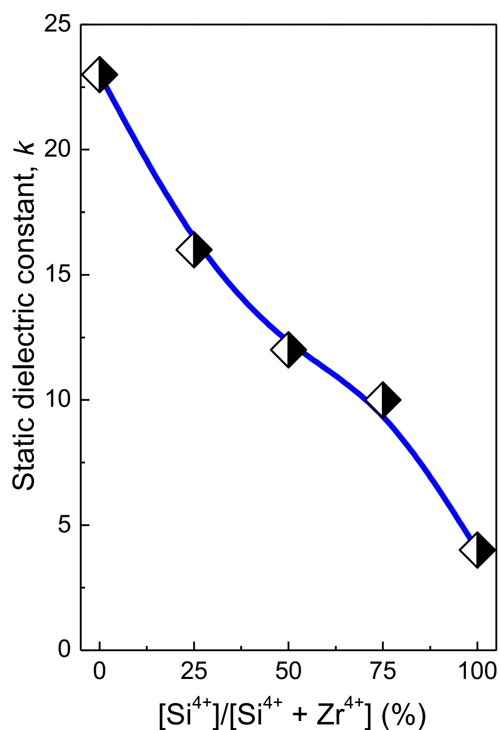

Figure 6- 15. Static dielectric constant of $Zr_{1-x}Si_xO_y$ films (at 30 kHz) as a function of [Si]/ [Si + Zr] atomic ratio. The solid line is a guide to the eye.

As seen in Figure 6-15, the k value varies between 23 for ZrO_x and 4.2 for SiO_x. it is obvious that such trend was expected for high k metal oxides combining with the low k ones. Particularly, the stochiometric $Zr_{50}Si_{50}O_x$ films exhibited a dielectric constant of 12 and it is in good agreement with the reported values in literatures as already illustrated in Table 6-2.

Another important parameter that a good dielectric should exhibit, is the stability in a MIM stack. The stability of $Zr_{1-x}Si_xO_y$ films were investigated by the Nyquist plots that are shown in Figure 6-16.

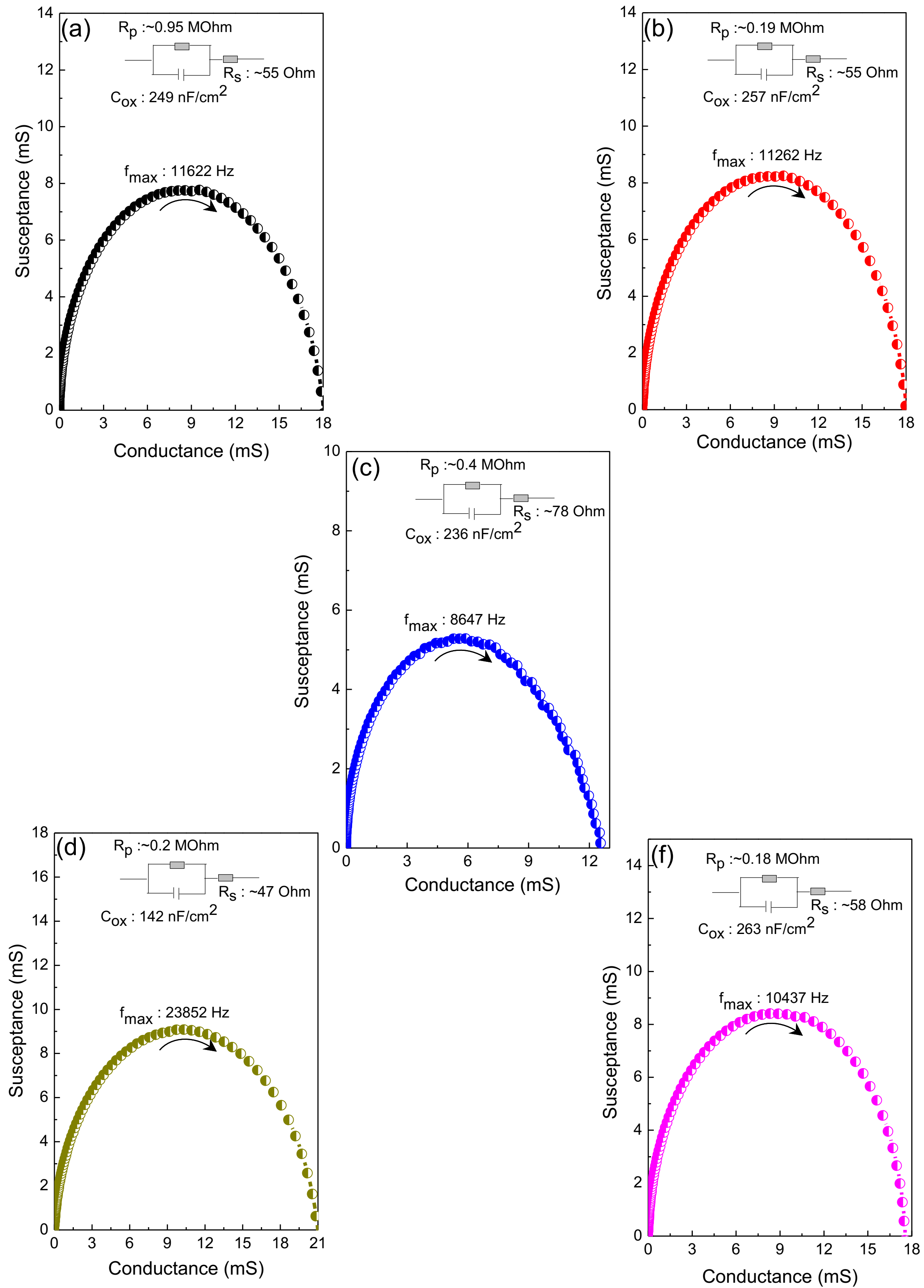

Figure 6- 16. Nyquist plots and equivalent circuit (inset) of (a) ZrO_x (b) $Zr_{75}Si_{25}O_x$ (c) $Zr_{50}Si_{50}O_x$ (d) $Zr_{25}Si_{75}O_x$ and (e) SiO_x films.

The stability of a Nyquist plot should exhibit a parabolic behaviour, starting from the origin and without any diffusion. As seen in the plots $Zr_{1-x}Si_xO_y$ films were stable in MIM stacks. Furthermore, the equivalent circuits in the inset of Figure 6-16 are the evidence of an excellent capacitive properties such as large shunt and low series resistance.

In relation to the trade-off between the static dielectric constant and optical bandgap of high-k dielectrics, Figure 6-17, demonstrate the relationship between the calculated static dielectric constant and optical bandgap of $Zr_{1-x}Si_xO_y$ films.

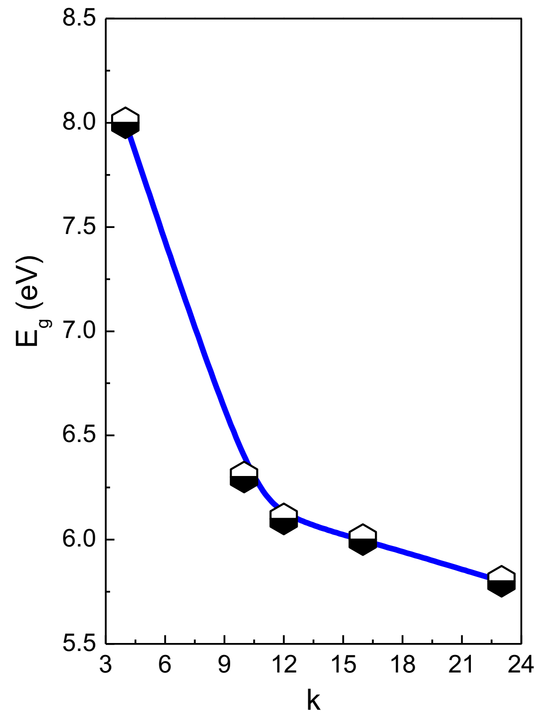

Figure 6- 17. Static dielectric constant versus optical bandgap of $Zr_{1-x}Si_xO_y$ films. The solid line is a guide to the eye.

As already seen in Figure 6-17, the optical bandgap of $Zr_{1-x}Si_xO_y$ films varies inversely with its static dielectric constant and such trend agrees with the trade-off between the optical bandgap and static dielectric constant of a number of other both solution and vacuum processed gate dielectrics [2][47][62]–[64].

6.8.2 I – V Characterization

The I – V measurements characterize the electrical properties $Zr_{1-x}Si_xO_y$ films, using the Agilent B1500A semiconductor parameter analyser. The leakage current density (J) of $Zr_{1-x}Si_xO_y$ films recorded at 1 MV/cm as a function of [Si]/ [Si + Zr] atomic ratio is shown in Figure 6-18.

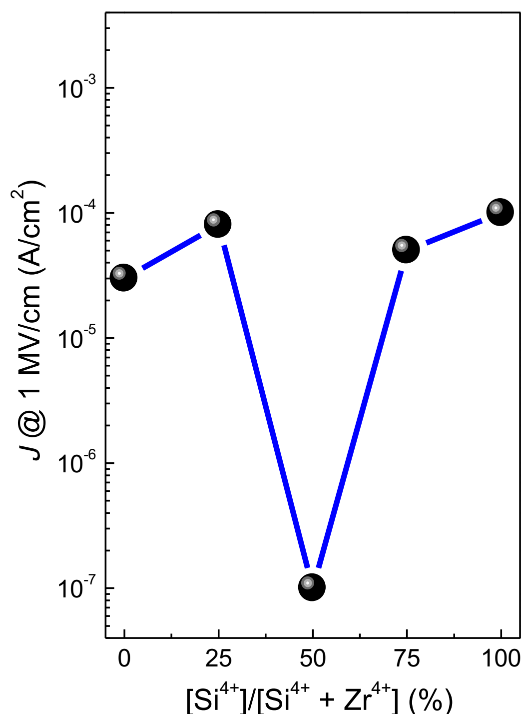

Figure 6- 18. J @ 1 MV/cm of $Zr_{1-x}Si_xO_y$ films as a function of [Si]/ [Si + Zr] atomic ratio. The solid line is guide to the eye.

Interestingly, the stochiometric $Zr_{1-x}Si_xO_y$ films exhibited the lowest leakage current density (10^{-7} A/cm^2) at 1 MV/cm. This is a significant achievement compared to the values reported in the literatures, where they obtained their leakage currents at very low voltages. For instance, Rittersma et al. [44], obtained a leakage current density of 10^{-3} A/cm^2 at 4 V for stochiometric $Zr_{1-x}Si_xO_y$ films deposited by ALD. Wilk et al. [41], similarly obtained a leakage current density of 10^{-6} A/cm^2 at 1 V for sputtered $Zr_{1-x}Si_xO_y$ films. Also, Chung et al. [45], obtained a leakage current density of 10^{-8} A/cm^2 at 1 V for $Zr_{1-x}Si_xO_y$ films deposited by ALD.

Furthermore, to elucidate the origin of leakage current in $Zr_{1-x}Si_xO_y$ films, the Schottky emission (SE), Fowler-Nordheim (FN) and Poole-Frenkel (PF) conduction mechanism [65] were investigated. Figures 6-19 to 6-21 show the SE, FN & PF plots of $Zr_{1-x}Si_xO_y$ films.

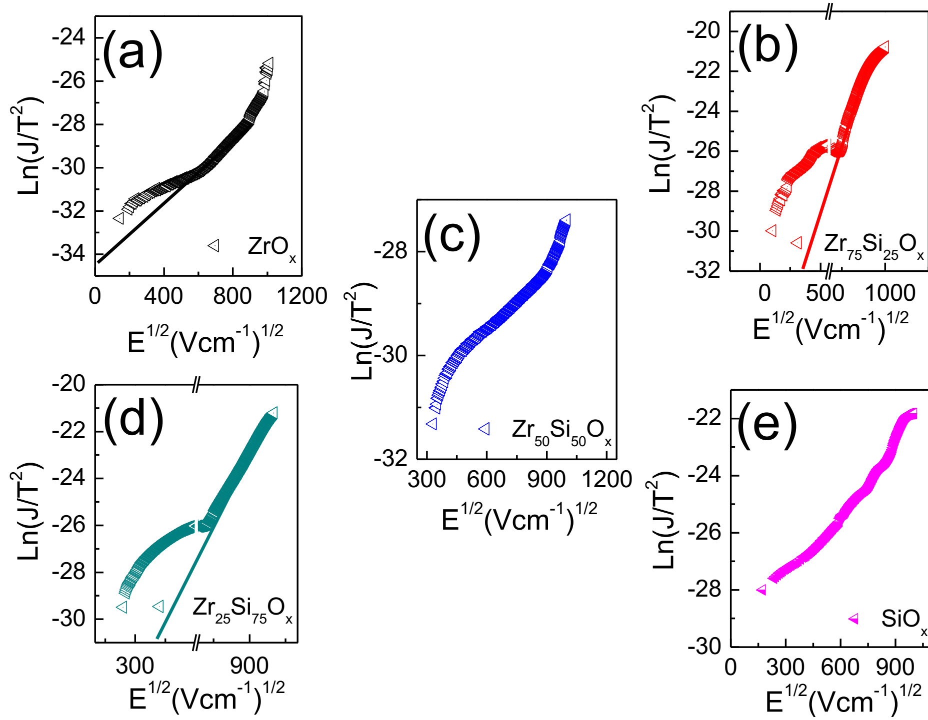

Figure 6- 19. Schottky emission plots of (a) ZrO_x (b) $Zr_{75}Si_{25}O_x$ (c) $Zr_{50}Si_{50}O_x$ (d) $Zr_{25}Si_{75}O_x$ and (e) SiO_x films.

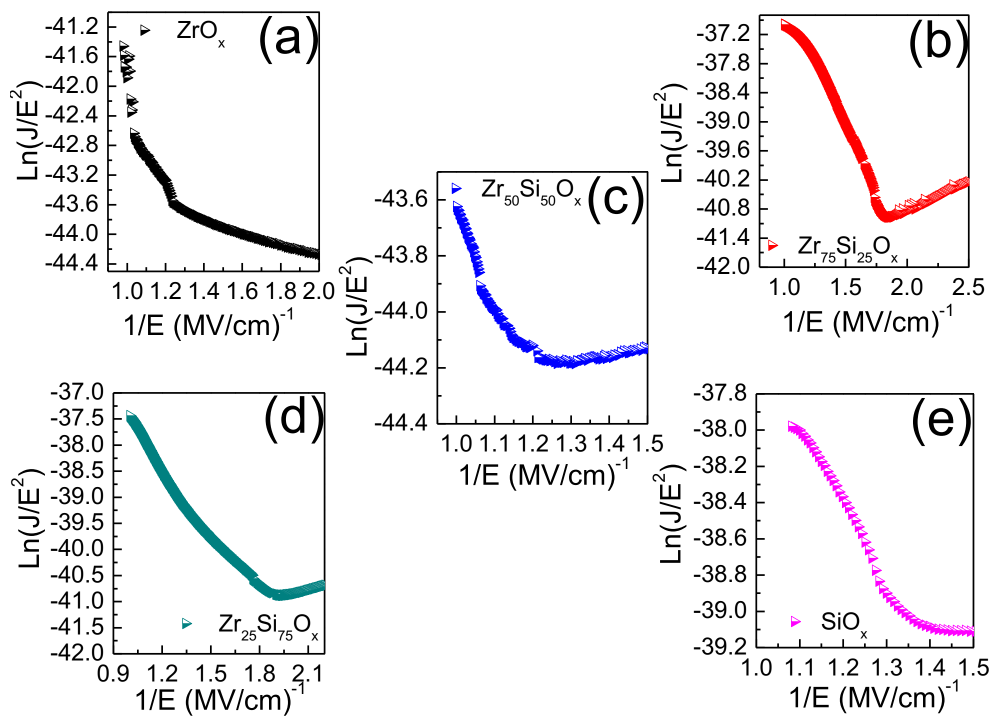

Figure 6- 20. Fowler-Nordheim plots of (a) ZrO_x (b) $Zr_{75}Si_{25}O_x$ (c) $Zr_{50}Si_{50}O_x$ (d) $Zr_{25}Si_{75}O_x$ and (e) SiO_x films.

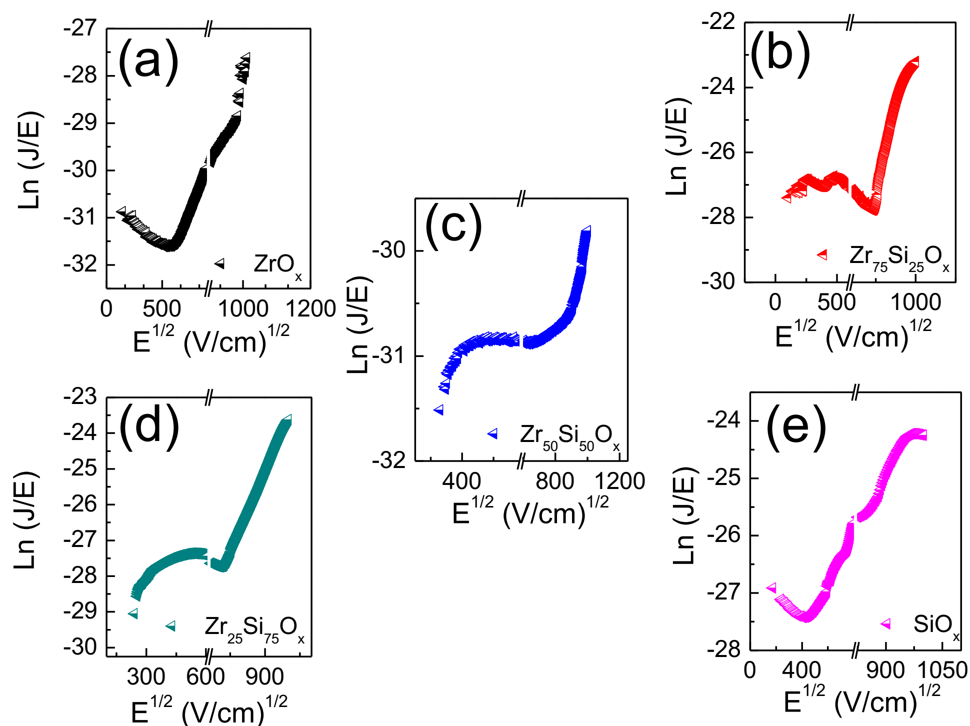

Figure 6- 21. Poole-Frenkel plots of (a) ZrO_x (b) $Zr_{75}Si_{25}O_x$ (c) $Zr_{50}Si_{50}O_x$ (d) $Zr_{25}Si_{75}O_x$ and (e) SiO_x films.

Analysing the SE plots shown in Figure 6-19(a-e), all $Zr_{1-x}Si_xO_y$ films exhibited linear behaviour at high electric fields except for SiO_x films. The former could potentially dominate the conduction in $Zr_{1-x}Si_xO_y$ films while the latter could not. Similarly, in the FN plots shown in Figure 6-20(a-e), the ZrO_x films exhibited linear behaviour at low electric fields, however, other $Zr_{1-x}Si_xO_y$ films, except for stochiometric $Zr_{1-x}Si_xO_y$ films, exhibited linear behaviour at high electric fields. Finally, the PF plots shown in Figure 6-21(a-e) varies linearly at high electric fields in all cases and as result could also be considered as dominant conduction in $Zr_{1-x}Si_xO_y$ films.

Comparing the plots (SE, FN and PF), one can simply conclude that the PF conduction mechanism is the most dominant mechanism in $Zr_{1-x}Si_xO_y$ films considering the fact that all the plots vary linearly over wide range of electric field. Paskaleva et al. [39], already reported that the leakage current in $Zr_{1-x}Si_xO_y$ films deposited by MOCVD is dominated by PF conduction at high voltages while the trap-assisted tunneling at low voltages. The former justifies the findings for the stochiometric $Zr_{1-x}Si_xO_y$ films while the latter was not investigated because it is not within the scope of the present study. Generally, in the PF mechanism, trapped electrons are released from their trapping centres by high electric field to excite them into the conduction band and thus, such is the case for the $Zr_{1-x}Si_xO_y$ films.

6.8.3 Field Effect Measurement

Finally, the performance of $Zr_{1-x}Si_xO_y$ films as gate dielectric for ZnO – based TFTs were investigated by employing the bottom-gate top-contact (BG – TC) TFT device architecture.

The schematic of the ZnO-based TFT employing $Zr_{1-x}Si_xO_y$ gate dielectric is shown in Figure 6-22.

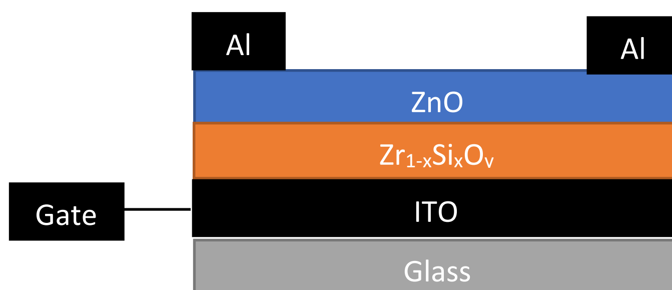

Figure 6- 22. BG – TC ZnO-based TFT architecture employing $Zr_{1-x}Si_xO_y$ gate dielectric.

The performance of the ZnO – based TFTs employing as-deposited $Zr_{1-x}Si_xO_y$ gate dielectrics were assessed by their transfer and output characteristics. From the transfer characteristic plots, the saturation mobility (μ), subthreshold swing (SS) and current modulation ratio ($I_{on/off}$) could be determined while the output characteristics plot will show the voltage operation of the TFT.

In Figures 6-23 – 6-27, the transfer and output characteristic plots of ZnO – based TFTs employing $Zr_{1-x}Si_xO_y$ gate dielectrics is shown, using the channel length and width of 100 μm and 2000 μm respectively. It is important to mention that the deposition of SiO_x films as gate dielectric were unsuccessful due to the film thickness (<15 nm) that requires very large volume of precursor solution to be deposited. As a result, the ZnO films were spray coated onto commercially available SiO_2 substrate for the TFT investigation. As for the TFT samples deposited on the ITO substrate, the thickness of the gate dielectrics was between 50 and 80 nm.

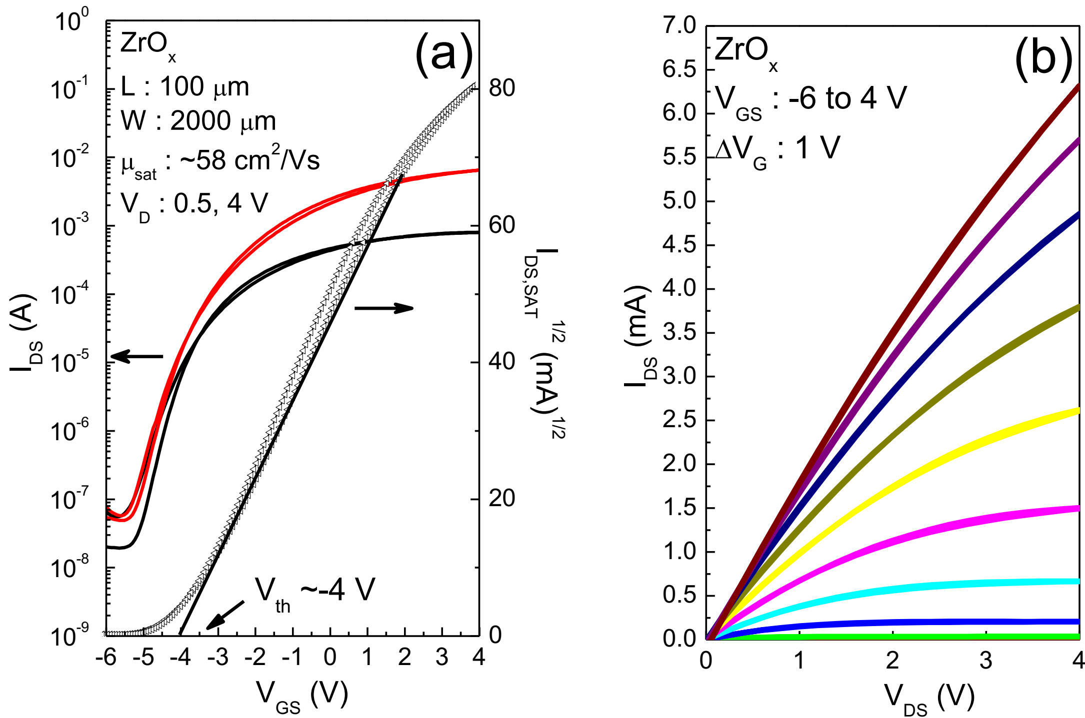

Figure 6- 23. (a) Transfer and (b) output characteristics of ZnO – based TFTs employing ZrO_x gate dielectric.

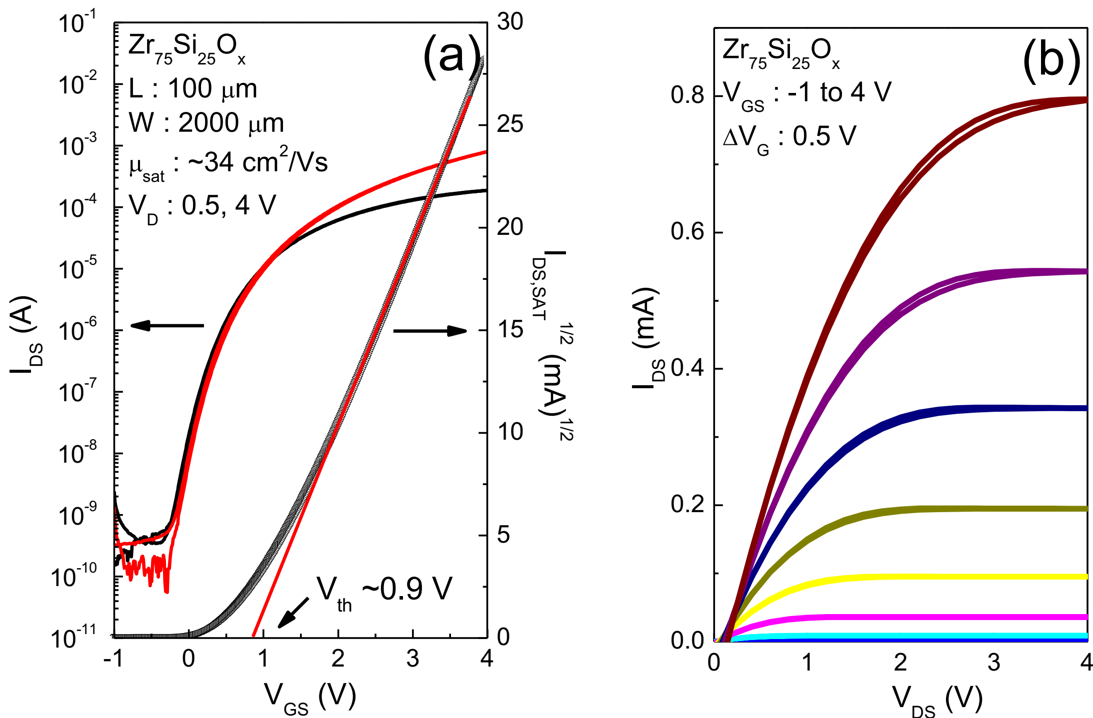

Figure 6- 24. (a) Transfer and (b) output characteristics of ZnO – based TFTs employing $Zr_{75}Si_{25}O_x$ gate dielectric.

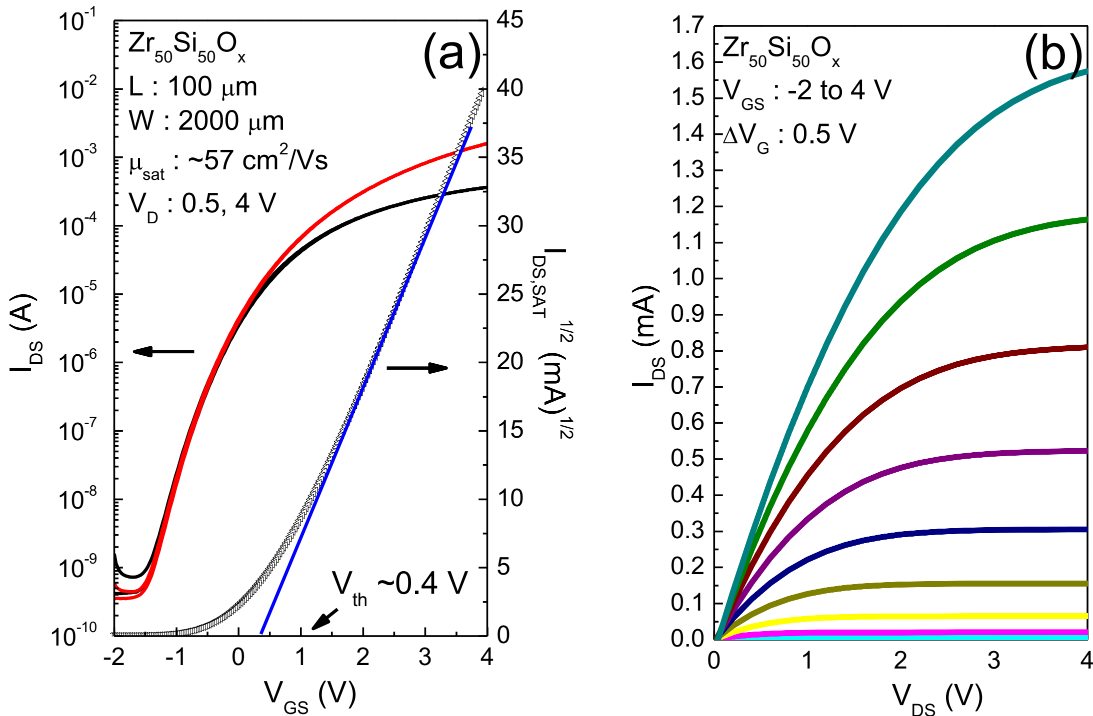

Figure 6- 25. (a) Transfer and (b) output characteristics of ZnO – based TFTs employing $Zr_{50}Si_{50}O_x$ gate dielectric.

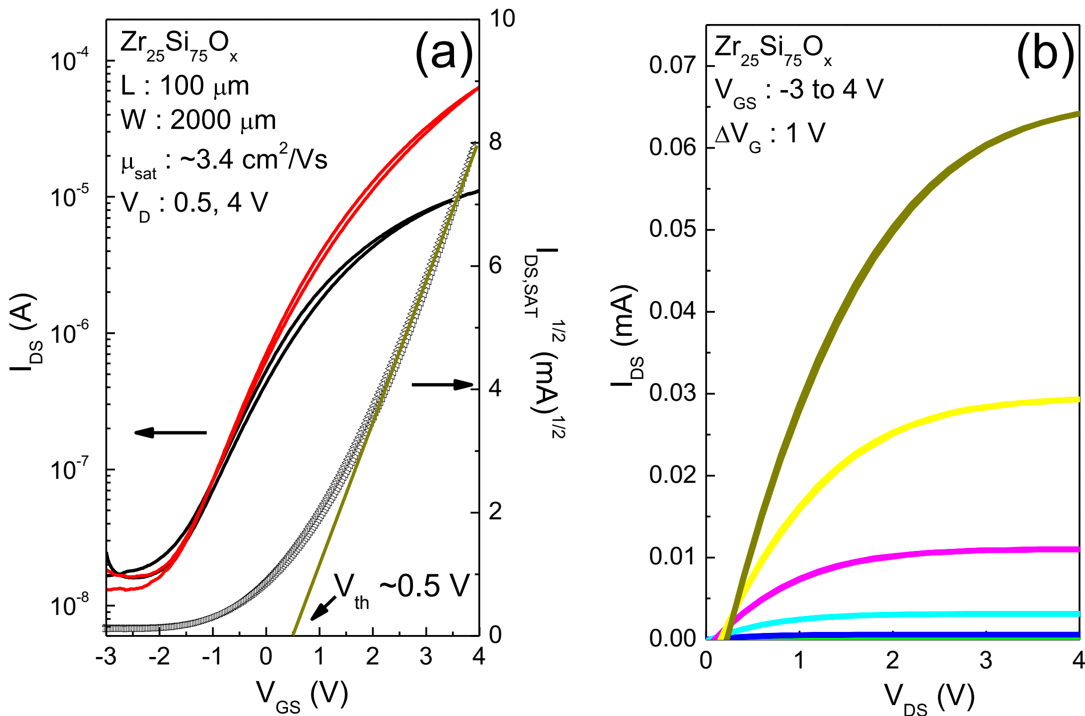

Figure 6- 26. (a) Transfer and (b) output characteristics of ZnO – based TFTs $Zr_{25}Si_{75}O_x$ gate dielectric.

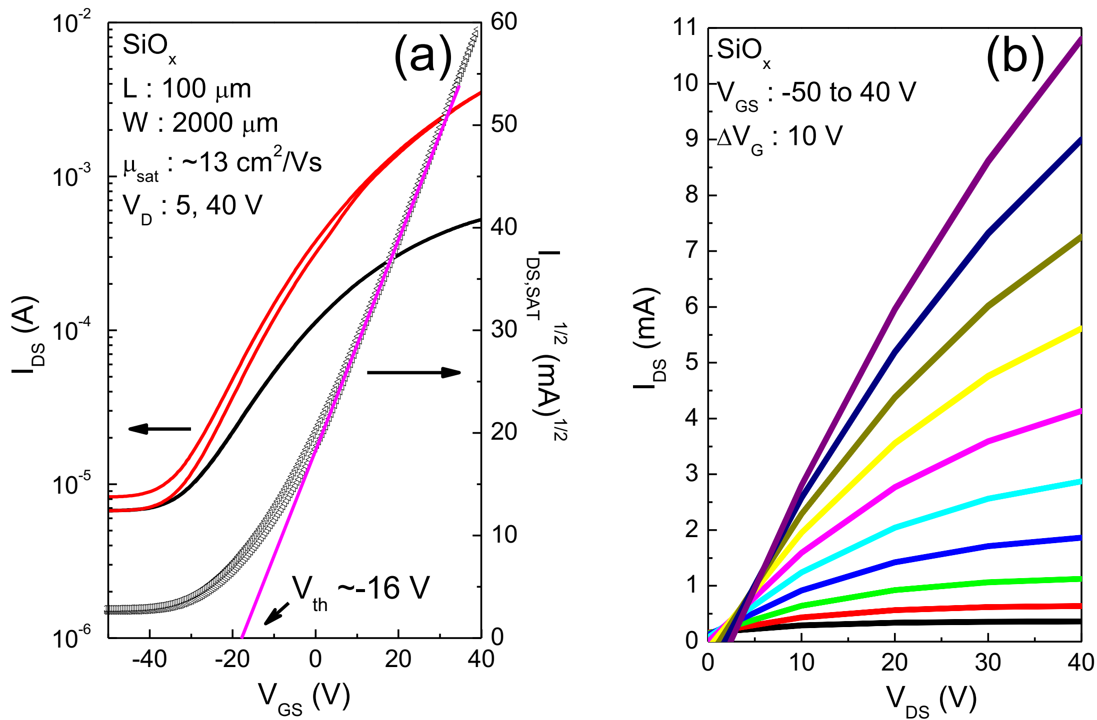

Figure 6- 27. (a) Transfer and (b) output characteristics of ZnO – based TFTs SiO_x gate dielectric.

As can be seen, all the TFTs exhibited low voltage operation of 4 V (except for SiO_x, which is a low-k gate dielectric) and negligible hysteresis. To further elaborate on the performance of the ZnO – based TFTs employing $Zr_{1-x}Si_xO_y$ gate dielectrics, Figure 6-28(a-e) show the dependence of the properties in terms of electron mobility (μ), current modulation ratio ($I_{on/off}$), threshold voltage (V_{th}), subthreshold swing (SS) and interface trap density as a function of [Si]/ [Si + Zr] atomic ratio.

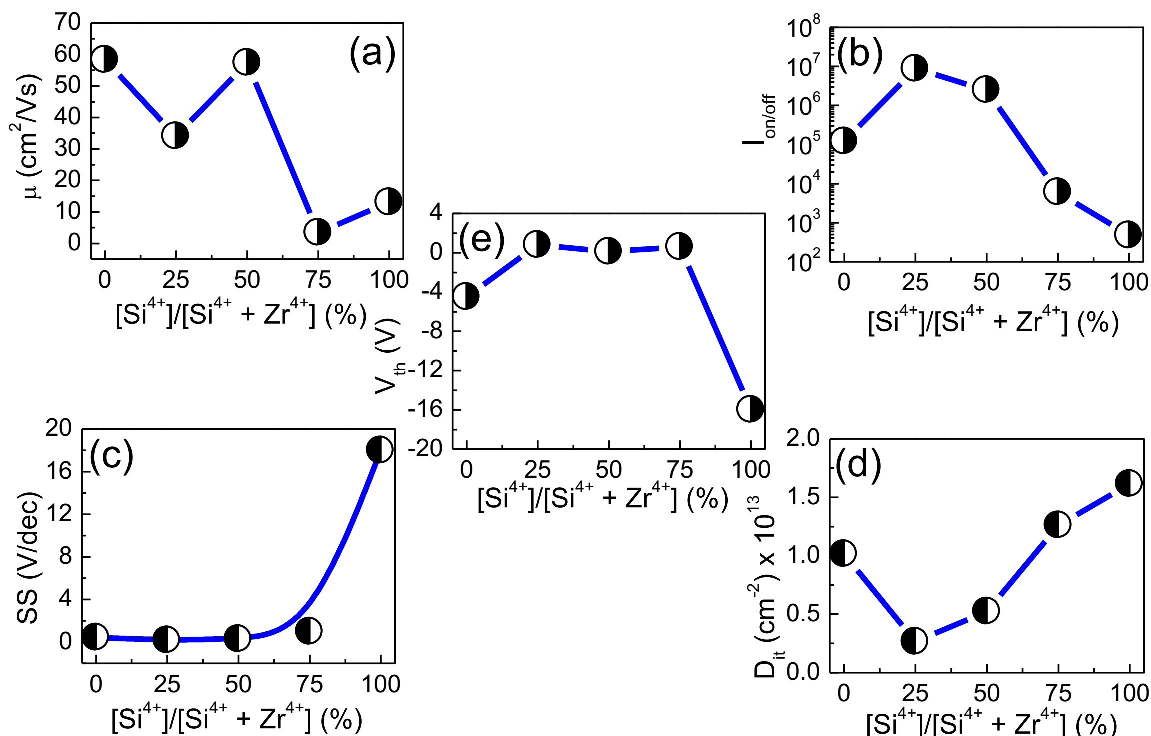

Figure 6- 28. (a) Electron mobility (b) Current modulation ratio, (c) Threshold voltage, (d) Subthreshold swing (SS) and (e) Interface trap density of ZnO – based TFTs employing spray coated stoichiometric $Zr_{1-x}Si_xO_y$ gate dielectric.

Analysing Figure 6-28(a), one can see that the ZnO – based TFTs employing Zr-rich gate dielectrics exhibited higher mobilities than the Si-rich ones. Interestingly, there wasn't any significant change in the μ (58 cm^2/Vs) of the TFTs between ZrO_x and stochiometric $Zr_{1-x}Si_xO_y$ gate dielectric. The $I_{on/off}$ plot (Figure 6-28b) however, shows slight improvement on the order of magnitude from 10^5 to 10^6.

The SS values also varies between 0.44 V/dec and 18 V/dec with increasing [Si]/ [Si + Zr] atomic ratio as seen in Figure 6-28 (c). As already known the SS values determines how quickly the gate voltage increases by an order of magnitude which is significant to the $I_{on/off}$. The lower the SS the faster the switching speed and is significant to the performance of the TFT.

The interface trap density (D_{it}) values were averaged 10^{13} cm^{-2} with increasing [Si]/ [Si + Zr] atomic ratio as seen in Figure 6-28(d). Martin et al. [66], reported the D_{it} value of 10^{13} and 2 x 10^{13} cm^{-2} for ZnO/dielectric and 1ZO/dielectric. They concluded that such values are quite acceptable for an oxide/oxide interface or an interface using high-k materials.

Finally, the V_{th} fluctuates between -4 V for ZrO_x and -16 V for SiO_x with increasing [Si]/ [Si + Zr] atomic ratio as seen in Figure 6-28(e). The negative V_{th} only occur for both pure ZrO_x and SiO_x gate dielectric. The reason for such occurrence especially for ZrO_x gate dielectric was not understood, however a much more negative threshold voltage for SiO_x gate dielectric may

be probably due to its low dielectric constant that further increases the interface trap density. Huang et al. [67], reported that the interface traps influence the polarity change in the V_{th} of an n-channel and p-channel TFTs. The D_{it} of SiO_x exhibited the highest among other $Zr_{1-x}Si_xO_y$ gate dielectrics, thus explains the reason for such -V_{th} in ZnO-based TFT employing SiO_x gate dielectric.

6.9 Conclusion

The properties of $Zr_{1-x}Si_xO_y$ films with different [Si] to [Zr] ratios were investigated by spray pyrolysis. It was observed that the optical bandgap and Urbach tail energy of $Zr_{1-x}Si_xO_y$ films vary between 5.8 and 8 eV and 200 and 540 meV respectively as a function of [Si]/ [Si + Zr] atomic ratio. All spray coated $Zr_{1-x}Si_xO_y$ films were amorphous except for ZrO_x films that showed presence of both cubic and tetragonal phase. The former and the latter yields an average crystallite size of 4 nm however, different lattice constant values (a = 5.0662 Å for c-ZrO_2 and a = 3.6194 Å and c = 4.9960 Å for t-ZrO_2). The topographical images of $Zr_{1-x}Si_xO_y$ films were taken and the surface roughness varies between 6.59 and 0.31 nm as a function of [Si]/ [Si + Zr] atomic ratio. The dielectric constant of $Zr_{1-x}Si_xO_y$ films were calculated and the values were in the range between 23 and 4 as a function of [Si]/ [Si + Zr] atomic ratio. The leakage current density at 1 MV/cm were measured and values $3 \times 10^{-5} – 10^{-4}$ A/cm^2 were obtained. Further investigations on the conduction mechanism showed that the current transport was dominated by Poole – Frenkel mechanism.

Particularly, the stochiometric $Zr_{1-x}Si_xO_y$ films exhibited some promising properties as gate dielectric for future implementation in TFTs. Such properties include wide optical bandgap of 6.1 eV, Urbach energy of 537 meV, it is amorphous, low surface roughness of 0.56 nm, high dielectric constant of 12 and low leakage current density of 10^{-7} A/cm^2 at 1 MV/cm.

Finally, the performance of ZnO – based TFTs employing $Zr_{1-x}Si_xO_y$ gate dielectric showed some electronic characteristics as a function [Si]/ [Si + Zr] atomic ratio. The electron mobility varies between 58 and 13 cm^2/Vs, the current modulation ratio was varied between 10^5 and 10^2, with the highest recorded as 10^7 for $Zr_{75}Si_{25}O_x$ gate dielectric, the subthreshold swing values were varied between 0.44 and 18 V/dec, the interface trap density values were varied between 10^{13} and 1.6×10^{13} cm^{-2} and finally the threshold voltage fluctuated between -4 and -16 V. All the transistors operated at the voltage of 4 V except for SiO_x gate dielectric that operated at 40 V due to its low dielectric constant.

Amongst all the transistors, the stochiometric $Zr_{1-x}Si_xO_y$ gate dielectric exhibited the best performance in terms of mobility of 57 cm^2/Vs even though it didn’t show any significant change compared to pure ZrO_x gate dielectric, current modulation ratio of 10^6 which improved by an order of magnitude compared to pure ZrO_x gate dielectric, threshold voltage of 0.1 V, low subthreshold swing of 0.28 V/dec and interface trap density of 5×10^{12} cm^{-2}.

6.10 References

[1] B. Bocher, P. Frach, and K. Goedicke, "Properties of SiO_2 and Al_2O_3 films for electrical insulation applications deposited by reactive pulse magnetron sputtering," *Surf. Coatings Technol.*, vol. 174–175, pp. 774–778, 2003.

[2] P. W. P. and J. Robertson, "Band offsets and Schottky barrier heights of high dielectric constant oxides," *J. Appl. Phys.*, vol. 92, no. 8, pp. 4712–4721, 2002.

[3] M. Andrieux, P. Ribot, C. Gasquères, B. Servet, and G. Garry, "Effect of the oxygen partial pressure on the toughness of tetragonal zirconia thin films for optical applications," *Appl. Surf. Sci.*, vol. 263, pp. 284–290, 2012.

[4] A. T. Oluwabi, A. Katerski, E. Carlos, R. Branquinho, A. Mere, M. Krunks, E. Fortunato, L. Pereira, and I. O. Acik, "Application of ultrasonic sprayed zirconium oxide dielectric in zinc tin oxide-based thin film transistor," *J. Mater. Chem. C*, vol. 8, no. 11, pp. 3730–3739, 2020.

[5] S. W. Kim, M. C. Nguyen, A. H. T. Nguyen, S. J. Choi, H. M. Ji, J. G. Cheon, K. M. Yu, J. H. Kim, S. Y. Cho, and R. Choi, "Solution-Processed Rb-Doped Indium Zinc Oxide Thin-Film Transistors," vol. 39, no. 9, pp. 2018–2021, 2018.

[6] B. R. Naik, C. Avis, M. D. H. Chowdhury, T. Kim, T. Lin, and J. Jang, "Improvement in performance of solution-processed indium-zinc-tin oxide thin-film transistors by UV/O_3 treatment on zirconium oxide gate insulator," *Jpn. J. Appl. Phys.*, vol. 55, no. 3, 2016.

[7] A. Zeumault and V. Subramanian, "Mobility Enhancement in Solution-Processed Transparent Conductive Oxide TFTs due to Electron Donation from Traps in High-k Gate Dielectrics," *Adv. Funct. Mater.*, vol. 26, no. 6, pp. 955–963, 2016.

[8] D. Wang, J. Lu, Y. Jeon, S. Ouyang, and Y. Xie, "Low temperature solution processed high-κ zirconium oxide gate insulator by Broadband-UV annealing," *Org. Electron.*, vol. 57, no. October 2017, pp. 341–344, 2018.

[9] A. D. Mottram, P. Pattanasattayavong, I. Isakov, G. W. Moon, H. Faber, Y. H. Lin, and T. D. Anthopoulos, "Electron mobility enhancement in solution-processed low-voltage In_2O_3 transistors via channel interface planarization," *AIP Adv.*, vol. 8, no. 6, 2018.

[10] R. N. Bukke, C. Avis, M. N. Naik, and J. Jang, "Remarkable Increase in Field Effect Mobility of Amorphous IZTO Thin-Film Transistors with Purified ZrO_x Gate Insulator," *IEEE Electron Device Lett.*, vol. 39, no. 3, pp. 371–374, 2018.

[11] J. W. Jo, K. H. Kim, J. Kim, S. G. Ban, Y. H. Kim, and S. K. Park, "High-Mobility and Hysteresis-Free Flexible Oxide Thin-Film Transistors and Circuits by Using Bilayer Sol-Gel Gate Dielectrics," *ACS Appl. Mater. Interfaces*, vol. 10, no. 3, pp. 2679–2687, 2018.

[12] S. Y. Han, M. C. Nguyen, A. H. T. Nguyen, J. W. Choi, J. Y. Kim, and R. Choi, "Effect of Li-doping on low temperature solution-processed indium–zinc oxide thin film transistors," *Thin Solid Films*, vol. 641, pp. 19–23, 2017.

[13] K. Hyunwoo, K. Sangsub, K. Hyunki, L. Jaeseob, K. Sangsoo, and C. Byoungdeog, "Electrical Properties of solution-processed nanolaminates of ZrO_2 and Al_2O_3 as gate

insulator materials for thin-film transistors," *J. Nanosci. Nanotechnol.*, vol. 17, no. 10, pp. 7209–7213, 2017.

[14] Q. ke, Q. Wu, L. Liang, Y. Pei, X. Lu, M. Li, K. Huang, X. Liu, and C. Liu, "Low-voltage organic thin-film transistors based on solution-processed hybrid dielectrics: Theoretical and experimental studies," *Semicond. Sci. Technol.*, vol. 32, no. 10, 2017.

[15] S. Mondal, A. Kumar, K. S. R. K. Rao, and V. Venkataraman, "Scaling behavior of fully spin-coated TFT," *AIP Conf. Proc.*, vol. 1832, no. May, pp. 23–26, 2017.

[16] P. Gao, L. J. Meng, M. P. Dos Santos, V. Teixeira, and M. Andritschky, "Study of ZrO_2-Y_2O_3 films prepared by rf magnetron reactive sputtering," *Thin Solid Films*, vol. 377–378, no. December, pp. 32–36, 2000.

[17] G. Adamopoulos, S. Thomas, P. H. Wobkenberg, D. D. C. Bradley, M. A. McLachlan, and T. D. Anthopoulos, "High-mobility low-voltage ZnO and Li-doped ZnO transistors based on ZrO_2 high-k dielectric grown by spray pyrolysis in ambient air," *Adv. Mater.*, vol. 23, no. 16, pp. 1894–1898, 2011.

[18] Y. Zhou, N. Kojima, and K. Sasaki, "Growth and dielectric properties of tetragonal ZrO_2 films by limited reaction sputtering," *J. Phys. D. Appl. Phys.*, vol. 41, no. 17, p. 175414, 2008.

[19] S. Sayan, N. V. Nguyen, J. Ehrstein, T. Emge, E. Garfunkel, M. Croft, X. Zhao, D. Vanderbilt, I. Levin, E. P. Gusev, H. Kim, and P. J. Mcintyre, "Structural, electronic, and dielectric properties of ultrathin zirconia films on silicon," *Appl. Phys. Lett.*, vol. 86, no. 15, pp. 1–3, 2005.

[20] "Zirconia (ZrO_2) Ceramics," *Advanced Ceramic Materials*, 2019. [Online]. Available: https://www.preciseceramic.com/products/zirconia-zro2/. [Accessed: 02-Jul-2020].

[21] I. Vrejoiu, D. G. Matei, M. Morar, G. Epurescu, A. Ferrari, M. Balucani, G. Lamedica, G. Dinescu, C. Grigoriu, and M. Dinescu, "Properties of ZrO_2 thin films prepared by laser ablation," *Mater. Sci. Semicond. Process.*, vol. 5, no. 2–3, pp. 253–257, 2002.

[22] A. Hojabri, "Structural and optical characterization of ZrO_2 thin films grown on silicon and quartz substrates," *J. Theor. Appl. Phys.*, vol. 10, no. 3, pp. 219–224, 2016.

[23] M. F. and L. T. F. Rebib, N. Laidani, G. Gottardi, V. Micheli, R. Bartali, Y. Jestin, E. Tomasella, "Investigation of structural and optical properties of sputtered Zirconia thin films," *Eur. Phys. JournalApplied Phys.*, vol. 43, pp. 363–368, 2008.

[24] K. Yildiz, U. Akgil, B. Coskun, and Y. Atici, "Rf-sputtering deposition of nano-crystalline zirconia thin films with high transparency," *Mater. Lett.*, vol. 94, pp. 161–164, 2013.

[25] Y. Shen, S. Shao, H. Yu, Z. Fan, H. He, and J. Shao, "Influences of oxygen partial pressure on structure and related properties of ZrO_2 thin films prepared by electron beam evaporation deposition," *Appl. Surf. Sci.*, vol. 254, no. 2, pp. 552–556, 2007.

[26] Y. Gao, J. Zhang, and X. Li, "Solution-Processed Zirconium Oxide Gate Insulators for Top Gate and Low Operating Voltage Thin-Film Transistor," *IEEE/OSA J. Disp. Technol.*, vol. 11, no. 9, pp. 764–767, 2015.

[27] M. Hasan, M. C. Nguyen, H. Kim, S. W. You, Y. S. Jeon, D. T. Tong, D. H. Lee, J. K. Jeong,

and R. Choi, “High performance solution processed zirconium oxide gate dielectric appropriate for low temperature device application,” *Thin Solid Films*, vol. 589, pp. 90–94, 2015.

[28] A. Liu, G. X. Liu, H. H. Zhu, F. Xu, E. Fortunato, R. Martins, and F. K. Shan, “Fully solution-processed low-voltage aqueous In_2O_3 thin-film transistors using an ultrathin ZrO_x dielectric,” *ACS Appl. Mater. Interfaces*, vol. 6, no. 20, pp. 17364–17369, 2014.

[29] S. M. Hwang, S. M. Lee, J. H. Choi, J. H. Lim, and J. Joo, “Fabrication of solution-processed InSnZnO/ZrO2 thin film transistors,” *J. Nanosci. Nanotechnol.*, vol. 13, no. 11, pp. 7774–7778, 2013.

[30] L. Xifeng, X. Enlong, and Z. Jianhua, “Low-temperature solution-processed zirconium oxide gate insulators for thin-film transistors,” *IEEE Trans. Electron Devices*, vol. 60, no. 10, pp. 3413–3416, 2013.

[31] J. H. Park, Y. B. Yoo, K. H. Lee, W. S. Jang, J. Y. Oh, S. S. Chae, and H. K. Baik, “Low-temperature, high-performance solution-processed thin-film transistors with peroxo-zirconium oxide dielectric,” *ACS Appl. Mater. Interfaces*, vol. 5, no. 2, pp. 410–417, 2013.

[32] X. Xu, Q. Cui, Y. Jin, and X. Guo, “Low-voltage zinc oxide thin-film transistors with solution-processed channel and dielectric layers below 150 °C,” *Appl. Phys. Lett.*, vol. 101, no. 22, pp. 3–6, 2012.

[33] H. Faber, B. Burtz, C. Dicker, E. Spiecker, and M. Halik, “Fully patterned low-voltage transparent metal oxide transistors deposited solely by chemical spray pyrolysis,” *Adv. Funct. Mater.*, vol. 23, no. 22, pp. 2828–2834, 2013.

[34] J. B. Seon, N. K. Cho, G. Yoo, Y. S. Kim, and K. Char, “Solution-processed amorphous ZrO_2 gate dielectric films synthesized by a non-hydrolytic sol-gel route,” *RSC Adv.*, vol. 8, no. 68, pp. 39115–39119, 2018.

[35] A. Azmi, J. Lee, T. J. Gim, R. Choi, and J. K. Jeong, “Performance Improvement of p-Channel Tin Monoxide Transistors with a Solution-Processed Zirconium Oxide Gate Dielectric,” *IEEE Electron Device Lett.*, vol. 38, no. 11, pp. 1543–1546, 2017.

[36] Y. J. Jeong, D. J. Yun, S. Nam, E. H. Suh, C. E. Park, T. K. An, and J. Jang, “Photo-patternable high-k ZrO_x dielectrics prepared using zirconium acrylate for low-voltage-operating organic complementary inverters,” *Org. Electron.*, vol. 33, pp. 40–47, 2016.

[37] M. C. Nguyen, M. Jiang, D. H. Lee, H. J. Bang, M. Lee, J. K. Jeong, H. Yang, and R. Choi, “Li-Assisted Low-Temperature Phase Transitions in Solution-Processed Indium Oxide Films for High-Performance Thin Film Transistor,” *Sci. Rep.*, vol. 6, no. April, pp. 1–13, 2016.

[38] D. Xiao, G. He, Z. Sun, J. Lv, P. Jin, C. Zheng, and M. Liu, “Microstructure, optical and electrical properties of solution-derived peroxo-zirconium oxide gate dielectrics for CMOS application,” *Ceram. Int.*, vol. 42, no. 1, pp. 759–766, 2016.

[39] A. Paskaleva, M. Lemberger, S. Zurcher, and A. J. Bauer, “Electrical characterization of zirconium silicate films obtained from novel MOCVD precursors,” *Microelectron. Reliab.*, vol. 43, no. 8, pp. 1253–1257, Aug. 2003.

[40] M. Lemberger, A. Paskaleva, S. Zurcher, A. J. Bauer, L. Frey, and H. Ryssel, “Electrical characterization and reliability aspects of zirconium silicate films obtained from novel MOCVD precursors,” *Microelectron. Eng.*, vol. 72, no. 1–4, pp. 315–320, 2004.

[41] G. D. Wilk and R. M. Wallace, “Stable zirconium silicate gate dielectrics deposited directly on silicon,” *Appl. Phys. Lett.*, vol. 76, no. 1, pp. 112–114, 2000.

[42] R. Lok, S. Kaya, and E. Yilmaz, “Thermal phase separation of $ZrSiO_4$ thin films and frequency- dependent electrical characteristics of the Al/$ZrSiO_4$/p-Si/Al MOS capacitors,” *Semicond. Sci. Technol.*, vol. 33, no. 5, 2018.

[43] L. Zhong, F. Chen, S. A. Campbell, and W. L. Gladfelter, “Nanolaminates of Zirconia and Silica Using Atomic Layer Deposition,” *Chem. Mater.*, vol. 16, no. 6, pp. 1098–1103, 2004.

[44] Z. M. Rittersma, E. Naburgh, T. Dao, A. H. C. Hendriks, W. F. A. Besling, E. Tois, E. Vainonen, M. Tuominen, and S. Haukka, “Physical and electrical properties of Zr-silicate dielectric layers deposited by atomic layer deposition,” *Electrochem. Solid-State Lett.*, vol. 6, no. 7, pp. 21–23, 2003.

[45] K. S. A. Y. J. Chung, D. C. Moon, J. H. Han, M. Park, J. W. Park, T. M. Chung, Y. K. Lee, and, “Trimethylsilylcyclopentadienyl tris(dimethylamino)zirconium as a single-source metal precursor for the atomic layer deposition of $Zr_xSi_{1-x}O_4$,” *Thin Solid Films*, vol. 564, pp. 140–145, 2014.

[46] D. Afouxenidis, R. Mazzocco, G. Vourlias, P. J. Livesley, A. Krier, W. I. Milne, O. Kolosov, and G. Adamopoulos, “ZnO-based thin film transistors employing aluminum titanate gate dielectrics deposited by spray pyrolysis at ambient air,” *ACS Appl. Mater. Interfaces*, vol. 7, no. 13, pp. 7334–7341, 2015.

[47] M. Esro, G. Vourlias, C. Somerton, W. I. Milne, and G. Adamopoulos, “High-mobility ZnO thin film transistors based on solution-processed hafnium oxide gate dielectrics,” *Adv. Funct. Mater.*, vol. 25, no. 1, pp. 134–141, 2015.

[48] F. M.-R. J. A. Perez-Tavares, R. Patakfalvi, L. Ortiz-Frade, C, Frausto-Reyes, Q. E. Saavedra-Arroyo, H. P-L. D. Guevara, J. Castaneda-Contreras, and V, “Acetylacetonate hydrous zirconium (Iv) complexes supported on hydrophilic polymers as new selective growth precursors of monoclinic and tetragonal zirconium oxide nanocrystals,” *Nanomater. Biostructures*, vol. 15, no. 1, pp. 185–195, 2020.

[49] J. Tauc, “Optical properties and electronic structure of amorphous Ge and Si,” *Mater. Res. Bull.*, vol. 3, no. 1, pp. 37–46, 1968.

[50] M. Esro, O. Kolosov, P. J. Jones, W. I. Milne, and G. Adamopoulos, “Structural and electrical characterization of SiO_2 gate dielectrics deposited from solutions at moderate temperatures in air,” *ACS Appl. Mater. Interfaces*, vol. 9, no. 1, pp. 529–536, 2017.

[51] A. R. Forouhi and I. Bloomer, “Optical dispersion relations for amorphous semiconductors and amorphous dielectrics,” *Phys. Rev. B*, vol. 34, no. 10, pp. 7018–7026, 1986.

[52] A. R. Forouhi and I. Bloomer, “Optical Properties of Crystalline semicond,” *Phys. Rev.*

B, vol. 38, no. 3, pp. 1865–1874, 1988.

[53] G. E. Jellison and F. A. Modine, “Parameterization of the optical functions of amorphous materials in the interband region,” *Appl. Phys. Lett.*, vol. 69, no. 3, pp. 371–373, 1996.

[54] D. A. Tashmukhamedova and M. B. Yusupjanova, “Emission and optical properties of SiO_2/Si thin films,” *J. Surf. Investig.*, vol. 10, no. 6, pp. 1273–1275, 2016.

[55] V. Astašauskas, A. Bellissimo, P. Kuksa, C. Tomastik, H. Kalbe, and W. S. M. Werner, “Optical and electronic properties of amorphous silicon dioxide by single and double electron spectroscopy,” *Journal of Electron Spectroscopy and Related Phenomena*, vol. 241. 2020.

[56] H-P. Ma, J-H. Yang, J-G. Yang, L-Y. Zhu, W. Huang, G-J. Yuang, J-J. Feng, T-C. Jen, and H-L. Lu, “Systematic study of the SiO_x film with different stoichiometry by plasma-enhanced atomic layer deposition and its application in SiO_x/SiO_2 super-lattice,” *Nanomaterials*, vol. 9, no. 1, pp. 1–13, 2019.

[57] D. A. N. and E. Cartier, “Materials characterization of and binary oxides deposited by chemical solution deposition,” vol. 1801, no. 2001, 2015.

[58] F. Bollino, E. Armenia, and E. Tranquillo, “Zirconia / Hydroxyapatite Composites Synthesized Via Sol-Gel: Influence of Hydroxyapatite Content and Heating on Their Biological Properties,” vol. 10, no. 757, pp. 1–19, 2017.

[59] S. N. Basahel, T. T. Ali, M. Mokhtar, and K. Narasimharao, “Influence of crystal structure of nanosized ZrO_2 on photocatalytic degradation of methyl orange,” *Nanoscale Res. Lett.*, vol. 10, no. 1, 2015.

[60] J. Morales, A. Maldonado, and M. D. L. L. Olvera, “Synthesis and characterization of nanoestructured TiO_2 anatase-phase powders obtained by the homogeneous precipitation method,” *2013 10th Int. Conf. Electr. Eng. Comput. Sci. Autom. Control. CCE 2013*, pp. 391–394, 2013.

[61] X. Zhang, S. Zhang, H. Zhu, X. Pan, C. Cheng, T. Yu, X. Li, Y. Cheng, G. Xing, D. Zhang, X. Luo, and B. Chen, “Frequency dispersion analysis of thin dielectric MOS capacitor in a five-element model,” *J. Phys. D. Appl. Phys.*, vol. 51, no. 5, 2018.

[62] J. Robertson and R. M. Wallace, “High-K materials and metal gates for CMOS applications,” *Mater. Sci. Eng. R Reports*, vol. 88, pp. 1–41, 2015.

[63] J. Robertson, “High K Dielectrics for Future CMOS Devices,” vol. 19, no. 2, pp. 579–591, 2009.

[64] J. Robertson, “Band offsets of wide-band-gap oxides and implications for future electronic devices,” *J. Vac. Sci. Technol. B Microelectron. Nanom. Struct.*, vol. 18, no. 3, pp. 1785–1791, 2000.

[65] F.-C. Chiu, “A Review on Conduction Mechanisms in Dielectric Films,” *Adv. Mater. Sci. Eng.*, vol. 2014, no. 7, pp. 1–18, 2014.

[66] R. Martins, P. Barquinha, I. Ferreira, L. Pereira, G. Goṇalves, and E. Fortunato, “Role of order and disorder on the electronic performances of oxide semiconductor thin film transistors,” *J. Appl. Phys.*, vol. 101, no. 4, 2007.

[67] C.-F. Huang, Y.-J. Yang, C.-Y. Peng, H.-C. Sun, C.W. Liu, Y.-C. Hsu, C.-C. Shih, and J.-S. Chen, “Polarity Change of Threshold Voltage Shifts for n-channel Polycrystalline Silicon Thin-Film Transistors Stressed by Negative Gate Bias,” *ECS Meet. Abstr.*, vol. 16, no. 10, pp. 163–167, 2008.

7 Summary, Conclusions and Further Work

7.1 Summary

The physical properties of solution processed metal oxide gate dielectrics and their implementations in ZnO – based TFTs have been investigated. The metal oxide films were deposited by a simple and low-cost effective spray coating technique at moderate temperatures (< 550 ^{o}C). Several characterization techniques including ultraviolet-visible (UV-Vis) spectroscopy, Fourier-transform infrared spectroscopy (FTIR), grazing incidence x-ray diffraction (GIXRD), atomic force microscopy (AFM), impedance spectroscopy, I – V and field effect measurements were investigated.

The thesis presented here was organised in two parts. The first part entails the theoretical aspect of the thesis while the second part entails the experimental chapters including the summary, conclusion and recommendations for future work.

The first part constitutes the introduction of metal oxide based TFTs (chapter 1), theory and operational characteristics of dielectrics (chapter 2) and experiment (chapter 3) while the second part constitutes the experimental chapters such as tantalum aluminate (chapter 4), hafnium titanate (chapter 5) and zirconium silicate thin films (chapter 6).

For tantalum aluminate thin films, it was observed that the optical bandgap increases with addition of Al content. It varies between 4.9 eV for TaO_x and 8.8 eV for AlO_x and the stochiometric $Ta_{1-x}Al_xO_y$ exhibited a bandgap of 5.4 eV. Additionally, it was observed that the Urbach energy varies from 375 – 1000 meV with the 40 % Al content exhibiting the lowest value of 288 meV. The latter was presumed to be probably the beginning of the formation of the stochiometric $Ta_{1-x}Al_xO_y$ films. For the structure and surface properties investigation, $Ta_{1-x}Al_xO_y$ films were amorphous and smooth with surface roughness of < 1 nm. The static dielectric constant of $Ta_{1-x}Al_xO_y$ films were investigated and it was observed that the values vary linearly between 24 and 7 due to the low dielectric constant of AlO_x (7) combining with high dielectric constant of TaO_x (24). Additionally, the Nyquist plots of $Ta_{1-x}Al_xO_y$ films reveals the stability of the films in a MIM stack and was supported by the equivalent circuits provided in the inset of the plots, indicating excellent capacitive properties such as large shunt and low series resistance. The leakage current densities of $Ta_{1-x}Al_xO_y$ films at 1 and 2 MV/cm showed a decreasing trend with addition of Al content. Typical values between 10^{-6} – 10^{-10} A/cm^2 and 10^{-3} – 10^{-9} A/cm^2 were obtained both at 1 and 2 MV/cm respectively. Further information regarding the nature of the leakage current findings, suggested that the current transport in $Ta_{1-x}Al_xO_y$ films may be dominated by Schottky emission (SE), Fowler Nordhiem (FN) and Poole Frenkel (PF) mechanism, however, more investigation is needed to determine the actual conduction mechanism such as the temperature dependence of the films. The effective electron mass and potential barrier height of $Ta_{1-x}Al_xO_y$ films were calculated from the slope of the FN and intercept of the SE plots. The values vary between 0.03 – 0.02 m_o and 1.02 – 1.01 eV for the effective electron mass and barrier height respectively. The stochiometric $Ta_{1-x}Al_xO_y$ films exhibited the maximum barrier height value of 1.16 eV, suggesting a good insulating device. Finally, the performance of ZnO – based TFTs employing stochiometric $Ta_{1-x}Al_xO_y$ gate dielectric showed promising characteristics such high electron mobility of 16 cm^2/Vs, high current modulation ratio of 10^5, threshold voltage (V_{th}) of 3.2 V, subthreshold

swing (SS) of 0.56 V/dec, interface trap density (D_{it}) of 7.7 x 10^{12} cm^{-2}, low operation voltage of 4 V and negligible hysteresis.

For hafnium titanate thin films, the properties were investigated in two parts. The first part of the investigation was based on as-deposited films while the second part was based on effect of post-deposition annealing of the films.

For the as-deposited films, the optical bandgap of $Hf_{1-x}Ti_xO_y$ films varies between 5.8 and 3.8 eV while its Urbach energy varies between 156 and 315 meV with increasing Ti content. The structure of $Hf_{1-x}Ti_xO_y$ films were amorphous with addition of Ti content except for pure HfO_x and TiO_x films that exhibited a monoclinic and tetragonal anatase phase respectively. The AFM images taken in contact mode showed a surface roughness of about 1 nm that demonstrate quality and smooth surface of $Hf_{1-x}Ti_xO_y$ films. As a gate dielectric, $Hf_{1-x}Ti_xO_y$ films exhibited a static dielectric constant between 14 and 60 and a current density at 1 MV/cm between 6 x 10^{-7} and 10 A/cm^2 with increasing Ti content. For the stability, only Hf rich samples including stochiometric $Hf_{1-x}Ti_xO_y$ films were stable as illustrated by the Nyquist plots. The non-stabilities of the Ti rich samples were attributed to the increasing leakage current due to low bandgap of $Hf_{1-x}Ti_xO_y$ films. The conduction mechanism of $Hf_{1-x}Ti_xO_y$ films were found to be dominated by Poole Frenkel mechanism suggesting a bulk process. It is important to mention that stochiometric $Hf_{1-x}Ti_xO_y$ films exhibited a bandgap of 4.4 eV, Urbach energy of 199 meV, static dielectric constant of 30 and leakage current density of 0.3 A/cm^2 at 1 MV/cm. The ZnO – based TFTs employing stochiometric $Hf_{1-x}Ti_xO_y$ gate dielectric showed an electron mobility of 7 cm^2/Vs, current modulation ratio of 10^7, V_{th} of 0.6 V, SS of 0.17 V/dec, D_{it} of 2.1 x 10^{12} cm^{-2}, low operation voltage of 3 V and huge hysteresis.

While for the effect of post-deposition annealing $Hf_{1-x}Ti_xO_y$ films, the composite films were annealed at 800 °C for 30 minutes in air since both pure HfO_x and TiO_x already exhibited crystalline phase. As result, the optical bandgaps were 4.4, 4.36 and 4.1 eV for $Hf_{75}Ti_{25}O_x$, $Hf_{50}Ti_{50}O_x$ and $Hf_{25}Ti_{75}O_x$ films respectively. Their Urbach energy values were 338, 223 and 475 meV respectively. The bandgap values were slightly lower than the as-deposited ones while the Urbach energy were slightly higher than the as-deposited ones. The former was expected considering the annealing effect of $Hf_{1-x}Ti_xO_y$ films while the latter was unexpected and may be due to oxygen vacancies caused by the defect of the TiO_x films. The GIXRD investigation revealed the formation of a stochiometric $Hf_{50}Ti_{50}O_x$ films that was confirmed to be an orthorhombic-like structure and it is consistent with the reported structure of $Hf_{1-x}Ti_xO_y$ films in the literatures. However, the non-stochiometric samples were also crystalline and were found to be mixture of HfO_2 + TiO_2 instead. Their surface properties were found to be rougher than the as-deposited ones due to the crystallization of the films caused by the annealing effect, which results to the RMS values of 2.15, 1.95 and 1.18 nm for $Hf_{75}Ti_{25}O_x$, stochiometric $Hf_{50}Ti_{50}O_x$ and $Hf_{25}Ti_{75}O_x$ films respectively. Their impedance studies showed a static dielectric constant of 20, 38 and 35 while their I – V measurements showed a current density (at 1 MV/cm) of 6 x 10^{-5}, 5 x 10^{-3} and 10 A/cm^2 respectively. The Nyquist plots showed stable system for only $Hf_{75}Ti_{25}O_x$ and stochiometric $Hf_{50}Ti_{50}O_x$ films. Further investigation on the conduction mechanism suggested not dominant conduction in SE and PF plots as both mechanisms demonstrated linearity over extended electric fields. However, in the FN plots only stochiometric $Hf_{50}Ti_{50}O_x$ showed linear behaviour over wide electric field suggesting an interface process and as a result, the effective mass of electron and barrier height of the films

were found to be 0.003 m_o and 0.49 eV. Such low barrier height value explains the excessive leakage current in stochiometric $Hf_{1-x}Ti_xO_y$ films, thus no working TFT device was achieved.

Finally for zirconium silicate thin films, the optical properties of the films showed a bandgap that varies between 5.8 and 8 eV with increasing Si content. Their Urbach values fluctuates between 220 and 300 meV and reaches maximum at 540 meV for stochiometric $Zr_{1-x}Si_xO_y$ films. Such maximum value is a characteristic feature of disordered material caused by addition of Si content. It is however important to mention that the Urbach energy of SiO_x was not calculated due to inability of the UV-Vis spectrometer to characterize wide bandgap materials greater than 6.5 eV. The GIXRD investigation revealed that only pure ZrO_x films exhibited diffraction peaks that were the reflection of either tetragonal or cubic phase ZrO_x films. The morphology of $Zr_{1-x}Si_xO_y$ films showed a decreasing surface roughness that varies between 6.59 and 0.31 nm with addition of Si content. As gate dielectrics, $Zr_{1-x}Si_xO_y$ films showed a decreasing static dielectric constant from 23 – 4.2, stable in all cases as confirmed by the Nyquist plots and leakage current density (at 1 MV/cm) from 3 x 10^{-5} – 10^{-4} A/cm^2 with the stochiometric $Zr_{1-x}Si_xO_y$ exhibiting the lowest value of 10^{-7} A/cm^2. Further investigations on the conduction mechanism suggested that Poole Frenkel is the dominant mechanism, suggesting a bulk process. For the TFTs, the ZnO – based TFTs employing stochiometric $Zr_{1-x}Si_xO_y$ gate dielectric exhibited the best properties such as high electron mobility of 57 cm^2/Vs, current modulation ratio of 10^6, SS of 0.28 V/dec, D_{it} of 5 x 10^{12} cm^{-2}, V_{th} of 0.1 V, low operation voltage of 4 V and negligible hysteresis.

By comparison, tantalum aluminate, hafnium titanate and zirconium silicate thin films demonstrated similar trends in some aspect of results. For instance, the optical bandgap and the static dielectric constant plots as a function of different ratios have already illustrated that when a high-k oxide combines with low-k one, a linear or an exponential trend is expected to occur either increasingly or decreasingly depending on the combination of the materials. However, it is equally important to mention that even with such similarities, different materials exhibit different properties.

In the tantalum aluminate chapter, the optical bandgap value (5.4 eV) was higher than the one (4.53 eV) reported Rico-Fuentes et al. [1], for stochiometric tantalum aluminate films deposited by ultrasonic spray pyrolysis technique. They further reported a dielectric constant of 15, which is close to the value 13 reported in this study. Also, their leakage current density at 1.2 MV/cm was in order of 10^{-7} A/cm^2 while 10^{-8} A/cm^2 was obtained for this study. These findings demonstrated significant improvement on Rico-Fuentes et al. [1], work for tantalum aluminate films. For the TFTs, this is the first ever investigated TFT device employing stochiometric tantalum aluminate gate dielectric and it has already demonstrated excellent performance for future integration into variety of electronic applications.

The hafnium titanate chapter emerged as the first ever solution processed one. In comparison with the ones deposited by the vacuum-based techniques, the optical bandgap of as-deposited stochiometric hafnium titanate film was found to be 4.4 eV which was in good agreement with value reported by Wang et al. [2], for sputtered hafnium titanate films. Further to their investigations, they reported a dielectric constant of 31.3, which is also in good agreement with the value 30 reported in this study. However, they reported a leakage current density of 1 mA/cm^2 at 3 V while 0.3 A/cm^2 at 1 MV/cm was measured for this study.

The measurement of the leakage current density at 3 V, was found to be 8 mA/cm^2, suggesting slight improvement on their achievement.

Finally the optical bandgap of stochiometric zirconium silicate films were found to be 6.1 eV which was slightly higher than the value 5.9 eV reported by Hays et al. [3], for RF sputtered zirconium silicate films. The calculated static dielectric constant of stochiometric zirconium silicate films was 12 and is in good agreement with the values reported by both Zhong et al. [4], (12.5) and Rittersma et al. [5], (13), for zirconium silicate films deposited by ALD respectively. The latter further reported a leakage current density of 1 mA/cm^2 at 4 V while for stochiometric zirconium silicate films it was 10^{-7} A/cm^2 at 1 MV/cm and 10^{-8} A/cm^2 at 4 V. This observation shows remarkable improvement on the electrical properties of zirconium silicate films as compared to the work carried out by Rittersma et al. [5].

7.2 Conclusion

To conclude on the investigated chapters, the deposition of high-k metal oxide gate dielectric as alternatives to conventional SiO_2 has been tremendously achieved. One of the most important criteria of choosing a suitable dielectric material is that it must be of a high dielectric constant typically between 10 and 30 and have a wide bandgap typically above 5 eV. High-k oxides with higher dielectric constant (> 30) can lead to fringe fields from the gate to the drain or source while very low dielectric constant (< 10) can lead to tunneling current thereby causing degradation in the performance of a TFT device. Additionally, wide bandgap dielectric metal oxides (> 5 eV) must act as an insulator by having a conduction and valence band offset of at least 1 eV to prevent carrier injection into the oxide bands of the dielectrics. Furthermore, a dielectric metal oxide must have an excellent quality interface between the oxide and the semiconductor and must be thermodynamically and chemically stable with the semiconductor to prevent reaction between the two layers.

In this thesis, the stochiometric tantalum aluminate, hafnium titanate and zirconium silicate thin films were all of interest and have practically satisfied most of these above-mentioned conditions especially when in contact with the ZnO ($E_g \sim 3.2$ eV) semiconducting channel.

For instance, the stochiometric tantalum aluminate films exhibited a high dielectric constant of 13 and a wide bandgap of 5.4 eV. The dielectric constant was within the acceptable range of choosing a suitable dielectric metal oxide as well as its bandgap. The conduction band offset of the latter was calculated as 1.7 eV while the valence band offset was 0.5 eV. These values were obtained from the calculated bandgap value of stochiometric tantalum aluminate films with the assumption that their bandgaps are located at the middle of the fermi energy level of the ZnO as already illustrated in chapter 5. The surface roughness of the films was < 1 nm indicating smooth films and showed quality interface with ZnO. Furthermore, the interface trap density of the TFT was calculated as 10^{12} cm^{-2} which is quite acceptable for oxide/semiconductor interface. Additionally, tantalum aluminate films were thermodynamically and chemically stable when in contact with ZnO.

Also, the stochiometric hafnium titanate films exhibited a high dielectric constant of 30 and bandgap of 4.4 eV. Despite satisfying the high-k condition, the narrow bandgap when in contact with ZnO is a concern as it does not satisfy the band offset condition. Further investigation on their calculated conduction and valence band offsets showed 1.2 eV and 0 eV respectively. However, the films exhibited smooth surface roughness of 1 nm, indicating quality interface with interface trap density of 10^{12} cm^{-2} and it is thermodynamically and chemically stable when in contact with ZnO films.

Finally, the calculated dielectric constant and bandgap of stochiometric zirconium silicate films were 12 and 6.1 eV respectively. The calculated conduction and valence band offsets when in contact with ZnO were 2 eV and 0.8 eV respectively. The surface roughness of stochiometric zirconium silicate films were calculated as 0.56 nm, indicating smooth surface and quality interface, interface trap density of 10^{12} cm^{-2} and it is thermodynamically and chemically stable with ZnO.

Based on the achieved results, one can conclude that only the stochiometric hafnium titanate films did not satisfy the conduction band offset condition due to its narrow bandgap when in contact with ZnO. The combination of oxides of hafnium and titanium hugely contributed to such narrow bandgap and can be improved by introducing small amount of titanium content (< 1 %) serving as dopant instead of composite, however, the material properties may entirely be different from the ones obtained for the stochiometric hafnium titanate films.

7.3 Further Work

Based on the promising results obtained, further work is essential and necessary improvements must be considered to improve the performance of the devices under investigation. As already seen in the conduction mechanisms of tantalum aluminate films, no dominant mechanism can be identified as all investigated mechanisms (SE, FN and PF) showed dominant conduction in all cases. However, such issues can be addressed by investigation based on temperatures to identify the actual conduction mechanism. Also, the field effect measurements of ZnO – based TFTs employing stochiometric tantalum aluminate gate dielectric showed excellent characteristics and such characteristics needs to be studied under bias stress measurement to further investigate the stability and reliability of the TFT device in terms of V_{th} shift, mobility and on current deterioration.

For the as-deposited stochiometric hafnium titanate films, the I – V measurements showed an excessive leakage current of the films dominated by PF conduction mechanism. Such leakage current issues can be addressed by depositing a thin layer of aluminium oxide film on the stochiometric hafnium titanate films to reduce the effect of the leakage current of the films. As already known aluminium oxide is one of the best dielectric films in terms of suppressing leakage current of devices because of it is amorphous structure and wide bandgap (8 eV).

Finally, for the zirconium silicate films, since the TFT devices were fabricated with Al S/D metals, it is also important to investigate the performance of the ZnO – based TFTs on

different work functions of S/D metals such as Au, Ca and Cu and to compare with the work function of Al metal. Additionally, the electron transport as a function of transistor channel length (L) as well as channel resistance at different gate voltages can equally be investigated for future study. The former will reveal how electron mobility depend on the channel length while the latter will reveal the effect of the channel resistance as a function of gate voltage for different work functions of S/D metals.

For wider research direction, multicomponent dielectrics such as hafnium silicate, hafnium aluminate, zirconium aluminate and tantalum silicate can equally be investigated for future study as alternatives to conventional SiO_2 gate dielectric. Such materials exhibit a higher dielectric constant than SiO_2 and wide bandgap (> 5 eV) for future integration into TFT applications. The ZnO or In_2O_3 semiconducting channel can be employed as the semiconducting channel with different metal work functions of source and drain contacts such as Al, Cu, or Au. Such results can be comparable to the ones obtained in this thesis.

7.4 References

[1] O. Rico-Fuentes, J. C. Alonso, G. Santana, and A. Ortiz, "Ultrasonic Spray Pyrolysis Deposition and Characterization of Tantalum–Aluminum Oxide Thin Films," *J. Electrochem. Soc.*, vol. 154, no. 12, p. G277, 2007.

[2] Y. H. Wang, J. Zhang, Y. Ye, Y. Wang, B. Wang, and Y. Jin, "Composition dependence of band alignment and dielectric constant for $Hf_{1-x}Ti_xO_2$ thin films on Si (100)," *J. Appl. Phys.*, vol. 107, no. 10, 2010.

[3] D. C. Hays, B. P. Gila, S. J. Pearton, B-J. Kim, and F. Ren, "Band alignment in $ZrSiO_4$/ZnO heterojunctions," *Vacuum*, vol. 125, pp. 113–117, 2016.

[4] L. Zhong, F. Chen, S. A. Campbell, and W. L. Gladfelter, "Nanolaminates of Zirconia and Silica Using Atomic Layer Deposition," *Chem. Mater.*, vol. 16, no. 6, pp. 1098–1103, 2004.

[5] Z. M. Rittersma, E. Naburgh, T. Dao, A. H. C. Hendriks, W. F. A. Besling, E. Tois, E. Vainonen, M. Tuominen, and S. Haukka, "Physical and electrical properties of Zr-silicate dielectric layers deposited by atomic layer deposition," *Electrochem. Solid-State Lett.*, vol. 6, no. 7, pp. 21–23, 2003.